Expanding the Toolbox: Exploring the Lewis Acid Assisted $^{19}F/^{18}F$-Isotopic Exchange Radiochemistry of BODIPY Dyes, and DiPODS: Development of a Novel Bioconjugation Reagent.

A Thesis Submitted to the College of

Graduate & Postdoctoral Studies

In Partial Fulfillment of the Requirements

For the Degree of Master of Science

In the Department of Chemistry

University of Saskatchewan

Saskatoon

By

Whitney Shannon

Permission to Use

In presenting this thesis in partial fulfillment of the requirements for a graduate degree from the University of Saskatchewan, I agree that the Libraries of this University may make it freely available for inspection. I further agree that permission for copying of this thesis in any manner, in whole or in part, for scholarly purposes may be granted by the professors who supervised this thesis work or, in their absences, by the Head of the Department or the Dean of the College in which my thesis work was done. It is understood that any copying or publication or use of this thesis or parts thereof for financial gain shall not be allowed without my written permission. It is also understood that due recognition shall be given to me and to the University of Saskatchewan in any scholarly use which may be made of any material in my thesis.

Requests for permission to copy or to make other use of material in this thesis in whole or in part should be addressed to:

Head of the Department of Chemistry

170 Thorvaldson Building, 110 Science Place

University of Saskatchewan

Saskatoon, Saskatchewan S7N 5C9

Canada

Dean of College of Graduate & Postdoctoral Studies

116 Thorvaldson Building, 110 Science Place

University of Saskatchewan

Saskatoon, Saskatchewan S7N 5C9

Canada

Abstract

Radiochemical diagnostics and therapeutics benefit from pairing with a compliment second imaging modality. However, methods to radiolabel and link these molecules to targeting vectors are problematic. In this dissertation, I explored new radiosynthetic strategies for producing fluorophore-based bimodal agents and new bioconjugation reagents for antibody drug conjugation with improved *in vivo* stability.

^{18}F-radiolabeled 4,4-difluoro-4-bora-3a,4a-diaza-*s*-indacene (BODIPY) fluorophores are hypothetically ideal bimodal imaging candidates. Preliminary experiments focused on facilitating ^{19}F/^{18}F-transfluorination of *Pseudomonas aeruginosa*-selective BODIPY dye, CDy11, using Lewis acidic [^{18}F]F-BODIPY labeling strategies described in literature. However, the conventionally applied tin(IV)-chloride ($SnCl_4$) Lewis acid's instability affords reaction yield variability, and further promoted degradation of the CDy11. Thus, research transitioned towards investigating an alternative Lewis acid. To our knowledge, we are the first to use hydrated magnesium nitrate [$Mg(NO_3)_2$] as an air-stable substitute for promoting ^{18}F-fluorination of commercially-available BODIPY dyes. Order of reagent addition significantly affected the ^{19}F/^{18}F-isotopic exchange reaction; with addition of azeotropically dried [^{18}F]F-TBAF to a mixture of the commercial dye and Lewis acidic agent proving most effective. ^{19}F/^{18}F-transfluorination was achieved using both $SnCl_4$ and $Mg(NO_3)_2$ to varying degrees. Increasing the equivalences of applied $Mg(NO_3)_2$ salt generally improved radiochemical yields.

Bioconjugation chemistry enables the covalent attachment of molecules of interest to larger proteins such as antibodies. While conjugation with thiol groups (cysteine) in antibodies is common, conventional maleimide-based coupling agents are prone to *in vivo* hydrolysis. Price lab research efforts sought to develop radioimmunoconjugates that operate through two phenyloxadiazolyl methyl sulfone (DiPODS) functionality to form irreversible bonds with antibody cysteine pairs. My contribution was to assist in synthesizing several of the multistep synthesis products and apply spectroscopic methods towards analysis of the initial step's product mixture, which was hypothesized to exist as a rotameric mixture. Several intermediate agents were

successfully synthesized to produce the desired DIPODS end product. The three components of the 5-[[(1,1-dimethylethoxy)carbonyl]amino]-1,3-dimethyl ester (compound **1**)product mixture were attributed to an inseparable mixture of rotamers, doubly-di-*tert*-butyl decarbonate (Boc)-protected derivative of the compound, and imidic acid tautomers using spectroscopic methods including variable temperature ^{1}H NMR. Lastly, an additional chemical species was observed via ^{1}H NMR as temperature was increased to 75 °C and attributed to a second set of product rotamers. Ultimately, this thesis served to improve future radiotherapeutic agents and radio-diagnostics through the investigation of alternative and reproducible [^{18}F]F-BODIPY labeling strategies and radioimmunoconjugates of improved stability.

Acknowledgements

In an attempt to thank all those who have made this body of work possible, foremost gratitude must be given to my co-supervisors, Dr. Eric Price and Dr. Steven Siciliano. Thank you both for your guidance, support, patience, and for the privilege to learn from both of your expertise. Sincerest thanks to my laboratory colleagues for many laughs and lessons. Special thanks must be given to the staff of the Sylvia Fedoruk Canadian Centre for Nuclear Innovation for providing a safe and enthusiastic work environment, Kelly Christopher for bringing so much life and enthusiasm into any and all research spaces and to Dr. Elaheh Khozeimeh Sarbisheh for being both a role model and mentor. Thank you for believing in me and pushing me to strive for excellence.

I would like to thank the Department of Chemistry, the College of Arts and Science, and the College of Graduate and Postdoctoral Studies at the University of Saskatchewan, my committee members as well as the funding agencies whom have contributed to the work performed during the course of my graduate studies; namely the NSERC CREATE SAFER program.

Lastly, to my family, whom has always been my greatest source of love and inspiration, none of this would have been possible without you. Thank you for exemplifying what it means to be both hard working and caring. To my parents especially, the person I am today is credited to you and being your daughter is my greatest source of pride.

Thanks Everyone,

Whitney Shannon

Table of Contents

List of Tables

List of Figures

List of Schemes

Glossary of Abbreviations and Symbols

$[^{177}Lu]Lu^{3+}$	Lutetium-177
$[^{18}F]F^{-}$	Fluorine-18
$[^{19}F]F^{-}$	Fluorine-19
$[^{18}O]O$	Oxygen-18
$[^{89}Zr]Zr^{4+}$	Zirconium-89
”	Inches
%	Percentage
°	Degrees
°C	Degrees Celsius
®	Registered trademark
Å	Angstrom
ADC	Antibody drug conjugate
AIDs	Acquired immunodeficiency disorders
AIO	All in One
Ar	Aromatic
ATR	Attenuated total reflection
bs	Broad singlet
Boc	Tert-butoxycarbonyl protecting group
BODIPY	4,4-difluoro-4-bora-3a,4a-diaza-s-indacene
^{13}C	Carbon-13
C18	Carbon-18, silica-bound 18-carbon aliphatic chains as a chromatophraphic stationary phase
calc	Calculated
CDy11	Compound of designation yellow 11
cm^{-1}	Reciprocal centimeter, wavenumber unit
COSY	Correlation spectroscopy
d	Doublet

$D°_{298}$	Standard bond dissociation value at 298 Kelvin
DCM	Dichloromethane
DEPT135	Distortionless enhancement by polarization transfer (135°)
DFT	Density functional theory
DIEA	*N*, *N*-diisopropylethylamine
DiPODS	Double phenyloxadiazolyl methyl sulfone
DMAP	4-Dimethylaminopyridine
DMF-d_7	Deuterated dimethylformamide
DMSO-d_6	Deuterated dimethyl sulfoxide
DNA	Deoxyribonucleic acid
e^-	Electron
EDC	1-Ethyl-3-(3-dimethylaminopropyl)carbodiimide
eDNA	Environmental deoxyribonucleic acid
eq	Equivalents
ESI^+	Electrospray ionization, positive ionization mode
EtOAc	Ethyl Acetate
EtOH	Ethanol
F^-	Fluoride anion
F_2	Difluoride, fluorine gas
Fap	Pseudomonas-associated functional amyloids
FDG	Fluorodeoxyglucose
FDI	Field desorption ionization
FTIR	Fourier Transform Infra-Red
g	Gram
G	Gibbs free energy
h	Hour
H	Enthalpy
H^+	Proton
^1H	Hydrogen-1
$\{^1H\}$	Proton decoupled
H1	Heater (Trasis mini All In One radiosynthesis system component)

H_2O	Water
HCl	Hydrochloric acid
HF	High flow
HIV	Human immunodeficiency virus
HMQC	Heteronuclear multiple bond correlation
HOMO	Highest occupied molecular orbital
HPLC-MS	High performance liquid chromatography-mass spectrometry
HRMS	High resolution mass spectrometry
HSAB	Hard Soft Lewis Acid Base
Hz	Hertz
ID	Internal diameter
IgG	Immunoglobulin G
IR	Infra-Red
J	Coupling constant
K	Proportionality constant relating detector response (in counts) to an activity concentration
K^+	Potassium cation
kcal	Kilocalorie
K_2CO_3	Potassium carbonate
keV	Kiloelectronvolts
Kryptofix® 222	4, 7, 13, 16, 21, 24-Hexaoxa-1,10-diazabicyclo[8.8.8] hexacosane
LA	Lewis Acid
LC	Liquid chromatography
LF	Low flow
LUMO	Lowest unoccupied molecular orbital
m	Multiplet (NMR), medium (FTIR)
M	Molar/molarity
$[M]^+$	Molecular ion
MBq	Mega Becquerel
MeCN	Acetonitrile
MeI	Methyl iodide

MeV	Mega electronvolts (unit value $x10^6$)
mg	Milligram
Mg^{2+}	Magnesium(II) cation
$Mg(NO_3)_2$	Magnesium nitrate
MHz	Mega hertz
min	Minute
mL	Millilitre
mm	Millimeter
mmol	Millimole
mol	Mole
MSBT	Methylsulfonyl benzothiazole
m/z	Mass to charge ratio
N	Normal/Normality (concentration)
Na_2CO_3	Sodium carbonate
NaOH	Sodium hydroxide
Na_2SO_4	Sodium Sulphate
nm	Nanometer
NMR	Nuclear magnetic resonance
OAc	Acetate functional group
OD	Outer diameter
OH	Hydroxide functional group
OTf	Triflate functional group
P	Activity Pump (Trasis mini All in One radiosynthesis system component)
PAO1	*Pseudomonas aeruginosa*
PET	Positron emission tomography
pH	Potential of hydrogen
PODS	Phenyloxadiazolyl methyl sulfone
ppm	Parts per million
psi	Pounds per square inch
PTFE	Polytetrafluoroethylene
$R\text{-}BF_2$	Functionalized difluoroboron

RCY	Radiochemical yield
rpm	Revolutions per minute
r.t.	Room temperature
s	Singlet (NMR), strong (FTIR)
S	Entropy
SA1/SA2	Syringe actuators 1 and 2 (Trasis mini All in One radiosynthesis system component)
SCCS	Saskatchewan Centre for Cyclotron Sciences
Sn^{2+}	Tin(II) cation
Sn^{4+}	Tin(IV) cation
$SnCl_4$	Tin(IV) tetra-chloride
SPE	Solid phase extraction
t	Triplet
T	Temperature
TBAB	Tetrabutylammonium bicarbonate
TBAF	Tetrabutylammonium fluoride
TEAB	Tetraethylammonium bicarbonate
TEAF	Tetraethylammonium fluoride
TFA	Trifluoroacetic acid
TfO_2	Trifluoromethanesulfonic anhydride
THF	Tetrahydrofuran
Ti^{4+}	Titanium(IV) cation
$TiCl_4$	Titanium tetrachloride
TMS	Trimethylsilane
TMSOTf	Trimethylsilyl trifluoromethanesulfonate
UHPLC	Ultra-high performance liquid chromatography
μm	Micrometer
μmol	Micromole
UV-Vis	Ultraviolet-visible spectroscopy
V	Vacuum (Trasis mini All in One radiosynthesis system component)
Va	Vacuum activation (Trasis mini All in One component status)

w	Weak
α	Alpha particle
β+	Positron
γ	Photon, typically representing gamma rays
Δ	Delta, change defined as final minus initial conditions
δ	Chemical shift
μL	Microliter
μm	Micrometer
ν_e	Neutrino
$\tilde{\nu}$	Wavenumber

.

General Introduction

Radiochemistry

Elements vary from one another by virtue of their characteristic atomic numbers or the number of protons associated with a specific atom. However, while the atomic number may classify two atoms as being of the same element, they may differ from one another based on the number of neutrons held at their cores. The nucleus is comprised of protons and neutrons, and when the number of protons remains the same but the number of neutrons varies, the result is different isotopes of the same element. Some isotopes are radioactive (radionuclides, radioisotope), which are isotopic variants with an unfavorable nuclear ratio of protons and neutrons, making the atom unstable. As such, unstable nuclei stabilize themselves through spontaneous transformation to alter the number of neutrons and protons at their core, emitting radiation in the process.

The type of energy emitted by a radioactive substance depends on how the radionuclide stabilizes itself. For example, heavy unstable nuclei opt to reduce their number of protons and neutrons through alpha-decay, wherein an alpha-particle ($^{4}_{2}\alpha$, $^{4}_{2}\mathrm{He}$) is emitted. Alpha-particles undergo high energy expulsion from the nucleus but quickly lose energy as the particle travels in space. The alpha particle's trajectory can thus be stopped by the outermost layer of skin or by a piece of paper. Nuclei that undergo beta-decay release smaller, more energetic particles. The charge of the particle depends on the nature of the nuclei from which it came. Neutron-rich species will convert a neutron into a proton, expelling an electron ($^{0}_{-1}\beta$), while proton-rich species, as will be discussed in further detail later, convert a proton into a neutron via non-emissive electron capture or positron emission ($^{0}_{+1}\beta$) processes. The lighter beta-particles travel with greater energy than alpha-particles but can still be halted by aluminum foil or a ~1 cm thick layer of glass or plastic. Finally, gamma-radiation, the emission of pure electromagnetic energy, is released as an excited unstable radioisotope rearranges itself into a lower excitation state.[1] Gamma-photons (γ) travel with such high energy, they readily pass through the barriers that would halt alpha- and beta-particles and even pass through the human body with minimal attenuation. Consequently, denser materials like lead and concrete are needed to shield from their emission (**Figure 1.1**).

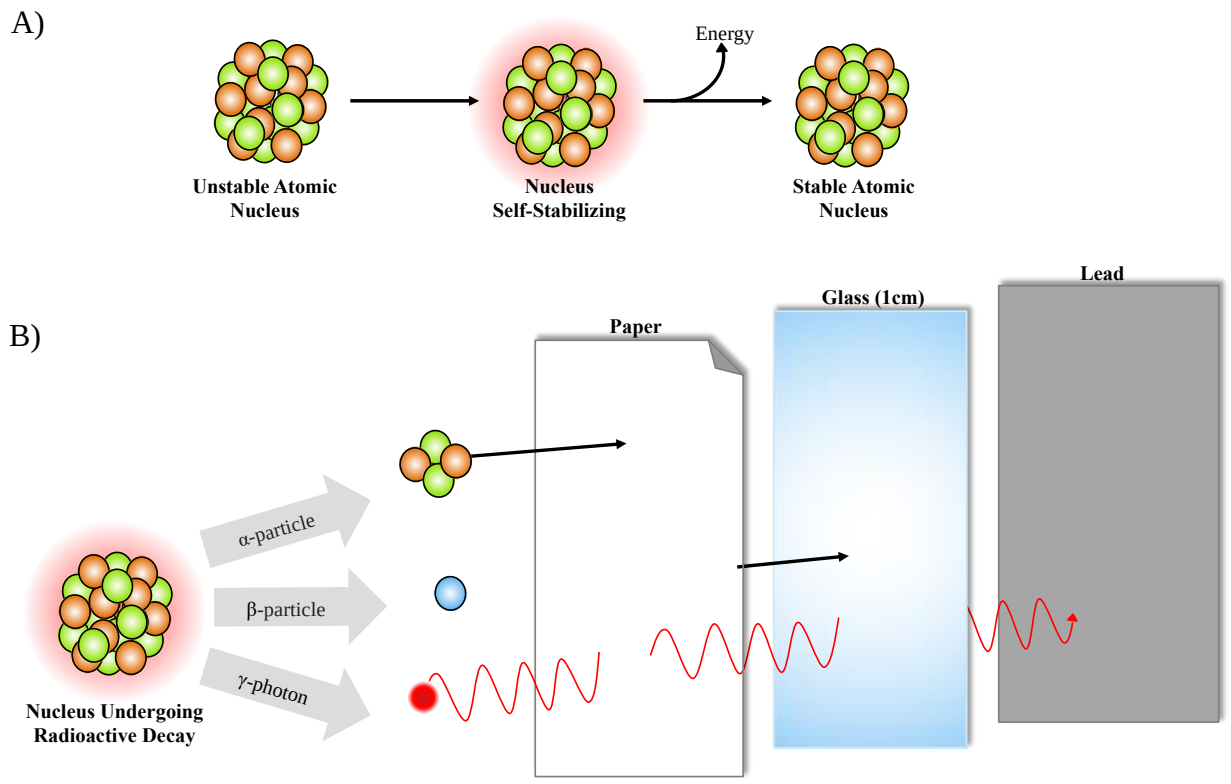

Figure 1.1. A) Illustration of an unstable nucleus stabilizing and releasing energy in the process. B) Three potential energy emission products and their penetrance through increasingly dense materials. Figure adapted from (Issard, 2015).[2]

Radiochemistry is the study of naturally occurring and man-made radionuclides and focuses on the following: 1) investigating the synthetic routes by which radionuclides are produced and/or incorporated into molecular frameworks, and 2) utilizing the emissive properties of radioactive substances for the purpose of investigating chemical and biochemical processes in the form of probes/diagnostics or altering the surrounding environment as biomedical treatments.[3 4] Radiochemical techniques are used in numerous scientific domains such as materials science, pharmaceutical research, and environmental sciences to name a few.[5] These research efforts vary significantly in their motivations and assess drastically differing systems. What is more, as the focus of research continuously changes, the radiochemistry associated with evaluating those interests must be modified to accommodate these differing needs. Increasingly specific radiochemical probes are needed to assess wider arrays of chemical and biological phenomena. New and increasing demands for radionuclide-bearing diagnostic and therapeutic agents facilitate

the demand for highly replicable radiolabeling methods for larger scale production. The success of imaging agents as well as the potency of theranostic agents can be ameliorated by improving the stability of their delivery scaffolds. The following will discuss matters pertaining to these issues in further depth.

1.1. Fluorine-18 ([^{18}F]F$^-$).

PET imaging techniques apply an array of radioisotopes to investigate biological processes. Of these, fluorine-18 ([^{18}F]F$^-$) is considered an attractive β^+-emitter for molecular imaging by virtue of the numerable advantages that its nuclear and physical properties provide.

1.1.1. Fluorine in Medicine.

Fluorine plays a vital role in medicinal chemistry, with fluorinated compounds comprising nearly a third of the best-selling pharmaceuticals. The enthalpic strength of the carbon-fluorine bond is comparatively stronger than that of carbon-hydrogen bonds (C-F, 112 kcal/mol vs C-H, 98 kcal/mol), contributing to fluorinated compounds' superior metabolic stability and bioavailability. Furthermore, fluorination of aromatic biomolecules increases their lipophilicity and consequently improves their tissue absorption and distribution.[6 7]

1.1.2. Fluorine-18 Radioisotope.

Radioactive decay of fluorine-18 occurs as the unstable "proton rich" nucleus of the parent fluorine-18 atom stabilizes by converting one of its protons into a neutron. This change is termed β^+-decay (positron decay) and is achieved through either electron capture or by positron emission processes.

Electron capture occurs as an electron from a proton rich atom's surrounding inner shell is drawn into its nucleus to combine with a proton and form a neutron; ejecting a chargeless neutrino (ν_e) in the process of producing the stable oxygen-18 daughter nuclide (**Scheme 1.1**). While a small number of fluorine-18 atoms do undergo electron capture, most of them stabilize their nuclei through positron emission.

$$^{18}_{9}\mathrm{F} + {}^{0}_{-1}\mathrm{e} \rightarrow {}^{18}_{8}\mathrm{O} + \nu_e$$

Scheme 1.1. Radioactive decay of fluorine-18 ($^{18}_{9}F$) to oxygen-18 daughter atom ($^{18}_{8}O$) through electron ($^{0}_{-1}e$) capture.

Positron emission occurs as a proton from the unstable nucleus is converted into a neutron through release of radiation in the form of a positron particle (β^+), the antiparticle of an electron, and a neutrino to yield the stable daughter nuclide (**Scheme 1.2 A**). While this is not always the case, the daughter atoms produced through these β^+-decay processes, while stable, might be in an excited electronic state. As they descend to a more stable ground state, the daughter atoms release a gamma photon (γ) (**Scheme 1.2 B**).

A) $$^{18}_{9}\mathrm{F} \rightarrow {}^{18}_{8}\mathrm{O} + {}^{0}_{+1}\beta + \nu_e$$

B) $$^{1}_{1}\mathrm{p} \rightarrow {}^{1}_{0}\mathrm{n} + {}^{0}_{+1}\beta + \nu_e + \gamma$$

Scheme 1.2. A) Radioactive decay of fluorine-18 atom ($^{18}_{9}$F) to oxygen-18 ($^{18}_{9}$O) through positron emission. B) Positron emission process converting proton-rich nucleus's proton ($^{1}_{1}$p) into a neutron ($^{1}_{0}$n) causing release of a positron (β^+), a chargeless neutrino (ν_e), and occasionally a gamma photon if an excited state daughter atom is produced (γ).

Fluorine-18 is frequently used for molecular imaging due to its short half-life of 109.7 minutes and short positron ranges; with maximum and average positron traveling ranges of 2.4 mm and 0.6 mm in water, respectively. It is widely considered a "gold-standard" within the field of nuclear diagnostics.[8 9] Fluorine is used as a bioisosteric substitute for atoms sharing similar physical and chemical properties such as size and electronegativity. As such, fluorine-18 serves as a suitable substitute for the hydroxyl groups of biomolecules by virtue of their similar Pauling electronegativity values; with values of ~3.55 and ~4.0 for hydroxide and fluoride functional groups, respectively.[10 11] Likewise, fluorine-18 serves as a isosteric replacement for hydrogen as they share comparable van der Waal's radii of 1.2 Å and 1.35 Å for hydrogen and fluorine, respectively.[12] In correspondence with these relationships, fluorine-18 is frequently incorporated

into small molecules, peptides, aptamers, and proteins by replacing a hydrogen, hydroxide, or specialized labile leaving group via nucleophilic or electrophilic substitution with a reactive precursor. A common example of this is the production of fluorine-18-labeled fluorodeoxyglucose ([^{18}F]F-FDG); a C2 analogue for glucose.

[^{18}F]F-FDG is a widely applied PET imaging agent used to identify a variety of hypermetabolic tumours and to assess the efficacy of oncological treatments. The premise for FDG's frequent application stems from the body's use of glucose as a common source of energy. Cancer cells require substantially high quantities of glucose to sustain their hyperactive growth and replication. In addition to their ability to obtain large amounts of glucose through induction processes such as angiogenesis, malignant cells circumvent slower mitochondrial glucose metabolic processes and preferentially apply the quicker glycolysis route of ATP production in what is known as the Warburg effect.[13] While FDG and glucose are both incorporated into the cancers through glucose transporters, the C2-fluorination that differentiates FDG from glucose also prevents the modified sugar from fully metabolizing, resulting in its accumulation within the cancerous cells.[13] FDG is frequently produced using both nucleophilic and electrophilic substitution methods as shown in **Scheme 1.3**.[14]

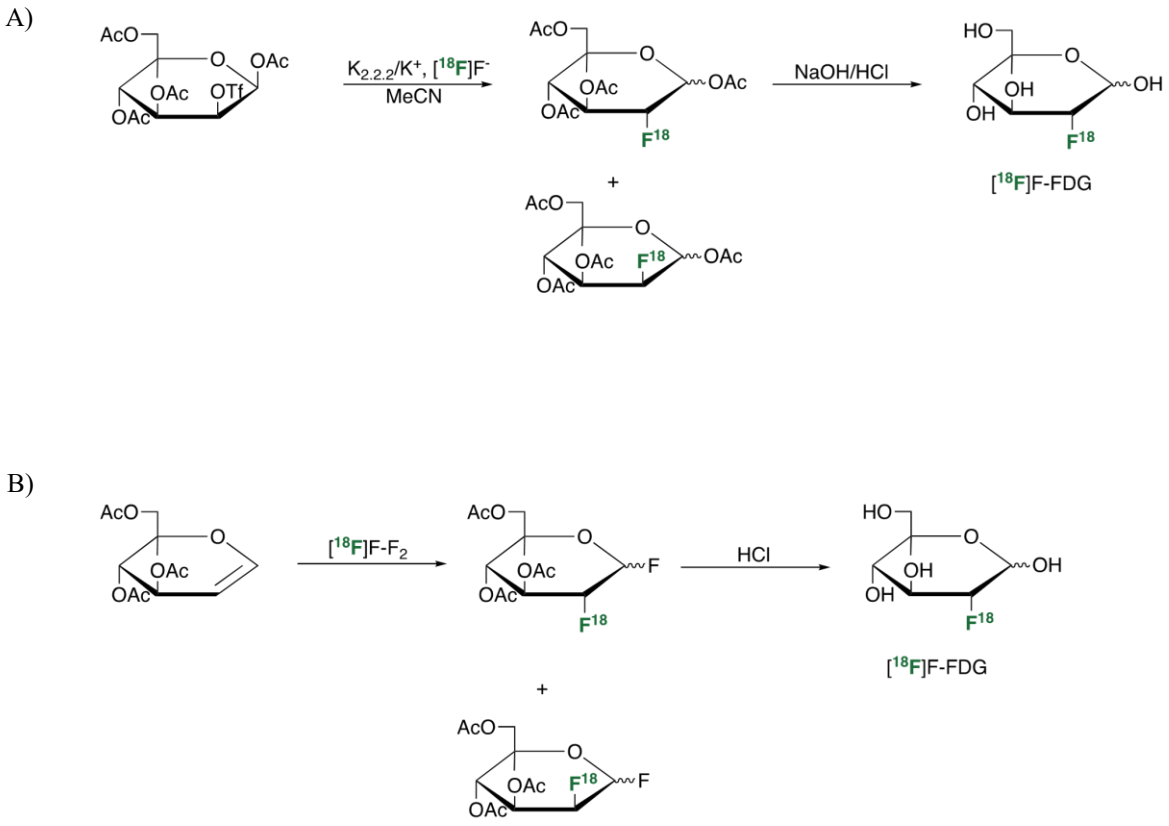

Scheme 1.3. Synthesis of D-[^{18}F]-fluorodeoxyglucose ([^{18}F]F-FDG) through: a) nucleophilic and B) electrophilic substitution strategies.

1.2. (4,4-difluoro-4-bora-3a,4a-diaza-s-indacene) BODIPY Dyes.

Initially reported in 1969 by Triebs and Kreuser,[15] 4,4-difluoro-4-bora-3a,4a-diaza-*s*-indacene, hereafter referred to as (BODIPY) and its associated derivatives are considered highly versatile fluorescent agents.[16] They are currently applied in numerous areas of research including photodynamic therapy,[17] energy transfer technologies,[18] and fluorescent diagnostics.[19] The structural framework of BODIPY (**Figure 1.2**) consists of a central six-membered ring flanked by two pyrrole sides.[20] [21] The planar quasi-aromatic framework of the BODIPY core has strong chromophoric π-electron delocalization.[22] [23] As such, the highly conjugated system displays unique spectroscopic properties including a high fluorescence quantum yield, relatively short Stokes Shift, and intense/narrow emission peaks.[24] [25] [26] Furthermore, BODIPY dyes are soluble in most organic solvent and possess superior thermal and photo-stability with respects to other commonly used fluorescent molecules, such as fluorescein and tetramethylrhodamine.[27]

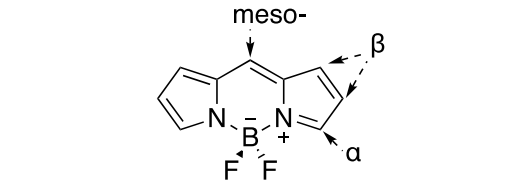

4,4-difluoro-4-bora-3a,4a-diaza-s-indacene
(BODIPY)

Figure 1.2. Chemical structure of the BODIPY core.

1.2.1. Optical Imaging.

Optical imaging has proven to be a dynamic platform for *in vivo* molecular imaging.[28] Compared to other visualization techniques, optical imaging offers superior spatial and temporal resolution while allowing for economical and non-invasive assessments of functional abnormalities at the subcellular level.[29] [30] Although these features are true for *in vitro* microscopy, optical imaging agents are notably limited *in vivo* by deep tissue light attenuation, and interference caused by autofluorescence from some tissue components.[31]

Optical methods apply fluorescent and bioluminescent sensors to probe various biochemical processes. Diagnostic information is then inferred using an optical camera to detect the fluorophores' location, intensity, and associated activities.[32] As optical imaging technologies continue to progress, the synthesis of novel fluorophores such as BODIPY's has become an increasingly active field of research.[33]

1.2.2. Positron Emission Tomography (PET).

Positron emission tomography (PET) is used for non-invasive early disease diagnosis. PET diagnostics can assess biological processes at the subcellular level, allowing physiological changes to be mapped within the body before they anatomically manifest.[34] It is important to note that although PET is a functional imaging technique capable of probing biological processes, the resolution of PET cannot obtain images at subcellular resolutions. PET images are typically in the range of 0.5-3 mm spatial resolution, depending on the radionuclide and PET camera.

PET imaging begins by administering a β^+-emitting radioactive tracer into the biological system of interest. As the radionuclide decays, the emitted positrons travel through the surrounding medium (for fluorine-18 the average distance travelled is 0.6 mm when H_2O is used as a surrogate for cellular tissue)[35] before losing kinetic energy and subsequently annihilating upon impact with an electron (e^-) from the environment. Upon annihilation, two photons (γ) are produced and travel in nearly 180° opposing trajectories where the two time-coincident events of the high-energy photons are detected by a cylindrical array of detectors placed around the subject system (**Figure 1.3**). For all positron annihilations, regardless of the parent radionuclide and the distance traveled by the positron, the resulting photons possess a characteristic energy of 511 keV. The sites at which the annihilation events take place and, by association, the radiotracer to which the positron emitter is bound, is calculated using the spatial information obtained from millions of these positron emission/annihilation events detected by the surrounding detectors.[36 37]

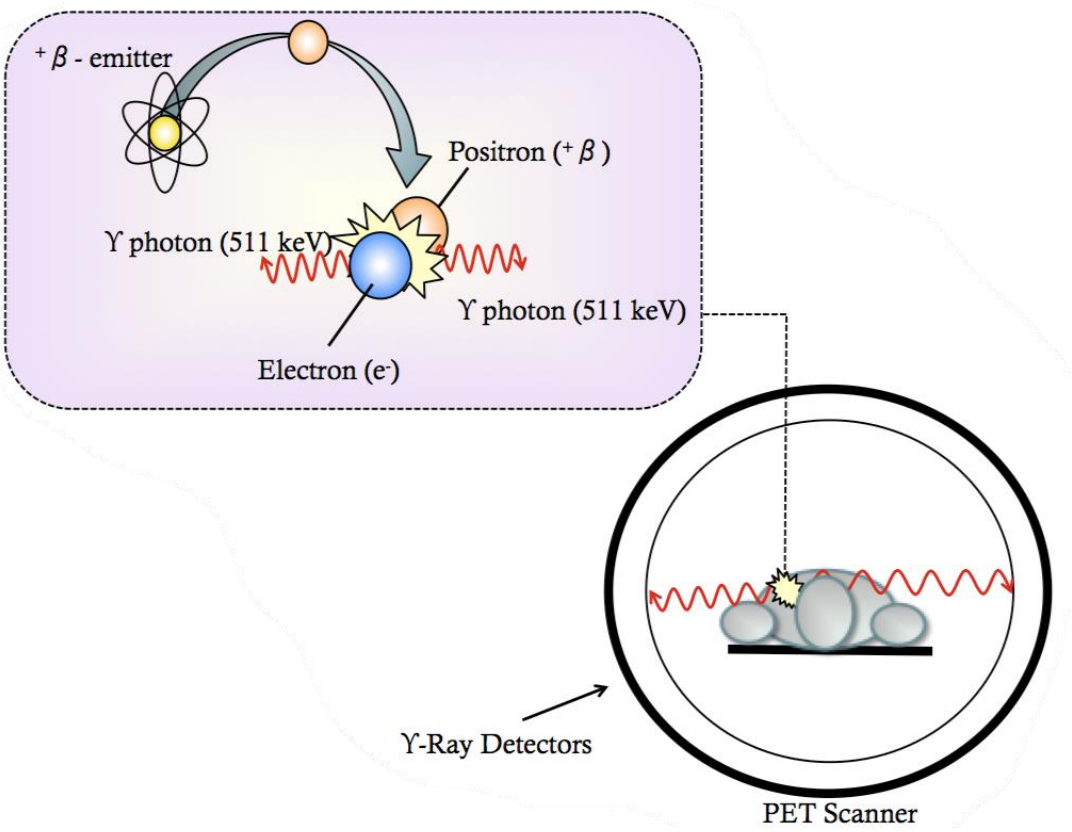

Figure 1.3. Schematic representation of the PET-imaging process. Figure adapted from (Berger, 2003 and Vaquero *et al.*, 2013).[38 39]

1.2.3. Optical/PET Dual-Modality.

Optical imaging techniques provide attributes complementary to PET (**Table 1.1**). While optical methods offer subcellular level resolution of molecular environments, fluorescent signals are diminished in deeper layers of tissue. In contrast, the photons generated from positron annihilation are gamma rays and possess enough energy to pass through biological tissue with minimal attenuation, enabling analysis of deep tissues. However, while nuclear imaging methods allow for the molecular processes to be assessed, PET diagnostics are limited by their lower spatial resolution (>1 mm).[40] As such, optical- and PET- imaging methods can be coupled with one another to optimally assess biological activity via synergistic exploitation of their complementing attributes.[41] BODIPY fluorophores present ideal candidates for bimodality. By subjecting the existing BF_2 structural component of their core framework to radiofluorination techniques, a positron emitting [^{18}F]F-BODIPY product is produced. What is more, the optical activity and chemical properties of the precursor are unchanged as the structural composition of the starting material and the radiolabeled product remains the same.

Table 1.1. Summary of the advantages & disadvantages of Optical and PET imaging techniques.

Optical Imaging	Positron Emission Tomography (PET)
High Spatial & Temporal Resolution	Deep Tissue Imaging
Optical Contrast	Non-Invasive
Inexpensive	Highly Sensitive
Poor Tissue Penetration	Limited Anatomical Resolution (>1 mm)
Photobleaching of Dyes	Limitations of Continual Decay ($t_{1/2}$)

1.3. [^{18}F]-Labeling Strategies for BODIPY Dyes.

1.3.1. Brønsted-Lowry Acid/Base Theory

Established in 1923 by chemists Johannes Nicolaus Brønsted and Thomas Martin Lowry,[42] [43] the Brønsted-Lowry theory of acids and bases outlines the relationship between acids and bases

as the proton transfer between chemical species in liquid and gas reaction mediums.[44] By definition, Brønsted-Lowry acids and bases are defined as proton (H^+) donors and acceptors respectively.[45] As shown in **Figure 1.4**, the proton transfer between a Brønsted acid (H-A) and base (B) produces a conjugate base (A^-) and acid ($H\text{-}B^+$) species.

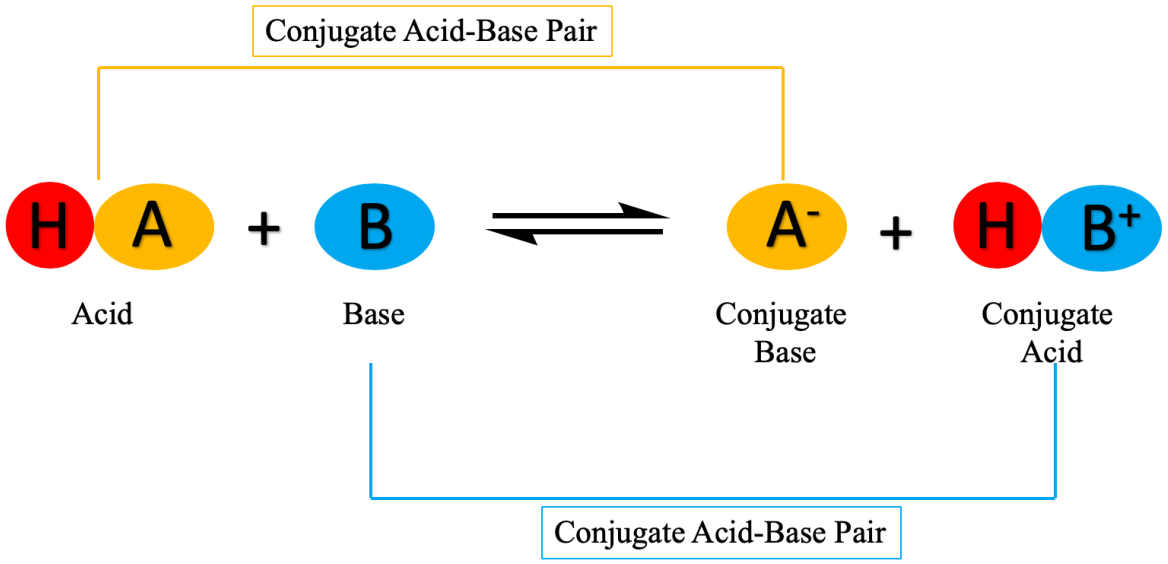

Figure 1.4. Illustrated Brønsted-Lowry acid-base reaction scheme.

1.3.2. Brønsted-Lowry Acid-Assisted $^{19}F/^{18}F$-Isotopic Exchange.

(Hendricks *et al.*, 2012)[46] had previously reported a two-pot synthetic route for the production of [^{18}F]F-BODIPY where a fluoride from the R-BF_2-moiety was abstracted by trimethylsilyl trifluoromethanesulfonate (TMSOTf) to afford an activated BODIPY-triflate intermediate. $^{19}F/^{18}F$-trans fluorination was subsequently facilitated when the triflate-intermediate, stabilized by 2, 6-lutidine, was subjected to *tert*-butanol and triflic anhydride. In the presence of free fluorine-18, these Brønsted acidic conditions reportedly afforded the desired [^{18}F]-labeled BODIPY dye in 67% radiochemical yield (**Scheme 1.4**). While Brønsted-Lowry acid-catalyzed $^{19}F/^{18}F$-exchange reactions are capable of successfully facilitating the desired reaction, the low pH conditions, typically pH 2-3, make them incompatible with BODIPY dyes functionalized with acid-sensitive substituents.

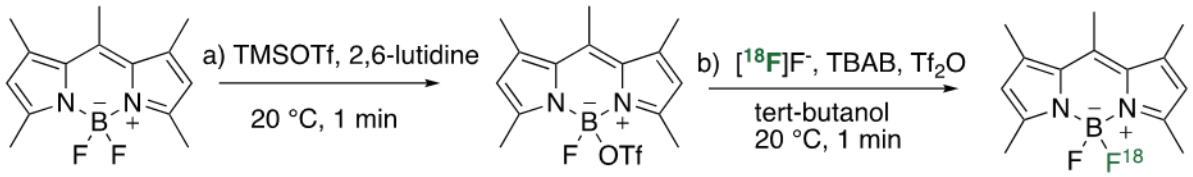

Scheme 1.4. Two-step radio-synthetic preparation of [^{18}F]F-BODIPY dye as performed by (Hendricks *et al.*, 2012), showing a two-step reaction with a) synthesis of the BODIPY-triflate intermediate from trimethylsilyl trifluoromethanesulfonate (TMSOTf), and b) radiofluorination of BODIPY-triflate intermediate as facilitated by Brønsted-acidic conditions. Tetrabutylammonium bicarbonate (TBAB) is applied in the above reaction process as a phase transfer agent.

1.3.3. Lewis Acids/Base Theory.

Brønsted-Lowry's definition of acid/base interactions pertains exclusively to reactions involving proton exchange. However, Gilbert N. Lewis theorized a more general definition of the acid/base dynamic wherein Lewis acids are distinguished by their ability to accept a pair of electrons and Lewis bases by their ability to donate them.[47] While Brønsted acids (H^+) can be considered Lewis acids given their ability to donate protons and effectively gain the electrons, Lewis's interpretation of acids and bases expands on Brønsted and Lowry's conceptualization to explain the formation of coordination complexes from ligating species (Lewis bases) and metal cations (Lewis acids).[48] The reaction between a Lewis acid and base forms a coordinate covalent bond between the two reagents as electrons, usually from the base's highest occupied molecular orbital (HOMO), are shared between itself and the Lewis acid's lowest unoccupied molecular orbital (LUMO),[49] producing a Lewis acid-base adduct (**Scheme 1.5**).

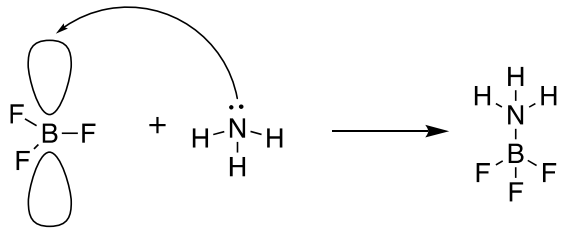

Scheme 1.5. Reaction of boron trifluoride (Lewis acid) with ammonia (Lewis Base) to form a Lewis acid-base adduct; ammonia boron fluoride.[50]

1.3.4. Hard Soft Lewis Acid Base (HSAB) Theory & Lewis Acid Selection.

Pearson's hard soft acid base (HSAB) theory is often used when discussing the trends in Lewis acid/base interactions. HSAB relates the affinities of acids and bases for one another to the degree by which each of the chemical species experiences distortion of their electron cloud in the presence of an electric field; otherwise known as the atom or ion's polarizability. The element's polarizability depends on the degree of dispersion between electrons within the atom or ion's electron cloud. A diffuse field of electron is easily distorted in the presence of nearby electric forces and thus distinguishes the associated atom's nature as "soft". Conversely, atoms that hold their surrounding electrons near the nucleus will experience less polarization and are referred to as having a "hard" electron shell. For metal cations, a general trend is that higher oxidation states correspond with a "harder" ion.

Several characteristics of hard and soft acids and bases are outlined in **Table 1.2** The complementary natures observed of hard electron shell-bearing acids and bases rationalizes their high affinity for one another to form strong ionic interaction. Likewise, the compatible attributes of soft acids and soft bases lead to favorable interactions with one another and native bond formation.[51] Based on these characteristic properties, fluoride anions are considered hard bases and preferentially interact with hard Lewis acids of low polarizability. In accordance with this, light metal ions hosting large positive charges with respect to their relatively small ionic radii serve as ideal Lewis acidic agents to abstract fluoride from the BF_2-moiety of BODIPY dyes. Examples of hard metal ions include magnesium (Mg^{2+}), tin(II) (Sn^{2+}) and, to a greater extent, tin(IV) (Sn^{4+}) by virtue of its higher oxidation number.[52]

Table 1.2. Characteristic attributes of hard and soft acids and bases.

Property	**Hard**		**Soft**	
-	***Acids***	***Bases***	***Acids***	***Bases***
Polarizability	Low	Low	High	High
Ionic Radii	Small acceptor	Small donor	Large acceptor	Large donor
Charge	High positive oxidation state	High electronegativity	Zero/low positive oxidation state	Low electronegativity
HOMO/LUMO	High energy LUMO	High energy HOMO	Low energy LUMO	Low energy HOMO

1.3.5. Lewis Acid-Assisted $^{19}F/^{18}F$-Isotopic Exchange.

The Lewis acid-assisted $^{18}F/^{19}F$-isotopic exchange has become the dominant means for promoting transfluorination of BODIPY molecules (**Scheme 1.6**).[53] During their initial study, (Liu *et al.,* 2013) had selected Lewis acids of intermediate strength as determined by Gutmann's anion accepting scale.[54] Of the Lewis acids assessed, $SnCl_4$ and $TiCl_4$ had shown the greatest success, achieving respective radiochemical conversion values of >95% and 90% for the unlabeled dye quickly (10 min) under mild conditions (25 °C). As such, they remain the primary means of choice for researchers seeking to employ BODIPY-based bimodal imaging agents.

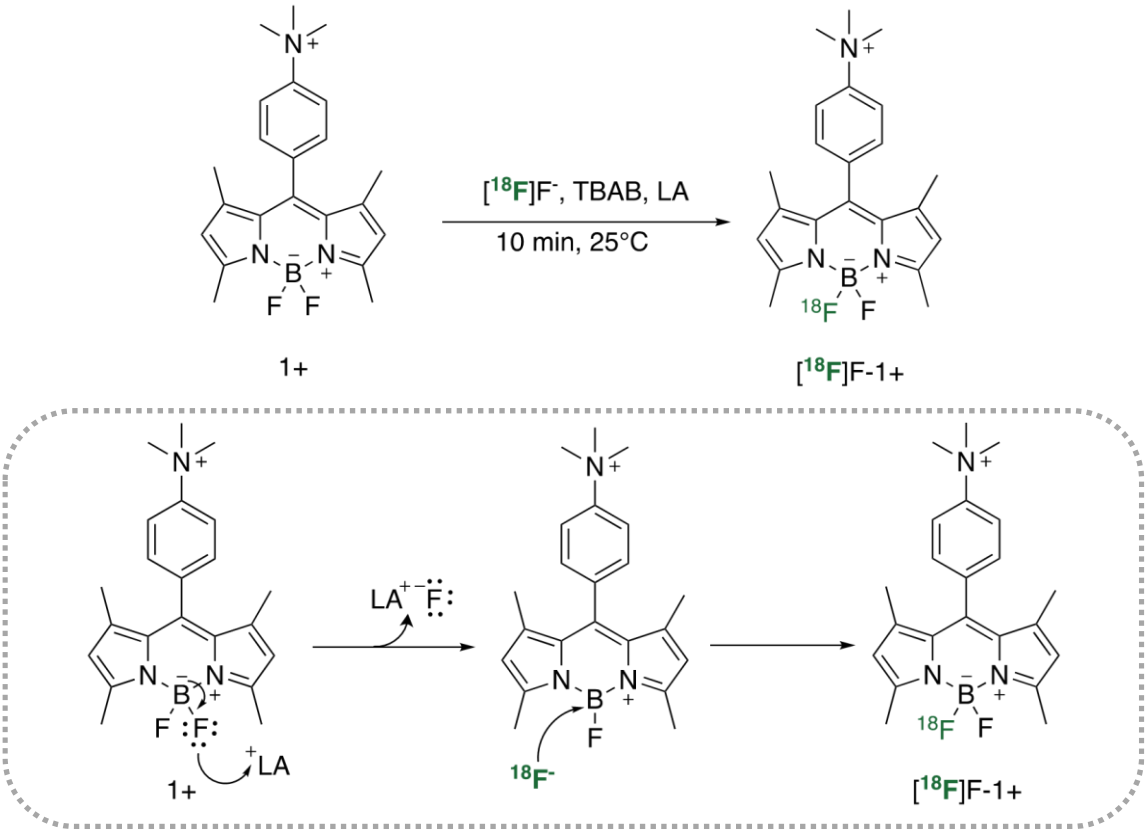

Scheme 1.6. $^{19}F/^{18}F$-Radioisotopic exchange reaction as described by (Liu *et al.*, 2013), wherein tetrabutylammonium bicarbonate (TBAB) acts as a phase transfer catalyst and various Lewis Acids were applied as catalysts to facilitate transfluorination of reagent 1^+.[53]

1.4. Antibody Drug Conjugates.

Although not directly related to BODIPY dyes and their radiochemistry, antibodies are very common targeting vectors used in molecular imaging and nuclear medicine. Bioconjugation chemistry is used to attach "payloads" to antibodies such as chelators/radiometals, dyes, or even chemotherapy drugs. In this way, a wide variety of antibodies can be transformed into imaging agents and/or therapeutics.[55] With these antibody platforms, the antibody provides receptor-specific targeting of cellular antigens and the payload is carried by the antibody of these cells via the covalent bioconjugation linkages. As such, antibody-drug conjugates are promising drug and diagnostic delivery platforms that offer selective administration of cytotoxic molecules targeted antigens.[56 57 58]

The bulk of the antibody conjugate's structure consists of either a laboratory-engineered human monoclonal or humanised antibody scaffold with high affinity and selectivity for a target antigen.[59] Molecular chains (linkers/spacers) covalently binds the active compound to solvent-exposed amino acids present in the antibody, forming an immunoconjugate (**Figure 1.5**). The antibody delivery platform's biological compatibility and receptor-selectivity acts as a prodrug and ultimately reduces systemic toxicity and improves the pharmacokinetic and pharmacodynamics properties of the drug.[60] Ideal ADCs only release their drug payload inside of or in the local environment of cancer cells.

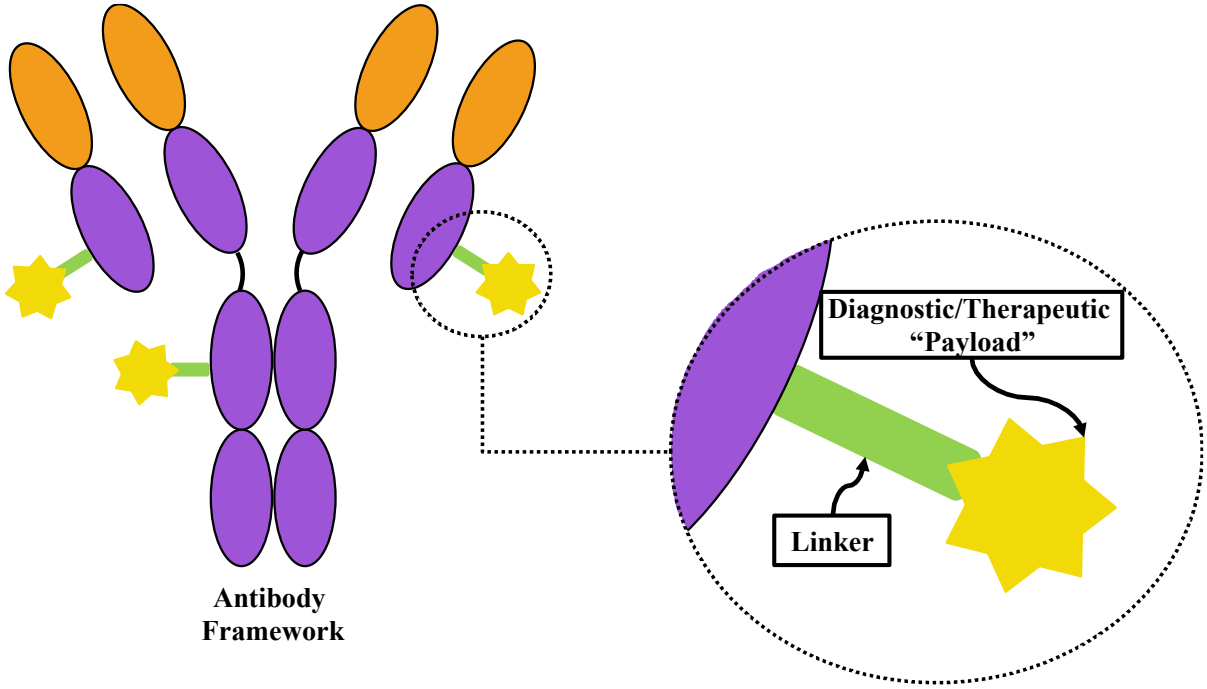

Figure 1.5. Illustration of immunoconjugate composition.

1.4.1. Cleavable and Non-Cleavable Linkers.

The design and structure of chemical linkers are crucial to the success of antibody drug conjugates. The linker requires sufficient stability so as not to prematurely release the active compound and adversely affect healthy tissues while the antibody drug conjugate circulates through the bloodstream. Once inside the target cell, the linker must liberate the bound payload efficiently.[61] Linkers are widely categorized as being either "cleavable" or "non-cleavable". Cleavable linkages are hydrolyzed in response to either the differing chemical environments of the

circulating blood and the cytoplasm of the target cells such as changes in pH and reducing environment or by cells' lysosomal enzymes. The bonds of non-cleavable linkers are non-susceptible to proteolytic degradation and thus more stable in comparison to their cleavable counterparts. Instead, the active diagnostic/therapeutic compound is afforded through the complete degradation of the antibody scaffold into its fundamental amino acids via cytosolic and lysosomal proteases.[62]

The best choice of ADC linker ultimately depends on the selected antibody, the biochemical properties of the attached payload, and the desired course of action. Cleavable linkers are advantageous for treating heterogeneous malignancies through delivery of cytotoxic payloads that yield membrane-permeable metabolites. As such, cleavably-linked antibody drug conjugates can promote the death of malignant cells expressing the target antigen receptor as well as those nearby that lack the surface antigen through the bystander killing effects.[63] In contrast, non-cleavable linkers are less likely to elicit bystander effects on unintended cells as the lysosomal degradation of the antibody carrier often yields polar metabolites unable to exit the cellular membrane.[64] Radioimmunoconjugates are constructed and function in largely the same fashion as outlined for ADCs, with a couple of key differences. Firstly, the drug is substituted for a radionuclide, which is often in the form of a chelator which can bind with radioactive metal ions. In the case of radiolabeled antibodies, non-cleavable linkers are imperative and stability is paramount so that the radioactive payload is not released and remains antibody-bound.

1.4.2. Immunoglobulin G (IgG).

Immunoglobulin (IgG) proteins are the most abundant antibody species in human serum, with IgG1 as the dominant subclass.[65] As such, most of the immunoconjugate research reported to date focuses on synthetic routes for modifying the IgG1 antibody framework to accommodate linker-bound therapeutic agents. These efforts concentrate heavily on the site-specific modification of nucleophilic lysine and cysteine side chains.[66 67] While the IgG1 antibody hosts roughly 80 lysine residues, only a fraction of them lie within solvent-accessible domains. What's more, the most accessible lysines are located on the protein's C_H2-domain, where lysine modification efforts can compromise the antibody's antigen binding affinity.[68 69] Cysteines, while less abundant, exist as sixteen accessible disulfide pairs on the IgG1 scaffold (**Figure 1.6**). This

lower number of potential binding sites decreases the number of potential isomers formed of the antibody conjugate; thereby reducing the antibody drug conjugate heterogeneity of cysteine relative to lysine overall.[70] [71] By reducing the heterogeneity of the product, the immunoconjugate compound elicits increasingly uniform pharmacological effects thereby improving its efficacy as a therapeutic agent. A caveat to this approach is that these disulfide-bridged cysteine residues are important structural components which hold large domains of the antibody together, and they must be reduced before bioconjugation of a payload can be performed. In contrast, lysine residues are not structurally integral and require no chemical modification before bioconjugation.

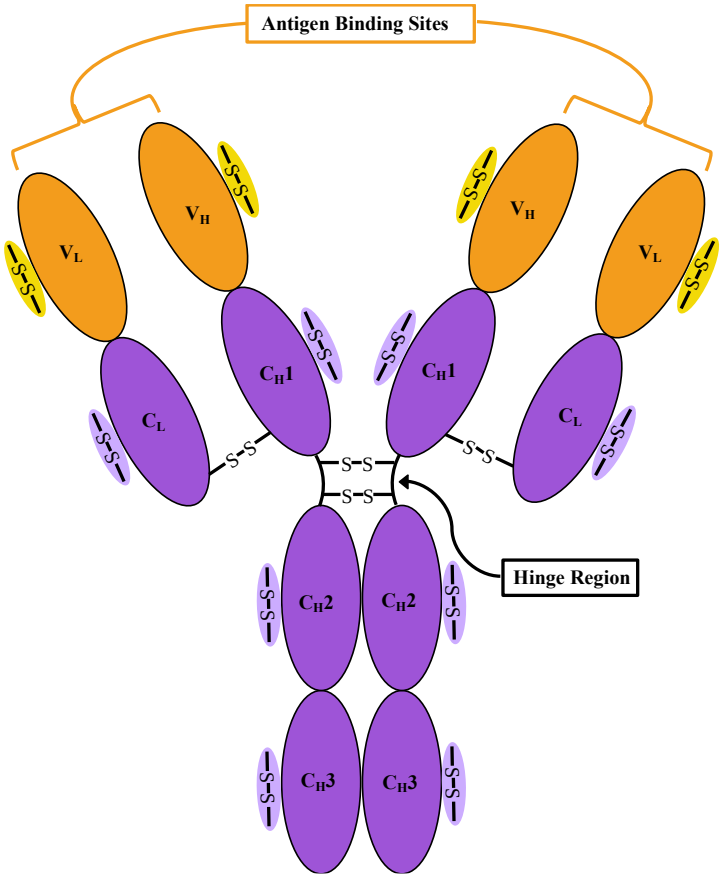

Figure 1.6. Illustration of IgG1 antibody structure depicting 4 inter- and 12 intra-chain disulfide bonds. Constant and variable chain components are defined by letters (C) and (H) respectively. Light and heavy chains are denoted by subscripts ($_L$) and ($_H$) respectively. Figure adapted from those provided in (Garciarz, 2017; Absolute Antibody, accessed 2020; and Liu and May, 2012).[72] [73] [74]

1.4.3. Disulfide Bridging Linkers.

While free cysteine residues can be engineered into the antibody sequence, native antibodies rarely host unpaired cysteines residues accessible for modification, but rather paired cysteines that bind to one another through oxidation and form disulfide bridges.[75] [76] [77] These covalent bonds are essential to both the formation and maintenance of the protein's tertiary structure, and subsequently their biological activity.[78] [79] Consequently, conjugation with most thiol-selective bioconjugation reagents result in the reaction of only a single cysteine residue, leading to disruption of the disulfide linkages and compromised structural integrity of the antibody.[80] [81] Disulfide rebridging linkers are designed to insert between paired cysteines and covalently bind to both thiol species to preserve the tertiary conformation of the protein.[82] As two thiol-reactive moieties are required in disulfide rebridging bioconjugation reactions, the site-specificity, and in turn, the product homogeneity of disulfide rebridging linkers is superior to that of cysteine-selective linkers occupying a single binding site (**Figure 1.7**).[83]

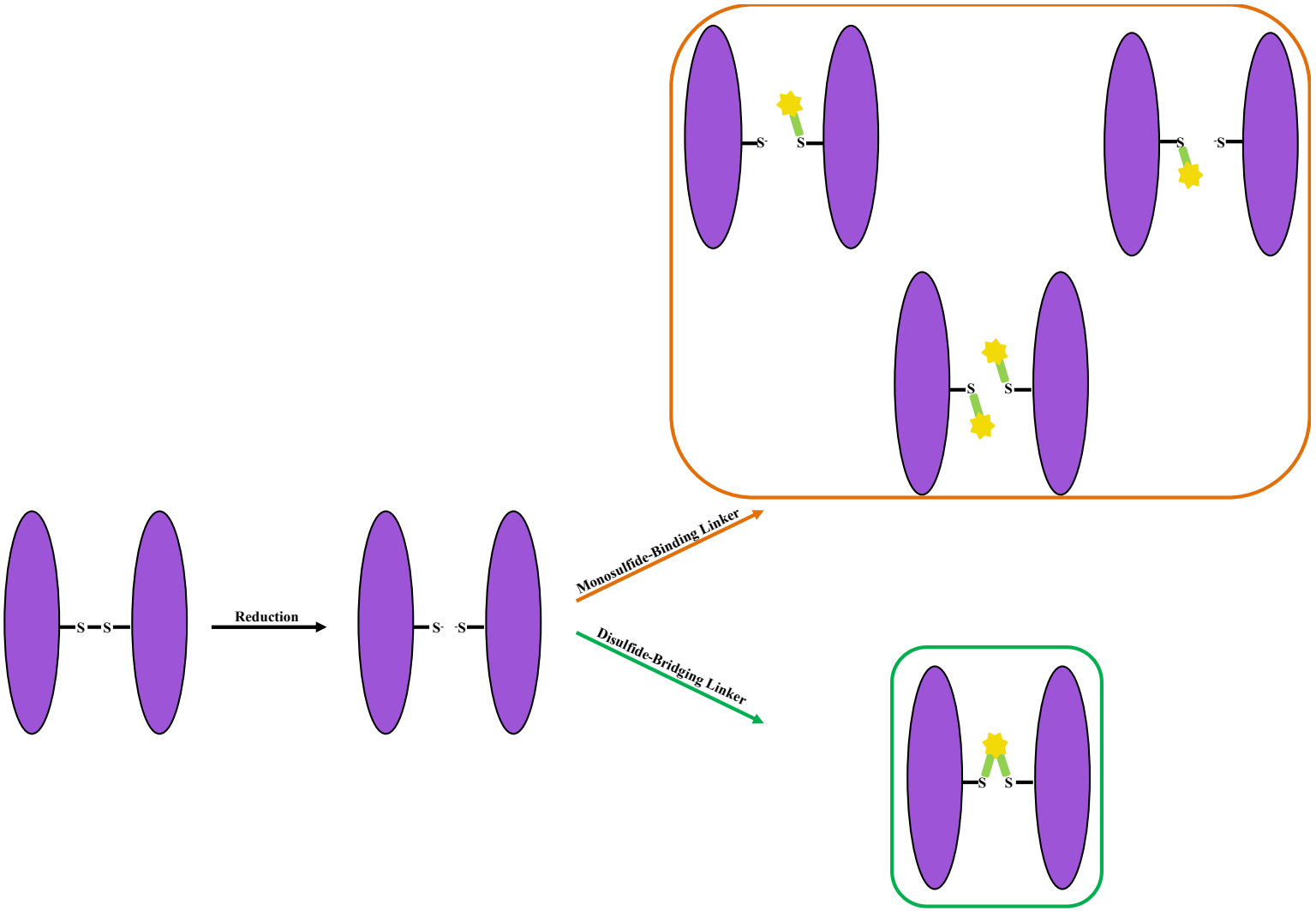

Figure 1.7. Illustrated reaction outcomes of antibody fragment subject to monosulfide-binding cysteine selective linkers and disulfide-bridging linkers demonstrating the differences in product heterogeneity. Figure adapted from (Nunes *et al*., 2015).[84]

1.5. Cysteine Bioconjugation.

Maleimide and maleimide derivatives are among the most frequently used non-cleavable linkers for cysteine residues; however, they could be considered to be "pseudo-cleavable" due to the inherent instability of the linkage and their propensity to undergo degradation via a retro-Michael reaction.[85] [86] The maleimide moiety undergoes the Michael addition reaction with thiolates, a common organic chemistry reaction, including cysteine thiolates found in antibodies. Maleimide acts as an electrophilic Michael acceptor for the thiolate nucleophile to attack and form a thioether adduct (**Scheme 1.7**).[87] [88]

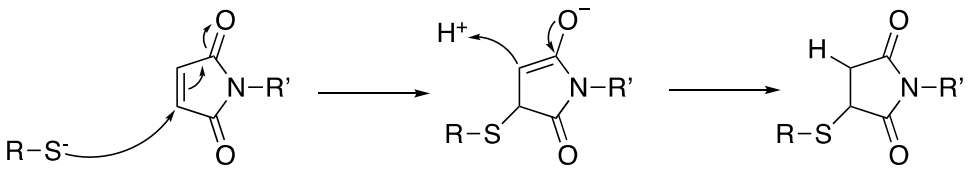

Scheme 1.7. Michael addition reaction applying maleimide as a Michael acceptor for nucleophilic attack of cysteine residue's thiolate moiety ($R\text{-}S^-$); yielding thioether product.

Maleimide and maleimide derivatives are extensively studied as both singular and rebridging cysteine linker variants. However, while maleimide is commonly applied by virtue of its specificity and fast reaction kinetics, the thiosuccinimide moiety is susceptible to *in vivo* retro-Michael (β-elimination) degradation of the immunoconjugate and release of the maleimide rebridging agent and it's attached payload from the antibody. What's more, the newly liberated maleimide-payload complex can then interact with other biologically available thiols, cysteines, and glutathiones (**Scheme 1.8**).[89] [90] [91] Consequently, the maleimide-linked immunoconjugates (drug or radionuclide) becomes a heterogeneous mixture of the antibody drug conjugate product and several by-products, which circulate through the blood stream leading to variable pharmacokinetics, therapeutic efficacy, and toxicity.[92] [93] These homogeneity issues observed of maleimide immunoconjugates have driven the research development of new linkers such as the promising phenyloxadiazolyl methyl sulfone (PODS) and its derivatives.[94]

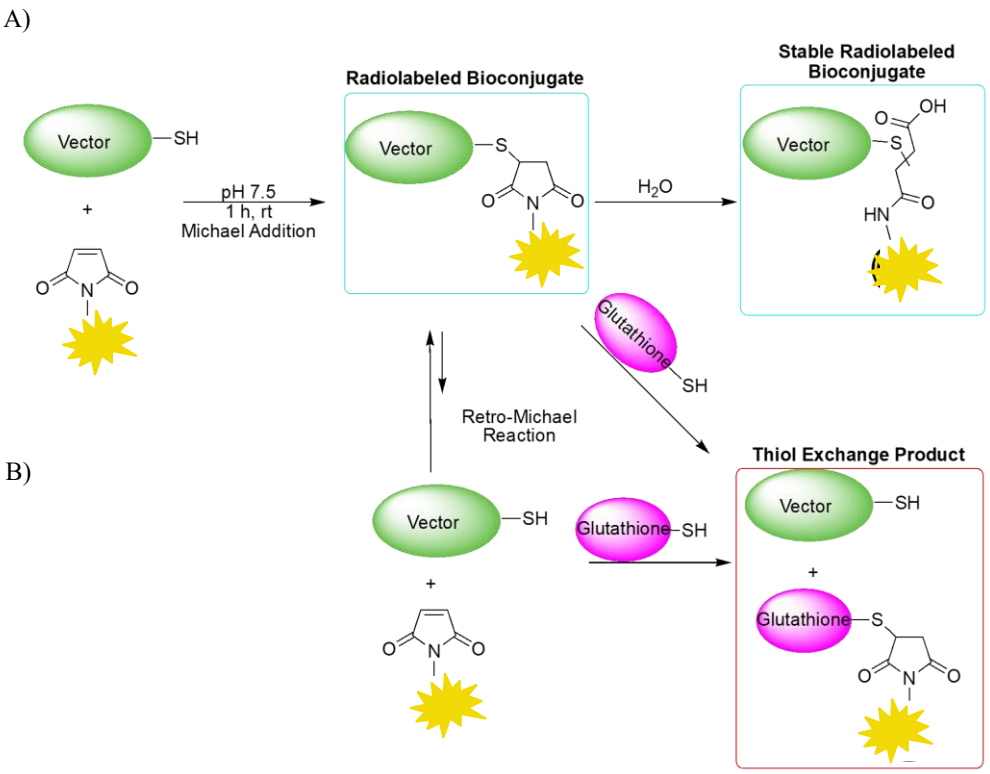

= fluorophores, cytotoxic molecules, and radiotherapeutic nuclides such as [^{89}Zr]Zr^{4+} and [^{177}Lu]Lu^{3+}.

Scheme 1.8. A) Bioconjugation of thiol-bearing biomolecule (green) and radionuclide-bearing maleimide via Michael addition and subsequent hydrolysis to form a stable thioether. B) retro-Michael reaction of the bioconjugated product in the presence of thiol-bearing molecules from the biological environment such as glutathione (pink). Figure adapted from (Adumeau *et al.*, 2018).[95]

1.5.1. Phenyloxadiazolyl Methyl Sulfone (PODS).

(Barbas *et al.*, 2013) investigated the use of several methylsulfonyl-functionalized heteroaromatic derivatives towards thiol conjugation based on the observed reactivity of methylsulfonyl benzothiazole (MSBT) blocking reagents.[96] They demonstrated selective nucleophilic aromatic substitution between phenyloxadiazole compounds and cysteine side-chains. Reactions applying Barbas' reagent took place at rates comparable to those applying maleimide and the resulting conjugates had comparatively superior stability (**Scheme 1.9**).[97]

While this agent proved promising and caught the interest of several researchers, at some point during commercialization of the Barbas reagent errors must have been made as the commercial reagent had very low purity and, consequently, diminished use. After noting the commercial agent's impurity issues and unwilling to denounce the compound's promise, the research labs of Dr. Thomas Mindt and Dr. Brian Zeglis, in separate works, recently resynthesized the Barbas reagent.[98] The Zeglis lab gave it the working acronym "PODS" and followed up on these efforts by incorporating the PODS functionality within the structure of two novel bifunctional chelators and successfully applying them towards the bioconjugation and radiolabeling of thiol- bearing biomolecules with [^{89}Zr]Zr^{4+} and [^{177}Lu]Lu^{3+}.[95] This work again demonstrated the vastly improved stability of the PODS linkage compared with maleimide and revived the underutilized PODS compound's potential.

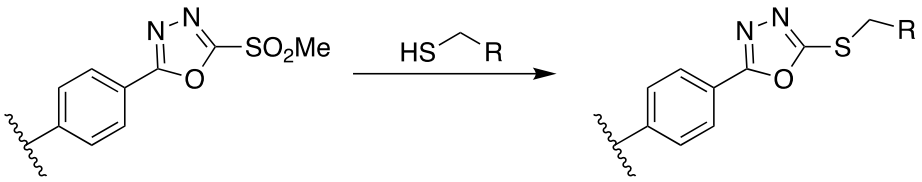

Scheme 1.9. Reaction of the Barbas reagent with a thiol, forming stable conjugate product. Scheme adapted from (Toda *et al*., 2013).[97]

1.6. Purpose Statement.

With the growing number of radiochemistry applications comes opportunity to expand the toolbox of applicable radiotherapeutics and diagnostics. These efforts, including the synthesis of new and selective bimodal diagnostic agents, alternative radiolabeling methodologies, and improved radioimmunoconjugate stability were explored by the three projects presented in this thesis and outlined herein.

The first project pertains to the imperative needs for diagnostic agents capable of localizing deep tissue bacterial infections. Compound of designation yellow (CDy11) is a BODIPY fluorophore that was previously found to selectively bind to the functional amyloids of the nosocomial pathogen *Pseudomonas aeruginosa* (PAO1). This project sought to improve the CDy11 dye's diagnostic potential by applying Lewis acid-assisted ^{19}F/^{18}F-transfluorination

methods to the CDy11 precursor to synthesize a bimodal imaging agent applicable towards non-invasive localization of *P. aeruginosa* infection and subsequent fluorescence-guided surgery.

The second project outlined in this thesis tackles the challenge of the common $SnCl_4$ Lewis acid agent commonly used to facilitate $^{19}F/^{18}F$-isotopic exchange on the BODIPY core framework. The moisture-sensitive nature of $SnCl_4$ results in the precipitation of tin hydroxide $Sn(OH)_4$ and/or SnO_2, which introduces variability to the overall reaction and can release HCl, potentially harming sensitive biomolecules or dyes. As such, the efficacy of hydrated magnesium nitrate $Mg(NO_3)_2$ was explored as a mild and air-stable alternative to the conventionally applied $SnCl_4$ for promoting $^{19}F/^{18}F$-transfluorination of a commercially available BODIPY dye. Furthermore, as the current literature lacks automated methods for the Lewis acid assisted [^{18}F]-labeling of BODIPY dyes, efforts to automate the optimized procedures applying the stable hydrated $Mg(NO_3)_2$ salt solutions are outlined in an effort to provide reproducible and reliable BODIPY labeling strategies.

Lastly, the third project discussed in this thesis outlines the synthesis of several of compounds involved in the multistep synthesis of the phenyloxadiazolyl methyl sulfone-based disulfide rebridging linker, DiPODS. These synthetic efforts were performed to assist in the production of the final DiPODS product as well as to investigate some intriguing observations made of the first synthetic product's proton NMR. As the first product's synthesis was believed to afford a mixture of rotamers, a series of variable temperature NMR experiments were performed to better discern the nature of the crude product mixture's components.

Chapter 2 Preamble

Chapter 2 describes the experimental efforts made towards radiolabelling compound of designation yellow (CDy11), a BODIPY dye found to selectively bind to the functional amyloids of the nosocomial pathogen *Pseudomonas aeruginosa* (PAO1), with [^{18}F]-fluoride. The objective of this project was to produce ^{18}F-radiolabeled CDy11 through Lewis acid-assisted ^{19}F/^{18}F-transfluorination methodologies. Once labelled, the newly ^{18}F-labeled dye was to be subjected to a series of *ex vivo* and *in vivo* analyses to determine its efficacy as a bimodal imaging agent for bacterial biofilms such as those found to develop in the moist environments of soils and bodily tissues.

The CDy11 precursor was synthesized by collaborators (Dr. Michael Givskov and Dr. Liang Yang) and shipped to USask, but was repurified using HPLC instrumentation and confirmed using mass spectrometry.[99] Success of the transfluorination experiments was evaluated through HPLC analysis using a system equipped with both UV-Vis- and radioactivity detectors. Although synthesis attempts of the desired [^{18}F]F-CDy11product failed primarily because of the precursor's instability, they illuminated inconsistencies in the jargon used to describe the Lewis-acid assisted radiofluorination methods, which require clarification. What is more, the moisture sensitivity of the Lewis acidic agent used in these reports, $SnCl_4$, complicates the process as the amount of viable $SnCl_4$ successfully introduced into the reaction medium is subject to a wide range of variability. The requirement of dispensing very small volumes of this reagent (~5-20 μL) using a Hamilton microsyringe results in the production of visible HCl gas and white tin precipitate on the end of the needle, reducing the replicability of the reaction conditions and therefore yields. Ultimately, the decision was made to discontinue labeling attempts on the CDy11 BODIPY dye due to the molecule's intrinsic instability, and instead turn focus towards improving the existing ^{19}F/^{18}F-transfluorination methods by assessing the use of Lewis acids with no HCl liberation and improved moisture stability as alternatives to $SnCl_4$. These endeavours are reported later in Chapter 3.

Chapter 2

2.1. Introduction.

2.1.1. Pseudomonas aeruginosa.

The *Pseudomonas aeruginosa* (PAO1) bacillus is a biofilm-producing, Gram-negative pathogen found to live ubiquitously in nature, thriving in the moist environments of water, soils, and biological hosts. [100] [101] [102] The pathogenicity of PAO1 bacterium is a multifaceted composite of extracellular and structural aspects, resulting in a range of associated diseases.[103] [104] PAO1's infectious nature is further exacerbated by years of selective pressures that afford the bacteria recalcitrant, multi-drug resistance; rendering prevalently used antibiotics ineffectual.[105] [106]

2.1.1.1. Pseudomonas aeruginosa and Human Health.

While rarely infecting healthy hosts, PAO1 is a common nosocomial pathogen found to frequently colonize clinical surfaces. Medical devices such as catheters,[107] respiratory equipment, and pacemakers are all capable of enabling the infectious bacteria's transfer to immunocompromised hosts;[108] [109] including patients suffering from various forms of cancer,[110] HIV and AIDs, [111] [112] burn victims and respiratory diseases. [113] [114] In particular, PAO1 is considered the leading cause of morbidity and fatality of cystic fibrosis patients.[115]

2.1.2. Bacterial Biofilms.

The superior resilience colonized PAO1 microbes exhibit towards environmental stress is attributed to their production of extracellular polymeric matrices otherwise referred to as "biofilms". The biofilm is a complex and adaptive system of self-organized bacterial species primarily comprising of extracellular polysaccharides, extracellular DNA (eDNA), and proteins (**Figure 2.1**).[116] [117]

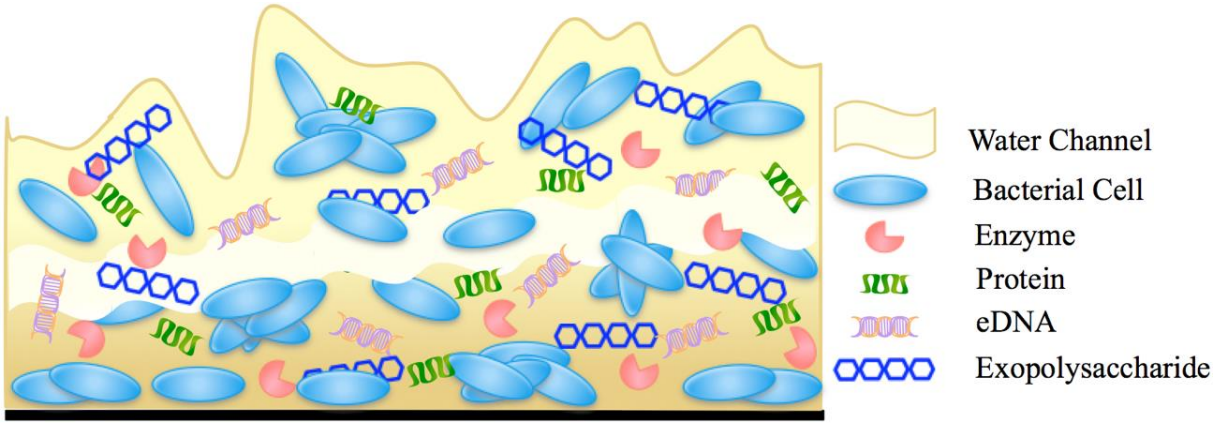

Figure 2.1. A simplified structure of the biofilm composition. Figure adapted from (Flemming and Wingender, 2010; and Mani *et al*., 2018).[116] [117]

2.1.2.1. Advantages of the Biofilm System.

The sessile lifestyle of biofilm-associated bacteria proves viably advantageous.[118] The colonized bacterium exhibit van der Waals force that attract the prokaryotes towards one another, allowing them to adhere to both abiotic and biotic surfaces.[119] These effects are enhanced by the bacteria's envelopment within a self-secreted exopolysaccharide vesicle, enabling the associated bacilli greater opportunity to adhere with one another and the affected environment.[120] The formation of the biofilm encapsulant affords the amassed micro-community superior tolerance to the harsh conditions biocides and antibiotics may afford.[121]

As the biofilm system matures, several physical and social properties emerge that offer the micro-community the means to sustain itself. The biofilm housed PAO1 bacteria display synergistic behavior with one another through social, metabolic and electrical interactions as well as their ability to capture and store nutritive materials.[122]

2.1.3. Biofilm Associated Functional Amyloids.

Pseudomonas-associated functional amyloids (Fap) are the principal proteinaceous constituent of PAO1 biofilms.[123] These insoluble fibrils extend from the bacteria's outer membrane where they serve as adhesives allowing the cells to stick to one another and ultimately

colonize.[124] [125] The adherent fibers also act as protein-scaffolds in the developing matrix; helping to maintain the biofilm system's structural integrity.[126]

2.1.4. Compound of Designation Yellow 11 (CDy11).

A new BODIPY-based fluorescent probe was reported by (Kim *et al*., 2016).[99] The novel biosensor, compound of designation yellow (CDy11) (**Figure 2.2**), was found to bind specifically to the Fap amyloids of *Pseudomonas aeruginosa* PAO1 biofilms. Initial *in vivo* assessments demonstrated CDy11's potential as an optical imaging agent in thin tissue layers; emitting a fluorescence response at 576 nm when bound to the *Pseudomonas*-associated functional amyloids (Fap) biomarker. However, CDy11's imaging abilities are limited by the effects of deep-tissue fluorescence attenuation and require further modification to fully realize its potential in the realm of clinical diagnostics.

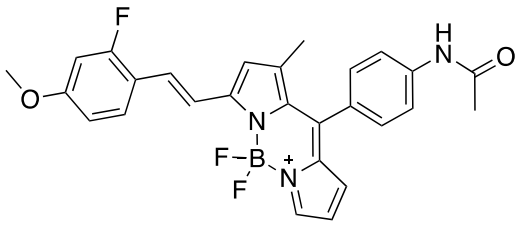

Figure 2.2. Chemical structure of CDy11.

2.1.5. Purpose Statement.

Resilient biofilm-associated bacterial infections, such as those caused by PAO1, require reliable selective diagnostic agents. This project aims to apply Lewis acidic [^{18}F]-labeling methods to produce a radiotracer from the existing, biofilm-selective, CDy11 precursor. It is hypothesised that the optical and PET dual modality of the radiolabeled dye will expand CDy11's diagnostic applicability beyond its limitations of fluorescence attenuation and allow for biofilm-associated bacterial infection localization at greater media depth.

CDy11 will be subjected to Lewis acid facilitated ^{19}F/^{18}F-transfluorination and subsequent characterization using radioactive and UV/Vis HPLC. Following the confirmed synthesis of [^{18}F]F-CDy11, the goal is to apply the isolated radiotracer in several *ex vivo* and *in vivo*

experimental models with the opportunistic PAO1 biofilms to assess the modified BODIPY dye's performance as a selective bimodal indicator for the colonized *Pseudomonas aeruginosa* bacteria.

2.2. Experimental.

2.2.1. Purification of CDy11.

The crude CDy11 precursor (0.050 g, 0.100 mmol) was received from our collaborators. Purifications and characterizations of the crude CDy11 compound were performed by applying HPLC-MS instrumentation using a Thermo Fisher Vanquish UHPLC system equipped with a Chromeleon 7 communication software, DIONEX UltiMate 3000 fraction collector, and C18 semi prep column (Spursil 5 μm C18, 250 × 21.2 mm reverse phase column, flow rate 8.00 mL/min). A similar system equipped with a reversed phase C18 UHPLC column with TMS endcapping (Luna® 5 μm C18(2) 100 Å, LC Column 250 × 4.60 mm, Ea, flow rate 0.50 mL/min) was used to assess radiofluorination of the CDy11 compound following experiments wherein differing $^{19}F/^{18}F$-isotopic exchange reaction conditions were applied. Gradient solvent systems of water: acetonitrile (95:5 to 5:95) and (70:30 to 5:95) with 0.1% formic acid were used for analysis and the methods were refined. Absorbance was measured at both 558 nm, the maximum absorbance of the CDy11 precursor, and 254 nm, a common wavelength for aromatic compounds.

2.2.2. CDy11 Radiofluorination.

2.2.2.1. CDy11 Solution Preparation.

CDy11 (1.10 mg, 2.25×10^{-3} mmol) was dissolved in a dry, sure seal vial using dry MeCN (1.10 mL) to afford a 1.00 mg/mL solution.

2.2.2.2. Fluorine-18 ($[^{18}F]F^-$)-Production.

Fluorine-18 ($[^{18}F]F^-$) was produced by staff at the Saskatchewan Centre for Cyclotron Sciences (SCCS). $[^{18}O]O\text{-}H_2O$ water was irradiated with high-energy protons using an ACSI TR24 cyclotron. The primary batch of $[^{18}F]F^-$ was used by the SCCS. Target-transfer lines were rinsed to obtain residual $[^{18}F]F^-$ for facility user experiments; provided as an aqueous $[^{18}F]F^-$ solution.

2.2.2.3. Azeotropic Drying of [^{18}F]F$^-$ Solution.

The aqueous [^{18}F]F$^-$ solution (~300 MBq) obtained from the SCCS was further diluted with deionized water (2.00 mL) and eluted through a potassium-carbonate ion exchange cartridge (Sep-Pak QMA). The QMA trapped [^{18}F]F$^-$ ions were subsequently eluted into a dry, sure-sealed overhead vial in the form of tetrabutylammonium [^{18}F]F-fluoride ([^{18}F]F-TBAF) by passing an ethanol-based solution of tetrabutylammonium bicarbonate (TBAB) (700 µL, 0.0750 M) through the cartridge. The [^{18}F]F-TBAF solution was azeotropically dried in the sure-sealed vial under a gentle stream of nitrogen gas by heating the vessel to 95 °C and adding MeCN (1.00 mL) to the existing solution. Solvent vapours were expelled from the vial through a vent needle as the process was repeated four times until a dry pale-yellow precipitate was visible along the inner walls of the vial (**Figure 2.3**).

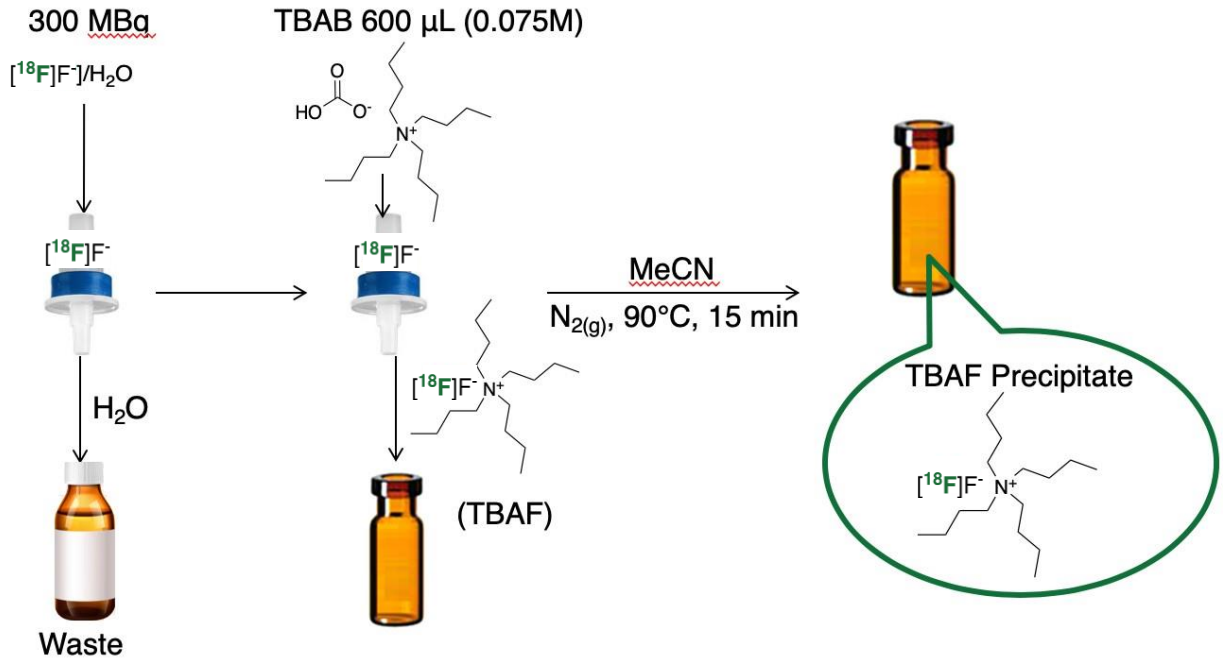

Figure 2.3. Illustration of the manual azeotropic dry down process.

2.2.2.4. ^{19}F/^{18}F-Exchange of CDy11.

Attempted radiosyntheses of [^{18}F]F-CDy11 applied methods adopted from (Carlucci *et al*., 2015; and Paulus *et al*., 2017).[127] [128] Azeotropically dried [^{18}F]F-TBAF was reconstituted with

anhydrous acetonitrile (200 μL). CDy11 was added to the solution and mixed for several minutes before addition of *"catalytic"* $SnCl_4$ to assist in the exchange of CDy11-bound fluorine with the available $[^{18}F]F^-$ ions in the reaction media. (**Scheme 2.1**).

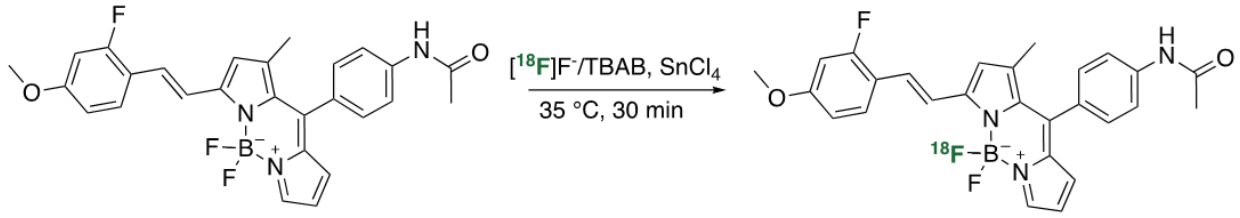

Scheme 2.1. Tin(IV) chloride ($SnCl_4$) catalyzed, one-step radio-synthetic preparation of $[^{18}F]$F-CDy11. The above reaction scheme uses TBAB to facilitate phase transfer of the reagents within the reaction media.

Parameters such as reaction time, temperature, and reagent concentrations, underwent individual assessment to optimize the reaction conditions and achieve successful radiofluorination of the CDy11 dye.

2.2.2.5. HPLC Analysis of CDy11 Post Reaction.

The CDy11 reaction was quenched with deionized water (100 μL). The resulting solution was eluted through a C-18 SepPak and washed with deionized water (10.0 mL) to remove free $[^{18}F]F^-$ ions from the sample. Organic components of the reaction mixture were eluted from the C-18 cartridge using MeOH; collecting 100 μL fractions at a time. The activity of each fraction was measured using a dose calibrator. The MeOH-compound elutions found to contain the greatest amount of radioactivity were combined. A sample of the radioactive solution (25.0 μL) was loaded onto a Thermo Fisher Vanquish UHPLC system equipped with an Eckert Ziegler radioactivity detector through a 20 μL sample loop for analysis. It is noted that HPLC chromatography data was not obtained from crude samples, but rather the small amount of isolated samples as a proof of concept for ^{18}F-labeling the Cdy11 molecule.

2.3. Results & Discussion.

2.3.1. Purification of CDy11.

The crude CDy11 mixture was dissolved completely in acetonitrile before slowly adding H_2O to make a solution with 3:8 solvent ratio respectively (2.04×10^{-3} M). The dark purple solution was sonicated and mixed with a vortex mixer several times before filtering with a 0.45 μm Promax PTFE filter. The resulting light red/pink solution was subjected to HPLC purification.

Mass spectrometry was used to confirm the CDy11 analyte's isolation at 32.6 minutes within the HPLC chromatogram (**Figure 2.4** and **Figure 2.5** respectively). The purified CDy11 was collected and presented as a clear vibrant fuchsia solution. Once collected, volatiles were removed via rotary evaporation and water was removed by freeze drying for 12 h before reconstituting with anhydrous acetonitrile (2.04×10^{-3} M). From this it was observed that of the original 0.0500 g of CDy11 dye provided, 7.00×10^{-3} g (15.9%) of the crude material was pure CDy11.

A second HPLC injection of the purified compound was performed immediately following the initial purification to confirm isolation of CDy11 from the crude mixture. However, within 24 h post purification, a third injection was performed prior to subjecting the CDy11 to [^{18}F]-labeling conditions to serve as cold reference, showed degradation of the purified agent in the form of a large secondary peak (**Figure 2.6**). Degradation was confirmed using mass spectrometry (**Figure 2.7**).

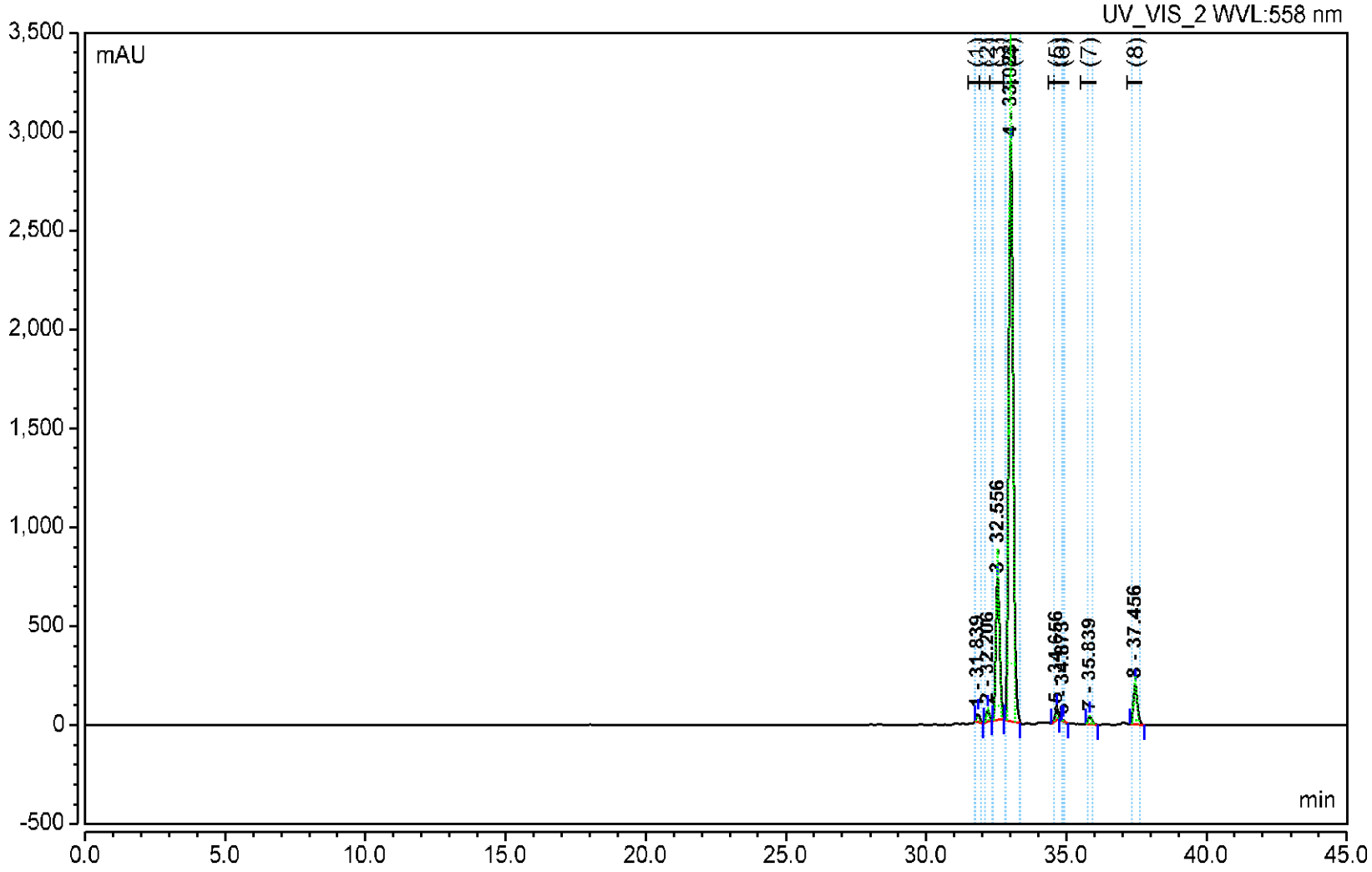

Figure 2.4. HPLC chromatogram of crude CDy11 compound mix at 558 nm wavelength. HPLC purification was carried out using the conditions previously outlined for semi-prep column use. Peak 3 (32.206 min) is associated with the purified CDy11 molecule.

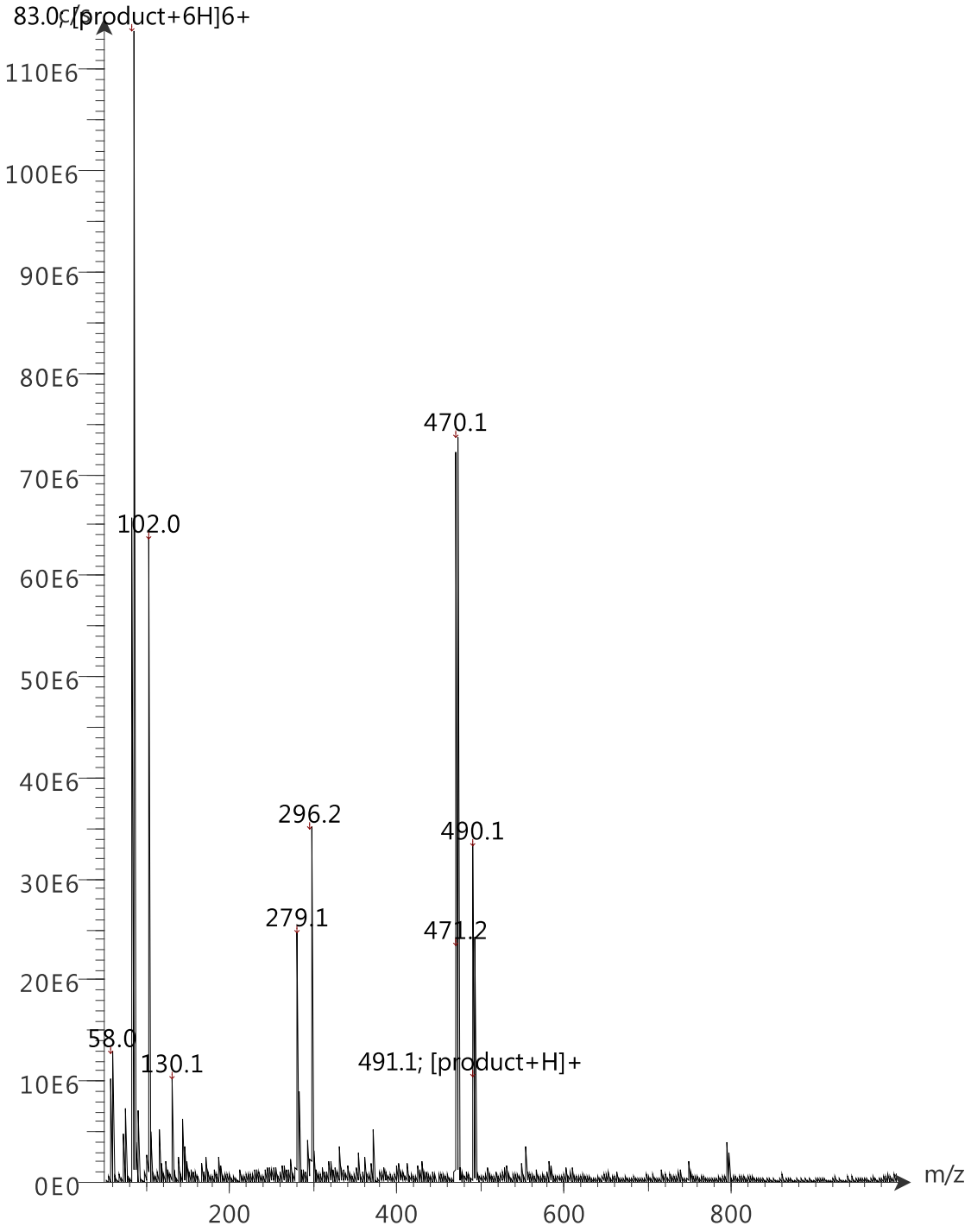

Figure 2.5. ESI $^{+}$ Mass spectrum of purified CDy11 molecule; exact mass 491.20 amu.

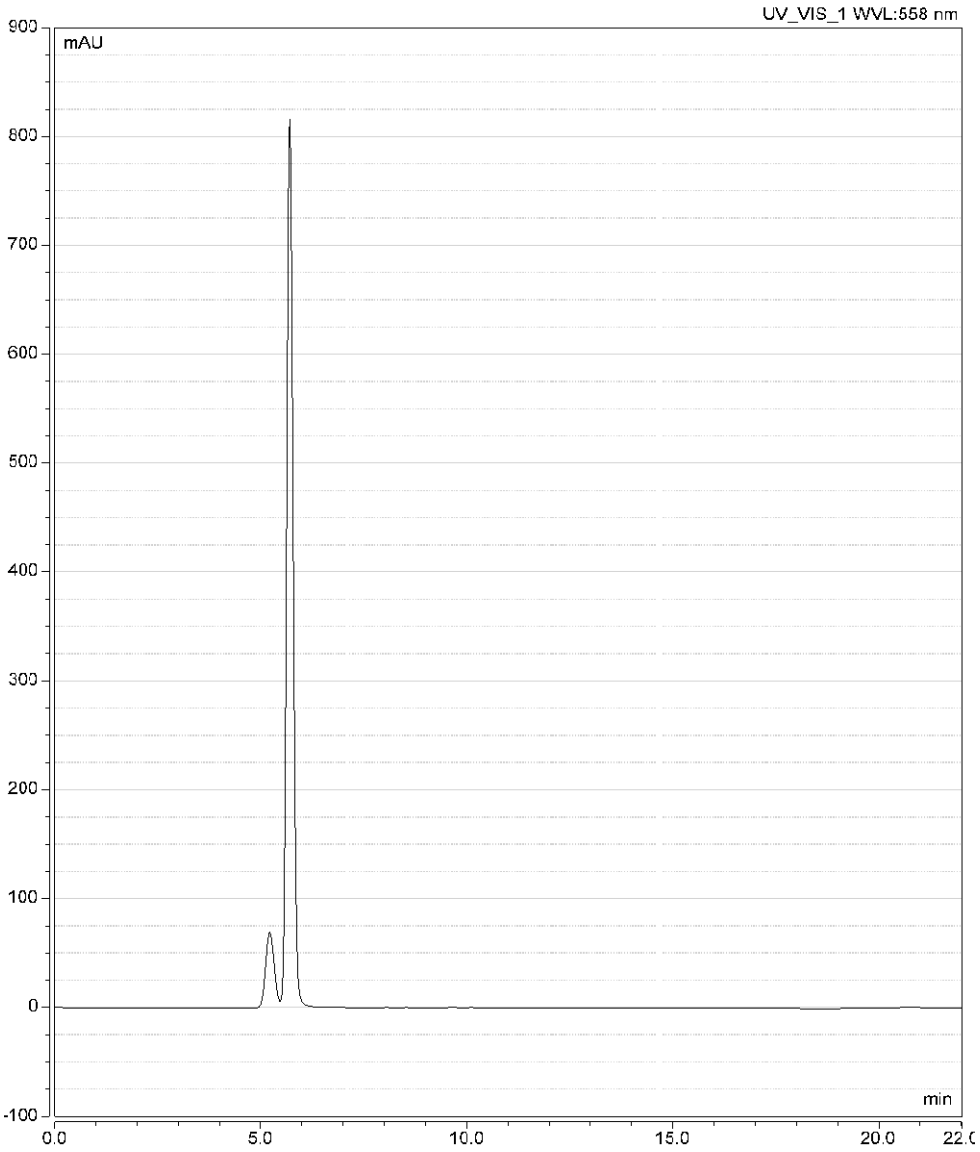

Figure 2.6. HPLC chromatogram of the purified CDy11 compound 24 h, post purification. Absorbance measured at 558 nm. HPLC analysis was carried out using a UHPLC analytical column.

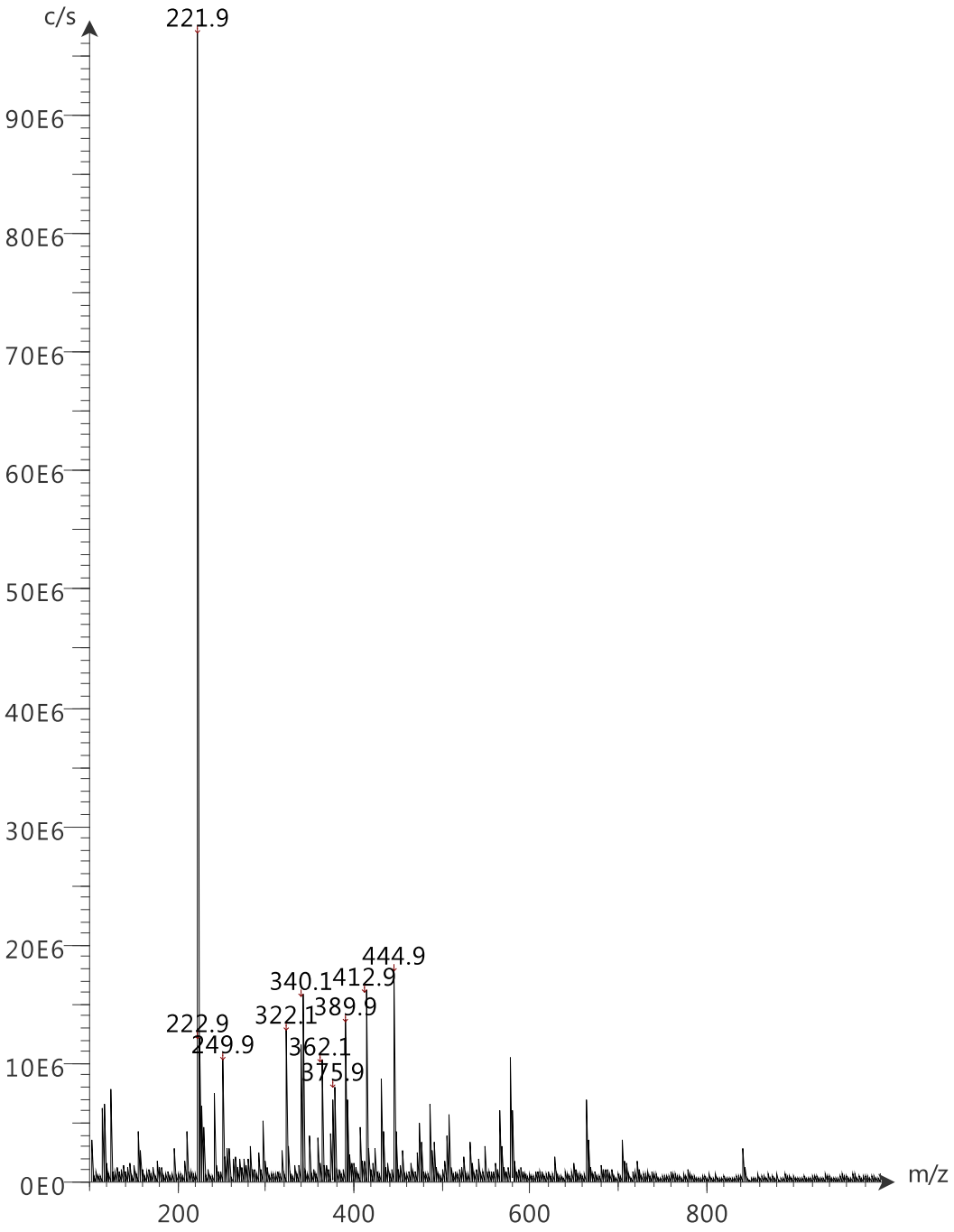

Figure 2.7. ESI^{+} Mass spectrum of reconstituted solution, post purification.

2.3.2. CDy11 Radiofluorination.

Prior to experimentation, several papers detailing BODIPY dye $^{19}F/^{18}F$-isotopic exchange were studied to ascertain a grasp of the reaction procedure. The degree to which these articles and their supporting information described the radiofluorination procedures varied significantly. While some articles gave very few details, others had outlined a nucleophilic reaction with $SnCl_4$ added to the BODIPY dye prior to introducing the $[^{18}F]F^-$ solution into the reaction environment. A recent article had used the term "catalytic" when describing the use of $SnCl_4$. Given the definition of a catalyst, this implies that the rate of $^{19}F/^{18}F$-isotopic exchange is increased by the introducing the Lewis acid into the reaction mixture as it provides a more energetically favorable route for transfluorination to proceed. In addition to this, the catalytic agent should be regenerated, that is it should undergo no net change once it completes its assistance of the reaction. It is imperative to clarify that the $SnCl_4$ reagent acts to abstract fluorine from the BODIPY core prior to the addition of the $[^{18}F]F^-$ solution. In doing such, a reaction site is generated that allows for nucleophilic incorporation of a $[^{18}F]F^-$ anion from the surrounding reaction media. That is to say, the Lewis acid must interact with the BODIPY precursor before incorporating the $[^{18}F]F^-$ solution into the reaction medium. This abstraction process does not occur however without the formation of tin(II) and tin(IV) fluorides (SnF_2 and SnF_4) and the original $SnCl_4$ reagent is not regenerated during the reaction. This misuse of the word "catalyst" deserves clarification as it introduces a source of discrepancy within the literature outlining the mechanism by which the Lewis acid assisted radiofluorination of BODIPY dyes is achieved.

The $SnCl_4$ reagent's moisture sensitivity is a potential source of variance for the reaction. The Lewis acid is drawn in very small quantities (~5-20 μL) from a commercial sure-sealed vessel using a beveled Hamilton syringe. During the short period of time when the syringe is removed from the bottle to puncture the sure-seal capping of the reaction vial, tin(II) and (IV) oxides precipitate at the tip of the needle while HCl gas is liberated. Not only are these solids insoluble within the reaction environment, they also obstruct the remaining solution's entry into the reaction vessel by either partially or fully clogging the needle. Both outcomes reduce the amount of Lewis acid available to facilitate the $^{19}F/^{18}F$-transfluorination reaction to an unknown and unpredictable amount. While this variance may affect the reaction to a lesser degree for a larger scale reaction, radiofluorination processes are carried out on a small-scale level. In this case, with a milligram or

less of precursor used, the smallest deviance from the intended volume can have a significant impact on the molar equivalent of $SnCl_4$ dispensed and therefore the reaction's outcome, and the replicability of the experiment's results.

While degradation was found to occur within 24 h of purification, the CDy11 mixture was subjected to several variations of the radiolabelling procedures to radiolabel the remaining CDy11 molecules within the sample. These attempts are outlined in **Table 2.1**. The success of the [^{18}F]F-CDy11 labeling attempts was assessed using HPLC analysis with both UV/Vis and radioactivity detectors. Given CDy11's existing optical activity, the successful radiofluorination of the molecule affords new radioactivity-detector signal; the retention time (t_R) of which corresponds with that observed of the fluorophore during UV-Vis HPLC analysis with a delay of ~0.7 min (radiation detector is placed after the UV-Vis detector in the flow-path).

Despite the experimental attempts made, the Lewis-acidic conditions of the ^{19}F/^{18}F-isotopic exchange reactions exasperated degradation of the CDy11 precursor. When comparing the UV-Vis chromatograms run of the unreacted CDy11 with reaction mixture, no CDy11 was found present post reaction. As such, while degradation products were labelled with [^{18}F]F^- anions during the attempted reactions, no [^{18}F]F-CDy11 was observed in the radioactivity chromatograms used to assess the efficacy of the applied experimental conditions.

Table 2.1. Summary of experimental parameters assessed during the attempted ^{18}F-labeling of CDy11. Quantities (µg), solution volumes (µL), solution concentrations (µmol), and the number of equivalence values of reagents applied per experiment with respect to the BODIPY starting material (eq) are provided for each of the attempted labeling processes. Reaction duration is provided in minutes (min). The radioactivity associated with successfully ^{18}F-labeled BODIPY is recorded for each of the outlined experimental efforts' TLC and HPLC analyses as a percentage (%) of the total amount of BODIPY standard applied at the start of the reaction. The specific activity values obtained through TLC and HPLC analyses are reported as a measure of radioactivity (Mega Becquerel) per volume of the reaction solution (MBq/ µmol). Activity values listed in this table are non-decay corrected (NDC).

Entry	CDy11 (µg, µmol)	Fixing Agent (µg, µmol)	$SnCl_4$ (µg, µmol)	Temperature (°C)	Time (min)	^{18}F-Labeling Reaction Efficacy NDC(%)	RCY NDC (MBq/µmol))
1	50.0, 0.102	TBAB 261, 0.786	268, 1.02	25	30	-	-
2	100, 0.204	K_{222}/K_2CO_3 3000, 7.97/ 554, 4.01 TBAB 1821, 6.00	5210, 20.0	80	30	-	-

Entry	CDy11 (μg, μmol)	Fixing Agent (μg, μmol)	$SnCl_4$ (μg, μmol)	Temperature (°C)	Time (min)	^{18}F-Labeling Reaction Efficacy NDC(%)	RCY NDC (MBq/μmol))
3	50.0, 0.102	TBAB 13658, 45.0	261, 1.00	50	30		-
4	100, 0.204	K_{222}/K_2CO_3 3000, 7.97/ 554, 4.01 TBAB 1821, 6.00	5315, 20.4	80	60	-	-

2.4. Conclusions & Future Directions.

CDy11 was obtained from our collaborator in low purity, with degradation of the re-purified compound observed within 24 h. Subjecting the purified CDy11 product to Lewis-acidic $^{19}F/^{18}F$-isotopic exchange conditions seemingly accelerated the compound's degradation, presumably due to the liberation of HCl from the $SnCl_4$ reagent. Consequently, [$^{18}F^-$]F-CDy11 was not produced under the applied reaction conditions.

While the desired product could not be isolated, the use of moisture-sensitive agents such as $SnCl_4$ presented as a notable source of variability for reaction's outcome. Investigating the efficacy of water-stable Lewis acids towards facilitating $^{19}F/^{18}F$-transfluorination at the BF_2-moiety of BODIPY fluorophores could offer alternative Lewis acidic agents for carrying out the reaction process with more consistent labeling yields. Follow up efforts exploring this notion are described in Chapter 3 of this thesis.

Chapter 3 Preamble

Chapter 3 explores the use of an alternative Lewis acidic agent to facilitate $^{19}F/^{18}F$-isotopic exchange at the BF_2-moiety due to the variability the $SnCl_4$ Lewis Acid introduces to the overall reaction process. To explore this idea, we selected a simple and commercially available BODIPY dye. As opposed to the moisture sensitive $SnCl_4$ Lewis acid frequently applied in literature reported BODIPY ^{18}F-labeling efforts, the following efforts describe the use of hydrated $Mg(NO_3)_2$ as a mild and stable alternative under the hypothesis that the agent will serve to effectively radiolabel the commercial precursor. The nitrate salt of magnesium was selected for maximum solubility so that a high-concentration stock solution could be prepared in water, and so that a minimum volume of water would be introduced into the radiochemistry reaction when transferring the solution. Efficacy of the $^{19}F/^{18}F$-transfluorination conditions were evaluated using an HPLC system equipped with both UV-Vis-, radiation-detectors, and radio-TLC imaging scanner. While further experimentation is necessary to obtain an optimized ^{18}F-labeling strategy applying hydrated $Mg(NO_3)_2$, initial efforts are reported and discussed herein.

This chapter also outlines the efforts made towards automating the optimized $Mg(NO_3)_2$ methods for radiofluorination of the commercial dye. Automation efforts were carried out an a Trasis miniAllInOne (miniAiO) synthesizer. While optimized methods remain under investigation, an automated method was established for the azeotropic drying and reconstitution of $[^{18}F]F^-$ anions.

Chapter 3

3.1. Introduction.

3.1.1. Tin Chlorides.

Of the reagents assessed by (Liu *et al.*, 2013).[53] during their original investigation into Lewis acid assisted [^{18}F]F-BODIPY dye labeling strategies, Sn(IV) chloride afforded the most successful results. Consequently, the majority of efforts that have reported the use of Lewis acids to facilitate the ^{19}F/^{18}F-transfluorination of BODIPY-based imaging agents utilizes $SnCl_4$ by convention. The Lewis acidic properties of tin(II) chloride and its milder counterpart tin(IV) chloride are commonly applied as catalysts. For example, on an industrial scale, tin chlorides often serve to promote the synthesis of polyester and Friedel-Crafts alkylation of aromatic rings.[129]

3.1.1.1. Instability & Safety Associated with Tin Chlorides.

Chloride salts of both the 2^+ and 4^+ oxidation states of tin have a wide degree of variability associated with their efficacy and pose health risks to personnel who come into contact with them. Both $SnCl_2$ and $SnCl_4$ are susceptible to hydrolysis in the presence of air and water; resulting in the loss of viable agent through the formation of tin hydroxide and/or oxide precipitates and HCl gas (**Scheme 3.1**). Thus, while tin chlorides can yield highly successful ^{19}F/^{18}F-transfluorination reactions for BODIPY dyes, the difficulty associated with handling them are a significant problem that requires resolution for improved replicability of results.

A) $SnCl_2 + 2H_2O \longrightarrow Sn(OH)_2 + 2HCl$

B) $SnCl_4 + 4H_2O \longrightarrow Sn(OH)_4 + 4HCl$

C) $SnCl_4 + 2H_2O \longrightarrow SnO_2 + 4HCl$

Scheme 3.1. Hydrolysis of: A) Sn(II) chloride and B) Sn(IV) chloride to produce Sn(II) and Sn(IV) precipitates respectively and HCl gas. C) Oxidation of Sn(IV) into insoluble Sn(IV) oxide and HCl gas.

3.1.2. Magnesium Salts.

Based on previous experiences where tin(IV) chloride was applied in the attempted radiofluorination of the BODIPY dye CDy11 (refer to Chapter 2), research objectives shifted towards investigating air-stable substitutes for the reactive Lewis acid. Although (Liu *et al.*, 2013) had originally assessed the success of several Lewis acid alternatives, the scope of their analysis focused only on transition and post transition metals such as titanium and tin. By broadening our searches for an alternate Lewis acid beyond those previously studied, we noted that magnesium shares similarities with tin(II) and tin(IV). As shown in **Table 3.1**, the effective ionic radii of magnesium ions lies within a similar range to that of Sn(IV).[130 131 132] What's more, magnesium interacts with fluoride to form bonds of comparable strength (bond dissociation values) to those observed with tin; with $(MgF)^+$ reacting with a second fluoride to form a bond with strength comparable to that forged between the anion and titanium; which (Liu *et al*., 2013) reported as the second most effective agent during their assessment.

Table 3.1. Energy of bond dissociation values reported for 298 Kelvin ($D°_{298}$, kJ/mol) and effective ionic radii (pm) of relevant bonds towards the selection of a new Lewis acid for assisted $^{19}F/^{18}F$-transfluorination of BODIPY dyes.

Bond	**$D°_{298}$ (kJ/mol)**	**Reference Number**	**Bond**	**$D°_{298}$ (kJ/mol)**	**Reference Number**	**Effective Ionic Radii (pm)**		**Reference Number**
B-H	345 ± 3	131	Mg(II)-H_2O	123 ± 13	131	Ti(IV)	60.5	132
B-F	766 ± 13	130	Mg(II)-OH	314 ± 33	131	Sn(IV)	69.0	132
BF-F	569	130	Mg-H	191 ± 6	131	Mg(II)	72.0	132
Sn(IV)-F	476 ± 8	131	Mg(II)-F	477 ± 50	131	Ti(II)	86.0	132
Ti(IV)-F	569 ± 33	131	Mg(II)F-F	544	130	-	-	-

3.1.2.1. Magnesium Nitrate Hexahydrate [$Mg(NO_3)_2$]·$6H_2O$.

Magnesium nitrate [$Mg(NO_3)_2$] is a hygroscopic inorganic salt that forms its hydrated variant when exposed to water, or to air with sufficient moisture content. Although absorbing water modifies the Lewis acidic agent, magnesium is stable in its 2+ oxidation state and the hydrated species is stable and thus easily handled without posing risk of precipitation. Unlike tin and titanium chlorides, magnesium salts do not rapidly precipitate or liberate HCl. The additional water of the hydrated species would conventionally be of concern for radiochemists as the nucleophilic interactions between the water protons and [^{18}F]F^- anions reduce the nucleophilicity of the fluoride and therefore the amount of radioactive isotope available for incorporation into the target compound. However, while ^{18}F-fluorination reactions are normally performed in polar aprotic solvents, recent reports suggest that the presence of a small amount of water, even as a co-solvent may not always be detrimental to radiofluorination reactions.[133] An example of a successful radiofluorination reaction that was performed under wet conditions is the production of *ortho*-phosphonium aryltrifluoroborate zwitterions via nucleophilic ^{19}F/^{18}F-isotopic exchange; which was carried out by (Li *et al*., 2012) with water as the primary solvent and polar aprotic acetonitrile only present in trace amounts (**Schemes 3.2**).[134] [135] As such, the requirement to dissolve the magnesium salt into water and therefore the addition of a small quantity of water to the BODIPY radiofluorination reaction was not a deterrent.

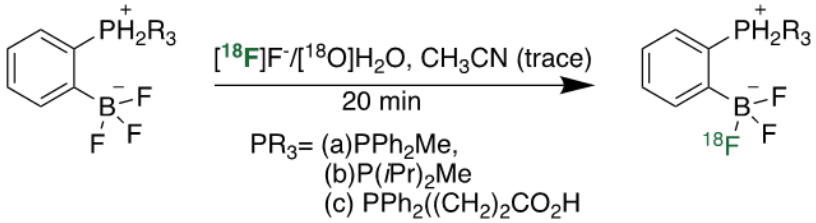

Scheme 3.2. ^{19}F/^{18}F-transfluorination of *ortho*-phosphonium aryltrifluoroborate zwitterions under aqueous conditions as reported by (Li *et al*., 2012).[134]

3.1.3. Automated Radiosynthesis.

The automation of synthetic procedures allows for the production (synthesis) of radiochemical agents to meet the standards of the good manufacturing processes (GMP) required for administering these agents within biological systems. Automation improves the replicability and reliability of radiolabeling methods by reducing the amount of human error that can in turn lead to variability between production batches and even production failure.[136] This standardization has the added benefit of reducing the radiation exposure of production personnel, as the automation boxes can carry out a complicated radiosynthesis remotely or from behind lead shielding, using a series of valves, tubes, pumps, cartridges, and even in-line HPLC systems. While manual efforts require handling radioactive substances for extended periods of time and increased risk of contamination, the closed system of the automated synthesizer can be safely monitored from a distance via the instantaneous production feedback of the automation software. Finally, this lower exposure risk allows for the use of higher radioactivity levels during synthesis and, in accordance with the larger amount of radioactive isotope available for incorporation, higher radiochemical production yields and specific activity values for the reaction product.[137]

3.1.3.1. Automated Synthesis Platforms.

Currently, two of the leading automated systems used to produce GMP-grade radiodiagnostic agents are the GE TRACERlab FX_{FN} and Trasis AIO (All in One) systems. Both synthesis modules have their benefits. As the TRACERlab FX_{FN} was the first to arrive to market, it has since become the most widely applied system for automation of radiosynthetic procedures, with the most common example being [^{18}F]F-FDG. Consequently, many of the automation and optimization strategies that have been published to date are in reference to the design and software of the TRACERlab system. However, because the system's components that encounter reagents and radioactivity are fixed within the TRACERlab's design, post-production cleaning steps require a further attention to assure GMP accreditation is maintained. However, the TRASIS AIO automated synthesizer is a cassette-based system that runs the reaction procedure through sterilized and commercially available disposable components. This design allows the user to modify the cassette to better suit the synthetic procedure being run on the system and dispose of the cassette

once synthesis is achieved, reducing the risk of cross contamination between production runs as well increasing the throughput of production. [138]

3.1.4. Purpose Statement.

While the Lewis acid-based ^{18}F-labeling strategies reported to date for BODIPY dyes afford high radiochemical yields, they are limited by the moisture sensitivity of the Lewis acidic agents applied to facilitate radiofluorination. Despite their described efficacy, the yields of the reactions applying tin and titanium as Lewis acids are subject to significant irregularity as their reactivity with water leads to varying amounts of reagent precipitation and the production of acidic fumes. Not only does this Lewis acid degradation prove problematic for manual labeling efforts as the precipitation results in reduced labeling yields and clogging of needles, reagent inlets, and outlets, but the deteriorative effects of the acidic fumes degradation on the synthesiser platform itself inhibit automation and GMP certification of BODIPY-based radiotracers altogether.

As the original survey performed by (Liu *et al.*, 2013) pertained to only a small range of applicable Lewis acids, there is room to improve the existing labeling strategies through assessing alternative Lewis acidic reagents. This project sought to explore the use of air-/shelf-stable Lewis acids with comparable chemical properties to those of Sn^{4+}/Ti^{4+} as promoters for the ^{18}F/^{19}F-isotopic exchange of BODIPY dyes. We hypothesized that magnesium(II) nitrate [$Mg(NO_3)_2$] could function effectively as ^{19}F/^{18}F-exchange promoting agent by virtue of its comparable acidic-strengths and bond dissociation energies with those of tin and titanium ions. Furthermore, through our relationship with the Sylvia Fedoruk Centre for Nuclear Innovation, researchers are given the opportunity to gain familiarity with the TRASIS AIO synthesis platform. As such, the final goal of this project was to automate the optimized magnesium-based radiofluorination of a proof-of-concept commercial BODIPY dye using the TRASIS AIO system to demonstrate the overall benefit of using magnesium Lewis Acid salts for labeling BODIPY-based imaging agents.

3.2 Experimental.

3.2.1. $Mg(NO_3)_2{\cdot}6H_2O$ Solution Preparation.

Concentrated solutions of $Mg(NO_3)_2{\cdot}6H_2O$ were prepared by dissolving the hydrated salt (0.500 g, 1.95 mmol) in a minimal amount of solvent. Both polar protic and polar aprotic solutions of $Mg(NO_3)_2{\cdot}6H_2O$ were made in this fashion and used for experimentation to assess the effects of solvent on the reaction yields (aqueous (polar protic) Lewis acid solutions were made using 0.418 mL of deionized water for a final concentration of 4.66 M and polar protic solutions were made using 1.40 mL of DMSO for a $Mg(NO_3)_2{\cdot}6H_2O$ solution Molarity of 1.39 M).

3.2.2. Tetraethylammonium Bicarbonate Solution Preparation.

Tetraethylammonium bicarbonate (71.7 mg, 0.375 mmol) was completely dissolved in deionized water (0.500 mL) and MeCN (4.50 mL), producing a freshly-made solution of phase transferring agent with 1:9 H_2O:MeCN solvent composition for each ^{18}F-radiolabeling experiment.

3.2.3. $^{19}F/^{18}F$-Isotopic Exchange of BODIPY Dye Standard.

3.2.3.1. $[^{18}F]F^-$ Solution Production.

Aqueous $[^{18}F]F^-$ anionic solutions were produced by staff at the Saskatchewan Centre for Cyclotron Sciences (SCCS) via a $^{18}O(p, n)^{18}F$ nuclear reaction using an ACSI TR24 cyclotron. The primary batch of fluoride-18 was used by the SCCS, and the target-transfer lines were rinsed to obtain residual $[^{18}F]F^-$ ions for these experiments provide as aqueous $[^{18}F]F^-$.

3.2.3.2. Manual Azeotropic Drying of $[^{18}F]F^-$ Solution.

Aqueous $[^{18}F]F^-$ (~300 MBq) obtained from the SCCS was diluted further with deionized water (2.00 mL) and eluted through a pre-conditioned Sep-Pak QMA cartridge. QMA trapped $[^{18}F]F^-$ ions were subsequently eluted in the form of $[^{18}F^-]$F-TEAF by passing a freshly made solution of TEAB (700 μL, 0.0750 M) through the cartridge. The $[^{18}F^-]$F-TEAF salt solution was azeotropically dried in a sure-sealed overhead vial immersed in an oil bath heated to 95 °C by adding MeCN (1.00 mL) and passing a constant stream of nitrogen gas through the vessel. Solvent

vapours were expelled from the vial through a vent needle. The azeotropic drying process was repeated four times and produced a dry pale-yellow precipitate along the inner walls of the vial.

3.2.3.3. Automation Test for Azeotropic Dry Down and Subsequent Reconstitution of [^{18}F]F$^-$-Solution.

Using a small amount of activity for initial testing, aqueous [^{18}F]F$^-$ (50-75 MBq) was transferred directly to the TRASIS MiniAIO automated synthesizer (**Figure 3.1**) through the activity inlet into the activity plunger. The synthesis module was operated in the following manner to successfully dry and reconstitute a bulk solution of [^{18}F]F$^-$ with dry acetonitrile.

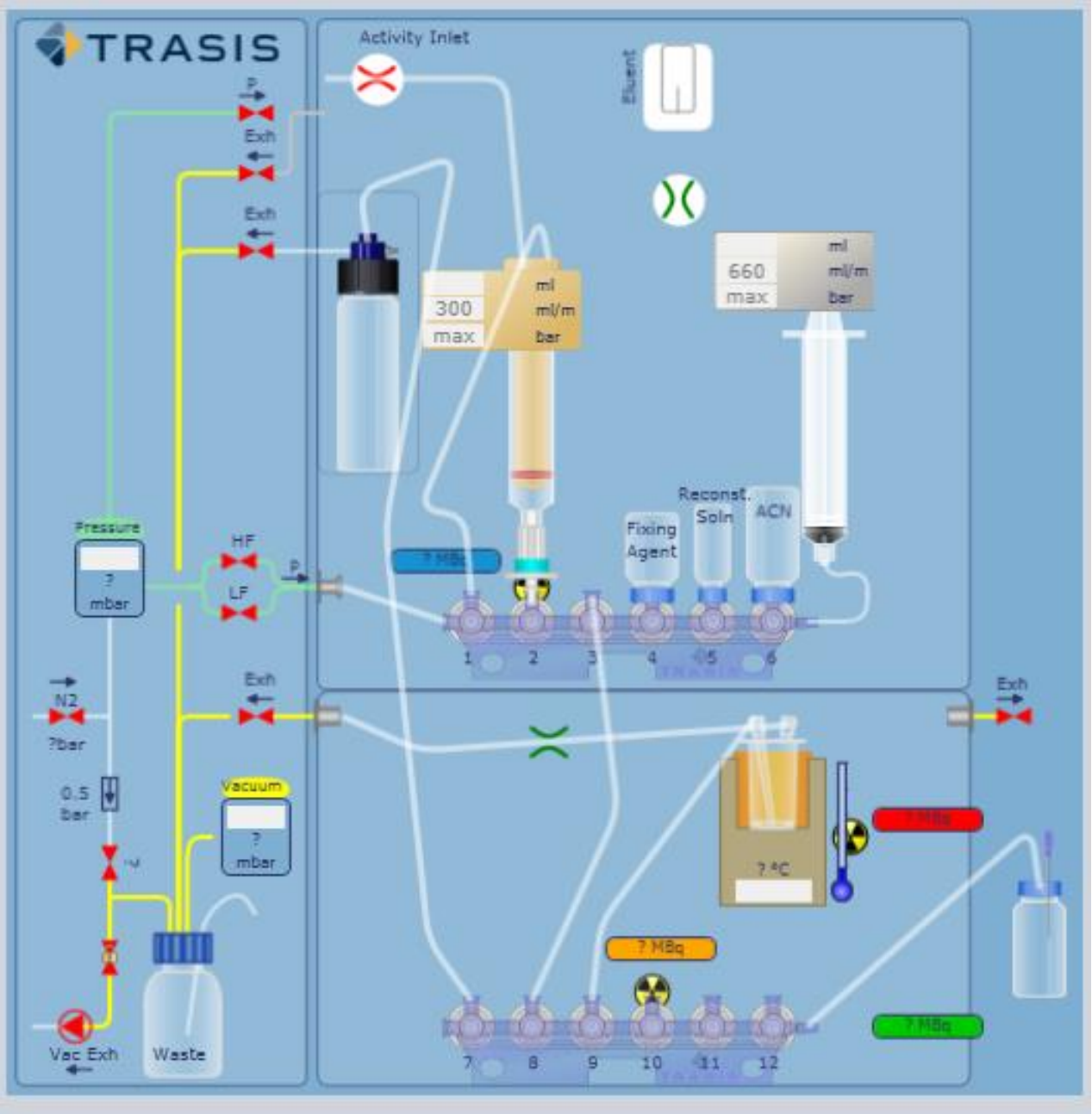

Figure 3.1. Diagram of the TRASIS MiniAIO automated synthesizer and cassette design used for the automated procedure.

The following steps were programmed into the TRASIS MiniAIO system to automate the purification and "dry down" procedure of fluorine-18, which was obtained in water following cyclotron production.

1. Aqueous [^{18}F]F^{-} (5.00 mL) was delivered to the TRASIS MiniAIO radiosynthesis module via the activity inlet. The aqueous [^{18}F]F^{-} ionic solution was eluted through the systems activity plunger and quantitatively trapped on a QMA carbonate ion exchange solid phase extraction (SPE) light cartridge (position 2).
2. The resin-bound [^{18}F]F^{-} anions were eluted from the QMA cartridge with a solution of tetraethylammonium bicarbonate (TEAB) (0.0750 M, 4.00 mL) (position 4) in the form of [^{18}F]F-tetraethylammonium fluoride ([^{18}F]F-TEAF).
3. The [^{18}F]F-TEAF solution was transferred into the reactor vial (line positions 3→8→9) and dried azeotropically by addition of anhydrous acetonitrile (1.00 mL) (position 6) under reduced pressure at 95 °C. This process was repeated four times to afford [^{18}F]F-TEAF as a dry, off-white/yellow solid lining the sides of the reactor vial.
4. The reactor vial was cooled to 40 °C using a stream of nitrogen gas before addition of anhydrous acetonitrile (3.00 mL) (position 5) for reconstitution of the dried [^{18}F]F-TEAF. The solution was transferring to a vented product vial.

3.2.3.4.^{19}F/^{18}F-Isotopic Exchange Reaction.

During several attempts to discern optimal reaction conditions through which magnesium nitrate could facilitate ^{19}F/^{18}F-transfluorination of a commercial BODIPY dye, various equivalents of magnesium nitrate hexahydrate and BODIPY dye standard were mixed at 37 °C for 5 minutes. Azeotropically dried [^{18}F]F-TEAF was reconstituted with anhydrous acetonitrile (200 μL) and added to the Lewis acidic mixture. Crude samples of the mixture were obtained as the reaction proceeded to assess the impact of time on the radiochemical yields obtained under the applied conditions. Reaction efficacy was assessed by subjecting the crude samples of the reaction mixture to radio-HPLC and radio-TLC analysis.

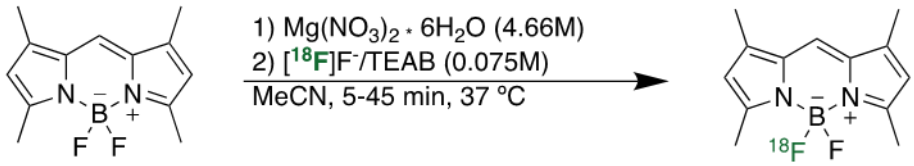

Scheme 3.3. General reaction scheme for $^{19}F/^{18}F$-isotopic exchange of the commercial BODIPY standard using magnesium nitrate hexahydrate [$Mg(NO_3)_2$] as a Lewis acid to enable the reaction to proceed forward.

3.2.3.5. HPLC Analysis of BODIPY Dye ^{18}F-radiolabeling Condition Efficacy.

A 20 µL-100 µL sample of the BODIPY standard solution was analysed using a ThermoFisher Vanquish UHPLC system equipped with a Chromeleon 7 communication software prior to each [^{18}F]-labeling attempt. Samples were run via reverse-phase chromatography by applying a gradient solvent mixture of H_2O: MeCN (70:30 to 5:95) with 0.1% formic acid. A C18 HPLC column with TMS endcapping (Luna® 5 µm C18(2) 100 Å, LC Column 250 × 4.6 mm, Ea) was used for experimental analysis of the BODIPY standard. Absorbance was measured at both the absorbance maximum of the commercial dye of 505 nm, and 254 nm; a common wavelength for aromatic compounds.

Crude samples of the reaction mixture were quenched with deionized water to afford a mixture of MeCN:H_2O solvent ratio of 2:8. The sample mixture was filtered through a ProMax nylon syringe filter (pore size 0.2 µm, diameter 13 mm). The activity of a 20 µL sample subset was measured using a dose calibrator before loading the known volume onto a Thermo Fisher Vanquish UHPLC system equipped with an Eckert Ziegler radioactivity detector through a 20.0 µL sample loop. Experimental analysis was performed using a reversed phase C18 HPLC column with TMS endcapping (Luna® 5 µm C18(2) 100 Å, LC Column 250 × 4.6 mm, Ea). Eckert Ziegler radioactivity detector was set at 2000 K sensitivity. Gradient solvent systems of H_2O: MeCN (70:30 to 5:95) with 0.1% formic acid were applied during analysis.

3.2.3.6. Thin Layer Chromatography (TLC) Analysis of BODIPY Dye ^{18}F-radiolabeling Condition Efficacy.

The efficacy of ^{18}F-labeling attempts were evaluated via thin layer chromatography (TLC). The effects of reaction parameters such as time and reagent equivalents were assessed by spotting the crude reaction sample on three separate Fisher Scientific precoated aluminium-backed silica TLC plates. TLC strips were run using acetonitrile as an eluent. Crude yields were determined by analysing the TLC plates with a Bioscan AR-2000 radio-TLC plate reader using Winscan Radio-TLC software (Bioscan Inc., Washington, DC).

3.3 Results & Discussion.

3.3.1. Preparation of $Mg(NO_3)_2 \cdot 6H_2O$ & TEAB Solutions.

$Mg(NO_3)_2 \cdot 6H_2O$ and TEAB solutions were prepared as outlined in the 3.2 Experimental section. TEAB was selected as phase transfer agent to elute $[^{18}F]F^-$ ions from the stationary phase of Sep-Pak QMA cartridges. The choice to use TEAB as an alternative for the TBAB previously employed during the ^{18}F-fluorination attempts of CDy11 outlined in Chapter 2 was based primarily on their interchangeable use in literature. Cost efficiency also played a role in this decision as the TBAB sold by a single vendor was of GMP quality, which was not required at this stage of experimentation (998.00 $/5.00 g vs 222.00 $/25.0 g).[139 140]

3.3.2. $^{19}F/^{18}F$-Isotopic Exchange of BODIPY Dye Standard.

To assess magnesium nitrate hexahydrate's efficacy towards facilitating $^{19}F/^{18}F$-isotopic exchange on a commercial BODIPY dye, experimental procedures were first carried out applying $SnCl_4$ as a Lewis acid. In doing such, reoptimized methods for the conventional Lewis acid were established as well as a general sense of the commercial dye's reactivity. Based on these efforts, the BODIPY dye used for experimentation displayed minimal reactivity when subjected to ^{18}F-radiolabeling efforts; with optimal efforts producing a ~30% non-decay corrected yield when subjected to 50 equivalents of the $SnCl_4$ Lewis acid for 30 minutes (**Figures A1.** and **A2)**. The commercial BODIPY precursor's minimal reactivity is attributed to the absence of electron withdrawing functionality within its molecular structure, which would afford inductive stability of the B-F bonds. While this increased inductive stability is not enough to hinder the breaking of B-F bonds under the Lewis acidic conditions provided by mixing the dye with the $Mg(NO_3)_2$ solution, it is enough to better support their reformation when a surplus of fluoride anions, such as the $[^{18}F]F^-$ solution, is introduced into the reaction medium.[141] As was previously evaluated during ^{18}F-labeling attempts applying $SnCl_4$, the order of reagents addition was assessed for experimental procedures utilizing the alternative $Mg(NO_3)_2 \cdot H_2O$ Lewis acid. The optimal order of addition did not change for reactions performed using the magnesium salt; the reaction did not proceed when the BODIPY and Lewis Acid were not combined prior to addition of the $[^{18}F]F^-$ solution.

Similar to experimental efforts with CDy11, several reaction parameters were assessed including the number of equivalents of applied reagents, reaction procession time, and the amount of fixing agent used. These results are summarized in **Table 3.2**.

Table 3.2. Experimental parameters and TLC/HPLC results from $^{19}F/^{18}F$-isotopic exchange attempts on commercial BODIPY dye. Quantities (µg), solution volumes (µL), solution concentrations (µmol), and the number of equivalence values of reagents applied per experiment with respect to the BODIPY starting material (eq) are provided for each of the attempted labeling processes. Reaction duration is provided in minutes (min). The radioactivity associated with successfully ^{18}F-labeled BODIPY is recorded for each of the outlined experimental efforts' TLC and HPLC analyses as a percentage (%) of the total amount of BODIPY standard applied at the start of the reaction. The molar activity values obtained through TLC and HPLC analyses are reported as a measure of radioactivity (Mega Becquerel) per volume of the reaction solution (MBq/ µmol). Activity values listed in this table are non-decay corrected (NDC). The reaction time sample used for HPLC analysis is indicated with the symbol (♦) for each of the listed experimental conditions.

Entry	BODIPY Standard (µg, µmol)	TEAB Fixing Agent (eq, µL, µmol)	$Mg(NO_3)_2$ Lewis Acid (eq, µL, µmol)	Reaction Time (min)	TLC Results (%)	TLC Molar Activity (MBq/µmol)	HPLC Results (%)	HPLC Molar Activity (MBq /µmol)
1	200, 0.806	55.8, 600 (0.075 M), 45	**10, 1.73 (4.66 M), 8.06 *in H_2O**	♦5	0.4 ± 0.2	0.5	0.8	1.0
				15	0.3 ± 0	0.4		
				30	2.2± 1.4	2.7		
				45	1.6 ± 2.3	2.0		
2	200, 0.806	55.8, 600 (0.075 M), 45	**25, 4.32 (4.66 M), 20.15 *in H_2O**	♦5	3.3 ± 0.3	4.0	1.9	2.4
				15	1.6 ± 0.3	2.0		
				30	2.9 ± 2.3	3.5		
				45	4.4 ± 1.0	5.4		

Entry	BODIPY Standard (µg, µmol)	TEAB Fixing Agent (eq, µL, µmol)	$Mg(NO_3)_2$ Lewis Acid (eq, µL, µmol)	Reaction Time (min)	TLC Results (%)	TLC Specific Activity (MBq/µmol)	HPLC Results (%)	HPLC Specific Activity (MBq /µmol)
3	200, 0.806	55.8, 600 (0.075 M), 45	**50, 8.65 (4.66 M), 40.3** ***in H_2O**	5	11.4 ± 0.2	14.1	1.2	1.5
				15	6.6± 1.7	8.1		
				♦30	14.1± 5.5	17.4		
				45	24.8	30.8		
4	200, 0.806	55.8, 600 (0.075 M), 45	**100, 17.3 (4.66 M), 80.6** ***in H_2O**	♦5	21.8 ± 1.4	27.1	4.5	5.6
				15	19.3 ± 3.1	23.9		
				30	22.0 ± 1.4	27.3		
				45	30.2 ± 20.3	37.5		
5	200, 0.806	55.8, 600 (0.075 M), 45	**150, 26.0 (4.66 M), 121** ***in H_2O**	♦5	1.6 ± 0.4	2.01	7.5	9.3
				15	22.6 ± 6.6	28.0		
				30	25.4 ± 3.1	31.5		
				45	23.7 ± 11.2	29.5		
6	400, 1.612	**27.9, 600 (0.075 M), 45**	100, 34.6 (4.66 M), 161.2 *in H_2O	♦5	11.2 ± 6.7	6.96	0.45	0.3
				15	16.0±0.1	9.92		
				30	17.9 ± 3.3	11.1		
				45	18.0 ± 1.1	11.2		

Entry	BODIPY Standard (µg, µmol)	TEAB Fixing Agent (eq, µL, µmol)	$Mg(NO_3)_2$ Lewis Acid (eq, µL, µmol)	Reaction Time (min)	TLC Results (%)	TLC Specific Activity (MBq/µmol)	HPLC Results (%)	HPLC Specific Activity (MBq /µmol)
7	200, 0.806	**75.0, 806 (0.075 M), 60**	100, 17.3 (4.66 M), 80.6 *in H_2O	♦5	1.2 ± 0.6	1.45	9.5	11.8
				15	2.2 ± 2.5	2.72		
				30	0.4 ± 0.2	0.529		
				45	1.5 ± 0.7	1.81		
8	200, 0.806	55.8, 600 (0.075 M), 45	**100, 58.0 (1.39 M), 80.6 *in DMSO**	♦5	1.2 ± 0.3	1.48	8.3	10.3
				15	1.7 ± 1.2	2.15		
				30	2.2 ± 1.3	2.76		
				45	1.3 ± 1.0.	1.61		
9	200, 0.806	55.8, 600 (0.075 M), 45	**10, 1.73 (4.66 M), *in H_2O *15.6 µL extra H_2O (total amount is the same as that added during 100 eq runs)**	♦5	0.6 ± 0.5	0.707	2.4	3.0
				15	0.9 ± 0.2	1.12		
				30	0.7 ± 0.4	0.819		
				45	0.8 ± 0.2	1.04		

To discern the best means for assessing the success of the BODIPY $^{19}F/^{18}F$-transfluorination procedures, both radio-TLC and radio-HPLC analysis were performed to varying degrees. All relevant spectra and chromatograms are reported in the Appendix section. Radio-TLC was primarily utilized as it was initially believed to provide a simple means of confirming the applied reaction conditions afforded labeling of the BODIPY precursor. Radio-HPLC analysis was performed as a secondary means of confirming reaction progress. However, based on the values provided in **Table 3.2**, clear discrepancies are noted between the radiochemical yields obtained via the two methods. Radio-HPLC analysis revealed an impurity peak, likely attributed to a hydrolyzed variant of the BODIPY molecule, in close proximity to that of the [^{18}F]F-labeled commercial dye. Although HPLC affords resolution between the radiolabeled BODIPY product and the reaction impurity, the radio-TLC plate reader is unlikely to afford this refined distinction between the two. As such, the data obtained from the TLC reader is likely a composite of the two [^{18}F]F-labeled compounds. This also offers explanation as to why the TLC data obtained over longer periods of time are significantly higher than those obtained for the same samples when analyzed with the HPLC system (entry 3 of **Table 3.2**). Technically, this reaction by-product was a radiofluorinated BODIPY dye and did indicate successful labeling, and the extent of decomposition into what was likely a hydrolyzed product would change depending on which BODIPY dye was being radiolabeled. As such, the presence of this impurity was not detrimental to the purpose of these experiments, which was to determine 1) if magnesium salts could facilitate this transfluorination reaction, and 2) what the optimum reaction conditions were. Future work would include applying these optimized methods to a variety of different BODIPY dyes.

Based on the results obtained through HPLC analysis (**Figure 3.2**), use of 75 equivalents of the TEAB fixing agent relative to the molar amount of BODIPY dye precursor and 100 equivalents of the magnesium nitrate hexahydrate salt dissolved in water afforded the highest radiochemical yields for the commercial BODIPY dye (entry 7 in **Table 3.2**). The large amount of excess Lewis acid required to facilitate ^{18}F-radiolabeling of the BODIPY agent as well as the order of compound addition again supports the notion of the Lewis acid's role as a reactant as opposed to serving as a regenerative catalyst. As the HPLC data lacks replicate analyses for statistical error and was not performed for each of the assessed parameter's time points, further

investigative efforts must be performed in the future to improve the analysis of experimental results and isolate the desired ^{18}F-labeled BODIPY product from the crude reaction mixture.

Figure 3.2. Entry number ranking of radiochemical yields listed in Table 3.2 and obtained from the HPLC analysis of ^{19}F/^{18}F-isotopic exchange efforts on the commercial BODIPY dye from lowest yield to highest.

Lewis acidic solutions of $Mg(NO_3)_2$ were prepared in both polar protic H_2O and polar aprotic DMSO as solvents to assess the effects of water on the ^{19}F/^{18}F-transfluorination process. Upon comparison of the values reported for entries 4 and 8 of **Table 3.2** wherein the only variable between these two reactions was the solvent used to dissolve the $Mg(NO_3)_2$ Lewis acidic agent, radio-HPLC analysis denoted nearly twice the radiolabeling yields from use of DMSO as solvent for the Lewis Acid solution. This suggests that water's presence within the reaction medium followed convention of reducing the [^{18}F]F$^-$-solution's nucleophilicity in the reaction medium. This consequently resulted in lower radiochemical yields for the reactions carried out with aqueous Lewis acidic solutions than what could have been achieved using $Mg(NO_3)_2$ dissolved in polar aprotic DMSO. In accordance with this, while the reaction conditions outlined in entry 7 of **Table 3.2** afforded the highest radiochemical yields based on radio-HPLC chromatogram data and were carried out using an aqueous Lewis acid solution, this reaction was carried out using a greater equivalence of $Mg(NO_3)_2$. It is likely that, based on the results of entries 4 and 8 of **Table 3.2**, had a polar aprotic Lewis acid solution been used instead of the aqueous one, an even higher radiochemical yield of [^{18}F]F-BODIPY would have been generated. As previously discussed, TLC chromatograms did not afford good resolution between the desired [^{18}F]F-BODIPY product and radiolabeled hydrolyzed degradation product which offers an explanation as to why the TLC results reported for entry 4 are significantly greater than those of entry 8. Entry 9 of **Table 3.2** outlines efforts to further assess the effects of water on the reaction process by incorporating a

larger amount of water within the reaction but with the same molar equivalents of $Mg(NO_3)_2$ Lewis acid. While initially it may seem surprising that the radiochemical yield reported for the HPLC analysis of entry 9 is greater than that of entry 1 wherein the same amount of Lewis acid was applied, both yields remain low and the lack of replicate analyses performed with radio-HPLC instrumentation leave a wide window of variance wherein these values may fall. Consequently, a firm conclusion cannot be drawn at this time and further experimental evaluation is required to adequately evaluate the difference between these two reaction conditions. As general trends, when all other variables were kept constant, it appears as though increasing the equivalents of magnesium from 10-150 increased yields as indicated by entries 1-5 in **Table 3.2**. As discussed above, with all other variables kept constant, using DMSO as a solvent for the magnesium solution increased the yield relative to using water. Further, the quantity of base utilized (TEAB) had an impact on yields, where entries 5 and 8 in **Table 3.2** show an increase in yields by increasing the quantity of base. In summary, more experiments are required to draw firm conclusions, but this work lays a good foundation to guide future experiments.

3.3.3. Automation of Azeotropic Dry Down and Reconstitution of [^{18}F]F$^-$ Solution.

Automation of the ^{18}F-fluorination process's azeotropic drying procedures presented several benefits. A major advantage of automating this procedure was that it provided a means for producing a bulk solution of the reconstituted [^{18}F]F$^-$-solution in a short period with reproducible "dryness". What's more, due to the lower risk of radiation exposure associated with automating the process, a larger amount of radioactivity could be used during production, which would increase the amount of [^{18}F]F$^-$ in the anionic solution available for incorporation in the BODIY ^{18}F-labeling experiments. This bulk solution could be split and used to assess several reaction conditions in a more-timely fashion. As the automated system eliminates human errors associated with timing and handling, the [^{18}F]F$^-$-solutions prepared using the automated method would have less variance between them than those produced manually. Lastly, once the design of the disposable cassette and programmed method were established, minor adjustments of the existing protocol to incorporate the optimized BODIPY labeling strategies, as determined through manual efforts, would enable the quick establishment of an automated method for synthesizing [^{18}F]F-BODIPY fluorophores.

To gain hands-on experience using the TRASIS miniAIO automated synthesis system and its operating software, a disposable cassette was designed for the automated dry down and reconstitution of [^{18}F]F$^-$ in anhydrous acetonitrile. The reagents and consumables required as well as their position on the TRASIS cassettes depicted in **Figure 3.1** are outlined below in **Table 3.3**. An automated method was established wherein an aqueous solution of [^{18}F]F$^-$ was injected into the TRASIS system, trapped and released from a Sep-Pak QMA cartridge, azeotropically dried four times, and cooled before reconstituting the dried [^{18}F]F-TEAF precipitate in 3.00 mL of dry acetonitrile and transferring the solution into a clean glass product vial. The commands for the 43-minute-long method are provided in Appendix section.

Once established, the method underwent trouble shooting to confirm that: 1) the [^{18}F]F$^-$ trap and release process was able to elute all solution volume through the QMA into the reactor vial, 2) The [^{18}F]F-TEAF salt was sufficiently dried under the applied conditions, and 3) that the product solution was properly transferred into the product vial. Initial tests were carried out using a small amount of activity (50-75 MBq) to monitor activity losses at various points during the automated procedure; namely the QMA cartridge and the reactor vial. After several test runs altering command times and nitrogen flow rates through the TRASIS system, the final test procedures for the azeotropic drying method afforded the desired [^{18}F]F$^-$ solution with nearly negligible radioactivity losses in the cassette.

Future efforts are required to finalize the automated ^{18}F-radiolabeling process. The direct inlet of aqueous [^{18}F]F$^-$ ions from the Fedoruk Centre's ACSI TR24 cyclotron through the TRASIS system's activity plunger attachment (position 2 in **Figure 3.1**) must still be assessed for the purpose of reducing user radioactivity exposure and handling. The [^{18}F]F-TEAF solution produced using the automated method must still be applied under previously assessed conditions to validate the product solutions efficacy towards ^{18}F-isotopic exchange. Lastly, the cassette will require further modification to incorporate the necessary reagents and intricacies of the optimized BODIPY ^{19}F/^{18}F-transfluorination reaction once they have been established for use of hydrated magnesium nitrate.

Table 3.3. Cassette composition and reagent loading for TRASIS MiniAlInOne synthesis module.

Position	Content/Connection
Left End	• Nitrogen Filter (0.20 μm) • Silicone Tubing (ID1mm, OD3 mm) With Male Luer Lock- 1/16" Barbed Fitting (× 2) **Connecting System to Cassette Pressure Port*
1	• Silicone Tubing With Male Luer Lock- 1/16" Barbed Fitting **Connecting Activity Pump to System*
2	• QMA Carbonate Ion Exchange Solid Phase Extractions (SPE) Light • 20 mL BD Luer Lock Syringe (Exterior Only) • Activity Plunger With Direct Inlet from Cyclotron Line Rinse Run Through Activity Inlet Pinch Valve
3	• PE with 2 Connectors Luer Lock Male, overmolded (250 mm, ID1 mm, OD2 mm) **Connecting to Position 8*
4	• Nylon Luer Lock Ring: Square Hole • Spike: Polyacetal Male Luer Slip • Barrel for 13mm Vial • $[^{18}F]F^-$ Fixing Agent (TEAB, 5 mL, 0.075 M)
5	• Nylon Luer Lock Ring: Square Hole • Spike: Polyacetal Male Luer Slip • Barrel for 13 mm Vial • Reconstitution Solvent (MeCN 99.8% Anhydrous, 3 mL)

Position	Content/Connection
6	• Nylon Luer Lock Ring: Square Hole • Spike: Polyacetal Male Luer Slip • Barrel for 13 mm Vial • Azeotropic Dry Down Solvent (MeCN 99.8% Anhydrous, 4 mL)
Right End	• Silicone Tubing With Female Luer Lock - 1/16" Barbed Fitting **Connecting to 20 mL BD Luer Lock Syringe*
Left End	Empty
7	• Silicone Tubing With Male Luer Lock- 1/16" Barbed Fitting (× 2) • 16 Gauge Needle Connecting [^{18}O]O-H_2O collection Vial
9	• Male Luer Lock- 1/16" Barbed Fitting **Connecting to Type 1 Glass Reactor-2 Tubes-8 Bar Validated Crimped Cap*
10	Empty
11	Empty
12	Empty
Right End	• Silicone Tubing With Female Luer Lock - 1/16" Barbed Fitting • 16 Gauge Needle (Connecting to Product Vial With Shielded Vent Needle Present)
Reactor	• Type 1 Glass Reactor-2 Tubes-8 Bar Validated Crimped Cap **Thin Tube Connecting to Position 9 via Male Luer Lock- 1/16" Barbed Fitting* **Thick Tube Run Through Heater Pinch Valve Connecting to Vacuum Cassette Inlet*

Specific Terms:	• *Activity Plunger:* serves as the inlet for the radioactive solution produced by the Cyclotron into the TRASIS cassette setup. • *Activity Inlet Pinch Valve:* opens and closes to control the entry of radioactive solution from the cyclotron production into the automated synthesis cassette setup. • *Barrel:* holds consumable sure seal vial and contents in place on the TRASIS miniAIO automated radiosynthesizer cassette setup. • *Spike:* pierces sure seal septum of reagent to allow TRASIS miniAIO system to access the reagent or solvent during the automated synthesis run.

3.4. Conclusions & Future Directions.

It is clear the $^{19}F/^{18}F$-isotopic exchange procedures outlined in this chapter require supplementary experiments to offer optimal reaction conditions for the commercial [^{18}F]F-BODIPY dye selected for this proof-of-concept study. Using Lewis acidic solutions made from the hydrated $Mg(NO_3)_2$ salt showed promising early results. Despite the need for further experimental investigation, several key aspects for future optimization and improved analysis of the radiolabelling conditions were emphasized. Despite recent reported successes of ^{18}F-fluorination efforts under wet conditions, the performance of $^{19}F/^{18}F$-transfluorination for the commercial BODIPY precursor was improved under the conventional polar aprotic solvent conditions. As such, future experiments should employ concentrated Lewis acidic solutions made from DMSO solvent. Further, a general trend was observed that increasing the molar equivalents of magnesium (range of 10-150 equiv. tested) increased the radiochemical yield. It was also observed the quantity of base used (TEAB) influenced radiochemical yields. Although experimental analysis performed using a radio-TLC plate reader proves sufficient for many radiolabeling procedures, the degradation associated with hydrolysis of the BODIPY precursor and the availability of water under the applied reaction conditions makes TLC analysis an unfavorable means for evaluating the success of the applied experimental parameters. Instead, radio-HPLC analysis of the crude reaction mixture yields affords the necessary resolution for assessing the efficacy of the applied conditions and should be used going forward as the sole means for instrumental analysis of the ^{18}F-labeling efforts performed on BODIPY fluorophores.

Attempts to devise an automated method for the $^{19}F/^{18}F$-isotopic exchange of BODIPY dyes afforded hands on experience with building a functional cassette for the TRASIS miniAIO radiosynthesis platform, composing a method on the system's associated operating software, and performing performance analyses of a new automated method and troubleshooting sources of error for the process overall. The initial azeotropic drying stage of the ^{18}F-labeling process was successfully programmed and run through several rounds of error analysis. As such, it is ready for quality analysis of the [^{18}F]F^--solution product and further programming of optimized labeling conditions once methods are established.

Chapter 4 Preamble

Chapter 4 outlines contributions made during collaborative efforts with Price lab postdoctoral fellow Dr. Elaheh Khozeimeh Sarbisheh to synthesize the novel disulfide-rebridging linker, double phenyloxadiazolyl methyl sulfone (DiPODS). Reported herein are the experimental procedures used to synthesize several of the compounds in the multistep synthesis of the final DiPODS linker. Syntheses of compounds **1-4** and **7** were confirmed with proton and carbon nuclear magnetic resonance (^{1}H and ^{13}C NMR) and high-resolution mass spectrometry. Peak assignments were supported by additional NMR experiments (DEPT135, HMQC, COSY).

While synthesizing compound **1** of the multistep procedure, curiosities peaked as the spectroscopic data associated with the crude product showed three signals with similar ^{1}H NMR splitting patterns to that of the desired product. These extra proton signals were not discussed in the original literature outlining the compound's synthesis. Additionally, use of the crude mixture and its differing molecular species afforded quantitative yields in the subsequent synthesis step. As such, all three components afforded the same reaction product and therefore must have been isomers or derivatives of compound **1**. It was thus hypothesized that the three sets of ^{1}H NMR signals in the crude compound **1** mixture's spectra were attributed to conformers or perhaps even rotamers of the compound **1** molecule. Detailed variable-temperature NMR and computational studies revealed this to be the case.

In correspondence with this, Chapter 4 also outlines the use of spectroscopic techniques such variable temperature ^{1}H NMR and FTIR spectroscopy to elucidate the structures of the compound **1** crude mixture components. In doing such, the major crude mixture components were characterized as a mixture of *anti* rotamers of the compound **1** product while spectroscopic data confirmed the minor constituents as doubly Boc-protected and imidic acid tautomer product variants. The efforts outlined within this chapter, in combination with those of Dr. Khozeimeh Sarbisheh and our collaborators in Dr. Zeglis's lab, are summarized in a recently published manuscript (Khozeimeh Sarbisheh et al., 2020).

Chapter 4

4.1. Introduction.

4.1.1. DiPODS.

Recent efforts in bioconjugation chemistry have acknowledged the imperative need to devise novel chemical linkers with improved *in vivo* stability. The recent success of our collaborators, (Zeglis *et al*., 2018),[95] upon revisiting the applicability of the "PODS" functionality towards radioimmunoconjugate synthesis reaffirmed the potential of phenyloxadiazole-based bioconjugation reagents for covalently attaching a variety of chemical or radiochemical payloads to biological targeting vectors. However, as is the case with other thiol-reactive bioconjugation reagents that only react with a single cysteine residue, the disulfide bridges which maintain the antibody's tertiary structure are broken. This lack of thiol rebridging reduces the stability of the antibody and increases the risk of fragmentation.

In a joint effort to build off the promising results of the PODS linkers, the Price and Zeglis labs sought to synthesize a novel disulfide-rebridging reagent, hereafter referred to as DiPODS. DiPODS (**Scheme 4.1**) contains two thiolate-reactive oxadiazolyl methyl sulfone moieties attached to the same aromatic ring system. It was hypothesized that this new DiPODS moiety would react with both cysteine residues from a reduced disulfide bond, affording doubly-conjugated disulfide-rebridged pairs and, subsequently, an improved stability of the conjugated antibody product.

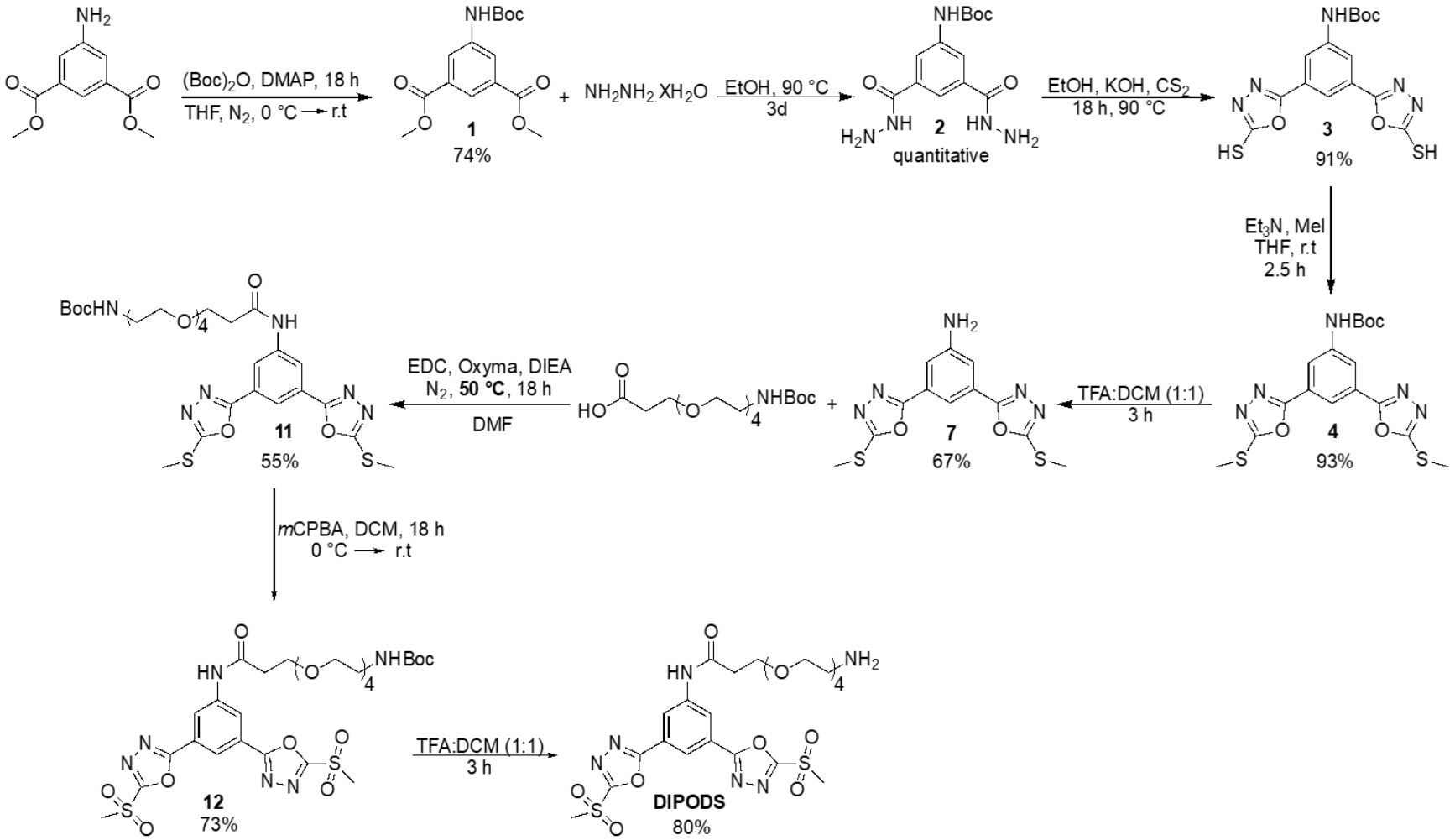

Scheme 4.1. Multistep synthesis procedure for DiPODS product. Reaction scheme reported in (Khozeimeh Sarbisheh *et al.*, 2020).[142]

4.1.2. Isomers Hypothesis.

Synthesis of the DiPODS bioconjugation reagent was primarily carried out by Dr. Elaheh Khozeimeh Sarbisheh; a postdoctoral fellow of the Price lab group. As Dr. Khozeimeh Sarbisheh was establishing the multistep synthesis of the DiPODS product, she had noted that several of the intermediate products, most prominently compound **1**, afforded a crude product mixture with some puzzling features. The spectra displayed multiple ^{1}H nuclear magnetic resonance (^{1}H NMR) peaks of similar splitting patterns and relative integration values to those of the desired product despite having subtly different shifts. In the case of compound **1**, the major desired product could be separated from the crude mixture components by flash chromatography. To discern the presumed impurities' effects on subsequent reaction yield for compound **2**, Dr. Khozeimeh Sarbisheh proceeded with the second reaction while changing one key parameter. During one experiment, the reaction was performed using the crude product mixture and the second, she used an equivalent amount of the major product material that was isolated via flash chromatography (~40% of crude product). In doing such, she determined nearly quantitative conversion into compound **2**, despite the presumption that the compound mixture contained possible impurities and thus, less of the actual compound **1**. The consolidation of the previously described observations led us to hypothesize the crude product constituents, previously assumed to be reaction impurities, were conformational isomers of the desired products. More specifically, we hypothesized these chemical species could be rotational isomers (rotamers) of compound **1**.

4.1.2.1. Rotamers.

Conformational isomers are the result of hindered rotation about a single σ-bond, producing a 3-dimensional variant of the molecular structure.[143] Typically, a bulky functional group provides steric hindrance and thus hindered rotation. Rapid interconversion between conformers is possible when the required activation energy for conversion between conformers is small, allowing a mixture of conformers of varying ratios to exist at any given point in time when dissolved in solution. Conformational isomers typically interconvert at such a rapid pace they are indistinguishable from one another spectroscopically due a low energy barrier for rotation, thus free rotation about the sigma bond. A classic example of conformational isomerism is the rotation about the C-C bond of ethane (**Figure 4.1**). Because the eclipsed form of ethane experiences

greater Van der Waals repulsion between the adjacent C-H bonds compared to its staggered counterpart, it requires a higher energy input from the surrounding environment (i.e. thermal energy) to allow rotation about the C-C bond. However, they rapidly interconvert at room temperature as the required energy to facilitate rotation between the staggered and eclipsed ethane conformers is relatively small. These energy barriers are governed by several aspects of the molecular structure such steric repulsion and intramolecular hydrogen bonding.[144 145] The more restricted the rotation about single bonds, the high the energy requirement; thus, rotational variants of the molecule, referred to as rotamers, are afforded. Rotamers preferentially adopt the conformation that is best accommodated/stabilized by the surrounding environment. That is to say, the most thermodynamically favourable rotamer/conformer is typically most abundant. The ratio of possible rotameric species within a given solution and, in correlation with this, the dominant rotamer can also be affected by conditions such as temperature and solvent properties (e.g. protic vs aprotic).[146 147]

A)

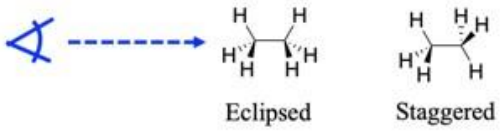

B)

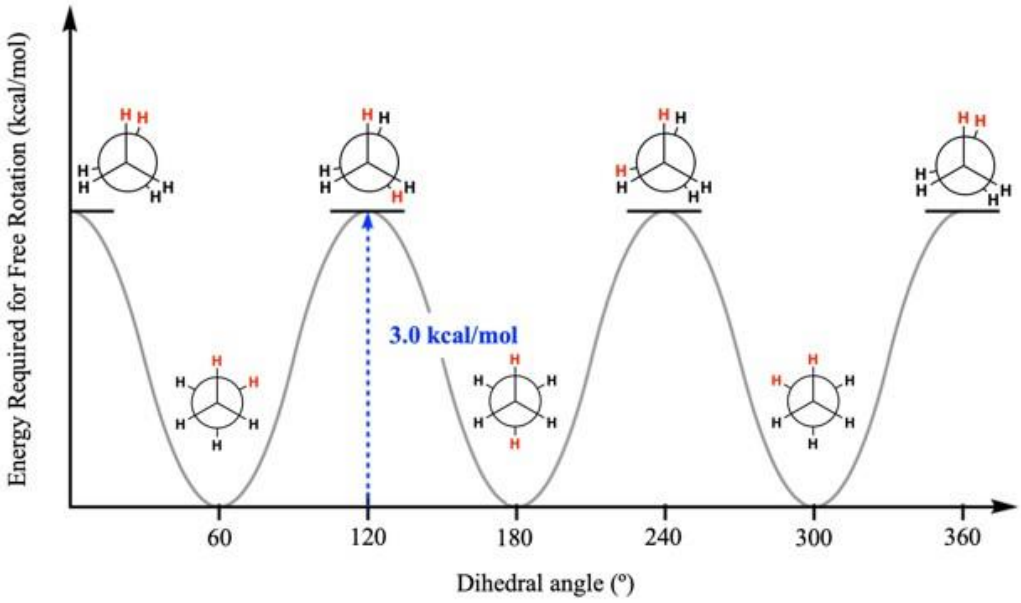

Figure 4.1. A) Eclipsed and staggered conformational variants of ethane molecule. B) Relative energy difference between staggered and eclipsed rotamers of ethane upon each 60° rotation about the molecule's C-C bond. Figure adapted from (Mastering Organic Chemistry, accessed 2020).[148]

4.1.3. Gibbs Free Energy & Conformational Stability.

Gibbs free energy (ΔG) is a thermodynamic potential that is used to denote the minimum energy required for spontaneous conversion of reversible chemical processes at a constant pressure.[149] [150] Comparison of the Gibbs free energy values associated with each of the rotameric species hypothesized to exist in the compound **1** crude product allows for prediction of the compound **1** product's thermodynamically favourable conformation. The Gibbs free energy associated with the conversion between rotamers of small molecules can be calculated by subtracting the product of the closed system's change in entropy (ΔS) and the temperature (T) at which the process takes place from the change in enthalpy (ΔH) (**Figure 4.2**). This can be calculated from experimental data obtained using variable temperature ^{1}H NMR, or it can be predicted via *in silico* computational experiments (e.g. density functional theory).

$$\Delta G = \Delta H - T\Delta S$$

Figure 4.2. Gibbs free energy equation applicable for closed systems at constant pressure and temperature.

4.1.3.1. Variable Temperature ^1H NMR.

^{1}H NMR spectroscopy makes use of the naturally high abundance of the ^{1}H isotope (99.9%) for elucidation of chemical structures. Each proton within a molecular framework can be thought of as hosting an individual charge. When the compound of interest is dissolved and placed into a magnetic field, proton nuclei will either align parallel with the surrounding field as a lower spin state (+1/2, spin up) or antiparallel to the external field as a higher spin state (-1/2, spin down).[151] Lower energy nuclei are promoted to the higher energetic spin-state by applying radiofrequency pulses. In doing such, the lower energy proton nuclei absorb different frequencies of the applied electromagnetic radiation based on their proximity to electron donating and withdrawing functional groups of the molecular structure that shield or deshield the nuclei from the applied radiation, respectively. Ultimately, these phenomena are detected by the NMR instrument, producing characteristic chemical shifts and signal patterns that enable characterization of the molecule's structure features.[152]

Variable temperature ^{1}H NMR allows structural analysis of small molecules to take place as a dependent variable of the change in temperature over time. Subjecting rotameric species to changes in temperature promotes conformational adjustments as the molecule attempts to ascertain its most stable state. The rotation of functional groups about single bonds within the structure alters the proximity of their associated protons with those of the core structure. By changing the sample temperature in a controlled fashion and acquiring spectroscopic data at fixed intervals in time, the conformational changes associated with a mixture of rotamers can be monitored over time as they reconfigure their structure to achieve their most stable state. The values associated with each rotamer species' changes in enthalpy, entropy, and Gibbs free energy are thus extrapolated from the experimental data obtained at each of the assessed temperatures.

4.1.4. Purpose Statement.

In a joint effort with Dr. Elaheh Khozeimeh Sarbisheh, this project sought to apply variable temperature ^{1}H NMR spectroscopy instrumentation to monitor observed changes in chemical shift and concentration of the differing chemical constituents of the compound **1** crude product mixture.

This data, in combination with the theoretical values calculated by Dr. Khozeimeh Sarbisheh using density functional theory (DFT), were used to assess our hypothesis that the three components of the compound **1** crude mixture were three differing rotameric species of the compound **1** material that, upon heating, would alter in conformation to yield the most stable rotamer.

Furthermore, to assist Dr. Khozeimeh Sarbisheh in her production of the final DiPODS product as well as hone several organic synthesis techniques, compounds **1**-**4** and **7** from the DiPODS synthetic procedures developed by Dr. Khozeimeh Sarbisheh (**Scheme 4.1**) were synthesized.

4.2 Experimental.

4.2.1. Spectroscopic Characterization of Compounds 1-4 and 7.

Characterization of the synthesized compounds **1-4** and **7** was achieved using NMR spectroscopy. ^{1}H, and ^{13}C NMR spectra were recorded on a 500 MHz Bruker Avance NMR spectrometer at 25 °C in DMSO-d_6. Variable Temperature ^{1}H NMR were recorded on a Bruker Avance III HD 600 MHz spectrometer. ^{1}H chemical shifts were referenced to the residual protons of the deuterated DMSO-d_6 and DMF-d_7 solvents at δ = 2.50 ppm and 2.75 ppm respectively;[153] ^{13}C chemical shifts were referenced to the DMSO-d_6 signal at δ = 39.52 ppm.[154] Coupling constants are reported to the nearest 0.5 Hz (^{1}H NMR spectroscopy) or rounded to integer values in Hz (^{13}C NMR spectroscopy). Assignments were supported by additional NMR experiments (DEPT135, HMQC, COSY). High resolution mass spectra were measured on a JEOL AccuTOF GCv 4G using field desorption ionization (FDI). For the isotopic pattern only, the mass peak of the isotopologue or isotope with the highest natural abundance is given. FTIR spectroscopy was performed using a Bruker Tensor 27 FTIR spectrometer equipped with ATR attachment and OPUS data collection program.

4.2.2. DiPODS Synthesis.

*4.2.2.1. Synthesis of 5-[[(1,1-dimethylethoxy)carbonyl]amino]-1,3-dimethyl ester (Compound **1**).*

Compound **1** was synthesized following procedures outlined in (Y. Ohta *et al*., 2011).[155] Using Schlenk techniques, dimethyl 5-aminoisophthalate (3.00 g, 14.34 mmol) and 4-(dimethylamino)pyridine (2.24 g, 18.36 mmol) were purged with $N_{2(g)}$ and dissolved in anhydrous THF (50.0 mL). The clear yellow mixture was cooled to 0 °C prior to the addition of di-*tert*-butyl dicarbonate (4.00 mL, 17.50 mmol); upon which a thick, white precipitate formed inside the reaction vessel. The reaction mixture was kept under $N_{2(g)}$ flow as it initially stirred at 0 °C and gradually warmed to room temperature as the reaction proceeded over 24 h. Volatiles were removed by rotary evaporation before reconstituting the mixture with EtOAc (100 mL). The organic solution was washed twice with 0.5 N HCl (2×100 mL), three times with brine solution (3×100 mL), and deionized water (100 mL) to achieve a neutral pH. The organic layer was dried over Na_2SO_4 before removing the solvent under reduced pressure to yield the crude product

mixture as an off-white solid with negligible amounts of the Boc-deprotected starting material observed by ^{1}H NMR (4.72 g, 106.4%) (**Scheme 4.2**). ^{1}H NMR of the crude mixture (500 MHz, DMSO-d_6, 25 °C, TMS): set **A** (*anti*-rotamers, *anti*-**1**) δ = 1.49 [s, 9H, $NHCO_2C(C\underline{H}_3)_3$], 3.88 [s, 6H, $CO_2C\underline{H}_3$], 8.08 (t, 1H, *J*= 1.43Hz, Ar-C<u>H</u>), 8.36 (m, 2H, Ar-C<u>H</u>), 9.89 (bs, 1H, N<u>H</u>) ppm; set **B** [doubly Boc-protected derivative of compound **1**, $(Boc)_2$-**1**]: δ = 1.39 {s, 18H, $N[CO_2C(C\underline{H}_3)_3]_2$}, 3.90 [s, 6H, $CO_2C\underline{H}_3$], 8.01 (d, 2H, *J*= 1.50Hz, Ar-C<u>H</u>), 8.41 (t, 1H, *J*= 1.50Hz, Ar-C<u>H</u>) ppm; set **C** (imidic acid tautomers of compound **1**, tautomer-**1**): δ = 1.42 [s, 9H, $NC(OH)OC(C\underline{H}_3)_3$], 3.91 [s, 6H, $CO_2C\underline{H}_3$], 8.17 (d, 1H, *J*= 1.55Hz, Ar-C<u>H</u>), 8.45 (t, 2H, *J*= 1.50Hz, Ar-C<u>H</u>) ppm; $^{13}C\{^{1}H\}$ NMR of the crude mixture (126 MHz, DMSO-d_6, 25 °C, TMS): set **A** (*anti*-**1**): δ = 28.1 [$NHCO_2C(\underline{C}H_3)_3$], 52.5 [$CO_2\underline{C}H_3$], 79.9 [$NHCO_2\underline{C}(CH_3)_3$], 122.5, 123.0 (Ar-<u>C</u>H), 130.6 (Ar-<u>C</u> attached to CO_2CH_3), 140.7 [Ar-<u>C</u> attached to $NHCO_2C(CH_3)_3$], 152.7 [$NH\underline{C}O_2C(CH_3)_3$], 165.4 [$\underline{C}O_2CH_3$] ppm; Signals associated with set **B** [$(Boc)_2$-**1**], and set **C** (tautomer-**1**) of the crude mixture could not be distinguished from one another by ^{13}C NMR techniques and are reported together herein. Crude mixture sets **B** and **C**: δ = 27.5, 27.5 {$N[CO_2C(\underline{C}H_3)_3]_2$} and [$NC(OH)OC(\underline{C}H_3)_3$], 52.8, 52,8 [$CO_2\underline{C}H_3$], 83.1, 84.4 {$N[CO_2\underline{C}(CH_3)_3]_2$} and [$NC(OH)O\underline{C}(CH_3)_3$], 128.3, 128.8 [Ar-<u>C</u>H], 131.0, 131.2 [Ar-<u>C</u> attached to CO_2CH_3], 133.0, 133.1 [Ar-<u>C</u>H], 139.5, 140.0 [Ar-<u>C</u> attached to {$N[CO_2C(CH_3)_3]_2$} and $NC(OH)OC(CH_3)_3$], 150.6, 150.8 {$N[\underline{C}O_2C(CH_3)_3]_2$} and [$NC(OH)OC(CH_3)_3$], 164.7, 164.8 [$(\underline{C}O_2CH_3)_2$] ppm; HRMS (FDI): *m/z* calcd for $C_{15}H_{19}NO_6$: 309.11977[*M*]$^{+}$; found: 309.11989; *m/z* calcd for $C_{20}H_{27}NO_8$+Boc: 409.17815[*M*+Boc]$^{+}$; found: 409.17820; IR (FTIR): $\tilde{\nu}$ = 3364.40 (w) [$NHCO_2C(CH_3)_3$, N-H], 2980.61 (w), 2954.57 (w) [{$N[CO_2C(CH_3)_3]_2$} & $NC(OH)OC(CH_3)_3$, C-H], 2360.57 (w), 2339.30 (w) [$NC(OH)OC(CH_3)_3$, N=C], 1741.50 (m), 1726.07 (s), 1704.85 (s) [CO_2CH_3, C=O] 1604.57 (w), 1549.61 (m) cm^{-1} [{$N[CO_2C(CH_3)_3]_2$}, C=O].

The first group of rotamers for compound **1** (set **A**, *anti*-**1**) was isolated from the crude mixture for further analysis via precipitation. The crude product (2.51 g, 8.12 mmol) was dissolved completely in a minimal amount of warm DCM and stored at -20 °C overnight. The set **A** crude mixture component was precipitated under the aforementioned storage conditions and were isolated from the mother liquor as a shiny white precipitate after vacuum filtration. The mother liquor was collected after vacuum filtration and subjected to rotary evaporation to remove solvent residues. The residual mother liquor solids were re-dissolved in minimal amounts of warm DCM

to repeat the precipitation process. Precipitation of the set **A** mixture component was repeated several times until a pure product could no longer be isolated from the mother liquor solution (1.56 g, 66.1%). ^{1}H NMR of set **A** (500 MHz, DMSO-d_6, 25 °C, TMS): δ = 1.49 [s, 9H, $NHCO_2C(C\underline{H}_3)_3$], 3.88 [s, 6H, $CO_2C\underline{H}_3$], 8.08 (t, 1H, *J*= 1.45Hz, Ar-C<u>H</u>), .8.35 (d, 2H, *J*= 0.851Hz, Ar-C<u>H</u>), 9.87 (bs, 1H, N<u>H</u>) ppm; ^{13}C{^{1}H} NMR of set **A** (126 MHz, DMSO-d_6, 25 °C, TMS): δ =28.0 [$NHCO_2C(\underline{C}H_3)_3$], 52.5 [$CO_2\underline{C}H_3$], 79.9 [$NHCO_2\underline{C}(CH_3)_3$], 122.4, 123.0 (Ar-<u>C</u>H), 130.6 (Ar-<u>C</u> attached to CO_2CH_3), 140.6 [Ar-<u>C</u> attached to $NHCO_2C(CH_3)_3$], 152.7 [$NH\underline{C}O_2C(CH_3)_3$], 165.4 [$\underline{C}O_2CH_3$] ppm; HRMS (FDI): *m/z* calcd for $C_{15}H_{19}NO_6$: 309.11977[*M*]$^{+}$; found: 309.12124; IR (FTIR): $\tilde{\nu}$ = 3363.43 (m) [$NHCO_2C(CH_3)_3$, N-H], 2952.65 (b) [$NHCO_2C(CH_3)_3$, C-H], 1718.36 (m), 1703.89 (s) [CO_2CH_3, C=O], 1608.43 (m), 1545.75 (s) cm^{-1}[Ar-CH].

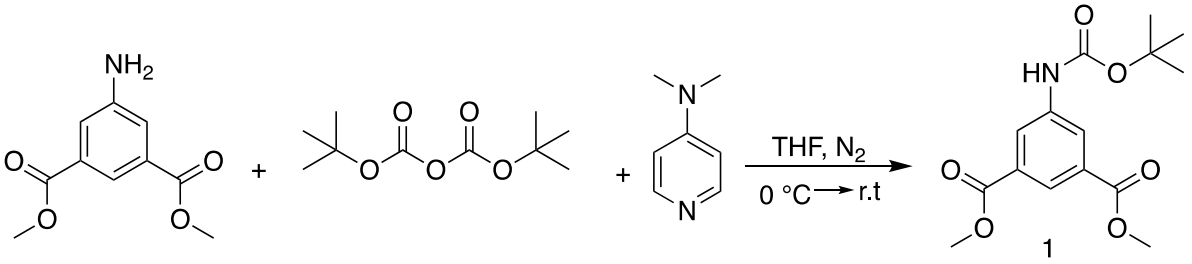

Scheme 4.2. Synthesis of compound **1**.

*4.2.2.2. Synthesis of Compound **2**.*

Hydrazine hydrate (28.0 mL, 451 mmol) was added to a clear colorless solution of **1** (3.49 g, 11.28 mmol) in EtOH (150 mL) at room temperature. The color of the solution turned a pale-yellow. The mixture was refluxed at 90 °C for 3 days. All volatiles were removed under reduced pressure to yield quantitative amounts of the product in the form of a fine, matte-white powder. The product material was used without further purification to proceed forward with the synthesis of compound **3** (3.49 g, quantitative yield) (**Scheme 4.3**). ^{1}H NMR (500 MHz, DMSO-d_6, 25 °C, TMS): δ = 1.48 [s, 9H, $NHCO_2C(C\underline{H}_3)_3$], 4.49 [bs, 4H, $CONHN\underline{H}_2$], 7.74 [t, 1H, *J*= 1.45Hz, Ar-C<u>H</u>], 7.96 [d, 2H, *J*= 1.01Hz, Ar-C<u>H</u>], 9.64 [bs, 3H, N<u>H</u>] ppm; ^{13}C{^{1}H} NMR (126 MHz, DMSO-d_6, 25 °C, TMS): δ = 28.1 [$NHCO_2C(\underline{C}H_3)_3$], 79.5 [$NHCO_2\underline{C}(CH_3)_3$], 118.8, 119.6 [Ar-<u>C</u>H], 134.3 [Ar-<u>C</u> attached to $CONHNH_2$], 139.8 [Ar-<u>C</u> attached to $NHCO_2C(CH_3)_3$], 152.8

[NH<u>C</u>O$_2$C(CH$_3$)$_3$], 165.8 [<u>C</u>ONHNH$_2$] ppm; HRMS (FDI): *m/z* calcd for $C_{13}H_{19}N_5O_4$: 309.14491[*M*]$^+$; found: 309.14370.

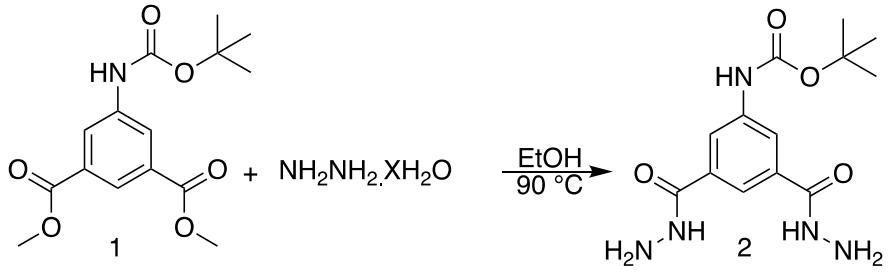

Scheme 4.3. Synthesis of compound **2**.

*4.2.2.3. Synthesis of Compound **3**.*

Potassium hydroxide (0.399 g, 7.11 mmol) was added to a suspension of **2** (1.00 g, 3.23 mmol) in EtOH (34.5 mL) and stirred for 10 minutes. Carbon disulfide (4.30 mL, 71.1 mmol) was added in dropwise fashion to the stirring emulsion; turning the solution a vibrant yellow prior to the formation of a large amount of white precipitate. The reaction mixture was heated at 90 °C reflux overnight (16 h), during which time, the mixture became a clear pale-yellow solution with small amounts of white precipitate. After cooling the reaction solution to room temperature, EtOAc (320 mL) was added until complete dissolution of the precipitate material was achieved. The resulting clear yellow mixture was washed two times with 1 M HCl (2×320 mL) followed by washing 3 times with deionized water (3×320 mL) until neutral pH was achieved. The yellow organic layer was washed with brine (320 mL), then dried over Na_2SO_4 and filtered before removing volatile components under reduced pressure. Compound **3** was obtained as a shiny, lightweight white solid (0.704 g, 55.4% yield) (**Scheme 4.4**). ^{1}H NMR (500 MHz, DMSO-d$_6$, 25 °C, TMS): δ = 1.51 [s, 9H, NHCO$_2$C(C<u>H</u>$_3$)$_3$], 7.82 [t, 1H, *J*= 1.50Hz, Ar-C<u>H</u>], 8.22 [d, 2H, *J*= 1.05Hz, Ar-C<u>H</u>], 10.05 [bs, 1H, N<u>H</u>], 14.75 [bs, 2H, S<u>H</u>] ppm; ^{13}C{^{1}H} NMR (126 MHz, DMSO-d$_6$, 25 °C, TMS): δ = 28.0 [NHCO$_2$C(<u>C</u>H$_3$)$_3$], 80.3 [NHCO$_2$<u>C</u>(CH$_3$)$_3$], 116.2, 117.5 [Ar-<u>C</u>H], 124.2 [Ar-<u>C</u> attached to C_2N_2O], 141.5 [Ar-<u>C</u> attached to NHCO$_2$C(CH$_3$)$_3$], 152.7 [NH<u>C</u>O$_2$C(CH$_3$)$_3$], 159.4 [<u>C</u>$_2$N$_2$O attached to Ar], 177.5 [<u>C</u>$_2$N$_2$O attached to SH] ppm; HRMS (FDI): *m/z* calcd for $C_{15}H_{15}N_5O_4S_2$: 393.05703[*M*]$^+$; found: 393.05654.

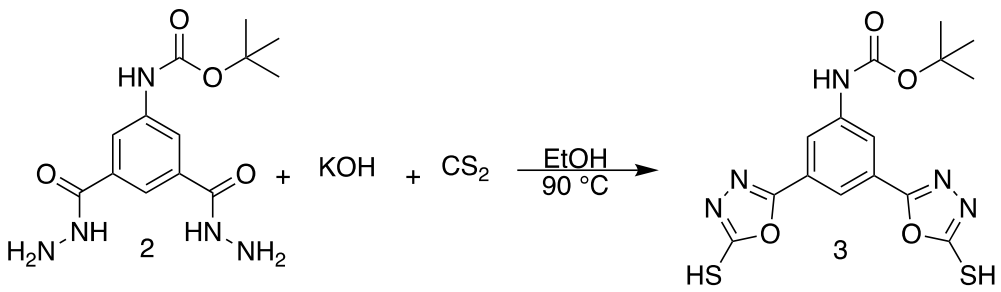

Scheme 4.4. Synthesis of compound **3**.

*4.2.2.4. Synthesis of Compound **4**.*

Triethylamine (3.39 mL, 24.2 mmol) was added to a clear yellow solution of Compound **3** (2.63 g, 6.68 mmol) in dry THF (63.5 mL). After 10 minutes of stirring at room temperature, the color of the reaction mixture changed to a peach hue. To prevent light sensitive reagents from degrading, the reaction vessel was covered with aluminum foil. Iodomethane (1.11 mL, 17.8 mmol) was slowly added to the reaction mixture and reacted for 3 h at room temperature. During the first 1-2 minutes of stirring, the clear peach solution quickly became opaque with white precipitate. Once the reaction was completed, the THF solvent was removed *in vacuo* to afford a mixture of white and tan colored solids. A crude form of the product material was extracted from the mixture with EtOAc (500 mL). The solution volume was reduced to 1/3 by evaporating volatiles under reduced pressure. This mixture was washed with a 0.1 M aqueous solution of Na_2CO_3 (2×100 mL); (pH=11). The deep-yellow organic phase was washed with brine (150 mL) and deionized water until a neutral pH was achieved. As the organic layer was neutralized, its coloring changed from deep yellow to a clear pale yellow. The organic phase was dried over Na_2SO_4 and filtered before removing solvent under reduced pressure. Product **4** was obtained as an off-white powder (2.61 g, 92.5% yield) (**Scheme 4.5**). ^{1}H NMR (500 MHz, DMSO-d_6, 25 °C, TMS): δ = 1.51 [s, 9H, $NHCO_2C(C\underline{H}_3)_3$], 2.79 [s, 6H, $SC\underline{H}_3$], 8.00 [t, 1H, *J*= 1.43Hz, Ar-C<u>H</u>], 8.30 [m, 2H, Ar-C<u>H</u>], 9.99 [bs, 1H, N<u>H</u>] ppm; ^{13}C{^{1}H} NMR (126 MHz, DMSO-d_6, 25 °C, TMS): δ = 14.4 [$S\underline{C}H_3$], 28.0 [$NHCO_2C(\underline{C}H_3)_3$], 80.2 [$NHCO_2\underline{C}(CH_3)_3$], 116.9, 117.7 [Ar-<u>C</u>H], 124.7 [Ar-<u>C</u> attached to C_2N_2O], 141.5 [Ar-<u>C</u> attached to $NHCO_2C(CH_3)_3$], 152.7 [$NH\underline{C}O_2C(CH_3)_3$],

164.2 [$\underline{C}_2N_2O$ attached to Ar], 165.3 [$\underline{C}_2N_2O$ attached to SCH_3] ppm; HRMS (FDI): *m/z* calcd for $C_{17}H_{19}N_5O_4S_2$: 421.08627[*M*]$^+$; found: 421.08784.

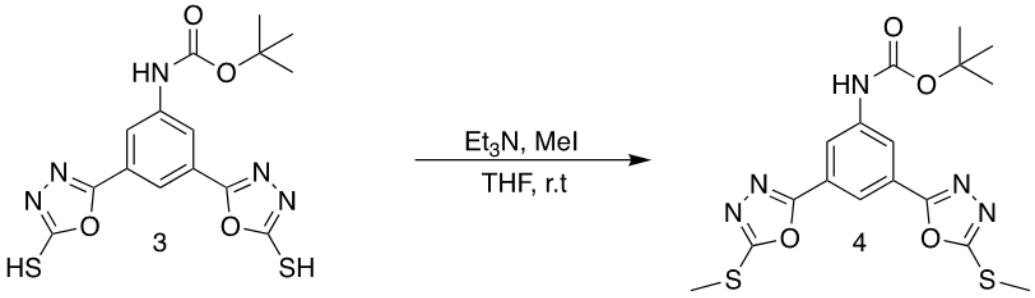

Scheme 4.5. Synthesis of compound **4**.

*4.2.2.5. Synthesis of Compound **7**.*

Compound **4** (0.310 g, 0.712 mmol) was dissolved in a 1:1 mixture of TFA:DCM (8.0 mL). The mixture was stirred for 3 h at room temperature. The reaction solvent was removed under reduced pressure while the majority of TFA was removed azeotropically by washing the reaction mixture several times with toluene. The crude product was washed with a 5:2 mixture (20 mL) of MeCN: H_2O and centrifuged at 4700 rpm for 9 minutes; yielding an off-white pellet and clear yellow solution. The pellet was washed twice with deionized water (2×20mL) and freeze-dried for 24 h to afford compound **7** as a fine, off white powder (0.154 g, 67.2%) (**Scheme 4.6**). ^{1}H NMR (500 MHz, DMSO-d_6, 25 °C, TMS): δ = 2.77 [s, 6H, SC$\underline{H}_3$], 5.96 [bs, 2H, N$\underline{H}_2$], 7.36 [d, 1H, *J*= 1.45Hz, Ar-C$\underline{H}$], 7.56 [d, 2H, *J*= 1.38Hz, Ar-C$\underline{H}$] ppm; ^{13}C{^{1}H} NMR (126 MHz, DMSO-d_6, 25 °C, TMS): δ = 14.3 [S$\underline{C}H_3$], 110.5, 113.5 [Ar-$\underline{C}$H], 124.7 [Ar-$\underline{C}$ attached to C_2N_2O], 150.3 [Ar-$\underline{C}$ attached to NH_2], 164.8 [$\underline{C}_2N_2O$ attached to Ar], 164.8 [$\underline{C}_2N_2O$ attached to SCH_3] ppm; HRMS (FDI): *m/z* calcd for $C_{12}H_{11}N_5O_2S_2$: 321.03545[*M*]$^+$; found: 321.03542.

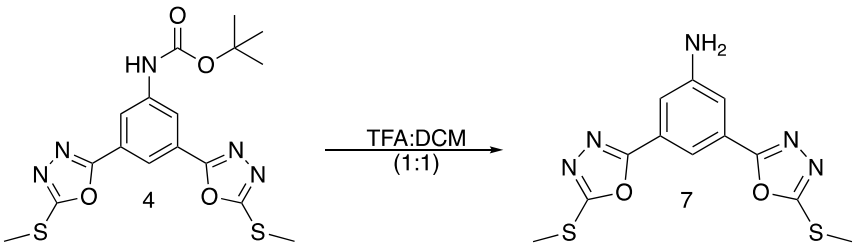

Scheme 4.6. Synthesis of compound **7**.

4.2.3. Variable Temperature ^{1}H NMR Spectroscopic Analysis of Compound 1 Isomeric Forms.

Two NMR samples were prepared in 5 mm Wilmad High throughput borosilicate NMR tubes. As previously described, compound **1** contained a mixture of components, which were partially separated by successive precipitation from a cold mother liquor solution. From this, two samples were made: 1) a solid precipitate of set **A** (*anti*-rotamers of compound **1**, *anti*-**1**) (5.21 mg, 1.68×10^{-2} mmol) 2) the vacuum-dried remains of the mother liquor solution; a 1.0:1.4:1.6 ratio of set **A**: set **B**: set **C** [*anti*-**1**, $(Boc)_2$-**1**, tautomer-**1**] (5.32 mg, 1.72×10^{-2} mmol). Both samples were dissolved in DMF-d_7 (0.401 mL and 0.409 mL respectively) immediately before subjecting them to ^{1}H NMR analysis at 25 °C (298.15 K) on a Bruker Avance III HD 600 MHz spectrometer; with 16 scans run every 10 minutes for 1 h. Once the last data point was obtained for the samples at 25 °C (298.15 K), sample temperatures were increased to 75 °C (348.15 K) and stabilized for 10 minutes before re-tuning, re-shimming and re-locking the system onto the deuterated solvent signal for acquisition of ^{1}H NMR data every 10 minutes for 1 h. These processes were repeated to collect ^{1}H NMR data sets for these two NMR samples at temperatures of 80 °C (353.15 K), 85 °C (358.15 K), and 90 °C (363.15 K) before rapidly cooling the samples with liquid nitrogen for data collection at -40 °C (233.15 K). The experimental process was repeated as described with new samples of the product mixture and the isolated *anti*-rotamers of compound **1** in DMSO-d_6 with the exception of data collection at -40 °C (233.15 K).

Calculations implementing the experimental data were based on the integrated values of the peaks located in the designated regions of the ^{1}H NMR spectra. For experiments carried out in DMF-d_7 solvent at room temperature, integration values of peaks located at 7.77 (m, 1H, Ar-C<u>H</u>), 8.51 (t, 1H, *J*=1.53 Hz, Ar-C<u>H</u>), 8.53 (d, 2H, *J*=1.26 Hz, Ar-C<u>H</u>), and 8.55 (t, 1H, *J*=1.53 Hz, Ar-C<u>H</u>) ppm were used for assessing the proportions of the Boc-deprotected derivative of compound **1**, set **B** [doubly-protected derivative of compound **1**, $(Boc)_2$-**1**], set **A** (*anti*-rotamers of compound **1**, *anti*-**1**), and set **C** (imidic acid tautomers of compound **1**, tautomer-**1**), respectively. As subjecting the crude ^{1}H NMR sample to elevated temperatures resulted in peak shifts within the spectra, the integration values of peaks located at 7.78 (t, 1H, *J*=1.54 Hz, Ar-C<u>H</u>), 8.47 (d, 2H, *J*=1.52 Hz, Ar-C<u>H</u>), 8.50 (t, 1H, *J*=1.53 Hz, Ar-C<u>H</u>), and 8.54 (t, 1H, *J*=1.54 Hz, Ar-C<u>H</u>) ppm were used for assessing the proportions of the Boc-deprotected derivative of compound **1**, set **A** (*anti*-rotamers of compound **1**, *anti*-**1**), set **B** [doubly Boc-protected derivative of compound **1**

$(Boc)_2$-**1**], and set **C** (imidic acid tautomers of compound **1**, tautomer-**1**), respectively for the remaining data sets. The formation of a fourth set of ^{1}H NMR peaks (set **D**, *syn*-rotamers of compound **1**, *syn*-**1**) was observed upon heating to 90 °C in DMF-d_7, however the data for set **D** in DMF-d_7 was not assessed as the signals overlapped with those of the set **A** *anti*-**1** signals.

Similarly, for experiments carried out in DMSO-d_6 solvent at room temperature, the integration values of peaks located at 8.09 (t, 1H, *J*=1.43 Hz, Ar-C<u>H</u>), 8.41 (t, 1H, *J*=1.43 Hz, Ar-C<u>H</u>), and 8.45 (t, 1H, *J*=2.95 Hz, Ar-C<u>H</u>) ppm were used for assessing the proportions of the set **A** (*anti*-rotamers of compound **1**, *anti*-**1**), set **B** [doubly Boc-protected derivative of compound **1**, $(Boc)_2$-**1**], and set **C** (imidic acid tautomers of compound **1**, tautomer-**1**), respectively. Integration values of peaks located at 7.88 (t, 1H, *J*=1.47 Hz, Ar-C<u>H</u>), 8.10 (t, 1H, *J*=1.50 Hz, Ar-C<u>H</u>), 8.14 (t, 1H, *J*=1.47 Hz, Ar-C<u>H</u>), 8.42 (t, 1H, *J*=1.50 Hz, Ar-C<u>H</u>), and 8.46 (t, 1H, *J*=2.82 Hz, Ar-C<u>H</u>) ppm were used for assessing the NMR percentage of the Boc-deprotected derivative of compound **1**, set **A** (*anti*-rotamers of compound **1**, *anti*-**1**), set **D** (*syn*-rotamers of compound **1**, *syn*-**1**), set **B** [doubly Boc-protected derivative of compound **1**, $(Boc)_2$-**1**], and set **C** (tautomers of compound **1**, tautomer-**1**), respectively for the data obtained at elevated temperatures.

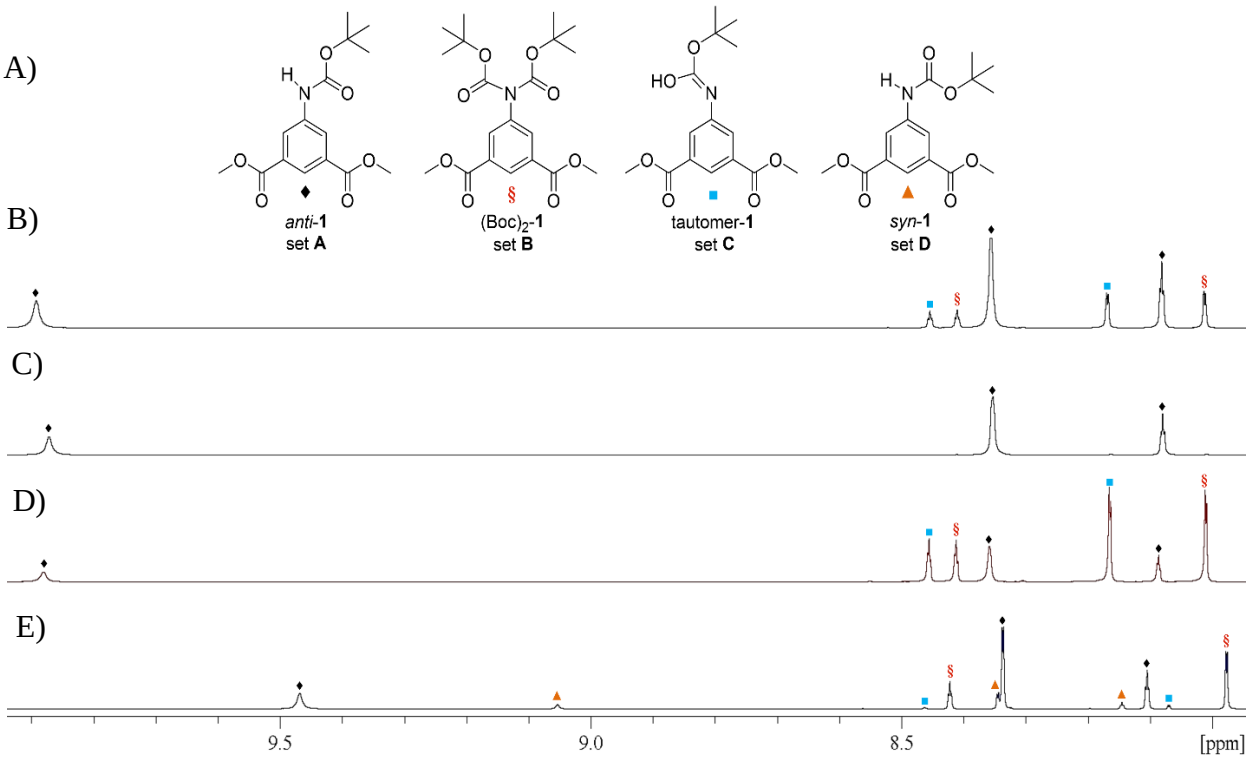

Figure 4.3. A) Structures of each component discovered in the compound **1** mixture and the corresponding ^{1}H NMR spectra in DMSO-d_6 of the aromatic region of:B) the crude mixture before precipitation or column chromatography. C) The isolated precipitate from cold DCM. D) The final mother liquor containing a mixture of all 3 components at 25 °C.and E) The final mother liquor mixture at 90 °C. Peaks associated with the *anti*-rotamers of compound **1** (*anti*-**1**, set **A**, ♦), a doubly Boc-protected derivative of compound **1** [(Boc)$_2$-**1**, set **B**, §], an imidic acid tautomer of compound **1** (tautomer-**1**, set **C**, ■), and *syn*-rotamers of compound **1** (*syn*-**1**, set **D**, ▲) are designated by the symbols ♦, §, ■, and ▲, respectively. For simplicity, only one conformer of each species is shown in the inset. Figure reported in (Khozeimeh Sarbisheh *et al.*, 2020).[142]

4.3. Results & Discussion.

4.3.1. Multistep Synthesis of DiPODS.

Compounds **1-4** and compound **7** were synthesized via procedures established by (Y. Ohta *et al.*, 2011) and (Khozeimeh Sarbisheh *et al.*; 2020).[155] [142] The success of these synthetic efforts was confirmed for each compound using a myriad of spectroscopic techniques; the spectra of which are provided in the appendix section of this dissertation. These newly synthesized compounds were intermediates of the multistep synthetic procedure utilized to produce the desired DiPODS end product. Ultimately, Dr. Khozeimeh Sarbisheh was able to successfully produce the DiPODS product, which has since been sent to our collaborators and assessed in terms of its stability and applicability as a disulfide-rebridging reagent. This work was recently published as a peer-reviewed manuscript in the American Chemical Society journal *Bioconjugate Chemistry*.

4.3.2. Precipitation of Compound 1 in Attempt to Isolate Rotamers.

The number and splitting pattens for the peaks that presented in the aromatic region of compound **1**'s crude product ^{1}H NMR spectrum were hypothesized to result from two symmetric and two asymmetric conformers (**Scheme 4.7**). As three distinct sets of proton signals were observed, it was believed that two of these signals were attributed to symmetric rotational isomers (A and B of **Scheme 4.7**) while the third set was presumed to be a mixture of the asymmetric product variants (C and D of **Scheme 4.7**). Assessing this hypothesis began with attempts to isolate the product conformers from one another via precipitation with the objective of recrystalizing the mixture constituents for X-ray crystallography and ascertain precise conformation information.

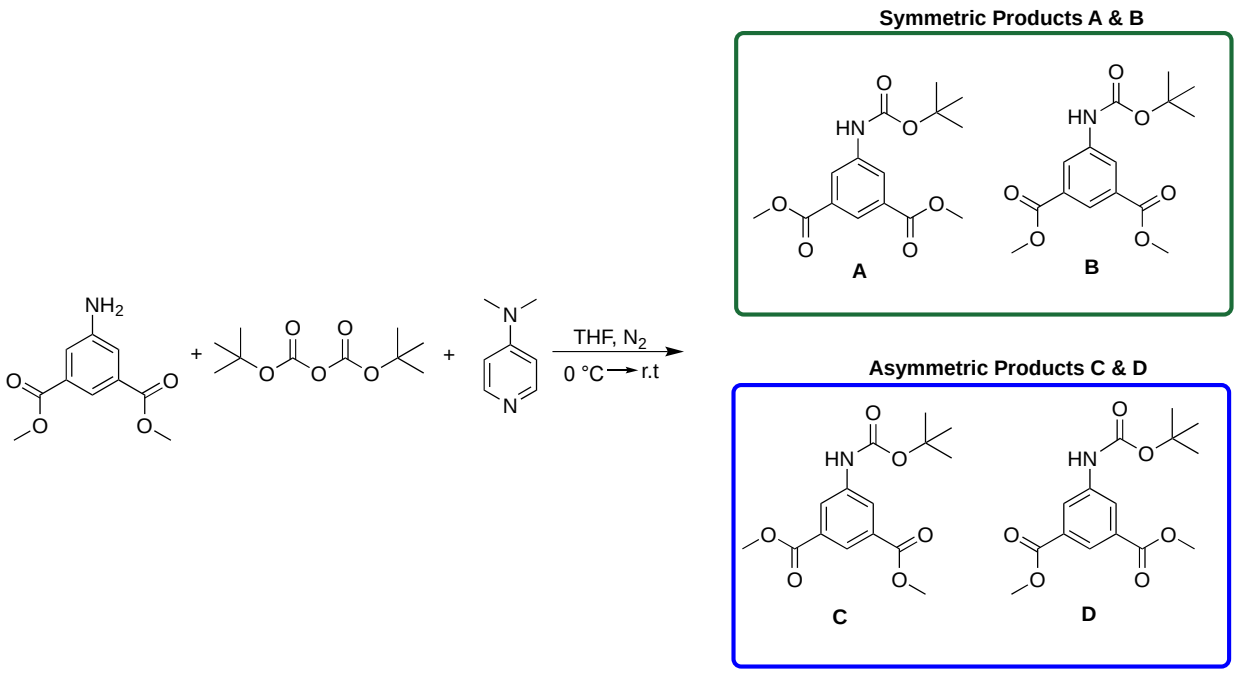

Scheme 4.7. Synthesis of compound **1** illustrating the hypothesized symmetric products A and B, and asymmetric products C and D.

A mother liquor of compound **1** crude product was subjected to six sequential precipitation attempts and afforded isolation of the major mixture component as shown by the decreasing intensity of the peaks associated with component set **A** in the ^{1}H NMR spectra of the dried mother liquor after each **Figures 4.3**. Yields associated with each round of precipitation are provided in **Table 4.1**. While the first two rounds of precipitation afforded a shiny needle-like precipitate of the mixture's primary component, further rounds of precipitation from the mother liquor afforded mixture of all three mixture constituents (**Figure 4.4**).

As both minor mixture components precipitated out of the mother liquor at the same time, they were not isolated from the solution. TLC analysis was used to assess the efficacy of different solvents and solvent ratios towards separating the minor mixture constituents from one another but proved unsuccessful. Furthermore, although attempts to recrystalize the isolated major mixture component were made using different solvents, solvent mixture ratios and temperatures, crystals of X-Ray crystallography quality were not obtained. Thus, further efforts to assess the compound **1** product mixture components focused on the use of spectroscopic instrumentation and DFT calculations; the latter of which were performed by Dr. Khozeimeh Sarbisheh.

Table 4.1. Precipitate yields for each isolation process.

Sample	Yield (g, %)	Mother Liquor (mL)	Mother Liquor (g)
Crude product	2.51, 100	5.00	-
Crystallization 1	0.796, 33.7	4.00	-
Crystallization 2	0.540, 22.9	2.50	-
Crystallization 3	0.224, 9.49	2.25	1.15
Crystallization 4	4.20×10^{-2}, 1.77	1.50	1.03
Crystallization 5	3.20×10^{-3}, 1.27	1.05	0.960
Crystallization 6	4.00×10^{-2}, 1.59	-	0.906

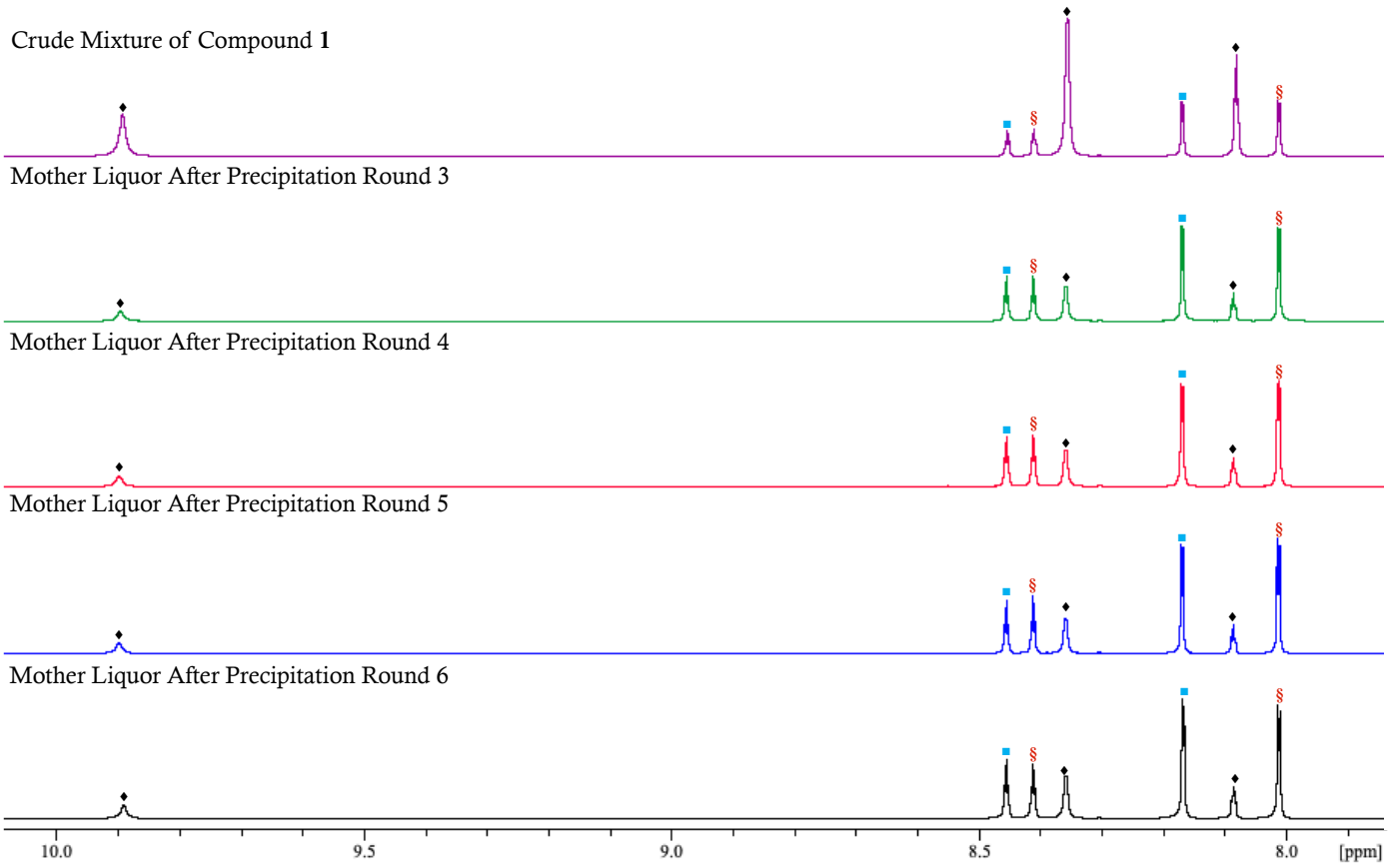

Figure 4.4. Stacked ^{1}H NMR spectra of compound **1** crude mixture and the resulting mother liquor obtained from repeated precipitation processes. Peaks associated with compound **1** mixture components are distinguished from one another with labels for set **A** (*anti*-rotamer, *anti*-**1**, ♦), set **B** [doubly Boc-protected derivative of compound **1**, $(Boc)_2$-**1**, §], and set **C** (imidic acid tautomer of compound **1**, tautomer-**1**, ■).

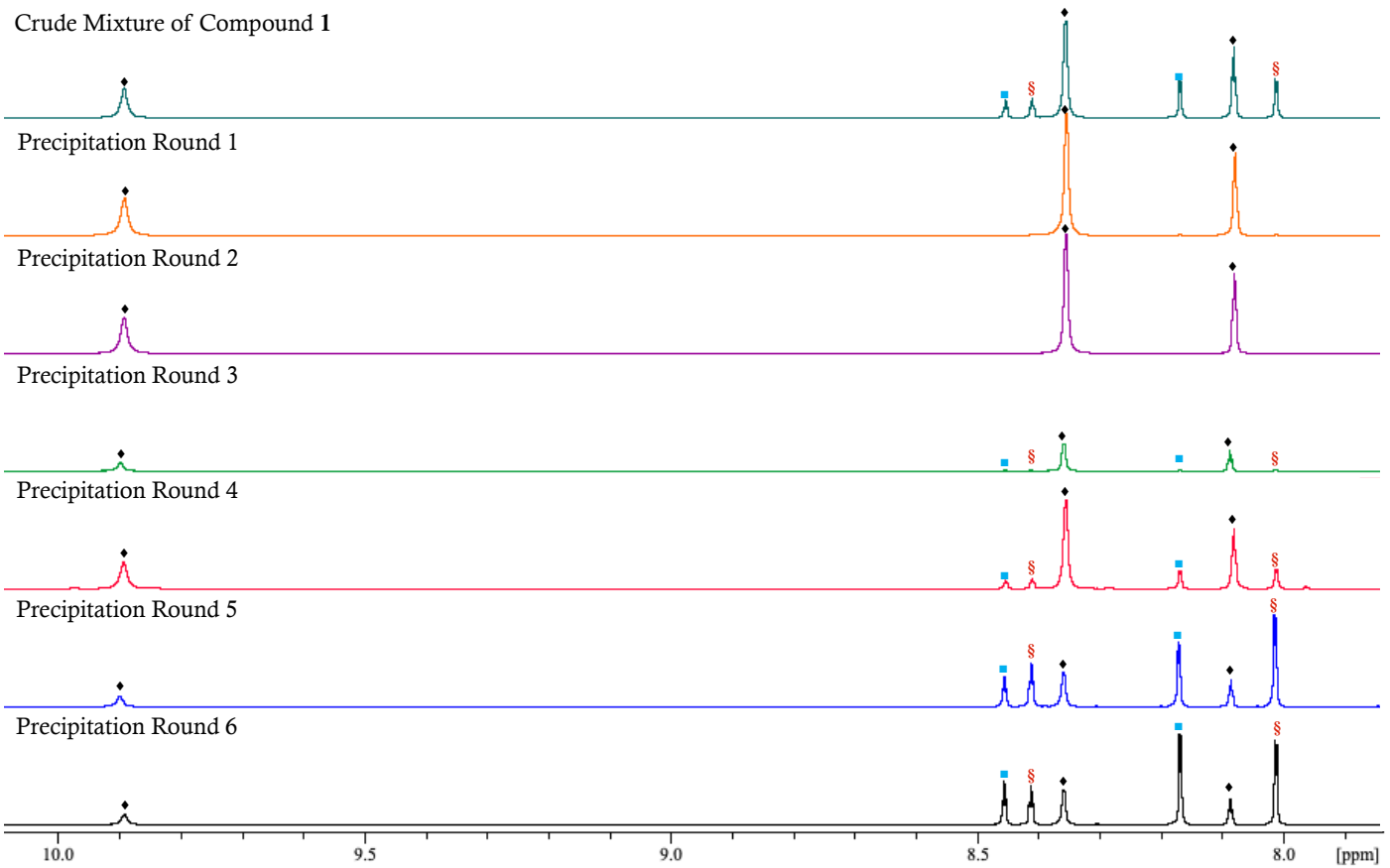

Figure 4.5. Stacked ^{1}H NMR spectra of compound **1** crude mixture and isolated mixture components obtained through repeated precipitation. Peaks associated with compound **1** mixture components are distinguished from one another with labels for set A (*anti*-rotamer, *anti*-**1**, ♦) , set **B** [doubly Boc-protected derivative of compound **1**, $(Boc)_2$-**1**, §] , and set **C** (imidic acid tautomer of compound **1**, tautomer-**1**, ■) . Spectra were obtained when from samples dissolved in DMSO-d_6 solvent.

4.3.3. Variable Temperature Analysis of Compound 1.

Variable temperature ^{1}H NMR experiments were performed on samples of both the compound **1** crude product mixture and the isolated major mixture component, modeling experimental procedures outlined by (Humbert *et al*., 2014).[156] The experiments were performed in polar aprotic solvents. Deuterated DMSO was originally used for experimental data collection. This was mirrored when Dr. Khozeimeh Sarbisheh established the DFT theoretical modeling of the conformational changes and their associated energies as she populated the surrounding environment of the model with DMSO as solvent. Deuterated DMF was used during follow up experiments given its comparatively lower freezing point (18 °C vs -61 °C), which enabled assessment of the compound **1** product mixture when subjected to low temperatures.[157]

As temperature was adjusted over time, signal intensity changes in the aromatic region of the compound **1** product mixture's ^{1}H NMR were monitored. **Figures 4.6** and **4.7** depict the aromatic regions of ^{1}H NMR spectra obtained during analysis of the compound **1** mixture for various temperatures at which data was collected in DMSO-d_6 and DMF-d_7 respectively. While the signals associated with aromatic framework's protons exhibited minor shifts upon the initial increase in temperature from 25 °C to 75 °C, the carbamate (N-H) peak of the major mixture constituent (set **A**) was found to move further upfield with every increase in temperature. This upfield shift suggests the carbamate functionality undergoes a rotational change that increases the amount of electron shielding experienced by the N-H proton at higher temperatures. Subsequent cooling of the heated sample, as performed during experiments carried out in DMF-d_7, caused the N-H peak to reposition itself downfield; further signifying the temperature dependent change in conformation about the molecule's N-C bond. Increases in temperature resulted in the formation of compound **1** degradation products such as the Boc-deprotected agent and isobutylene. In addition to this, increasing temperatures afforded a new set of peaks (set **D**) that were visible within the ^{1}H NMR spectra of the product mixture obtained in DMSO-d_6. The absence of this set of peaks, believed to result from a new set of conformers taking form under these conditions, from the DMF-d_7 spectra is likely due to overlap with larger peaks that mask their presence. Lack of peak splitting during variable temperature ^{1}H NMR analysis discredited the notion of peak overlap as an explanation for the higher integration values of one of the molecules' *tert*-butyl functional groups, thus supporting the notion that the second set of peaks within the ^{1}H NMR spectra (set **B**) resulted

from the presence of a doubly Boc-protected variant of the product. This information offered sufficient explanation as to why the second set of peaks lacked a signal indicative of a secondary amine proton (carbamate, Boc-protected amine) as incorporation of a second *tert*-butyl carbamate functionality within the molecular structure was via substitution of the N-H proton; forming a doubly Boc-protected tertiary amine.

While these observations proved helpful towards the understanding of the goings on within the compound **1** mixture at elevated reaction temperature, they did not afford any further explanation towards the absence of a N-H proton signal for the remaining minor mixture constituent (^{1}H NMR peak set **C**). As such, further analysis of the compound **1** mixture was performed by implementing FTIR spectroscopy. By comparing the FTIR spectra of the product mixture (**Figure 4.8**) with that of the isolated major constituent (**Figure 4.9**) it became clear that the three original sets of proton signals previously hypothesized to be different conformers of the product molecule were instead the product material (set **A**), a doubly Boc-protected derivative of the compound **1** molecule (set **B**) and imidic acid tautomers of compound **1** (set **C**). The presence of imidic acid tautomers is primarily supported by the solid compound **1** mixture sample producing an additional FTIR signal at 2339.30 cm^{-1} indicative of a carbon-nitrogen double bond (N=C). While a literature reference supporting this aromatic ring-bound carbon-nitrongen double bond could not be found, the approximate value of the imidic acid tautomer is supported by computational calculations for the theoretical FTIR spectral analysis performed by Dr. Khozeimeh Sarbisheh.[142]

Further comparisons between the experimental results and the computational models performed by Dr. Khozeimeh Sarbisheh suggest that the ^{1}H NMR signals collectively identified as peak set **A**are attributed to several *anti*-rotamers of the compound **1** product with respect to the priority assignment of the functional groups bound to the structure's N-C bond. These conformational isomers are believed to reside within a relatively similar energy domain and as such, present as a single set of peaks within the ^{1}H NMR spectra due to rapid rotational interchangeability occurring within the timescale of the instrument's acquisition period. As previously mentioned, heating the product mixture sample dissolved in DMSO-d_6 solvent afforded a fourth set of peaks (set **D**). This fourth set of peaks is believed to indicate the formation of *syn*-rotameric variants of compound **1** with respect to the priority assignment of functional groups

about the molecule's N-C bond which, based on the DFT models performed by Dr. Khozeimeh Sarbisheh, require greater energy input from the surrounding to ascertain this conformation and are therefore a less favourable conformation. The formation of less favourable *syn*-**1** rotamers has been previously reported by both (Moraczewski *et al.* 1998) and Marcovici-Mizrahi *et al.*, 1996).[158] [159] The formation of the *syn*-compound **1** rotamers (peak set **D**) was not observed in the experimental data obtained using the isolated *anti*-conformers of compound **1**, their formation in this case cannot be attributed to temperature-facilitated rotation about the N-C bond of the *anti*-compound but rather must result from the structural changes of the minor mixture constituents i.e. the doubly Boc-protected and imidic acid product **1** tautomers. However, from the experimental data ascertained, it cannot be determined which if not both of these mixture components afford the *syn*-rotamers of compound **1** at higher temperatures.

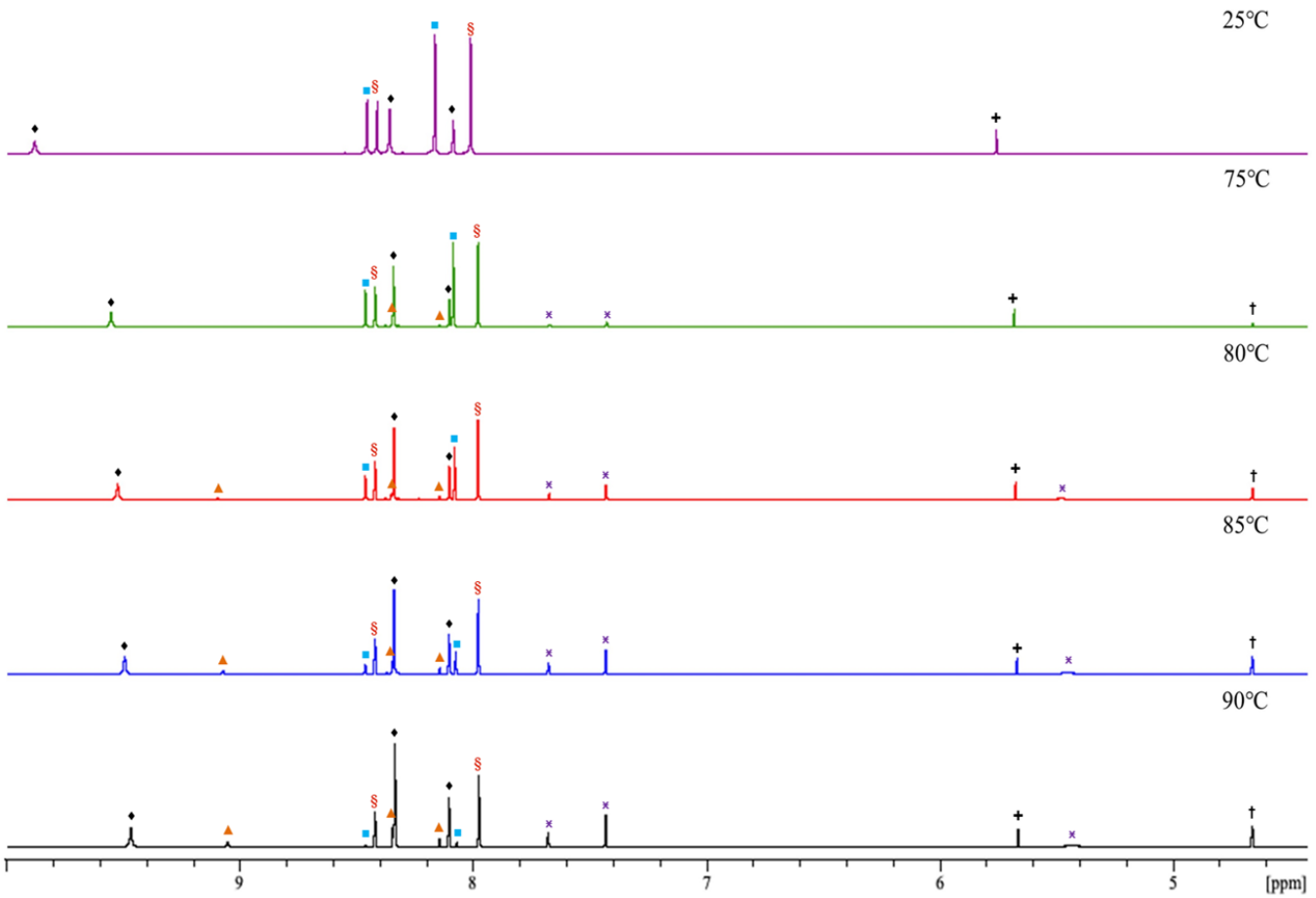

Figure 4.6. ^{1}H NMR spectrum of the compound **1** product mixture in DMSO-d_6 solvent at 25 °C to 90 °C. Peaks associated with the *anti*-rotamers of compound **1** (*anti*-**1**, set **A**), a doubly Boc-protected derivative of compound **1** [$(Boc)_2$-**1**, set **B**), an imidic acid tautomers of compound **1** (tautomer-**1**, set **C**), *syn*-rotamers of compound **1** (*syn*-**1**, set **D**), and the deprotected derivative of compound **1** are designated by the symbols ♦, §, ■, ▲, and x, respectively. Peaks associated with dichloromethane are denoted by the symbol +. Peaks associated with isobutylene are denoted by the symbol †. Figure reported in (Khozeimeh Sarbisheh *et al.*, 2020).[160]

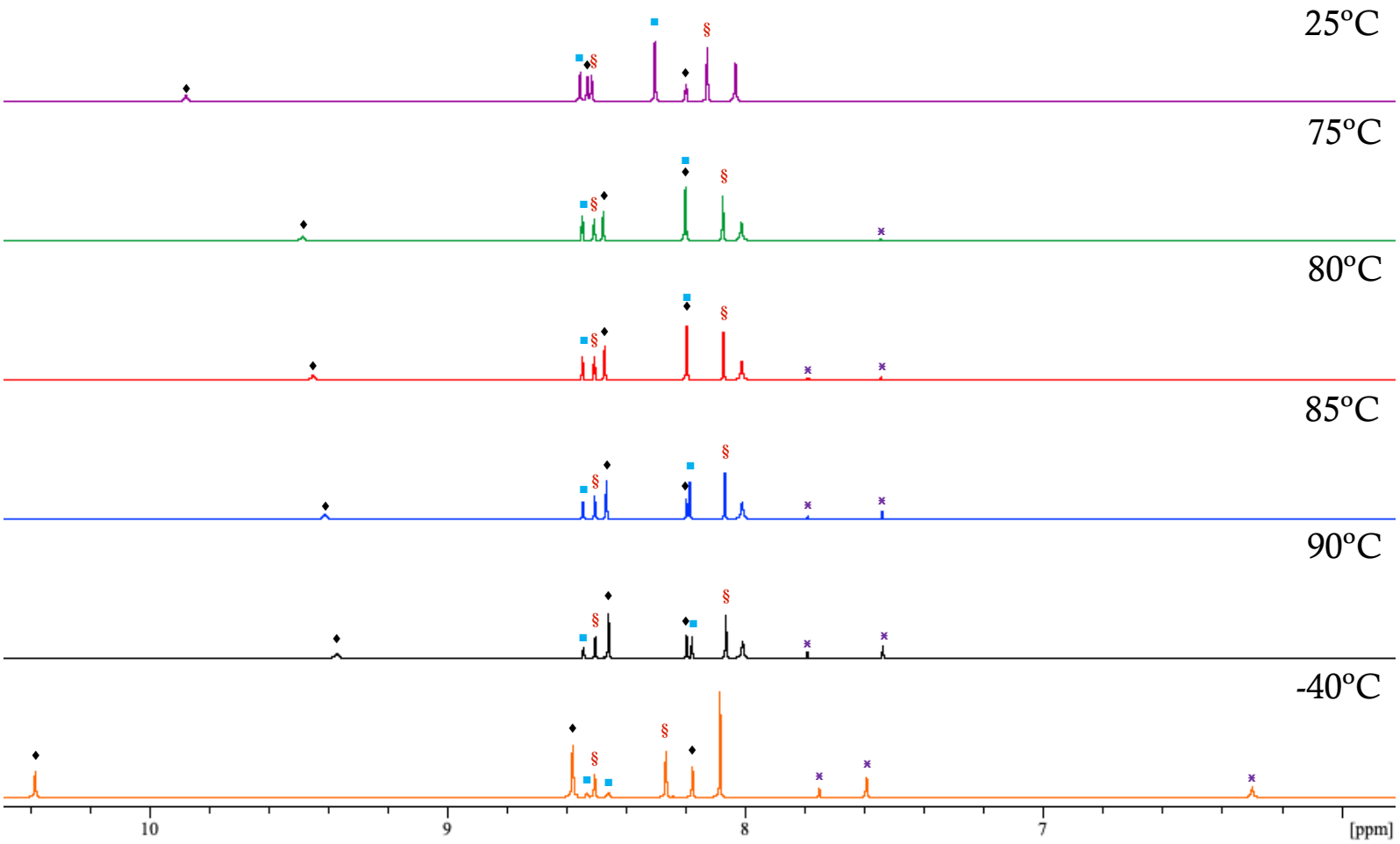

Figure 4.7. ^{1}H NMR spectrum of the compound **1** product mixture in DMF-d_7 solvent at 25 °C to 90 °C. Peaks associated with the *anti*-rotamers of compound **1** (*anti*-**1**, set **A**), a doubly Boc-protected derivative of compound **1** [$(Boc)_2$-**1**, set **B**), an imidic acid tautomers of compound **1** (tautomer-**1**, set **C**), and the deprotected derivative of compound **1** are designated by the symbols ♦, §, ■, and x, respectively.

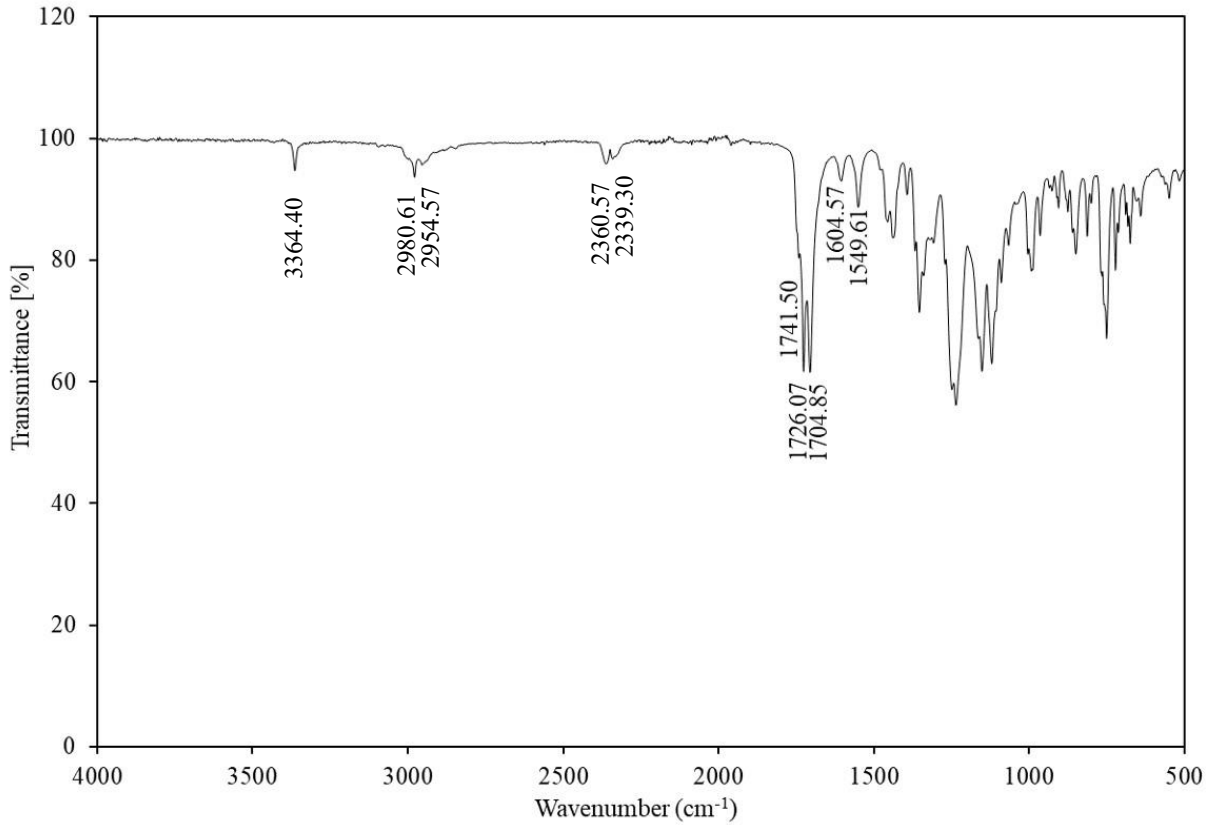

Figure 4.8. FTIR spectrum of compound **1** product mixture from the final mother liquor of successive precipitations (mixture of set **A, B, and C**), including the *anti*-rotamers of compound **1** (*anti*-**1**, set **A**), a doubly Boc-protected derivative of compound **1** [$(Boc)_2$-**1**, set **B**), and an imidic acid tautomers of compound **1** (tautomer-**1**, set **C**). Additional signals were observed in the ~1704-1742 cm^{-1} range when compared with the *anti*-rotamers of compound **1** (*anti*-**1**, set **A**) (**Figure 4.9**), which are likely arising from the additional Boc group in set **B** and the presence of the imidic acid in set **C**. Figure reported in Figure reported in (Khozeimeh Sarbisheh *et al.*, 2020).[160]

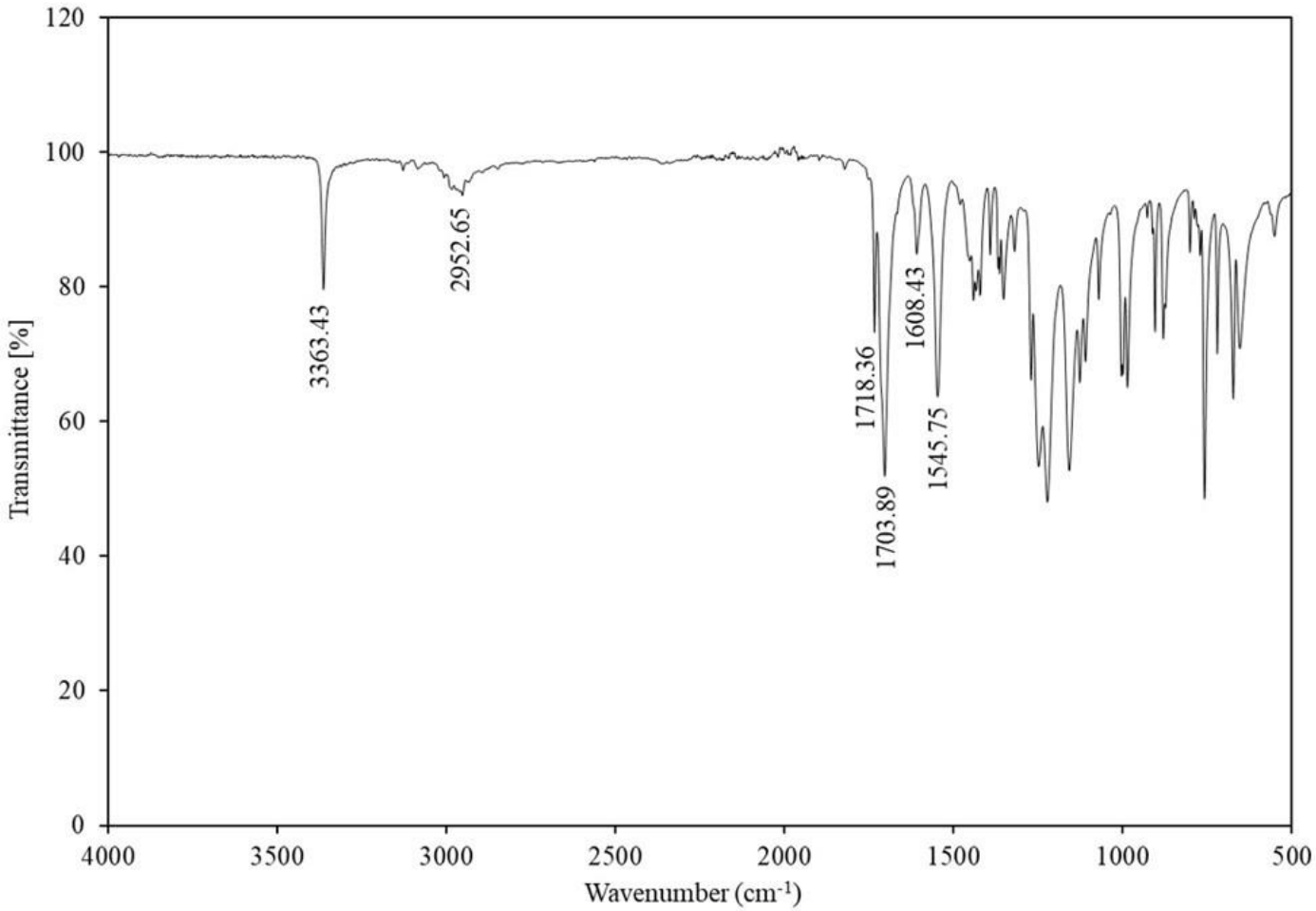

Figure 4.9. FTIR spectrum of the *anti*-rotamers of compound **1** (*anti*-**1**, set **A**) isolated as a precipitate from cold DCM. Figure reported in (Khozeimeh Sarbisheh *et al.*, 2020).[160]

As the sample mixture was no longer believed to contain isolated rotameric species of the product molecule, the Gibb's free energy calculations that were originally intended to result from performance of the ^{1}H variable temperature NMR experiments could not be made for differing conformers as we had previously anticipated.

While the variable temperature experimental data could not be used to afford experimental values for the calculation of Gibbs free energy, it did offer some explanation as to why both the isolated compound **1** product and the mixture of various constituents both provided nearly quantitative yields of the subsequent product during the multistep synthesis of the final DiPODS product when utilized. As shown by the trends of **Tables 4.2** and **4.3**, the integration values of peaks associated with the compound **1** product (set **A**) increased with increasing temperature over time while the peaks associated with both the imidic acid tautomers of the compound **1** product and the doubly Boc-protected variant decrease. While small amounts of the minor mixture constituents likely contribute to the increasing amounts of degraded material that were also observed within the ^{1}H NMR spectra, they also contribute to the increasing proportions of *anti*-**1** observed in the spectra over time through either tautomerizing from imidic acid to the amide or by losing one of the Boc-protecting groups to yield the singly Boc-protected product set **A** (*anti*-**1**).

Table 4.2. Percentages (%) and differences in percentages (%) between compound **1** isomeric mixture components at the initial and final stages of heating for the listed temperatures in DMSO-d_6 solvent. Table reported in (Khozeimeh Sarbisheh *et al.*, 2020).[160]

Time (min)	Temperature (°C)	**Set A** (%)	**Set B** (%)	**Set C** (%)	**Set D** (%)	**Boc-deprotected** (%)	**ΔSet A** (%)	**ΔSet B** (%)	**ΔSet C** (%)	**ΔSet D** (%)	**ΔBoc-deprotected** (%)
0	25	24.3	36.7	39.0	0.0	0.0	0.04	0.54	-0.58	0.00	0.00
50		24.3	37.3	38.4	0.0	0.0					
0	75	25.8	36.3	34.9	1.2	1.7	4.14	-0.41	-9.15	1.92	3.50
50		29.9	35.9	25.8	3.1	5.2					
0	80	31.7	35.7	22.6	3.5	6.5	5.23	-0.68	-9.78	1.94	3.28
50		36.9	35.1	12.8	5.4	9.8					
0	85	38.6	34.7	9.9	5.9	11.0	5.17	-2.33	-6.43	1.50	2.09
50		43.7	32.3	3.4	7.4	13.1					
0	90	44.9	31.7	2.1	7.7	13.6	7.88	-7.25	-2.06	0.53	0.90
130		52.8	24.5	0.0	8.2	14.5					

Table 4.3. Percentages (%) and differences in percentages (%) between compound **1** isomeric mixture components at the initial and final stages of heating for the listed temperatures in DMF-d_7 solvent.

Time (min)	Temperature (°C)	**Set A** (%)	**Set B** (%)	**Set C** (%)	**Boc-deprotected** (%)	**ΔSet A** (%)	**ΔSet B** (%)	**ΔSet C** (%)	**ΔBoc-deprotected** (%)
0	25	24.2	35.3	40.3	0.16	-0.50	0.41	0.07	0.02
50		23.7	35.7	40.4	0.18				
0	75	26.4	35.1	37.9	0.6	0.67	-0.28	-1.3	0.93
40		27.0	34.8	36.6	1.6				
0	80	28.5	34.7	34.7	2.1	3.79	-0.63	-5.3	2.1
50		32.3	34.1	29.4	4.2				
0	85	33.5	34.3	27.1	5.1	4.76	-0.55	-6.9	2.7
50		38.3	33.7	20.2	7.8				
0	95	40.2	33.6	17.3	8.9	7.80	-1.57	-10.7	4.4
90		48.0	32.0	6.61	13.3				
0	-40	45.7	32.4	8.19	13.7	0.38	-0.69	0.01	0.29
50		46.1	31.7	8.20	14.0				

4.4. Conclusions & Future Directions.

In summary, this chapter reports the synthesis of compounds **1-4** and **7** which were ultimately applied towards production of the novel disulfide-rebridging DiPODS bioconjugation reagent. ^{1}H variable temperature NMR experimentation did not afford data from which Gibbs free energy values could be calculated for the hypothesized rotameric species of the compound **1** crude product mixture. However, these experiments, in combination with FTIR spectroscopic analysis, enabled structural identification of the mixture constituents. The effects of increased temperature, such as that applied during the subsequent reaction of the multistep synthetic procedure, were observed to afford increasing amounts of the major compound **1** *anti*-rotameric constituents and thermal deprotection products; isobutylene and dimethyl 5-aminoisophthalate. Increasing the temperature of the dissolved compound **1** crude product mixture also resulted in the reduced concentration of doubly Boc-protected and imidic acid tautomer product variants [$(Boc)_2$-**1** and tautomer-**1**]. Finally, a fourth set of peaks was observed upon heating the product mixture sample. Based on the computational models performed by Dr. Khozeimeh Sarbisheh, we believe this fourth set of peaks is attributed to the formation of *syn*-rotamers of compound **1**. The efforts outlined within this chapter, in combination with those of Dr. Khozeimeh Sarbisheh and our collaborators in Dr. Zeglis's lab, are summarized in a recently published manuscript.

General Discussion & Conclusion

As a whole, the primary objective of this thesis was to explore and improve the application and methodologies associated with radiochemistry. The research discussed in this dissertation mirror the multifaceted nature of this field. What started out as a simple application of pre-existing methodologies in Chapter 2 with the attempted $^{19}F/^{18}F$-transfluorination of the CDy11 BODIPY dye developed into a new research objective that sought to address the complications experienced with CDy11 and improve the existing labeling strategies. While this project requires further investigative efforts to flesh out its bones, the work presented in Chapter 3 is a step forward towards reliable and reproducible synthesis of BODIPY-based radiotracers. To our knowledge, this project afforded the first application of air stable $Mg(NO_3)_2 \cdot 6H_2O$ solutions towards the synthesis of a ^{18}F-labeled BODIPY fluorophore. Future research endeavors should investigate the efficacy of a wide range of stable Lewis acids towards facilitating $^{19}F/^{18}F$-isotopic exchange at the BF_2-moiety. In doing such, GMP certification could be achieved for BODIPY-based imaging agents; opening the door to a greater number of potential PET diagnostic agents.

The research outlined in Chapter 3 pertained to the performance of $^{19}F/^{18}F$-fluoride exchange on a BODIPY core hosting relatively inert functional groups which contributed negligible electron donating or withdrawing effects to the quasi-aromatic framework. Future initiatives should focus on surveying the effects of various functional groups and their position on the planar ring system on the radiochemical yields obtained from the $^{19}F/^{18}F$-transfluorination process. A library of this nature would provide further insight into optimal design characteristics for synthesis of novel BODIPY precursors and the radiolabeling conditions best suited to transform them into bimodal imaging agents.

The research focus shifted in Chapter 4 from the application and investigation of improved radiolabeling methodologies previously discussed in Chapters 2 and 3 to improving the stability and subsequently the delivery of radioimmunoconjugate. By taking note of the observations made between the multistep reactions **1** and **2** and the ^{1}H NMR compound **1** crude mixture spectra it was discerned that further purification processes were not required before progressing to the next stage of the synthesis. Spectroscopic analysis of the isomers and crude mixture constituents of compound **1** from the multistep DiPODS synthesis provides further insight towards the synthetic

process as a whole. This effectively increased the amount of available reagent material for the subsequent reaction from 66% to nearly quantitative values as those used during the first reaction as the reaction of all the compound **1** crude mixture components were able to form the subsequent compound **2** product under the applied reaction conditions. What's more, performing these spectroscopic analyses and reporting the observations and lessons learned from our findings proves beneficial for future synthetic strategy development and the investigation of means by which to optimize the overall reaction yields of multistage processes. These efforts were incorporated into a manuscript accompanying the contributions made by Dr. Khozeimeh Sarbisheh and our collaborators in Dr. Zeglis's lab outlining the successful synthesis and *ex vivo* disulfide rebridging assessment of the DiPODS linker molecule.. Future research efforts may aim to modify the DiPODS structure to optimize the linker structure further as well as *in vivo* experimentation.

In summary, the various approaches and research interests outlined in this dissertation provide further insight towards improving future radiotherapeutics and PET diagnostics. In doing such, these efforts serve towards the future expansion of the toolbox of applicable radiochemical agents for radiochemical diagnostics and treatment of malignancies.

Appendix

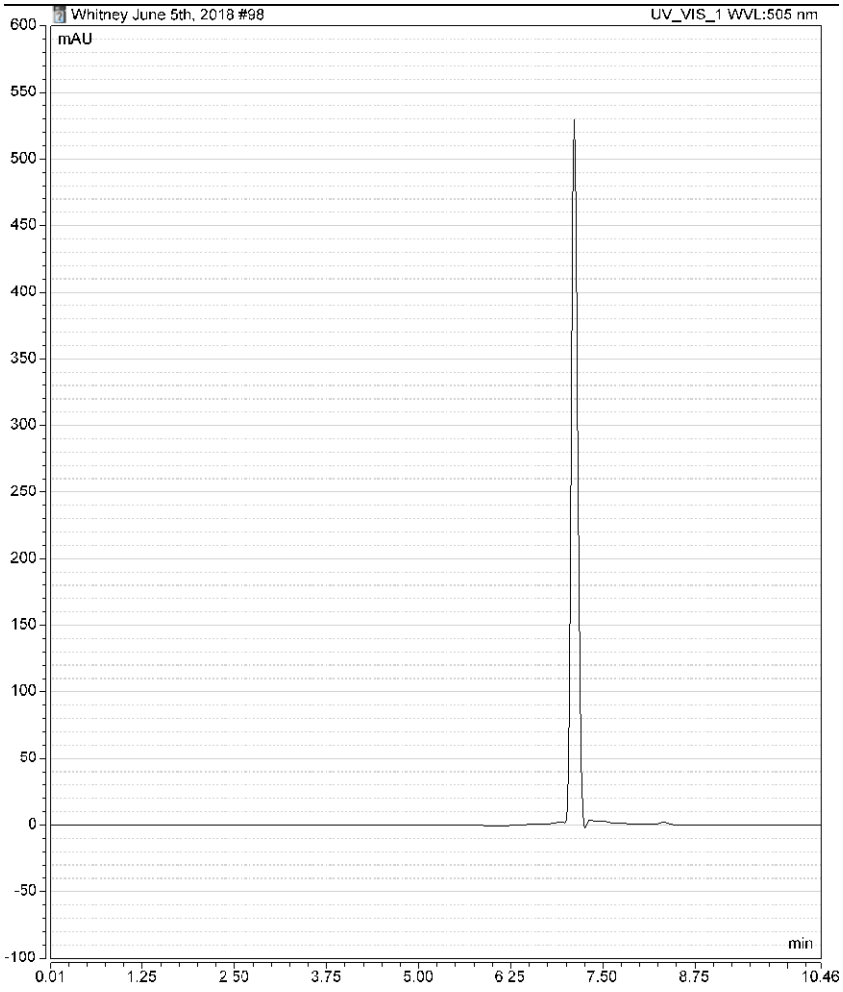

Figure A.1. HPLC chromatogram of [^{19}F/^{18}F]-isotopic exchange reaction mixture for commercial BODIPY standard when subject to 50 eq $SnCl_4$, 37°C, TBAB fixing agent at wavelength 505nm. Chromatogram obtained using Thermo Fisher Vanquish UHPLC system.

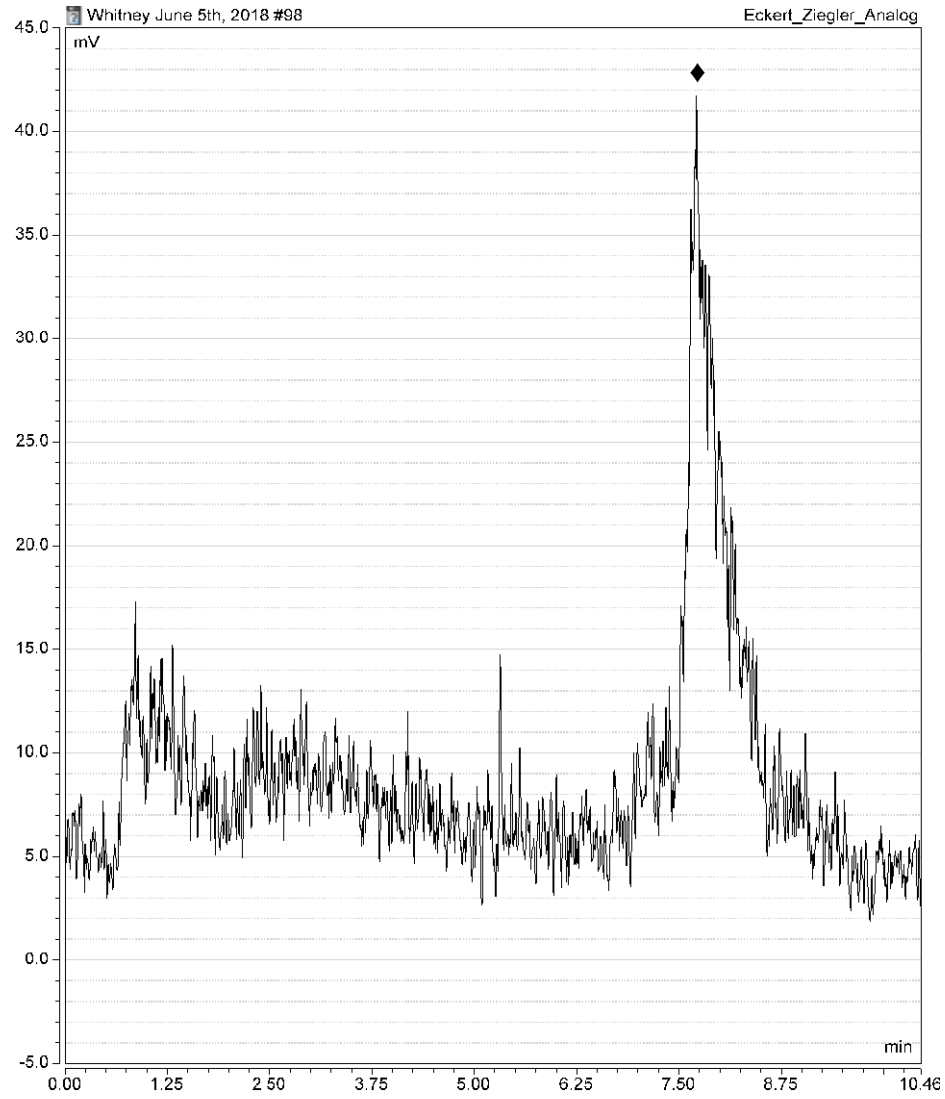

Figure A2. HPLC chromatogram of [^{19}F/^{18}F]-isotopic exchange reaction mixture for commercial BODIPY standard when subject to 50 eq $SnCl_4$, 37°C, TBAB fixing agent. Chromatogram obtained using Thermo Fisher Vanquish UHPLC system equipped with radioactivity detector set at 2000K sensitivity. Peak associated with the radiolabeled commercial BODIPY dye is denoted with the symbol (♦).

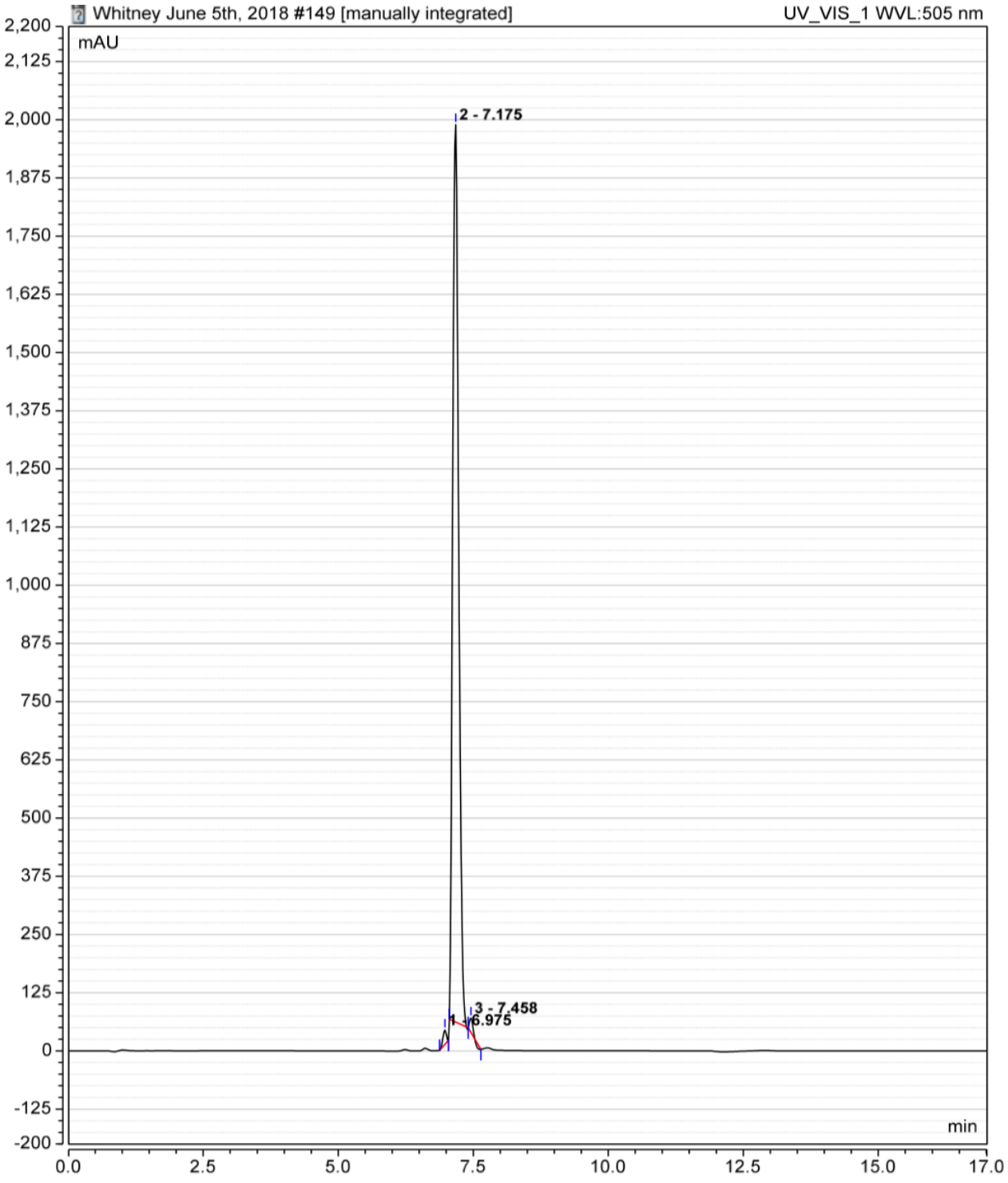

Figure A3. Representative HPLC chromatogram of commercial BODIPY standard. Chromatogram was obtained using a Thermo Fisher Vanquish UHPLC system equipped with a UV-Vis detector set to measure at 505 nm. Peak 2 (7.175 min) is associated with the commercial BODIPY dye.

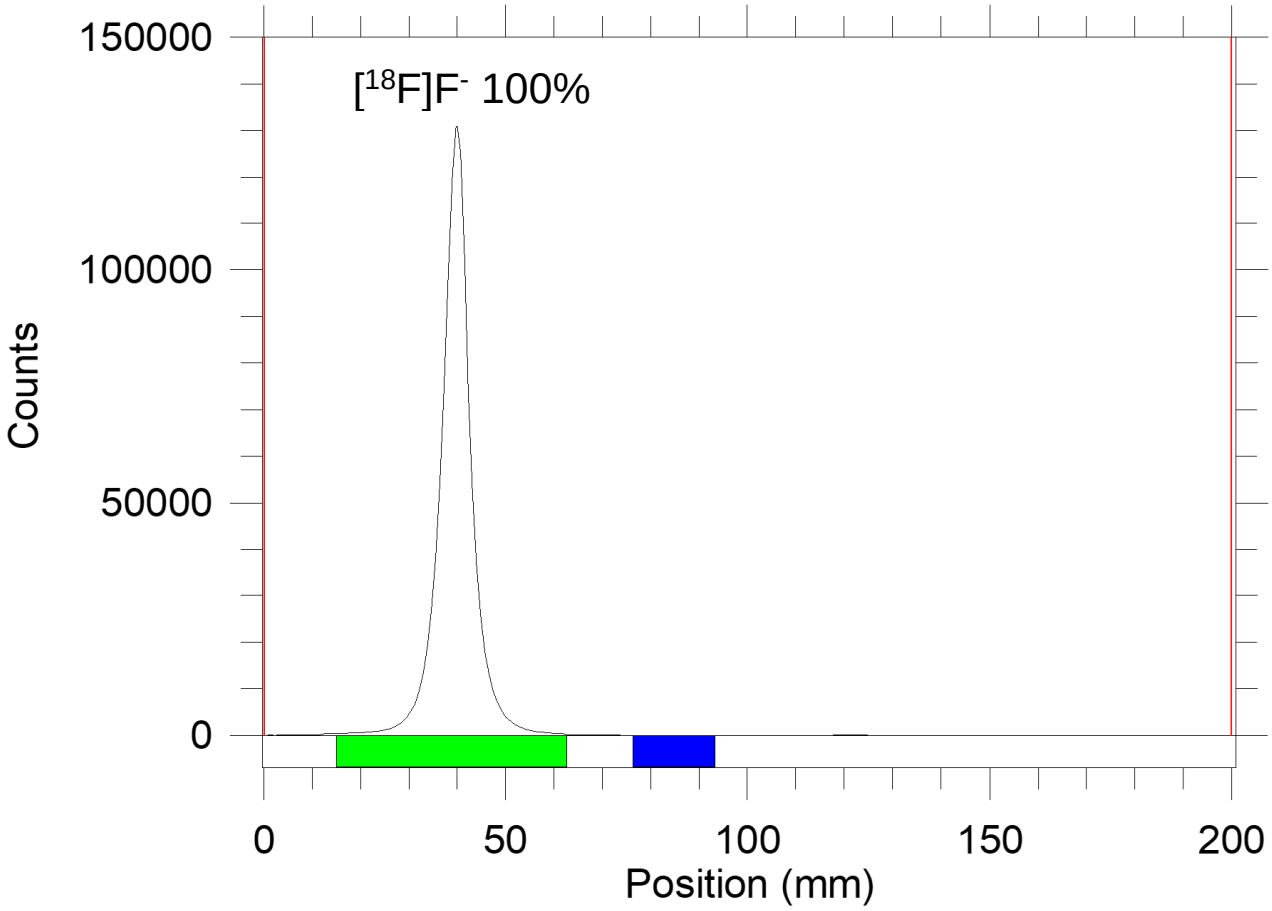

Figure A4. Representative TLC chromatogram of [^{19}F/^{18}F]-isotopic exchange reaction mixture for commercial BODIPY standard when subjected to 10 eq $SnCl_4$, 37 °C, TBAB fixing agent. Experimental conditions applied are outlined in entry 1 of **Table 3.2**. Chromatogram obtained using Bioscan AR-2000 radio-TLC plate reader. The radioactivity peak associated with free [^{18}F]F^- is labeled as such.

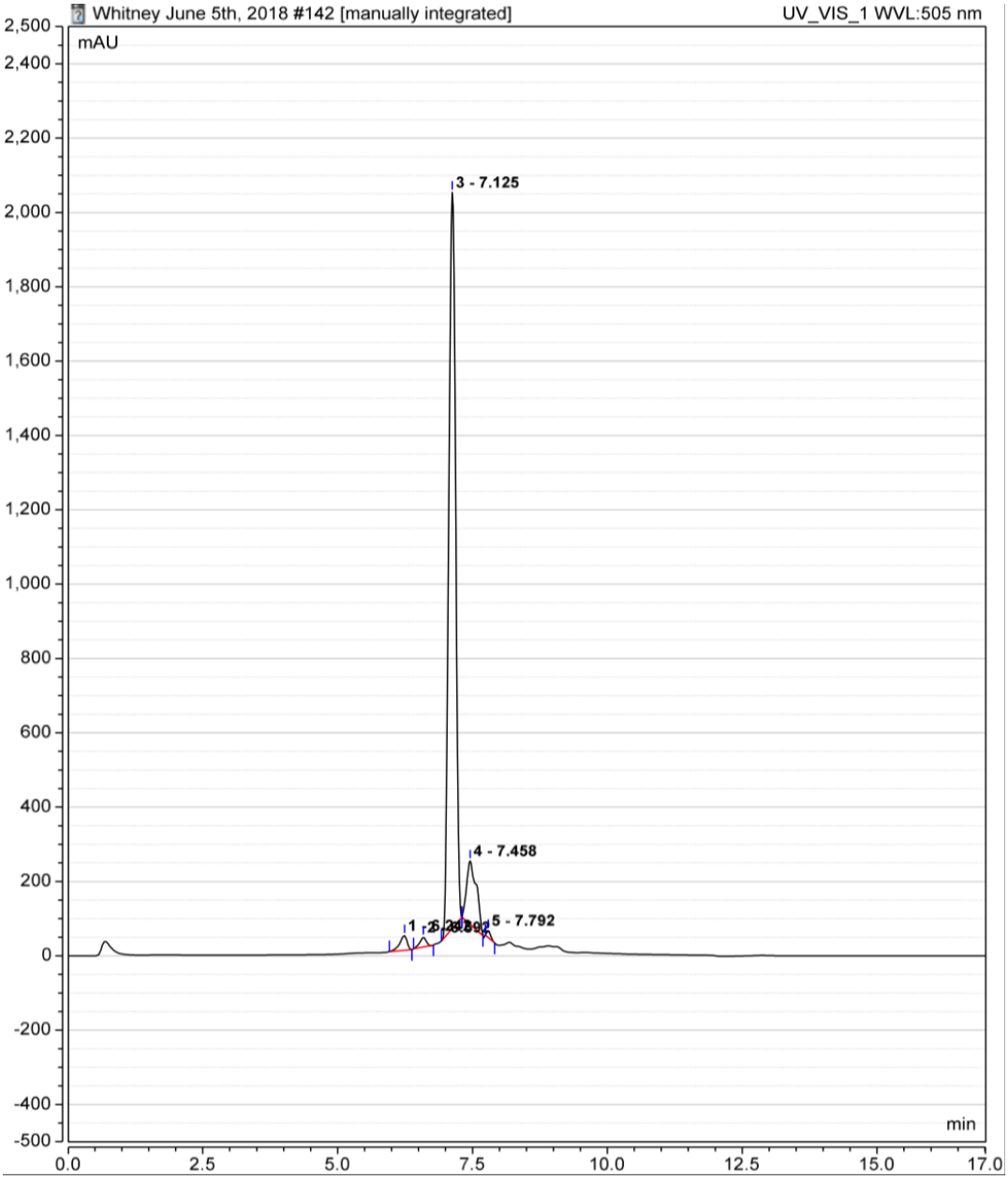

Figure A5. HPLC chromatogram of [^{19}F/^{18}F]-isotopic exchange reaction mixture for commercial BODIPY standard when subject to 10 eq $Mg(NO_3)_2$, 55.8 eq TEAB fixing agent at 37 °C for 5 minutes. Experimental conditions applied are outlined in entry 1 of **Table 3.2**. Chromatogram was obtained using a Thermo Fisher Vanquish UHPLC system equipped with a UV-Vis detector set to measure at 505 nm. Peak 3 (7.125 min) is associated with the commercial BODIPY dye.

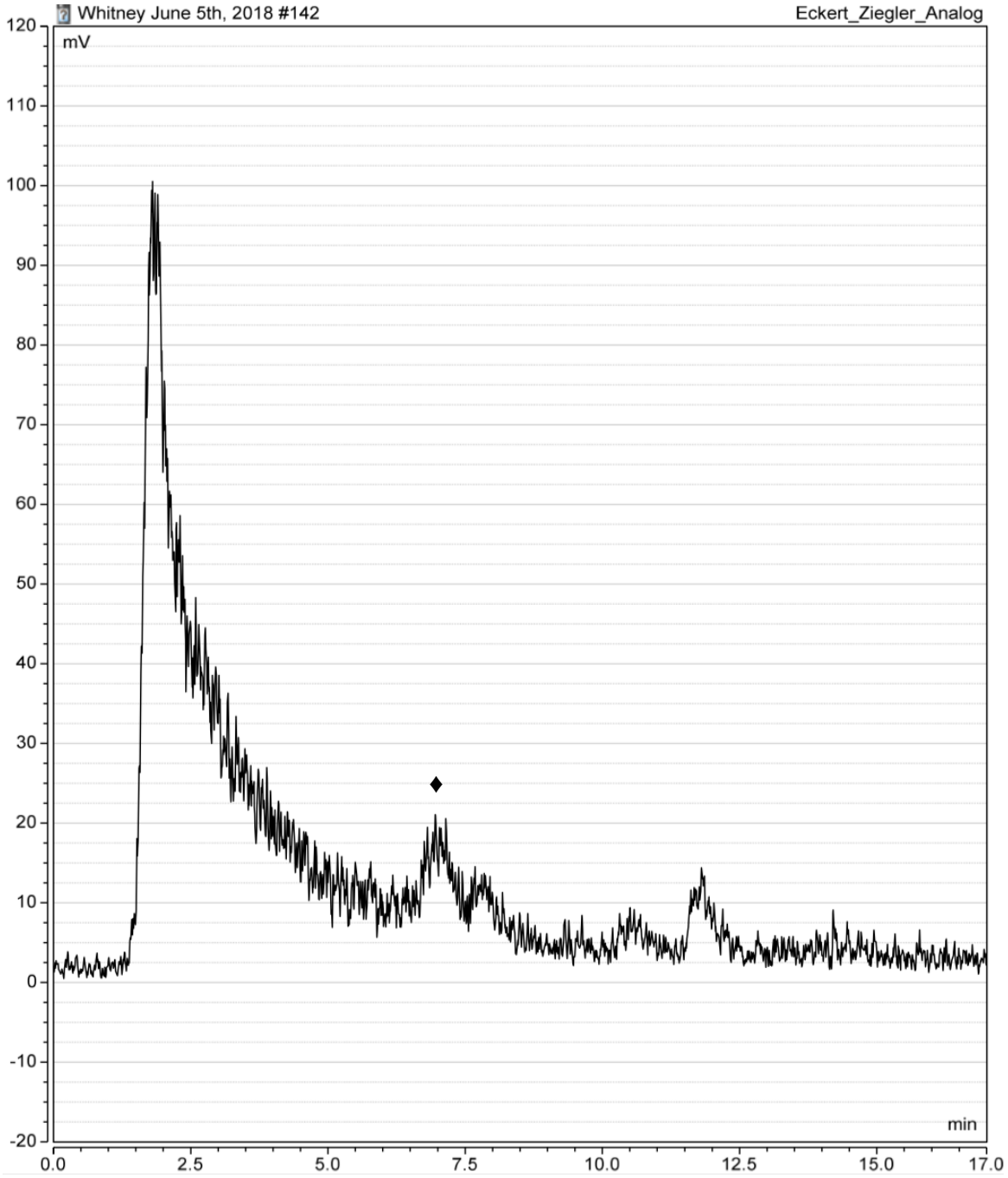

Figure A6. HPLC chromatogram of [^{19}F/^{18}F]-isotopic exchange reaction mixture for commercial BODIPY standard when subject to 10 eq $Mg(NO_3)_2$, 55.8 eq TEAB fixing agent at 37 °C for 5 minutes. Experimental conditions applied are outlined in entry 1 of **Table 3.2**. Chromatogram was obtained using a Thermo Fisher Vanquish UHPLC system equipped with a radioactivity detector set to 2000K sensitivity. Peak associated with the radiolabeled commercial BODIPY dye is denoted with the symbol (♦).

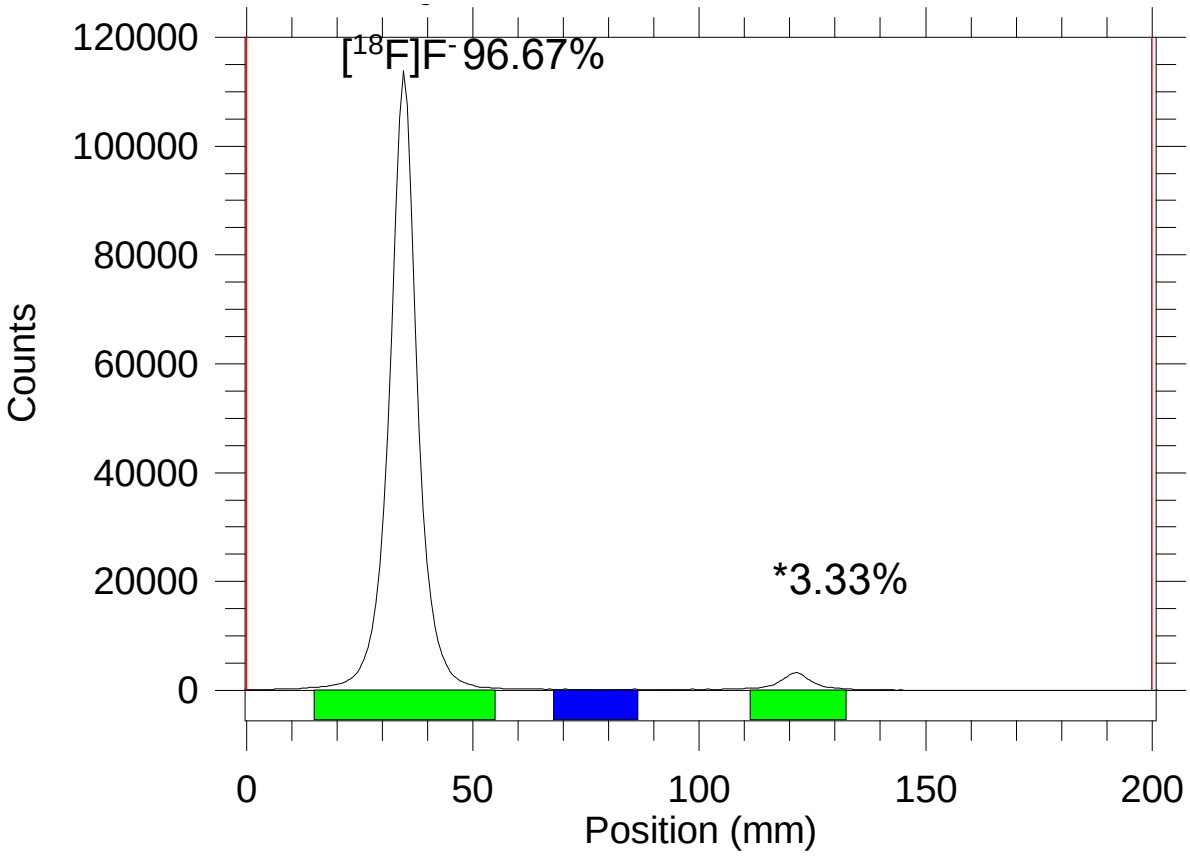

Figure A7. TLC chromatogram of [^{19}F/^{18}F]-isotopic exchange reaction mixture for commercial BODIPY standard when subject to 25 eq $Mg(NO_3)_2$, 37 °C, 55.8 eq TEAB fixing agent for 5 minutes. Chromatogram obtained using Bioscan AR-2000 radio-TLC plate reader. This data is associated with entry 2 of **Table 3.2**. The radioactivity peak associated with free [^{18}F]F$^-$ is labeled as such while the product peak is indicated by the symbol (*).

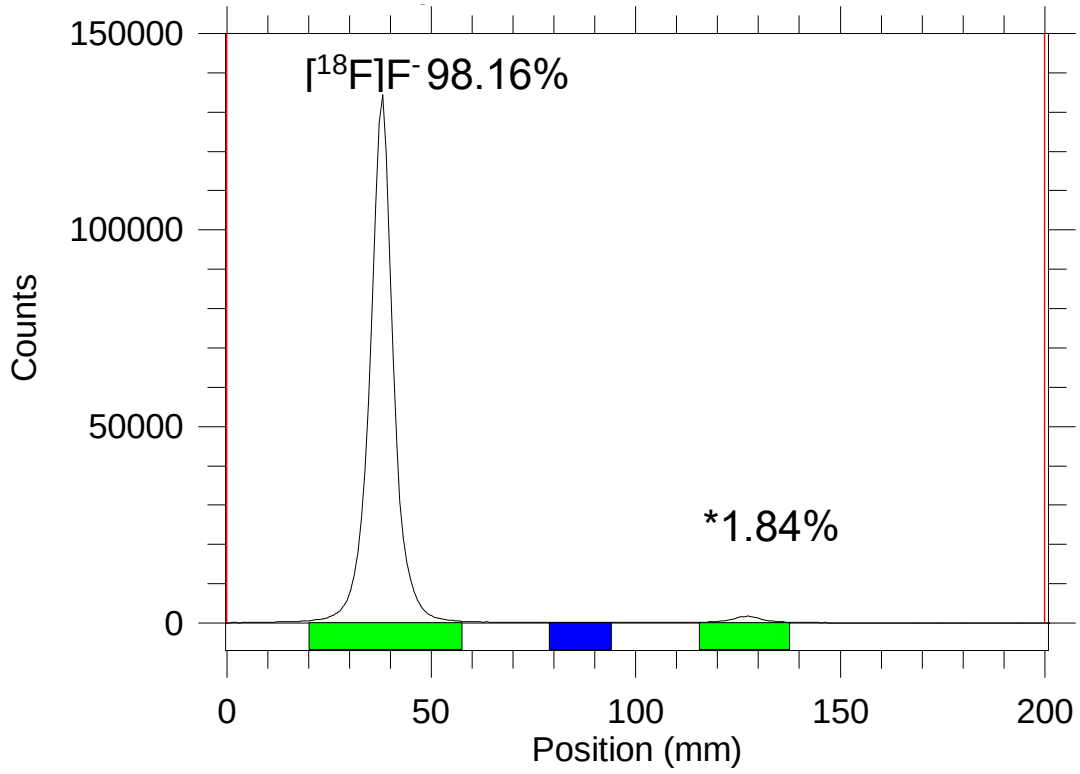

Figure A8. TLC chromatogram of [^{19}F/^{18}F]-isotopic exchange reaction mixture for commercial BODIPY standard when subject to 25 eq $Mg(NO_3)_2$, 37 °C, 55.8 eq TEAB fixing agent for 15 minutes. Chromatogram obtained using Bioscan AR-2000 radio-TLC plate reader. This data is associated with entry 2 of **Table 3.2**. The radioactivity peak associated with free [^{18}F]F$^-$ is labeled as such while the product peak is indicated by the symbol (*).

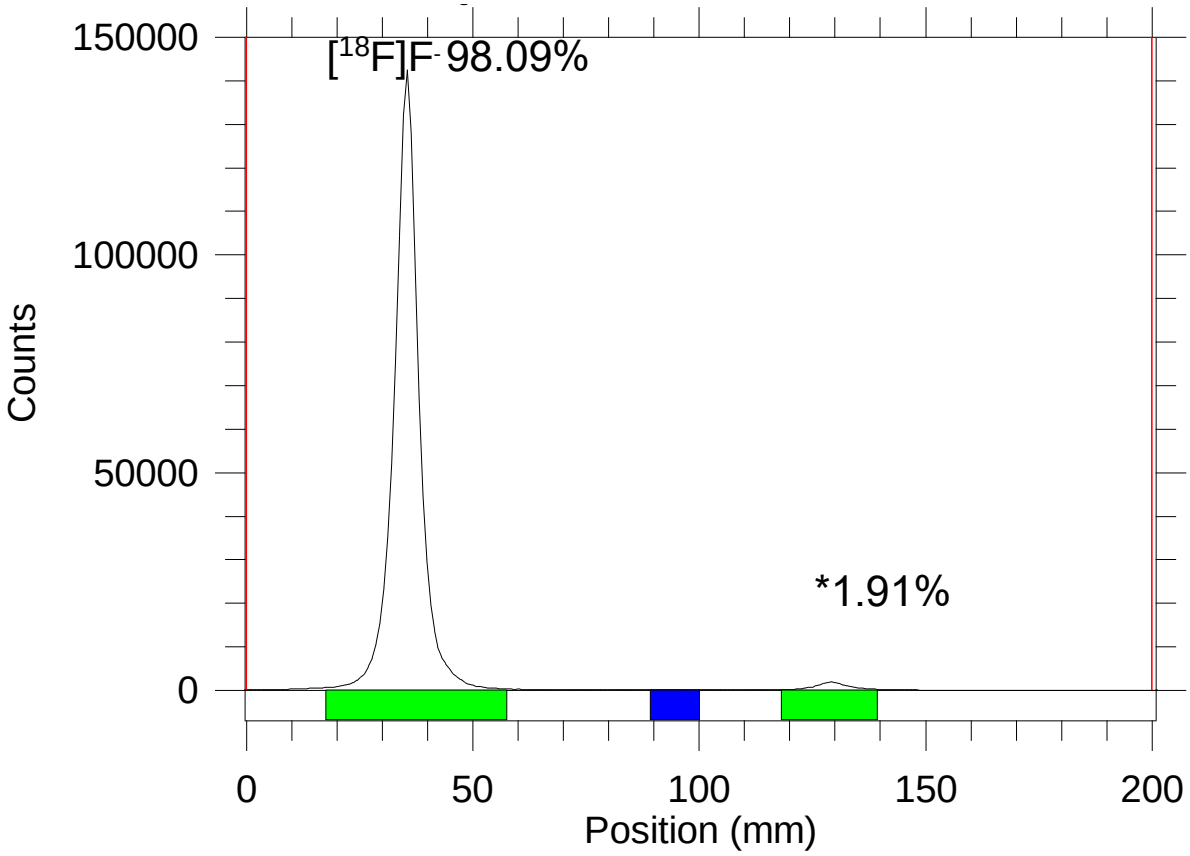

Figure A9. TLC chromatogram of [^{19}F/^{18}F]-isotopic exchange reaction mixture for commercial BODIPY standard when subject to 25 eq $Mg(NO_3)_2$, 37 °C, 55.8 eq TEAB fixing agent for 30 minutes. Chromatogram obtained using Bioscan AR-2000 radio-TLC plate reader. This data is associated with entry 2 of **Table 3.2**. The radioactivity peak associated with free [^{18}F]F$^-$ is labeled as such while the product peak is indicated by the symbol (*).

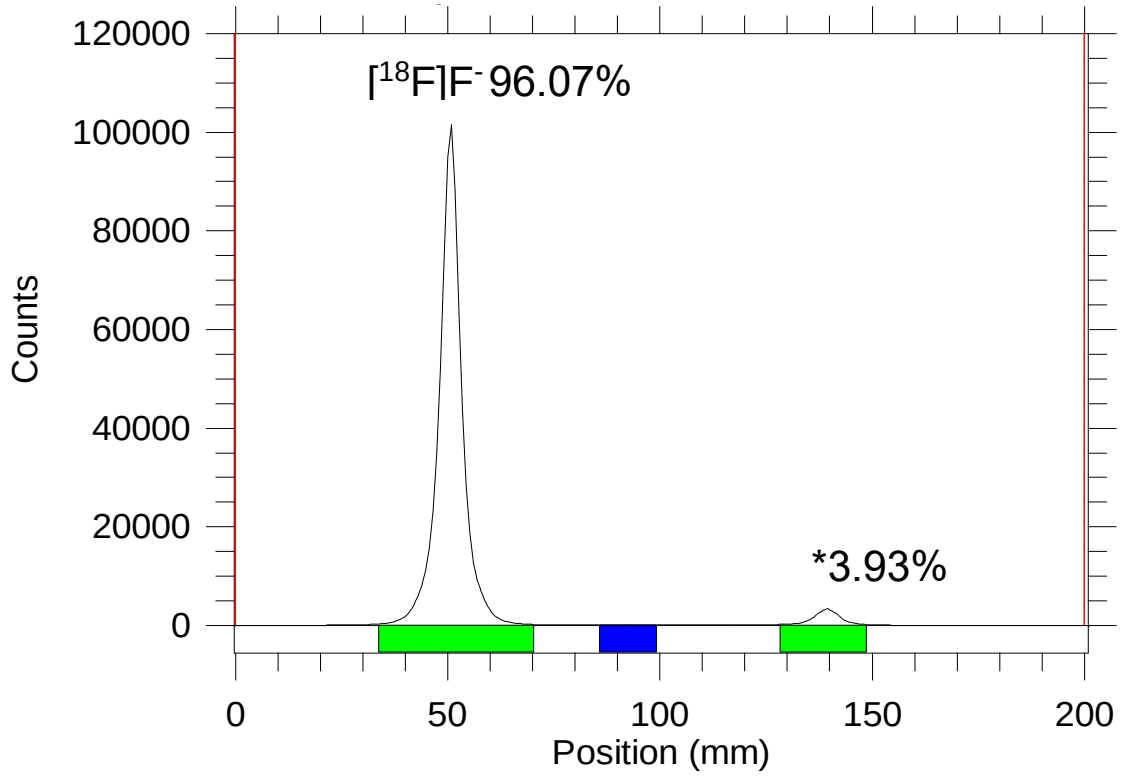

Figure A10. TLC chromatogram of [^{19}F/^{18}F]-isotopic exchange reaction mixture for commercial BODIPY standard when subject to 25 eq $Mg(NO_3)_2$, 37 °C, 55.8 eq TEAB fixing agent for 45 minutes. Chromatogram obtained using Bioscan AR-2000 radio-TLC plate reader. This data is associated with entry 2 of **Table 3.2**. The radioactivity peak associated with free [^{18}F]F$^-$ is labeled as such while the product peak is indicated by the symbol (*).

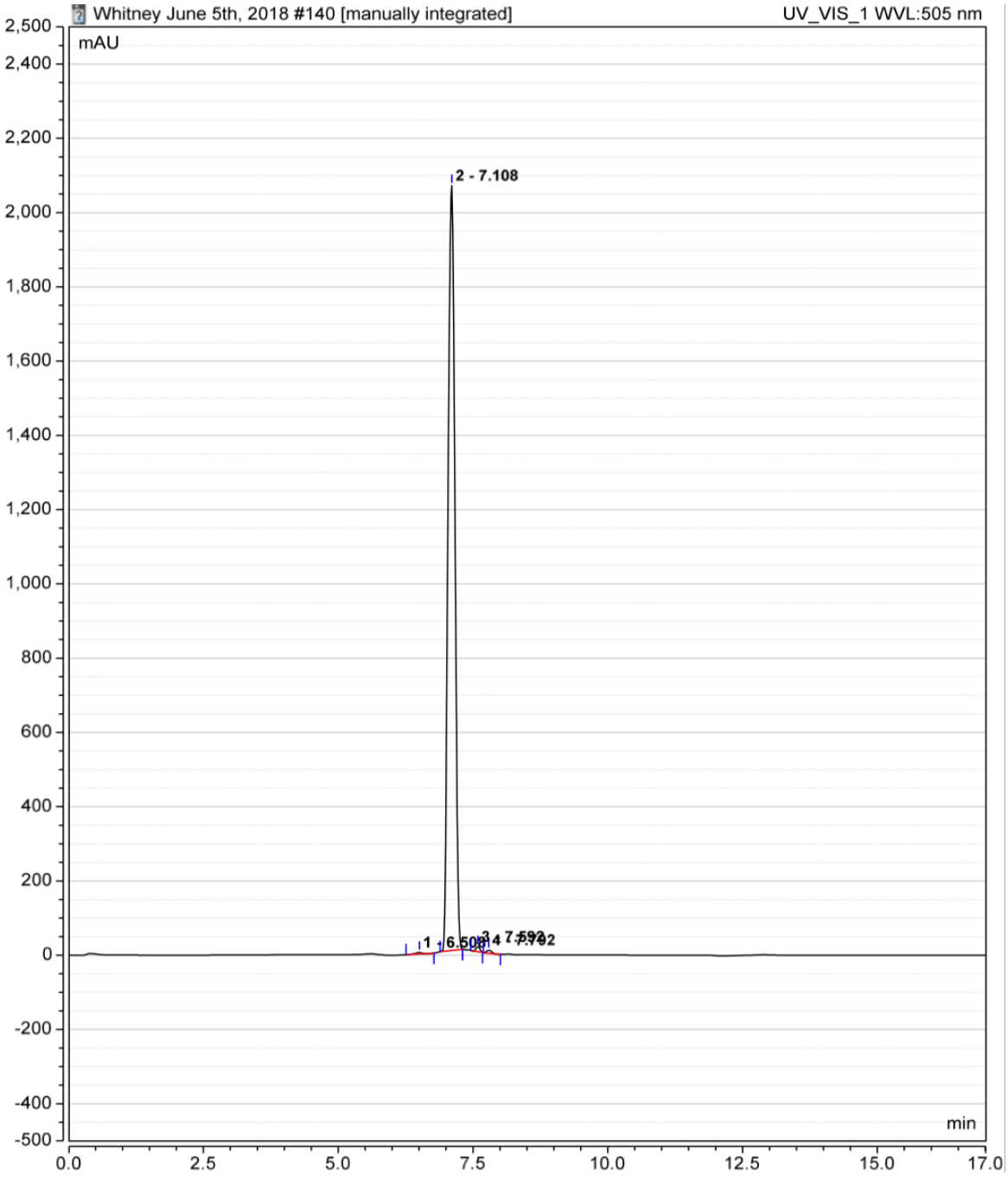

Figure A11. HPLC chromatogram of [^{19}F/^{18}F]-isotopic exchange reaction mixture for commercial BODIPY standard when subject to 25 eq $Mg(NO_3)_2$, 55.8 eq TEAB fixing agent at 37 °C for 5 minutes. Experimental conditions applied are outlined in entry 2 of **Table 3.2**. Chromatogram was obtained using a Thermo Fisher Vanquish UHPLC system equipped with a UV-Vis detector set to measure at 505 nm. Peak 2 (7.108 min) is associated with the commercial BODIPY dye.

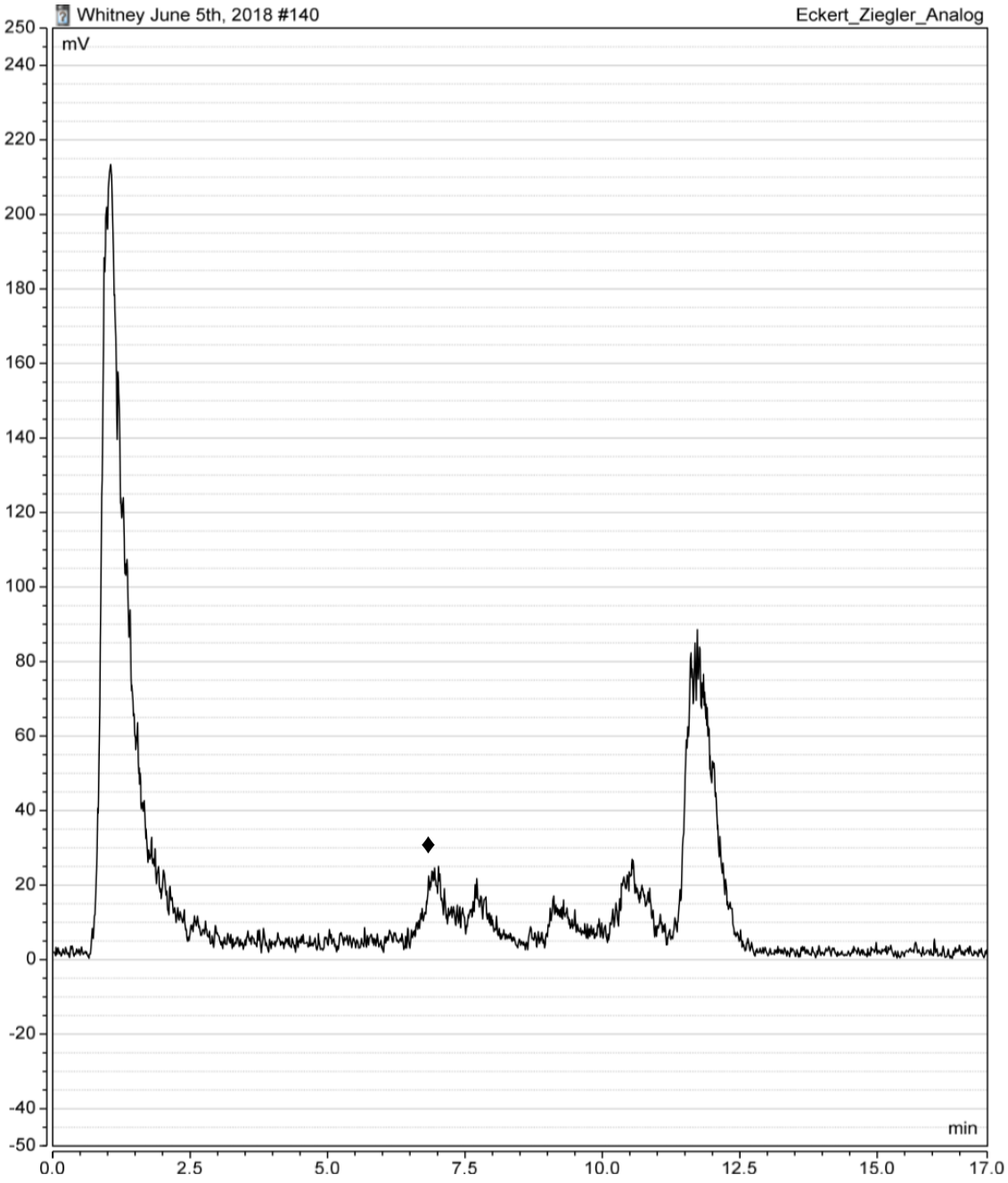

Figure A12. HPLC chromatogram of [^{19}F/^{18}F]-isotopic exchange reaction mixture for commercial BODIPY standard when subject to 25 eq $Mg(NO_3)_2$, 55.8 eq TEAB fixing agent at 37 °C for 5 minutes. Experimental conditions applied are outlined in entry 2 of **Table 3.2**. Chromatogram was obtained using a Thermo Fisher Vanquish UHPLC system equipped with a radioactivity detector set to 2000K sensitivity. Peak associated with the radiolabeled commercial BODIPY dye is denoted with the symbol (♦).

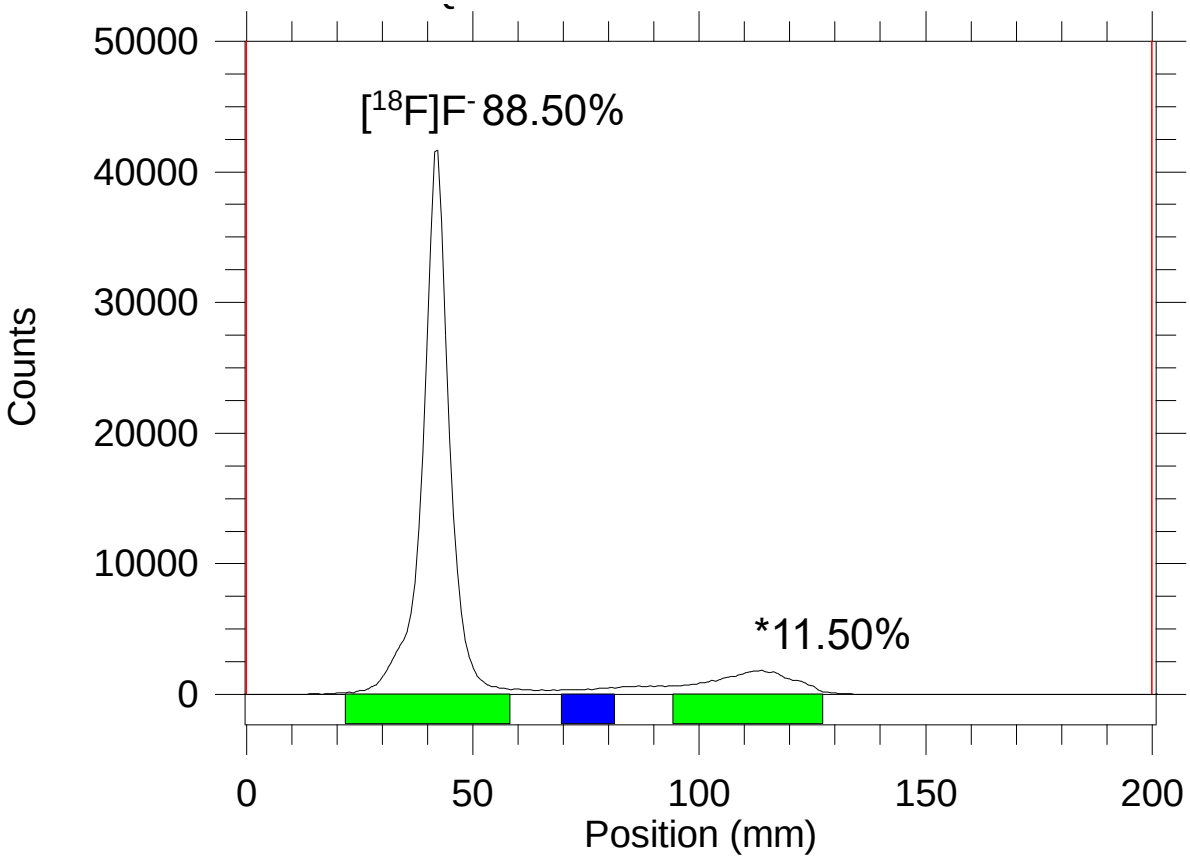

Figure A13. TLC chromatogram of [^{19}F/^{18}F]-isotopic exchange reaction mixture for commercial BODIPY standard when subject to 50 eq $Mg(NO_3)_2$, 37 °C, 55.8 eq TEAB fixing agent for 5 minutes. Chromatogram obtained using Bioscan AR-2000 radio-TLC plate reader. This data is associated with entry 3 of **Table 3.2**. The radioactivity peak associated with free [^{18}F]F$^-$ is labeled as such while the product peak is indicated by the symbol (*).

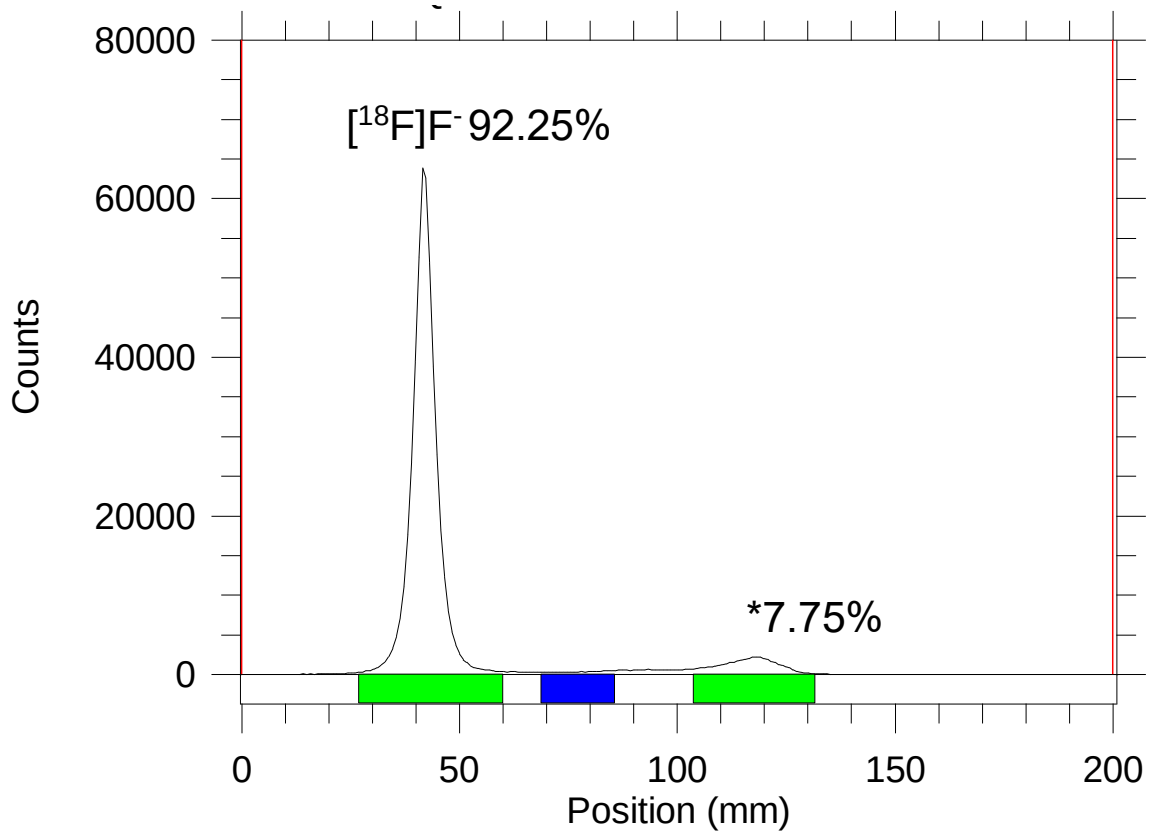

Figure A14. TLC chromatogram of [^{19}F/^{18}F]-isotopic exchange reaction mixture for commercial BODIPY standard when subject to 50 eq $Mg(NO_3)_2$, 37 °C, 55.8 eq TEAB fixing agent for 15 minutes. Chromatogram obtained using Bioscan AR-2000 radio-TLC plate reader. This data is associated with entry 3 of **Table 3.2**. The radioactivity peak associated with free [^{18}F]F$^-$ is labeled as such while the product peak is indicated by the symbol (*).

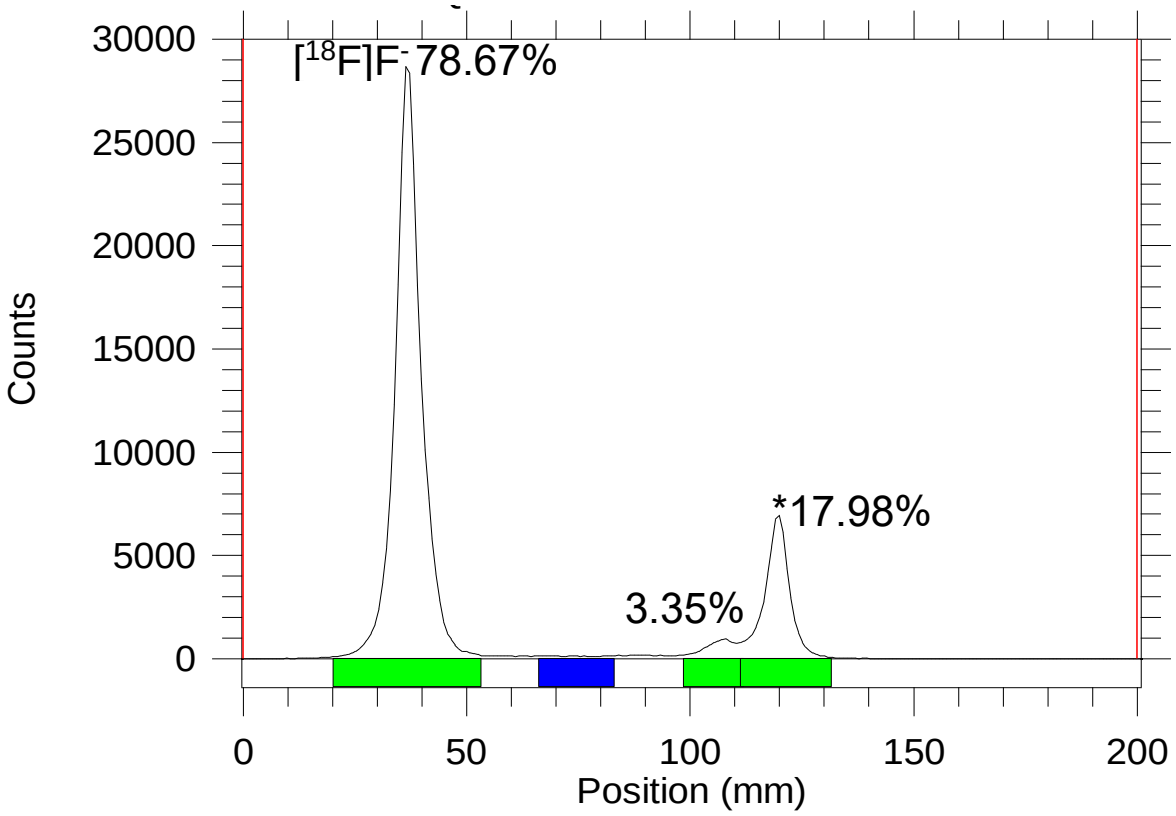

Figure A15. TLC chromatogram of [^{19}F/^{18}F]-isotopic exchange reaction mixture for commercial BODIPY standard when subject to 50 eq $Mg(NO_3)_2$, 37 °C, 55.8 eq TEAB fixing agent for 30 minutes. Chromatogram obtained using Bioscan AR-2000 radio-TLC plate reader. This data is associated with entry 3 of **Table 3.2**. The radioactivity peak associated with free [^{18}F]F$^-$ is labeled as such while the product peak is indicated by the symbol (*).

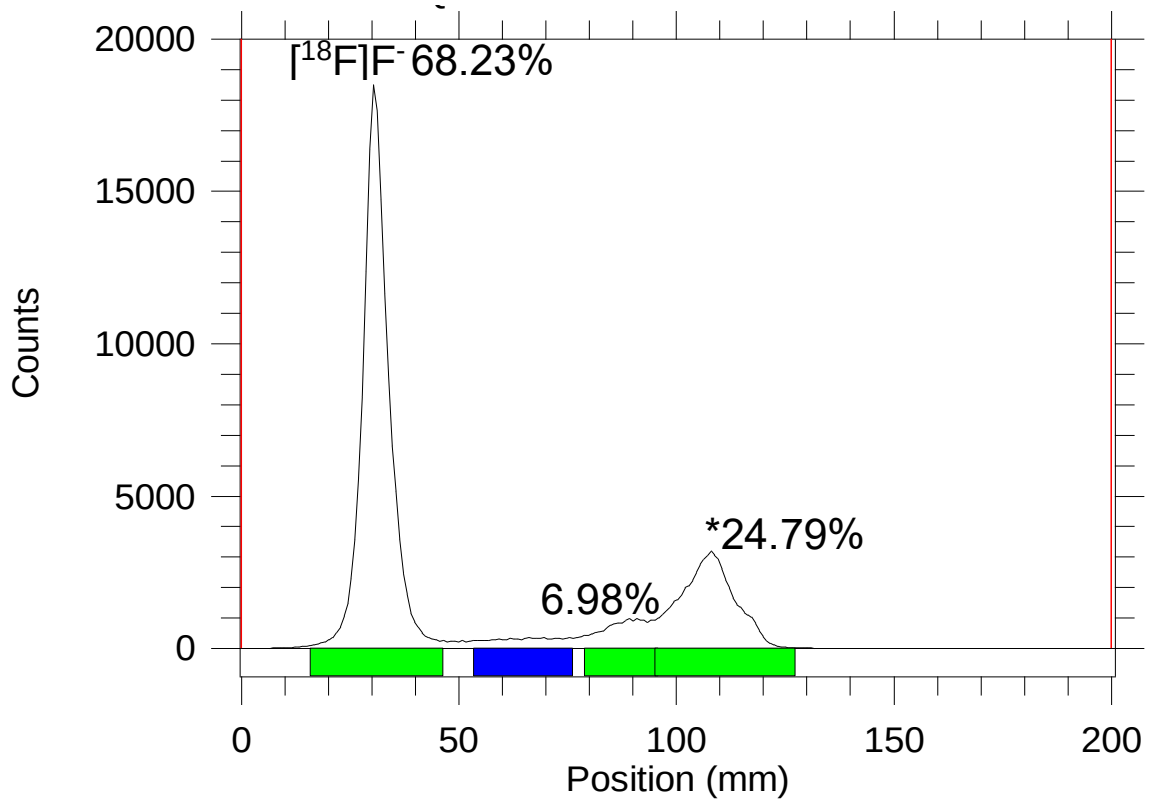

Figure A16. TLC chromatogram of [^{19}F/^{18}F]-isotopic exchange reaction mixture for commercial BODIPY standard when subject to 50 eq $Mg(NO_3)_2$, 37 °C, 55.8 eq TEAB fixing agent for 45 minutes. Chromatogram obtained using Bioscan AR-2000 radio-TLC plate reader. This data is associated with entry 3 of **Table 3.2**. The radioactivity peak associated with free [^{18}F]F$^-$ is labeled as such while the product peak is indicated by the symbol (*).

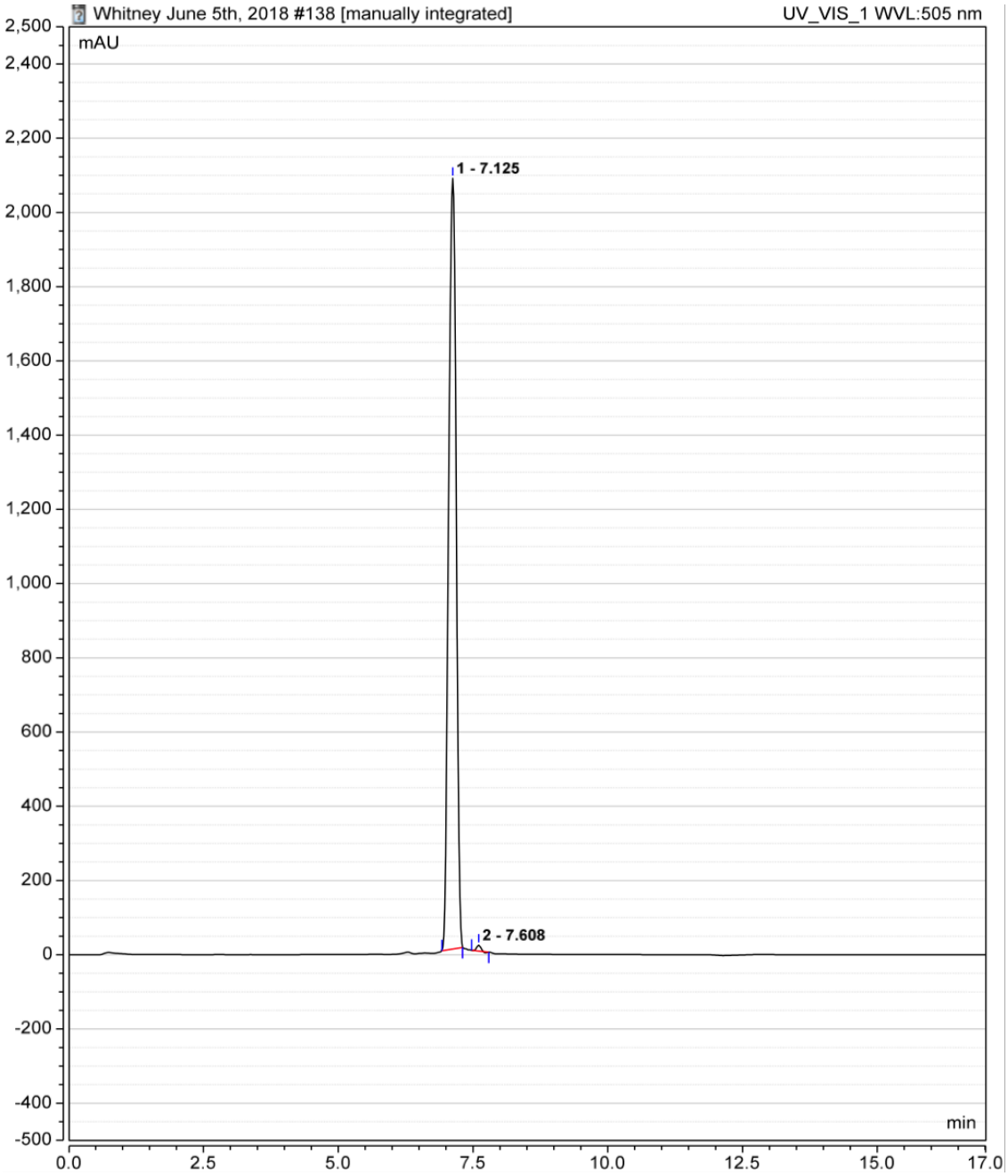

Figure A17. HPLC chromatogram of [^{19}F/^{18}F]-isotopic exchange reaction mixture for commercial BODIPY standard when subject to 50 eq $Mg(NO_3)_2$, 55.8 eq TEAB fixing agent at 37 °C for 30 minutes. Experimental conditions applied are outlined in entry 3 of **Table 3.2**. Chromatogram was obtained using a Thermo Fisher Vanquish UHPLC system equipped with a UV-Vis detector set to measure at 505 nm. Peak 1 (7.125 min) is associated with the commercial BODIPY dye.

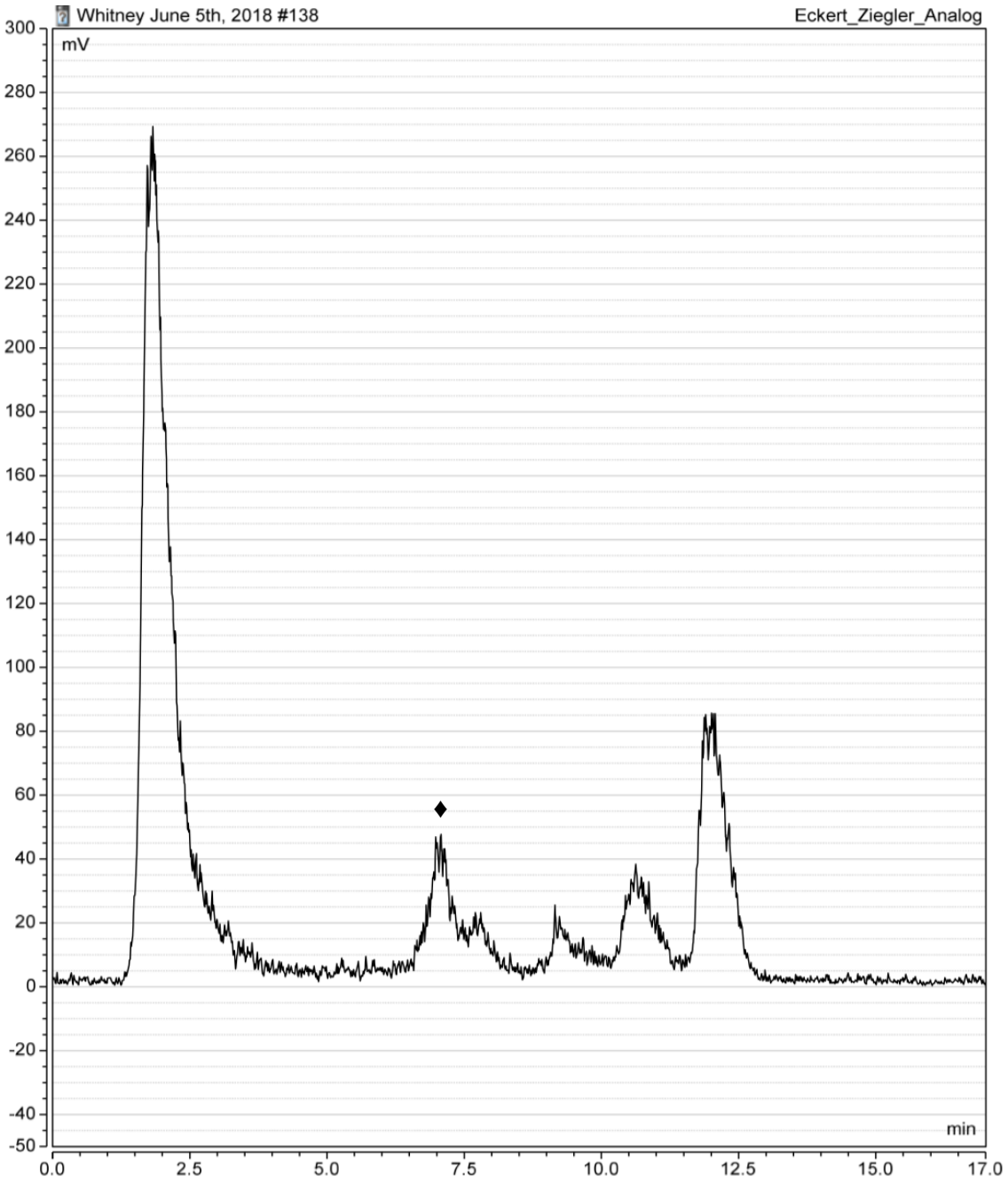

Figure A18. HPLC chromatogram of [^{19}F/^{18}F]-isotopic exchange reaction mixture for commercial BODIPY standard when subject to 50 eq $Mg(NO_3)_2$, 55.8 eq TEAB fixing agent at 37 °C for 30 minutes. Experimental conditions applied are outlined in entry 3 of **Table 3.2**. Chromatogram was obtained using a Thermo Fisher Vanquish UHPLC system equipped with a radioactivity detector set to 2000K sensitivity. Peak associated with the radiolabeled commercial BODIPY dye is denoted with the symbol (♦).

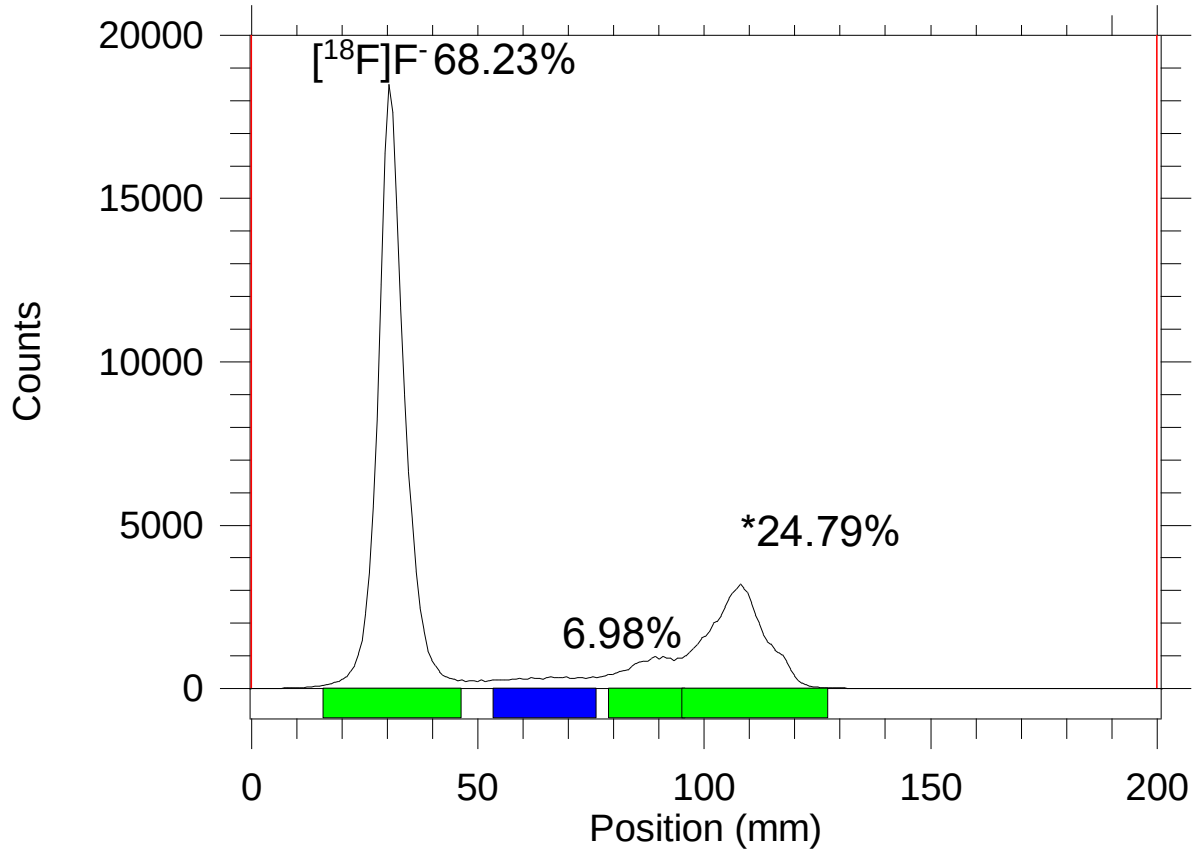

Figure A19. TLC chromatogram of [^{19}F/^{18}F]-isotopic exchange reaction mixture for commercial BODIPY standard when subject to 100 eq $Mg(NO_3)_2$, 37 °C, 55.8 eq TEAB fixing agent for 5 minutes. Chromatogram obtained using Bioscan AR-2000 radio-TLC plate reader. This data is associated with entry 4 of **Table 3.2**. The radioactivity peak associated with free [^{18}F]F$^-$ is labeled as such while the product peak is indicated by the symbol (*).

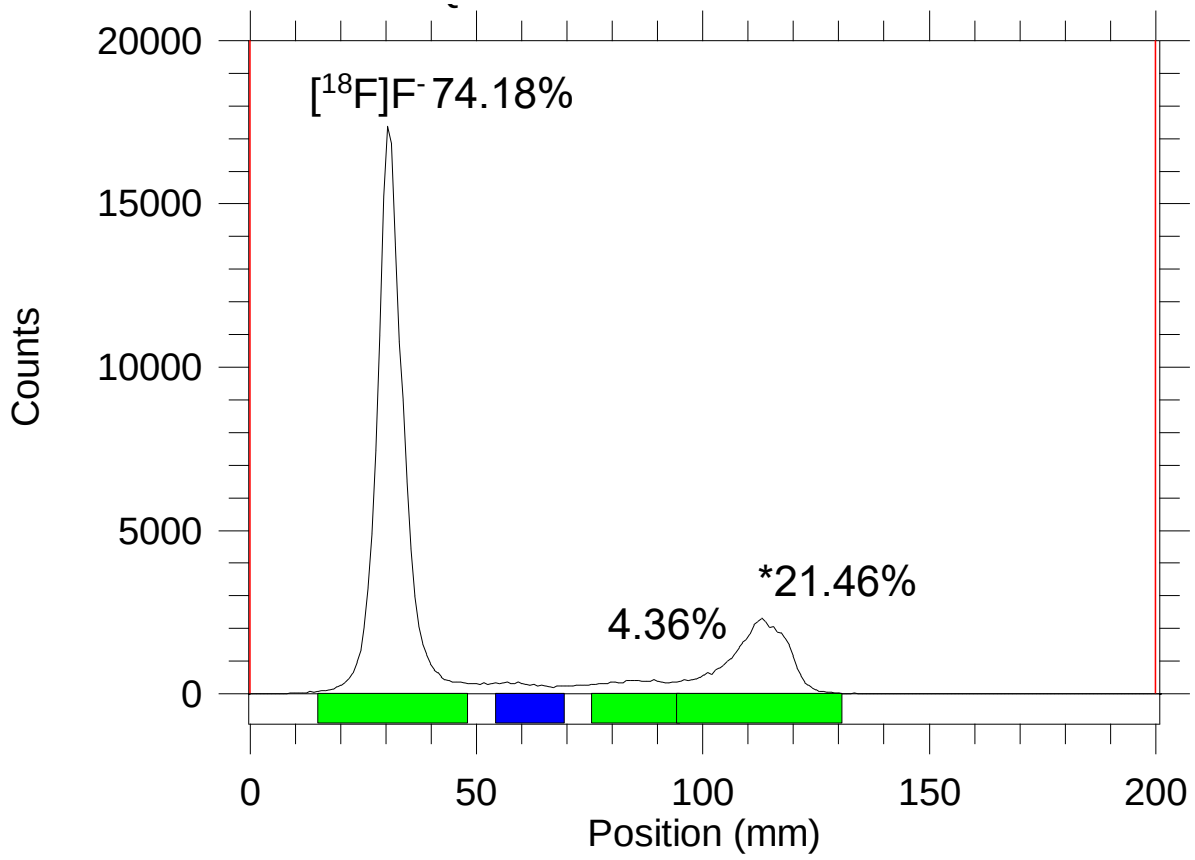

Figure A20. TLC chromatogram of [^{19}F/^{18}F]-isotopic exchange reaction mixture for commercial BODIPY standard when subject to 100 eq $Mg(NO_3)_2$, 37 °C, 55.8 eq TEAB fixing agent for 15 minutes. Chromatogram obtained using Bioscan AR-2000 radio-TLC plate reader. This data is associated with entry 4 of **Table 3.2**. The radioactivity peak associated with free [^{18}F]F$^-$ is labeled as such while the product peak is indicated by the symbol (*).

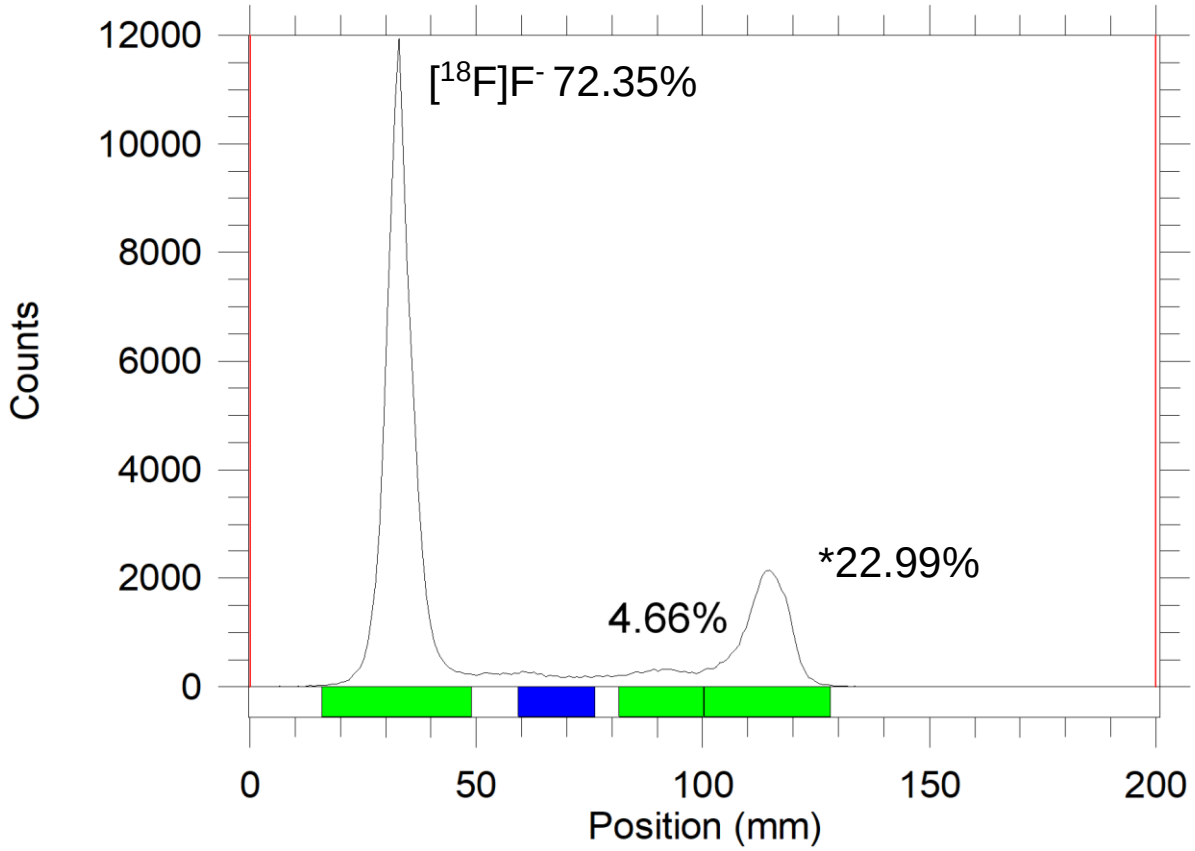

Figure A21. TLC chromatogram of [^{19}F/^{18}F]-isotopic exchange reaction mixture for commercial BODIPY standard when subject to 100 eq $Mg(NO_3)_2$, 37 °C, 55.8 eq TEAB fixing agent for 30 minutes. Chromatogram obtained using Bioscan AR-2000 radio-TLC plate reader. This data is associated with entry 4 of **Table 3.2**. The radioactivity peak associated with free [^{18}F]F$^-$ is labeled as such while the product peak is indicated by the symbol (*).

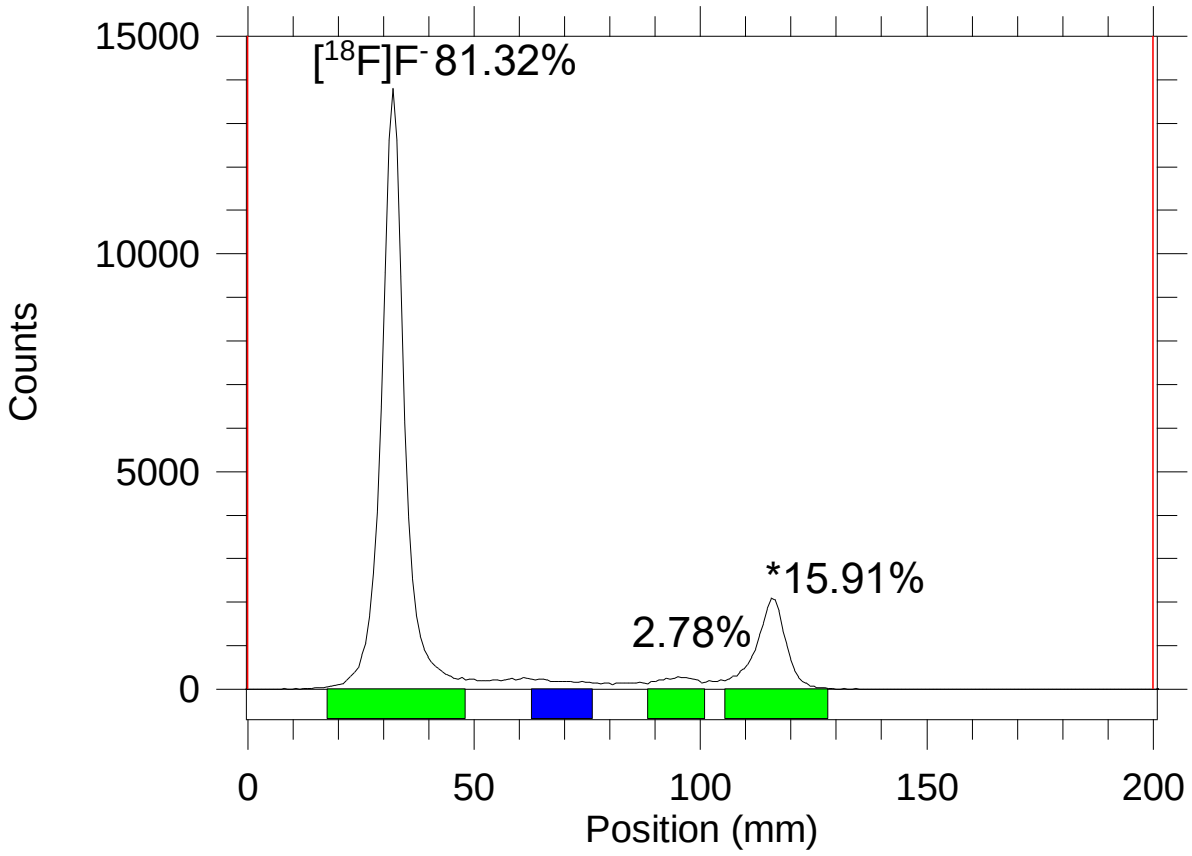

Figure A22. TLC chromatogram of [^{19}F/^{18}F]-isotopic exchange reaction mixture for commercial BODIPY standard when subject to 100 eq $Mg(NO_3)_2$, 37 °C, 55.8 eq TEAB fixing agent for 45 minutes. Chromatogram obtained using Bioscan AR-2000 radio-TLC plate reader. This data is associated with entry 4 of **Table 3.2**. The radioactivity peak associated with free [^{18}F]F$^-$ is labeled as such while the product peak is indicated by the symbol (*).

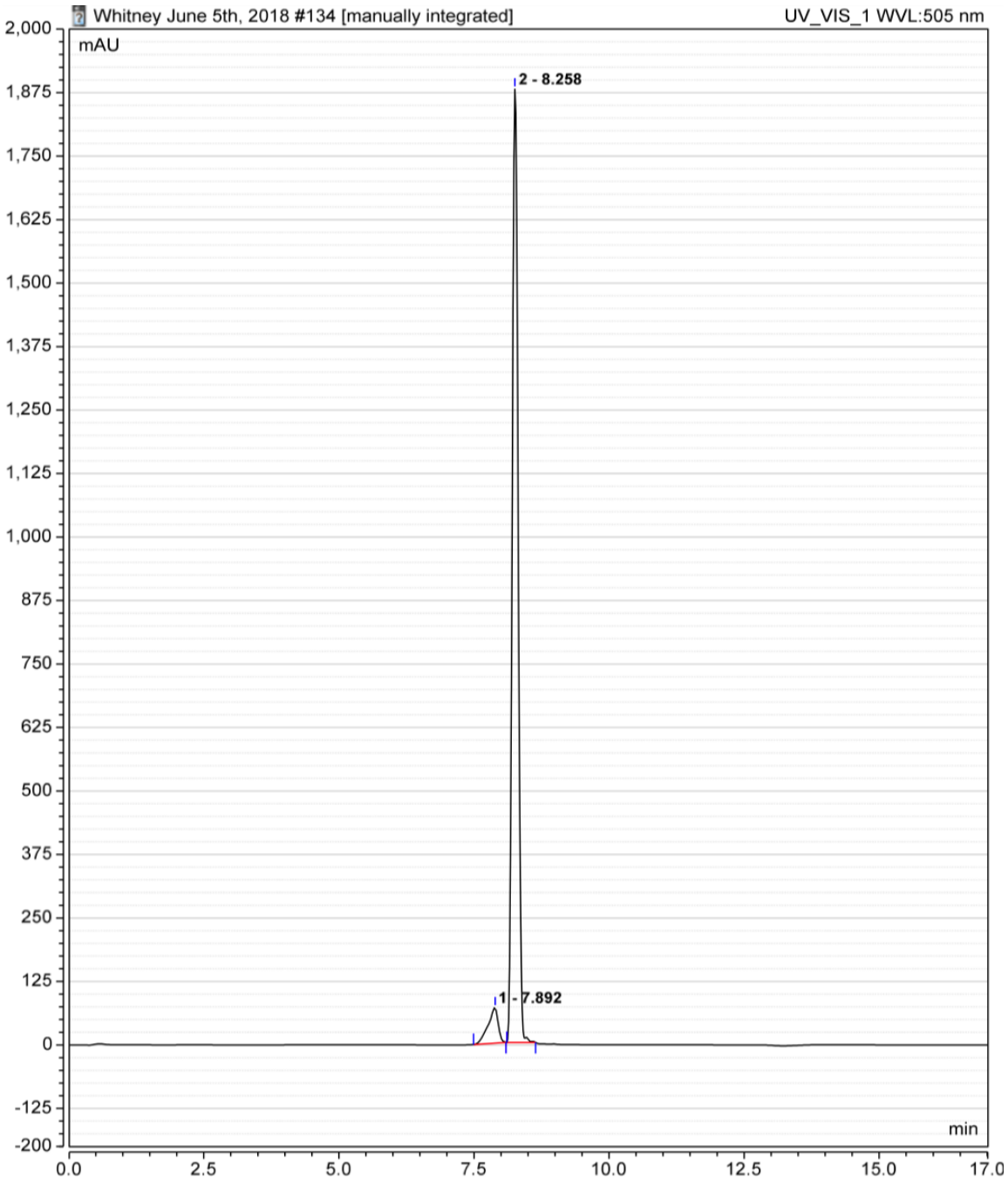

Figure A23. HPLC chromatogram of [^{19}F/^{18}F]-isotopic exchange reaction mixture for commercial BODIPY standard when subject to 100 eq $Mg(NO_3)_2$, 55.8 eq TEAB fixing agent at 37 °C for 5 minutes. Experimental conditions applied are outlined in entry 4 of **Table 3.2**. Chromatogram was obtained using a Thermo Fisher Vanquish UHPLC system equipped with a UV-Vis detector set to measure at 505 nm. Peak 2 (8.258 min) is associated with the commercial BODIPY dye.

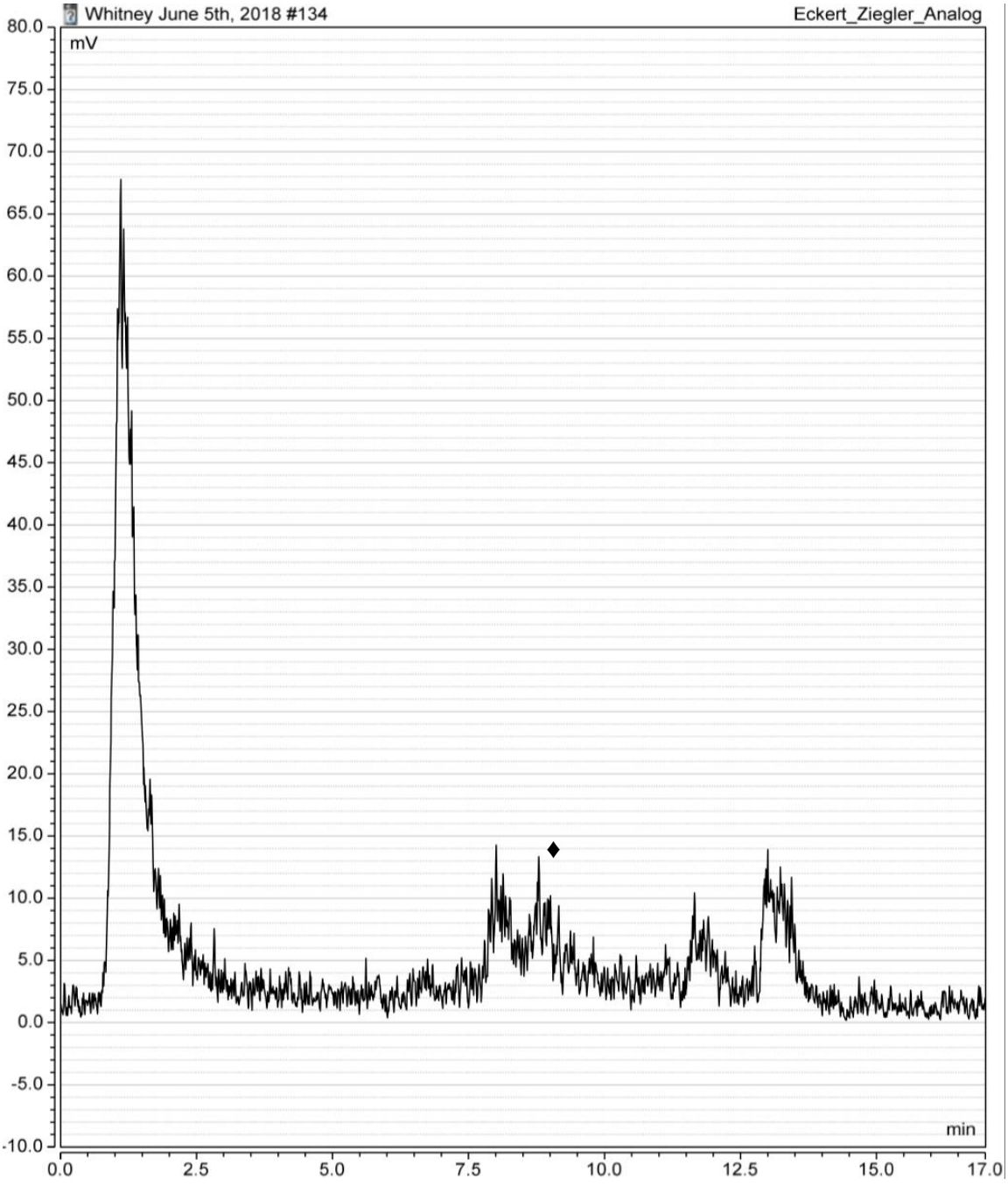

Figure A24. HPLC chromatogram of [^{19}F/^{18}F]-isotopic exchange reaction mixture for commercial BODIPY standard when subject to 100 eq $Mg(NO_3)_2$, 55.8 eq TEAB fixing agent at 37 °C for 5 minutes. Experimental conditions applied are outlined in entry 4 of **Table 3.2**. Chromatogram was obtained using a Thermo Fisher Vanquish UHPLC system equipped with a radioactivity detector set to 2000K sensitivity. Peak associated with the radiolabeled commercial BODIPY dye is denoted with the symbol (♦).

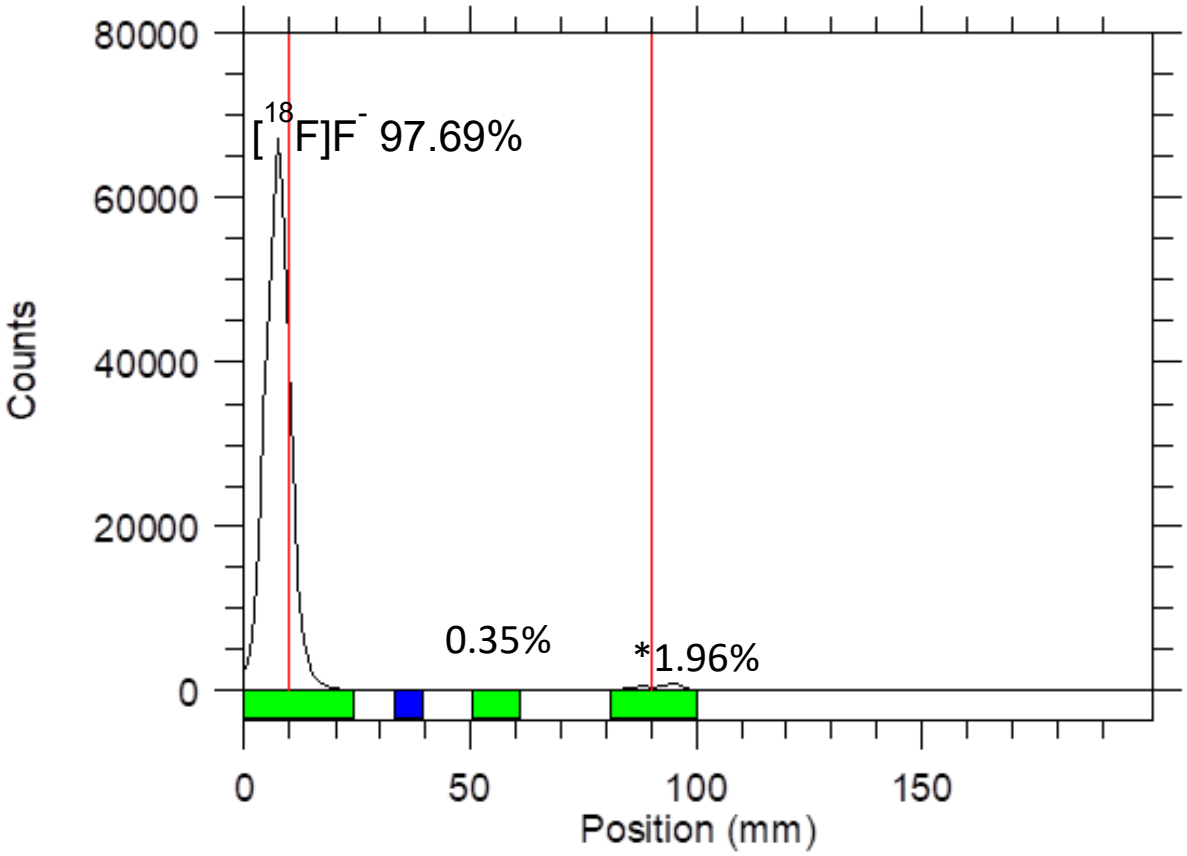

Figure A25. TLC chromatogram of [^{19}F/^{18}F]-isotopic exchange reaction mixture for commercial BODIPY standard when subject to 150 eq $Mg(NO_3)_2$, 37 °C, 55.8 eq TEAB fixing agent for 5 minutes. Chromatogram obtained using Bioscan AR-2000 radio-TLC plate reader. This data is associated with entry 5 of **Table 3.2**. The radioactivity peak associated with free [^{18}F]F$^-$ is labeled as such while the product peak is indicated by the symbol (*).

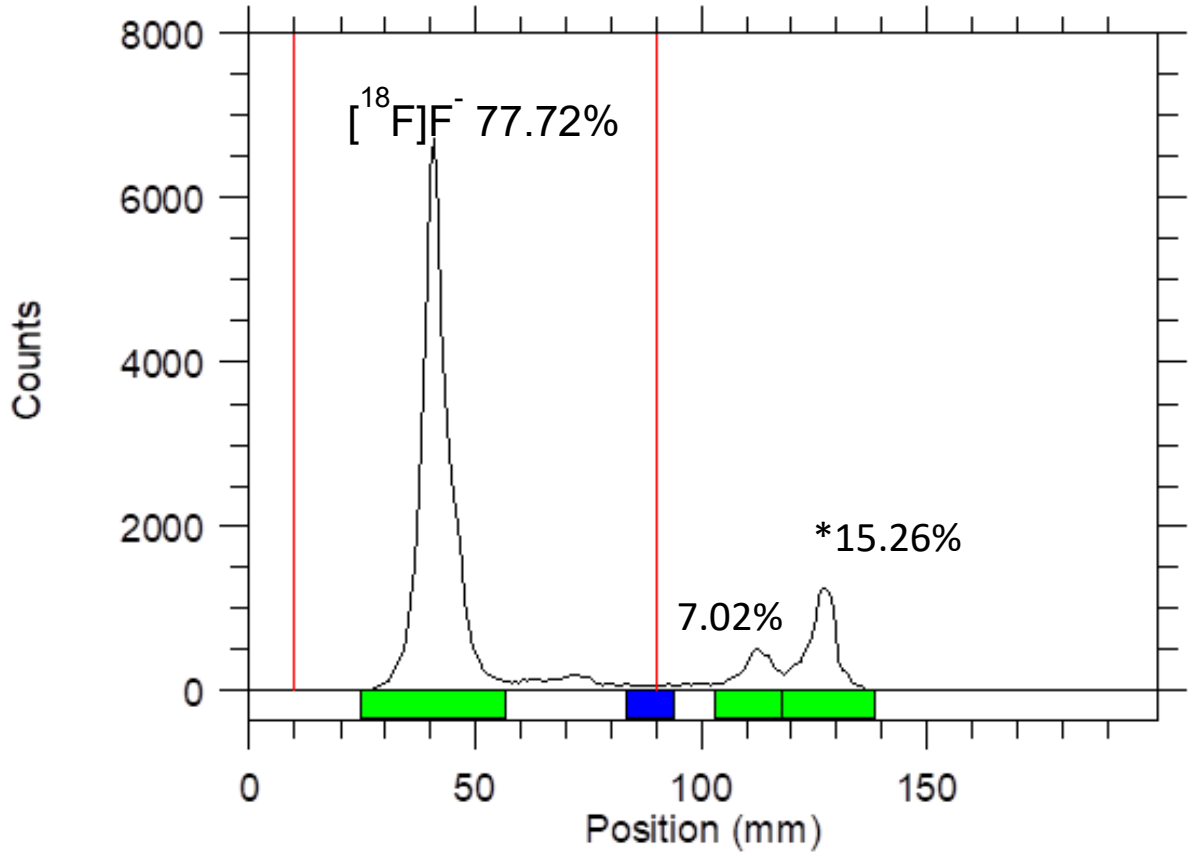

Figure A26. TLC chromatogram of [^{19}F/^{18}F]-isotopic exchange reaction mixture for commercial BODIPY standard when subject to 150 eq $Mg(NO_3)_2$, 37 °C, 55.8 eq TEAB fixing agent for15 minutes. Chromatogram obtained using Bioscan AR-2000 radio-TLC plate reader. This data is associated with entry 5 of **Table 3.2**. The radioactivity peak associated with free [^{18}F]F$^-$ is labeled as such while the product peak is indicated by the symbol (*).

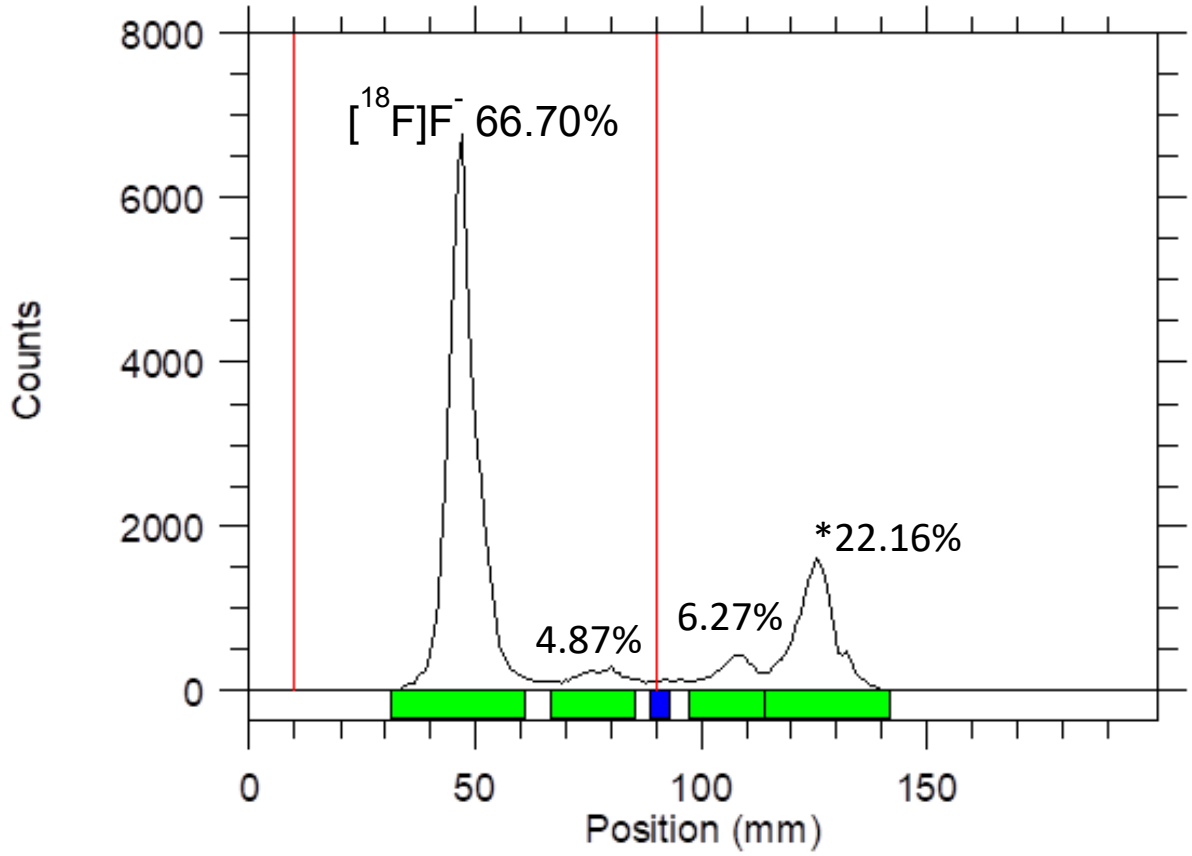

Figure A27. TLC chromatogram of [^{19}F/^{18}F]-isotopic exchange reaction mixture for commercial BODIPY standard when subject to 150 eq $Mg(NO_3)_2$, 37 °C, 55.8 eq TEAB fixing agent for 30 minutes. Chromatogram obtained using Bioscan AR-2000 radio-TLC plate reader. This data is associated with entry 5 of **Table 3.2**. The radioactivity peak associated with free [^{18}F]F$^-$ is labeled as such while the product peak is indicated by the symbol (*).

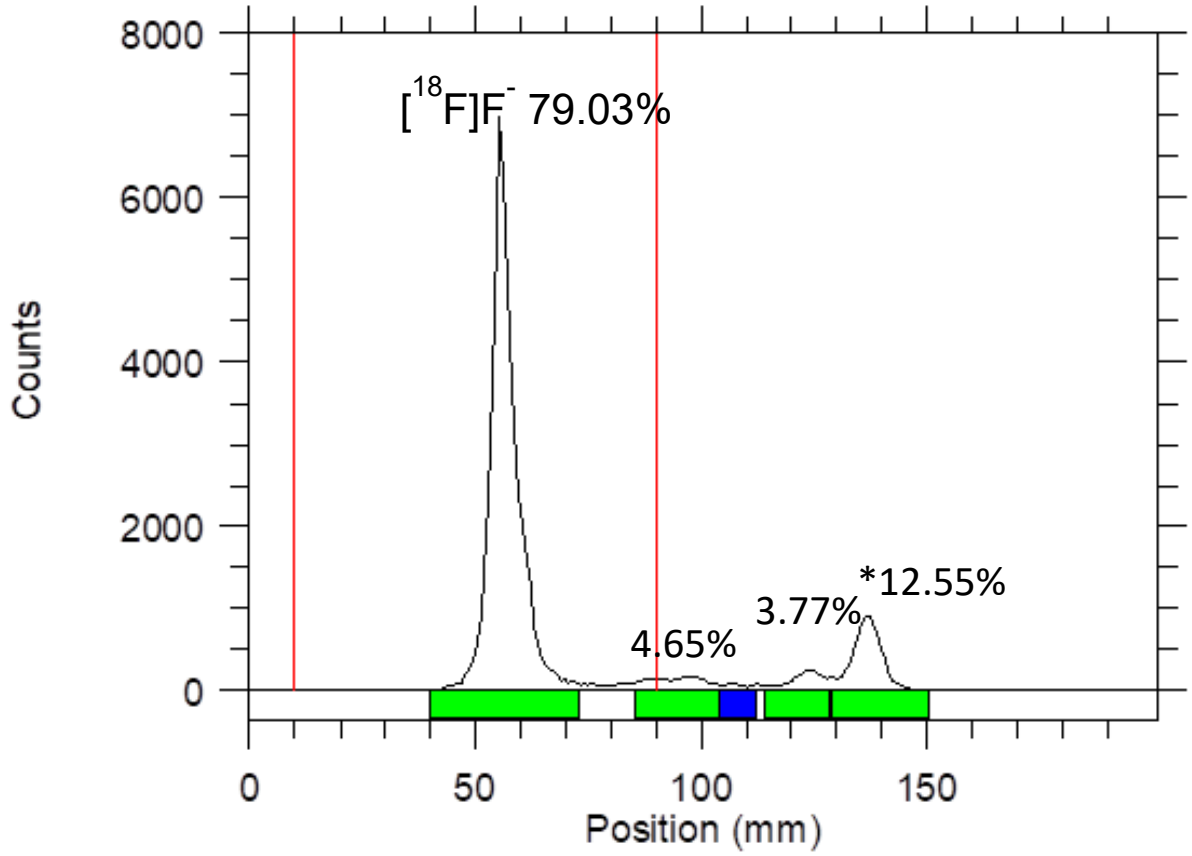

Figure A28. TLC chromatogram of [^{19}F/^{18}F]-isotopic exchange reaction mixture for commercial BODIPY standard when subject to 150 eq $Mg(NO_3)_2$, 37 °C, 55.8 eq TEAB fixing agent for 45 minutes. Chromatogram obtained using Bioscan AR-2000 radio-TLC plate reader. This data is associated with entry 5 of **Table 3.2**. The radioactivity peak associated with free [^{18}F]F$^-$ is labeled as such while the product peak is indicated by the symbol (*).

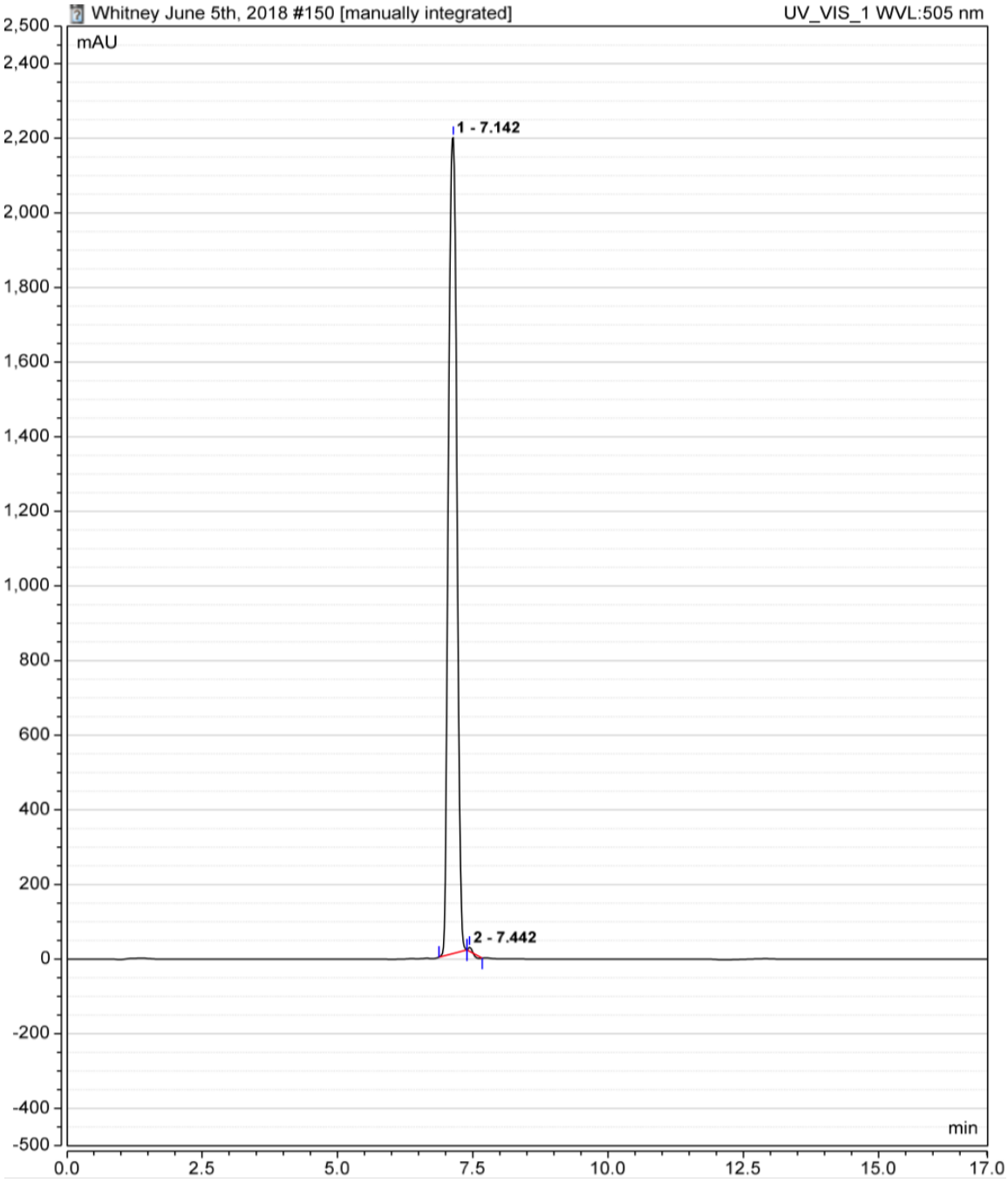

Figure A29. HPLC chromatogram of [^{19}F/^{18}F]-isotopic exchange reaction mixture for commercial BODIPY standard when subject to 150 eq $Mg(NO_3)_2$, 55.8 eq TEAB fixing agent at 37 °C for 5 minutes. Experimental conditions applied are outlined in entry 5 of **Table 3.2**. Chromatogram was obtained using a Thermo Fisher Vanquish UHPLC system equipped with a UV-Vis detector set to measure at 505 nm. Peak 1 (7.142 min) is associated with the commercial BODIPY dye.

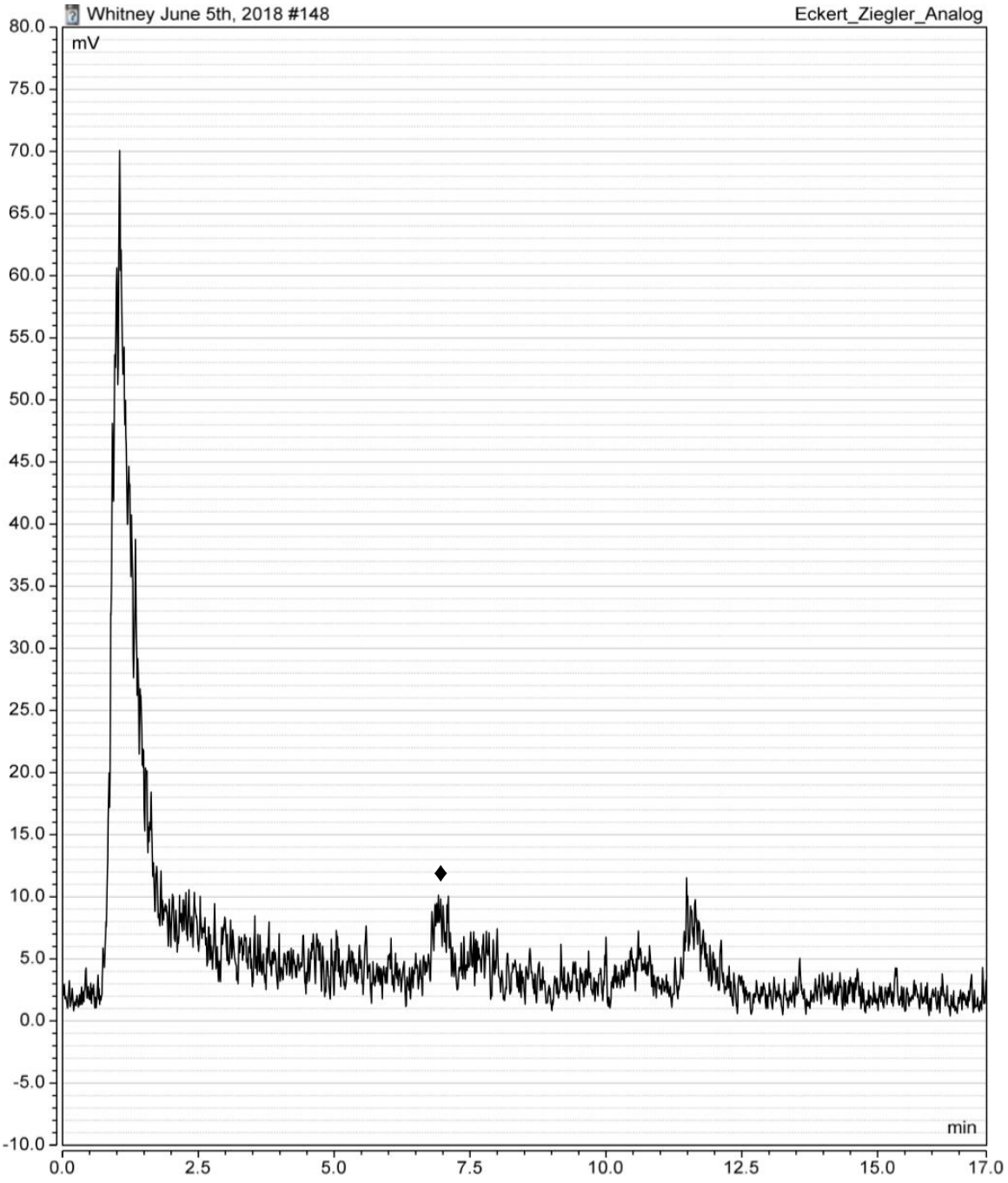

Figure A30. HPLC chromatogram of [^{19}F/^{18}F]-isotopic exchange reaction mixture for commercial BODIPY standard when subject to 150 eq $Mg(NO_3)_2$, 55.8 eq TEAB fixing agent at 37 °C for 5 minutes. Experimental conditions applied are outlined in entry 5 of **Table 3.2**. Chromatogram was obtained using a Thermo Fisher Vanquish UHPLC system equipped with a radioactivity detector set to 2000K sensitivity. Peak associated with the radiolabeled commercial BODIPY dye is denoted with the symbol (♦).

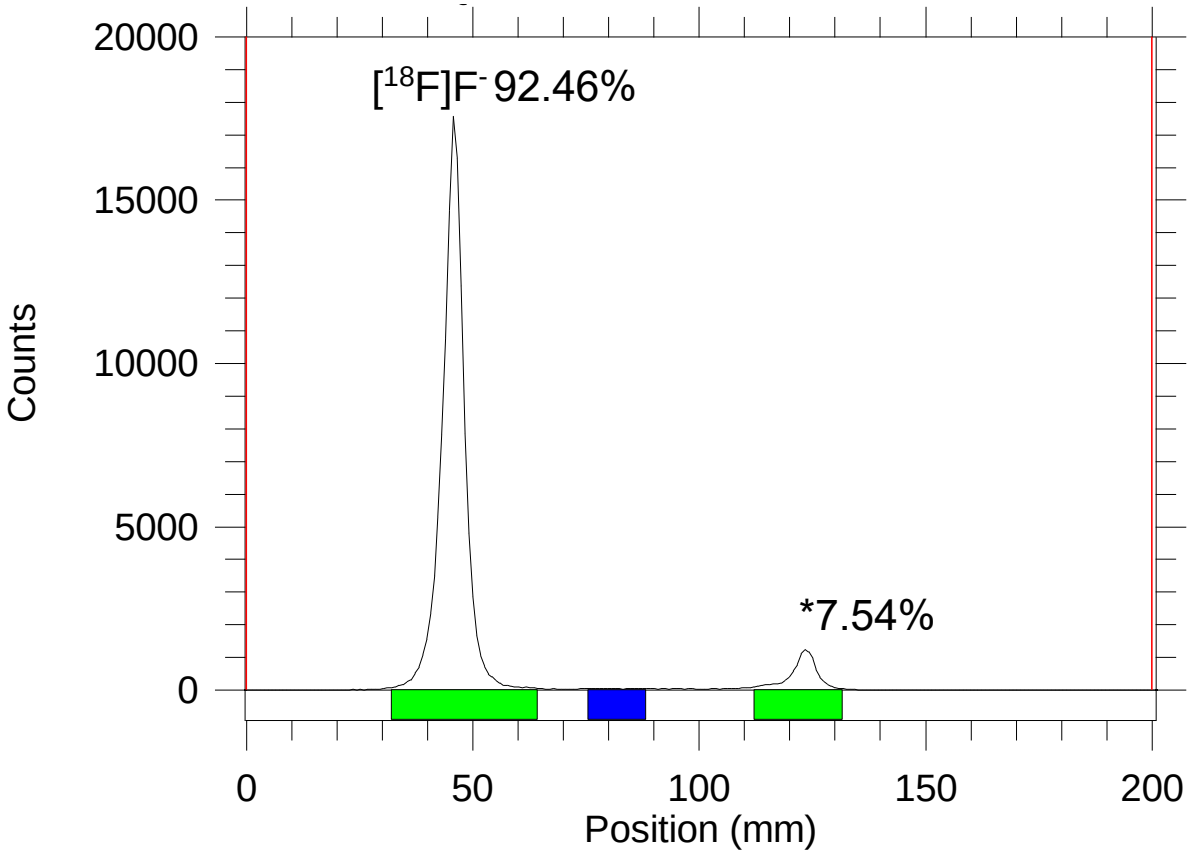

Figure A31. TLC chromatogram of [^{19}F/^{18}F]-isotopic exchange reaction mixture for commercial BODIPY standard when subject to 100 eq $Mg(NO_3)_2$, 37 °C, 27.9 eq TEAB fixing agent for 5 minutes. Chromatogram obtained using Bioscan AR-2000 radio-TLC plate reader. This data is associated with entry 6 of **Table 3.2**. The radioactivity peak associated with free [^{18}F]F$^-$ is labeled as such while the product peak is indicated by the symbol (*).

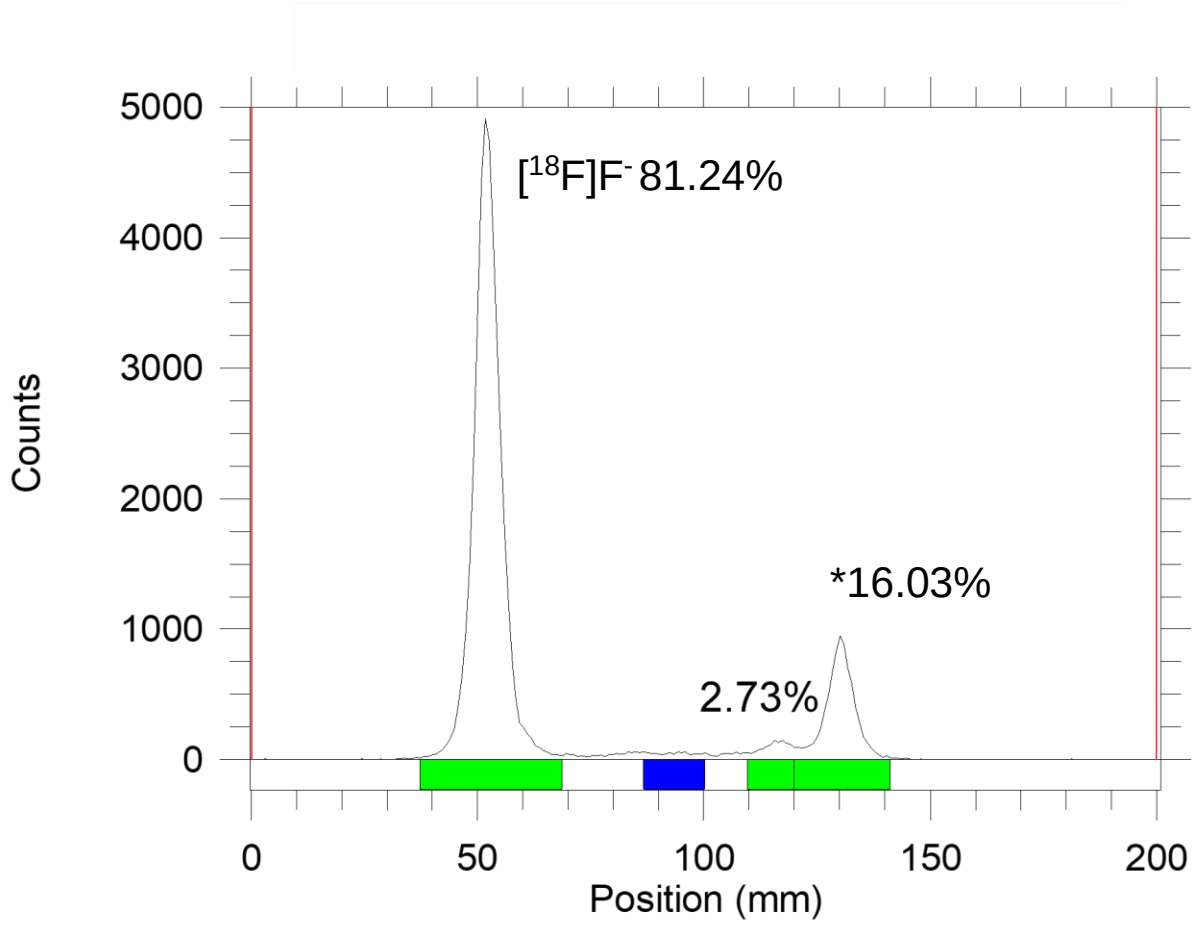

Figure A32. TLC chromatogram of [^{19}F/^{18}F]-isotopic exchange reaction mixture for commercial BODIPY standard when subject to 100 eq $Mg(NO_3)_2$, 37 °C, 27.9 eq TEAB fixing agent for 15 minutes. Chromatogram obtained using Bioscan AR-2000 radio-TLC plate reader. This data is associated with entry 6 of **Table 3.2**. The radioactivity peak associated with free [^{18}F]F$^-$ is labeled as such while the product peak is indicated by the symbol (*).

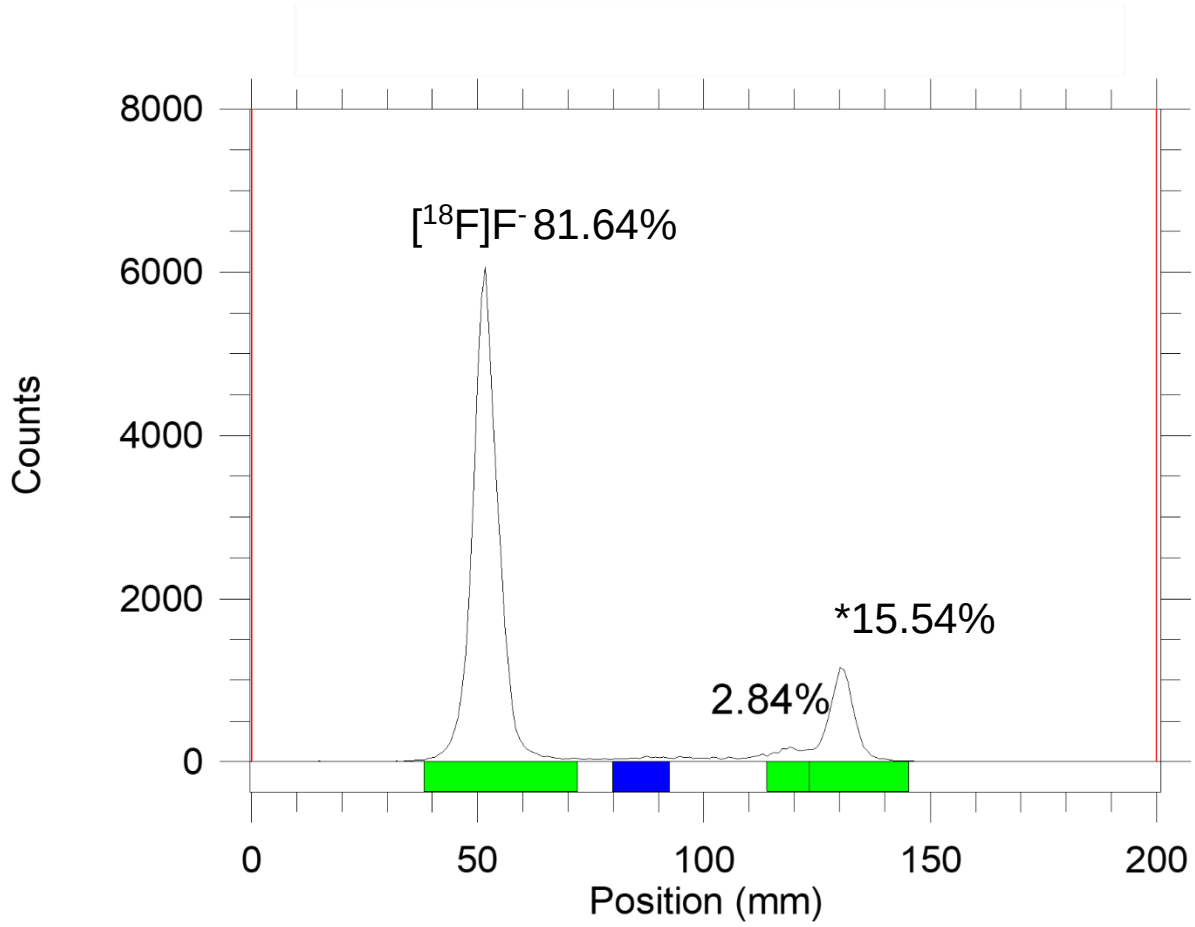

Figure A33. TLC chromatogram of [^{19}F/^{18}F]-isotopic exchange reaction mixture for commercial BODIPY standard when subject to 100 eq $Mg(NO_3)_2$, 37 °C, 27.9 eq TEAB fixing agent for 30 minutes. Chromatogram obtained using Bioscan AR-2000 radio-TLC plate reader. This data is associated with entry 6 of **Table 3.2**. The radioactivity peak associated with free [^{18}F]F$^-$ is labeled as such while the product peak is indicated by the symbol (*).

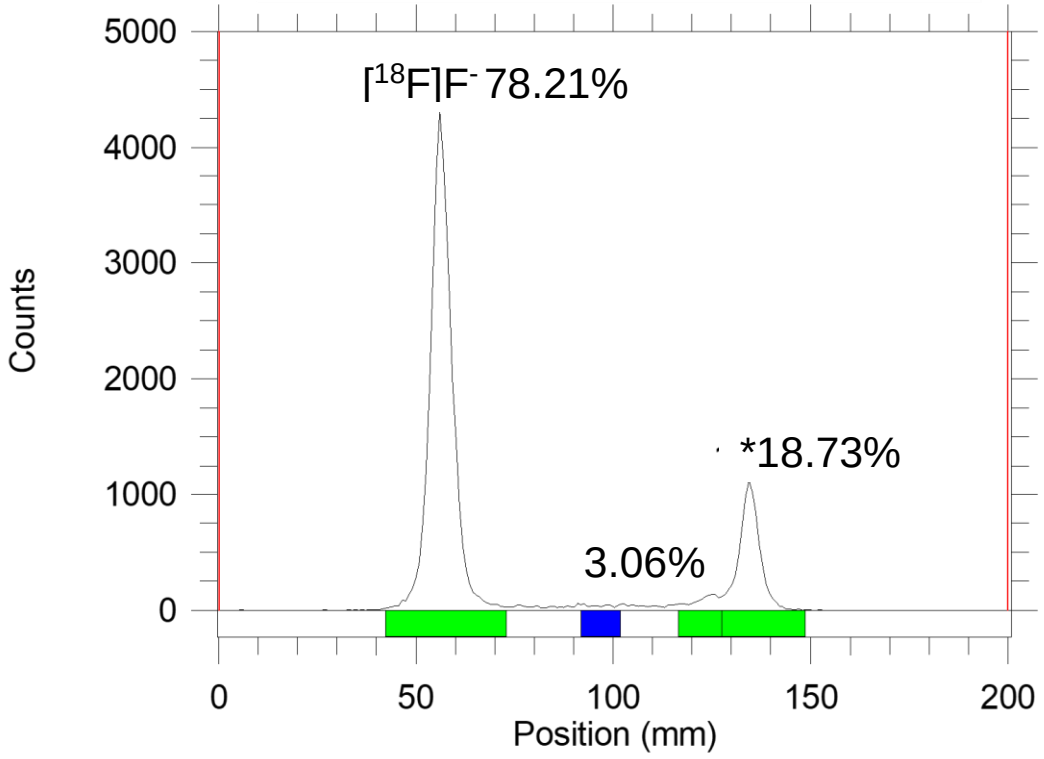

Figure A34. TLC chromatogram of [^{19}F/^{18}F]-isotopic exchange reaction mixture for commercial BODIPY standard when subject to 100 eq $Mg(NO_3)_2$, 37 °C, 27.9 eq TEAB fixing agent for 45 minutes. Chromatogram obtained using Bioscan AR-2000 radio-TLC plate reader. This data is associated with entry 6 of **Table 3.2**. The radioactivity peak associated with free [^{18}F]F$^-$ is labeled as such while the product peak is indicated by the symbol (*).

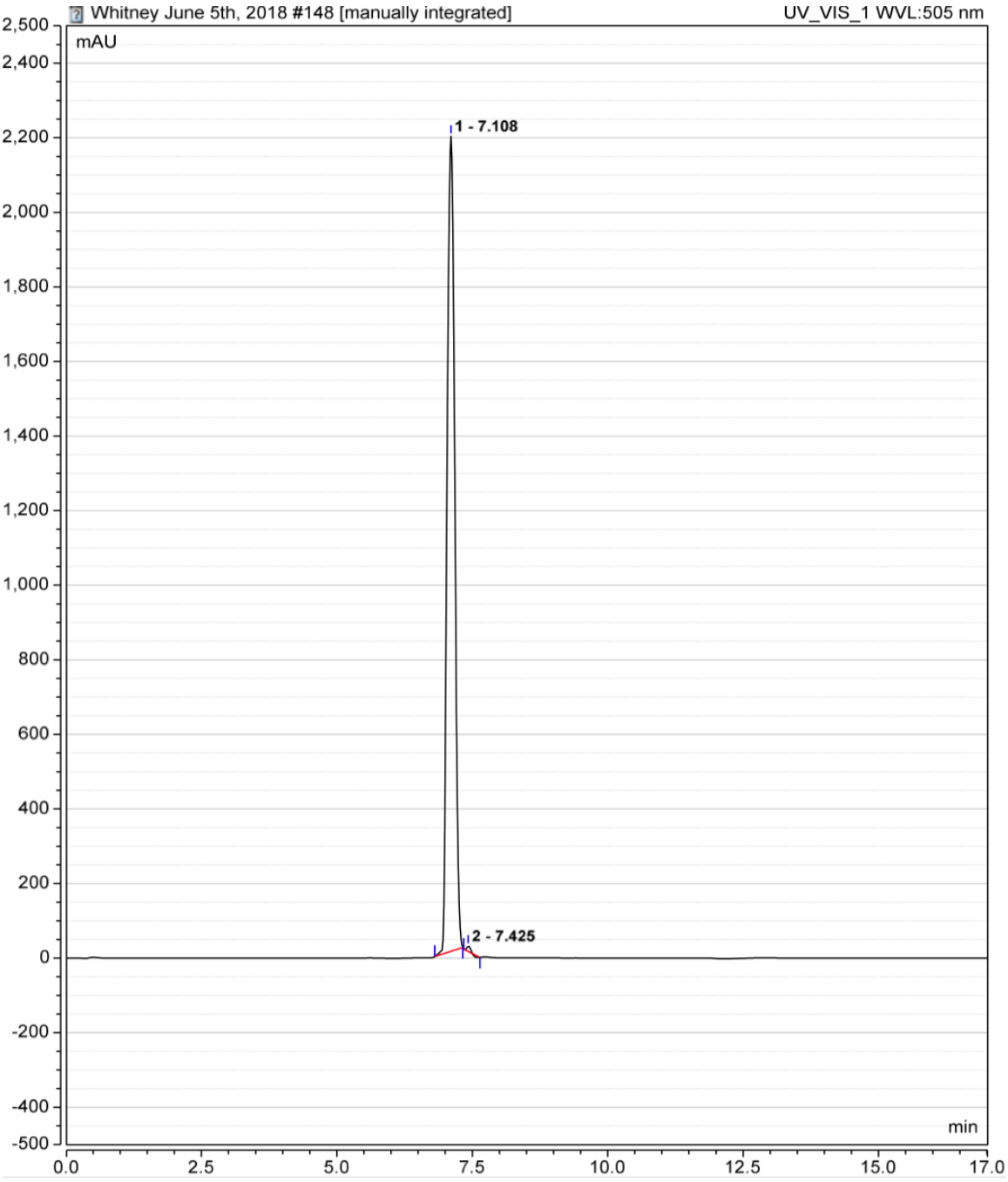

Figure A35. HPLC chromatogram of [^{19}F/^{18}F]-isotopic exchange reaction mixture for commercial BODIPY standard when subject to 100 eq $Mg(NO_3)_2$, 27.8 eq TEAB fixing agent at 37 °C for 5 minutes. Experimental conditions applied are outlined in entry 6 of **Table 3.2**. Chromatogram was obtained using a Thermo Fisher Vanquish UHPLC system equipped with a UV-Vis detector set to measure at 505 nm. Peak 1 (7.108 min) is associated with the commercial BODIPY dye.

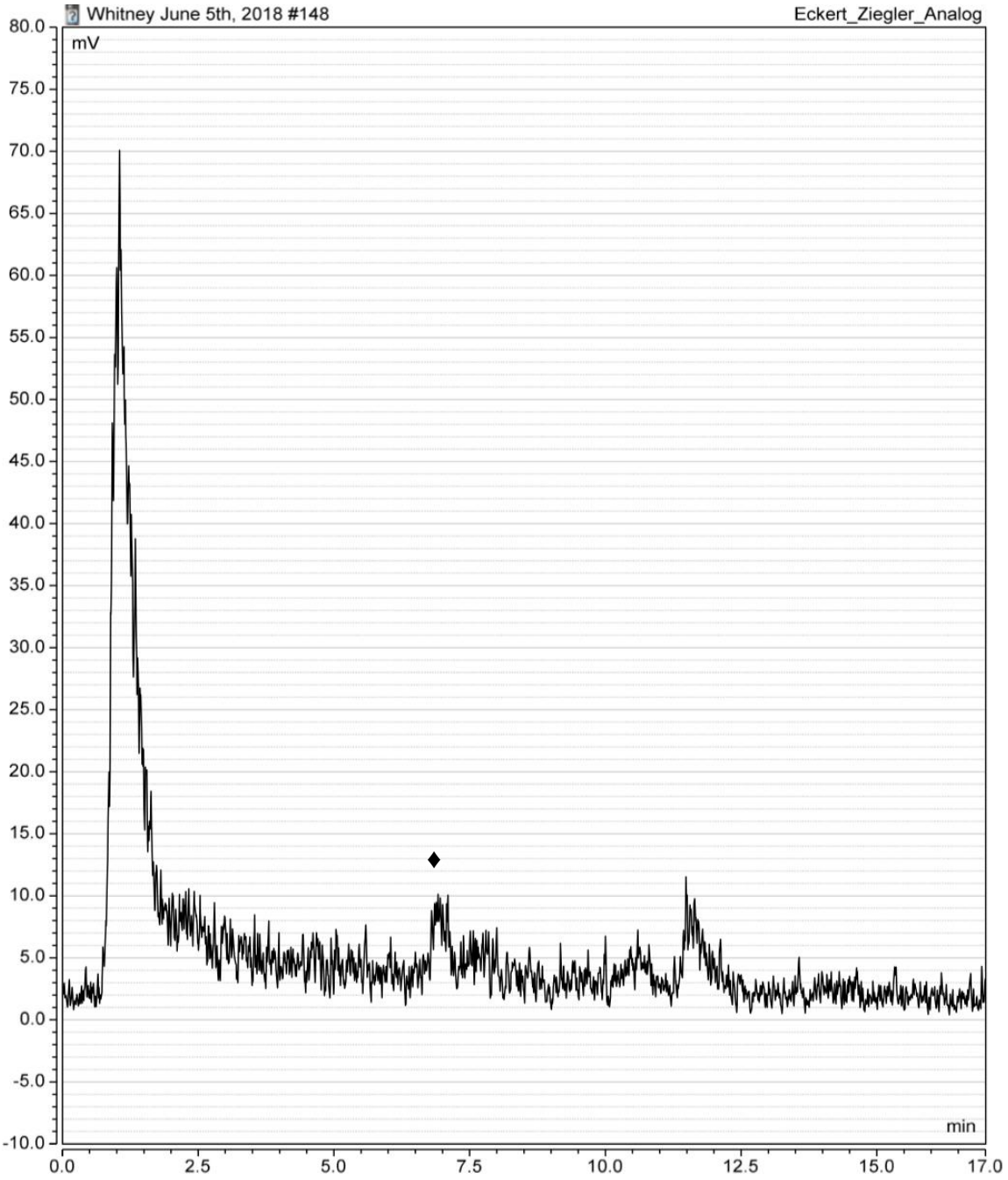

Figure A36. HPLC chromatogram of [^{19}F/^{18}F]-isotopic exchange reaction mixture for commercial BODIPY standard when subject to 100 eq $Mg(NO_3)_2$, 27.8 eq TEAB fixing agent at 37 °C for 5 minutes. Experimental conditions applied are outlined in entry 6 of **Table 3.2**. Chromatogram was obtained using a Thermo Fisher Vanquish UHPLC system equipped with a radioactivity detector set to 2000K sensitivity. Peak associated with the radiolabeled commercial BODIPY dye is denoted with the symbol (♦).

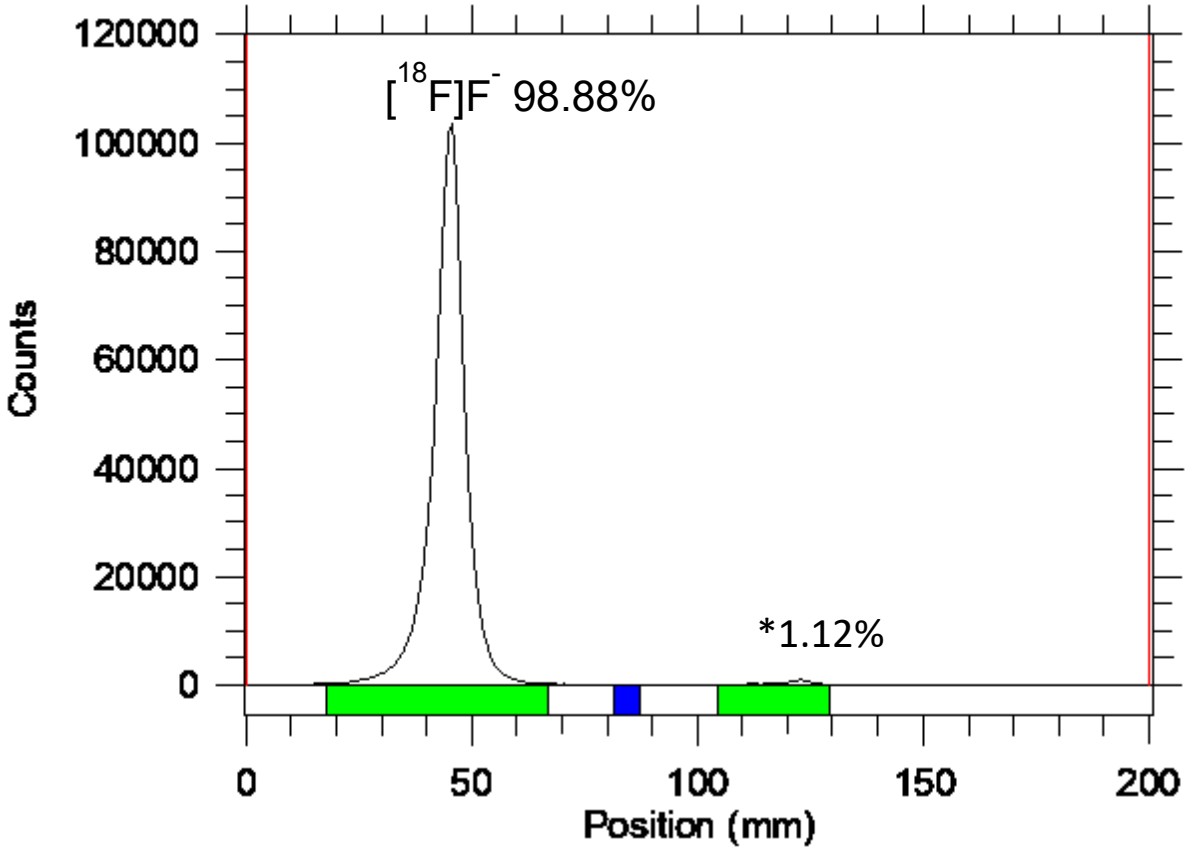

Figure A37. TLC chromatogram of [^{19}F/^{18}F]-isotopic exchange reaction mixture for commercial BODIPY standard when subject to 100 eq $Mg(NO_3)_2$, 75.0 eq TEAB fixing agent for 5 minutes. Chromatogram obtained using Bioscan AR-2000 radio-TLC plate reader. This data is associated with entry 7 of **Table 3.2**. The radioactivity peak associated with free [^{18}F]F$^-$ is labeled as such while the product peak is indicated by the symbol (*).

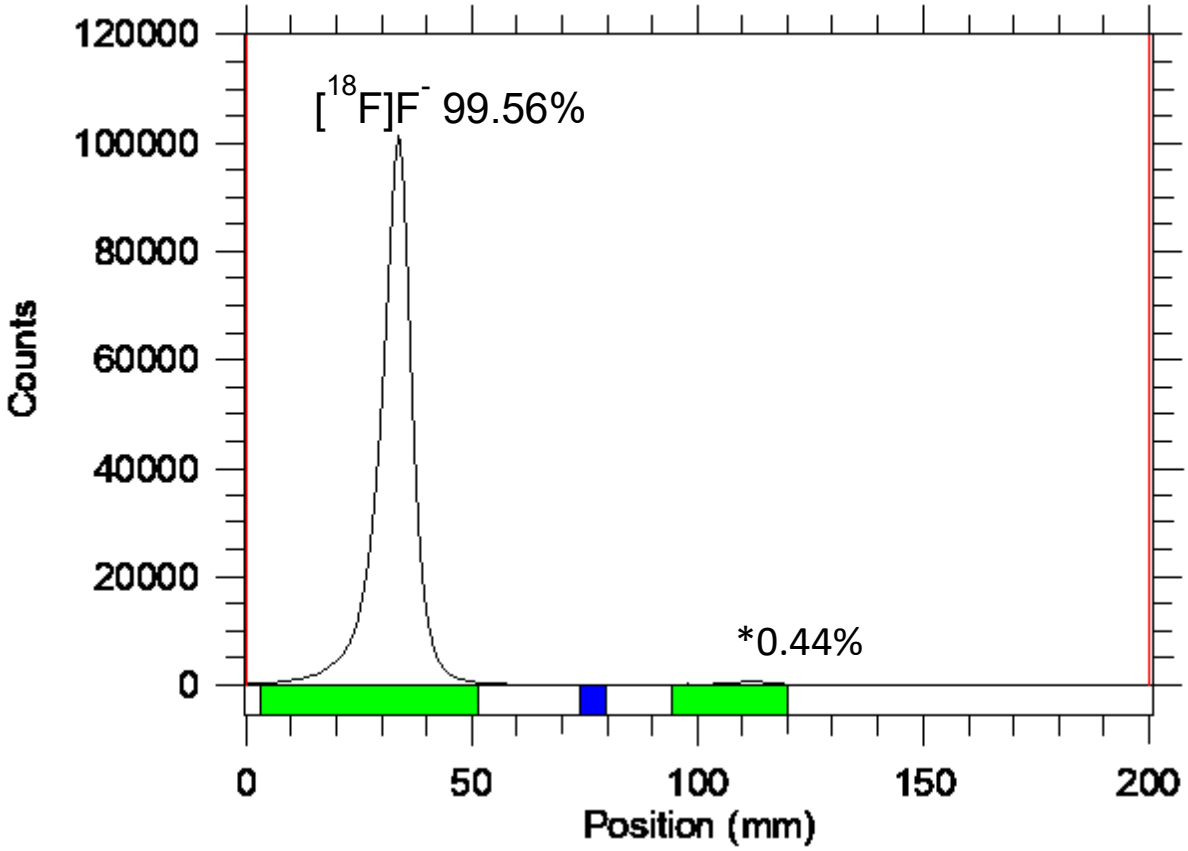

Figure A38. TLC chromatogram of [^{19}F/^{18}F]-isotopic exchange reaction mixture for commercial BODIPY standard when subject to 100 eq $Mg(NO_3)_2$, 75.0 eq TEAB fixing agent for 15 minutes. Chromatogram obtained using Bioscan AR-2000 radio-TLC plate reader. This data is associated with entry 7 of **Table 3.2**. The radioactivity peak associated with free [^{18}F]F$^-$ is labeled as such while the product peak is indicated by the symbol (*).

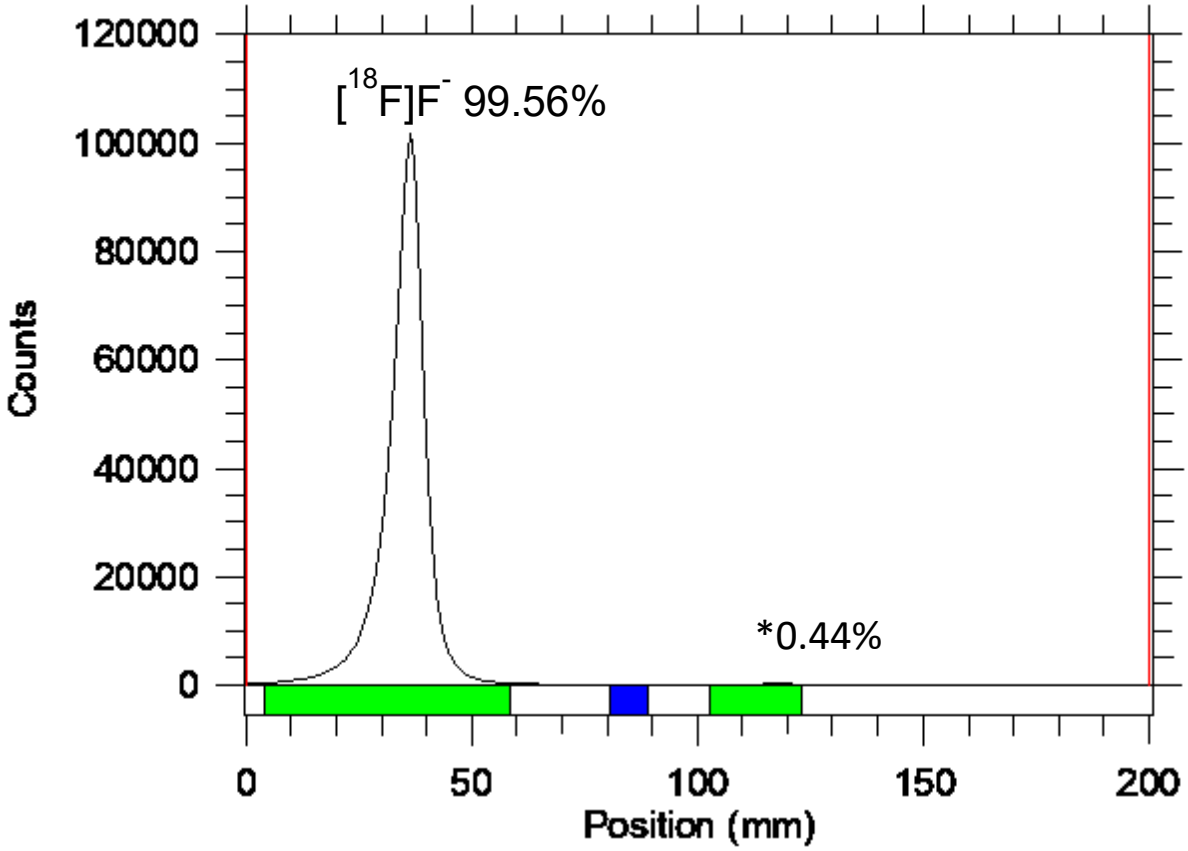

Figure A39. TLC chromatogram of [^{19}F/^{18}F]-isotopic exchange reaction mixture for commercial BODIPY standard when subject to 100 eq $Mg(NO_3)_2$, 75.0 eq TEAB fixing agent for 30 minutes. Chromatogram obtained using Bioscan AR-2000 radio-TLC plate reader. This data is associated with entry 7 of **Table 3.2**. The radioactivity peak associated with free [^{18}F]F^- is labeled as such while the product peak is indicated by the symbol (*).

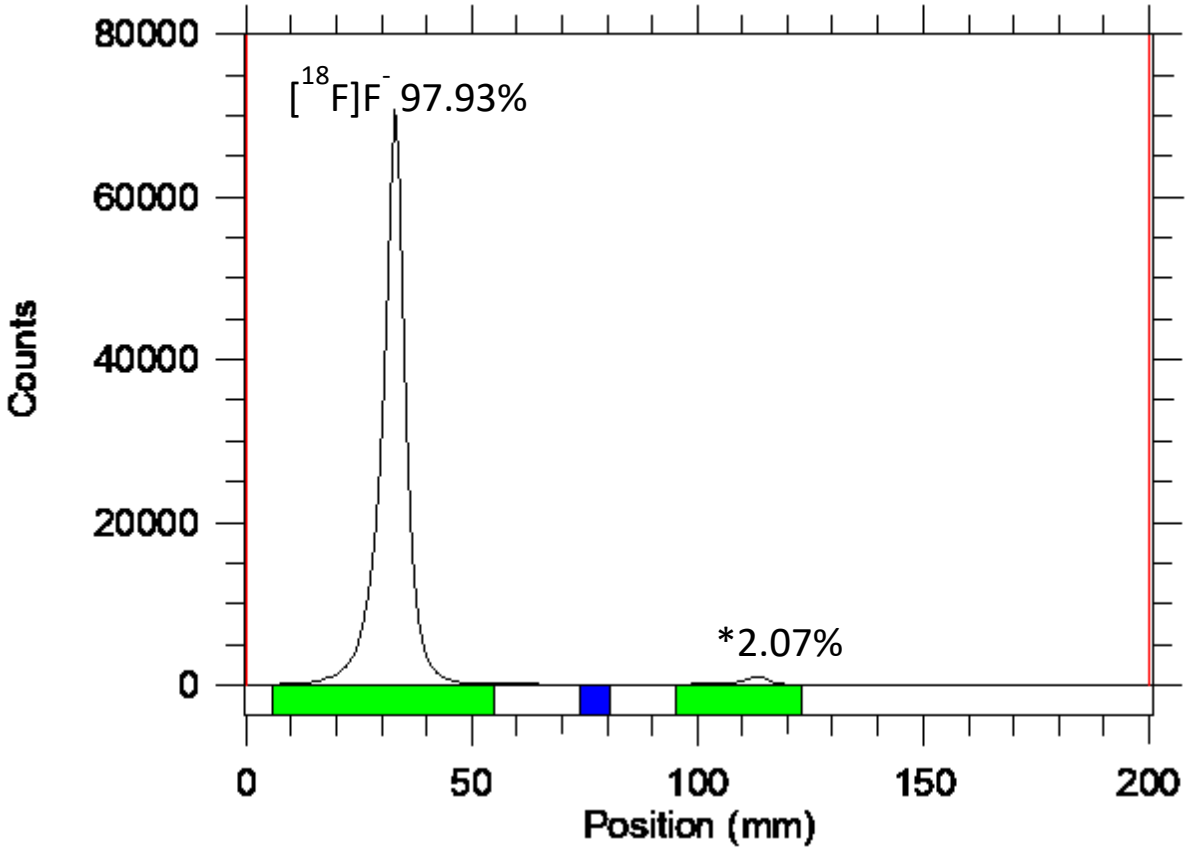

Figure A40. TLC chromatogram of [^{19}F/^{18}F]-isotopic exchange reaction mixture for commercial BODIPY standard when subject to 100 eq $Mg(NO_3)_2$, 75.0 eq TEAB fixing agent for 45 minutes. Chromatogram obtained using Bioscan AR-2000 radio-TLC plate reader. This data is associated with entry 7 of **Table 3.2**. The radioactivity peak associated with free [^{18}F]F$^-$ is labeled as such while the product peak is indicated by the symbol (*).

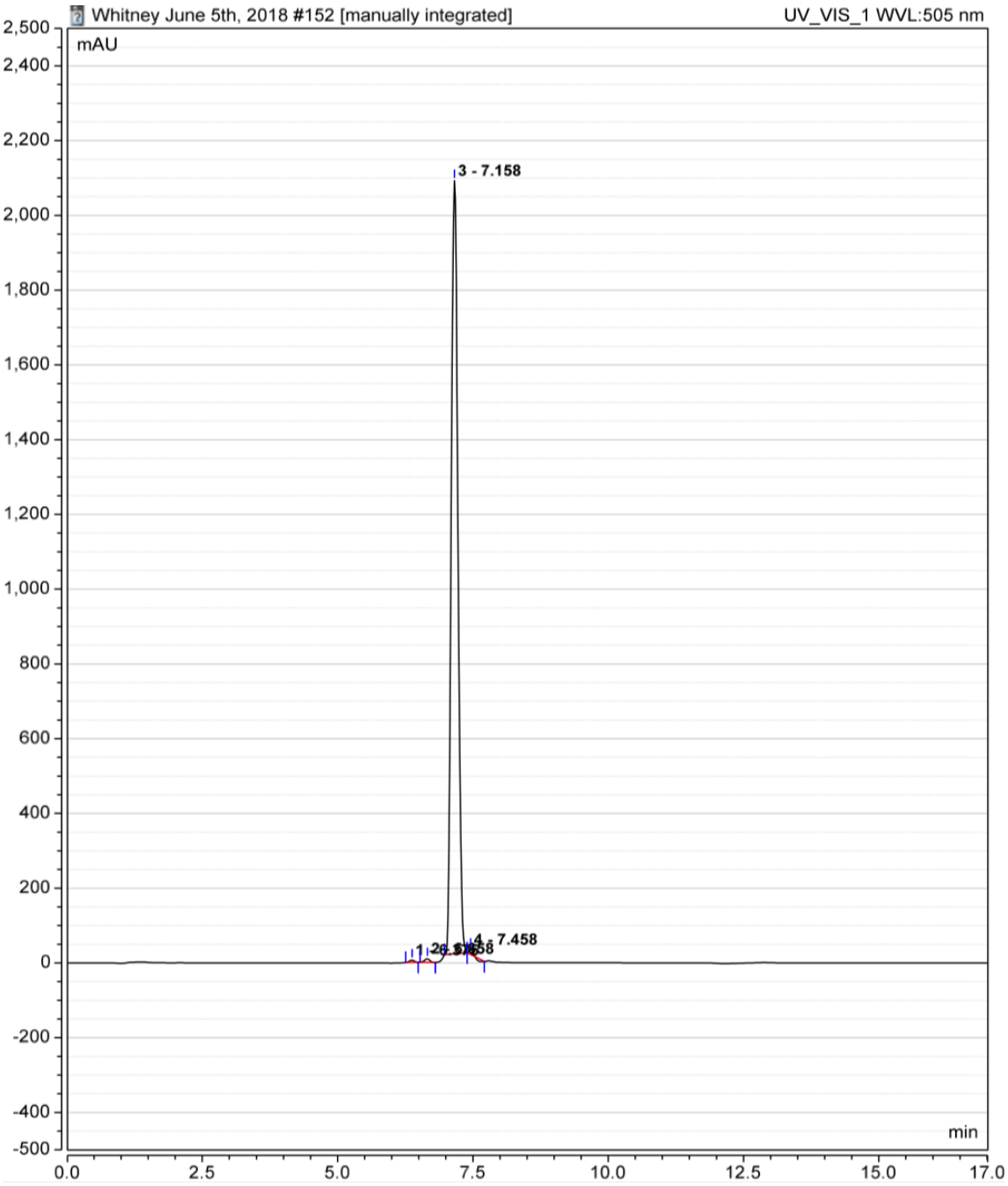

Figure A41. HPLC chromatogram of [^{19}F/^{18}F]-isotopic exchange reaction mixture for commercial BODIPY standard when subject to 100 eq $Mg(NO_3)_2$, 75.0 eq TEAB fixing agent at 37 °C for 5 minutes. Experimental conditions applied are outlined in entry 7 of **Table 3.2**. Chromatogram was obtained using a Thermo Fisher Vanquish UHPLC system equipped with a UV-Vis detector set to measure at 505 nm. Peak 3 (7.158 min) is associated with the commercial BODIPY dye.

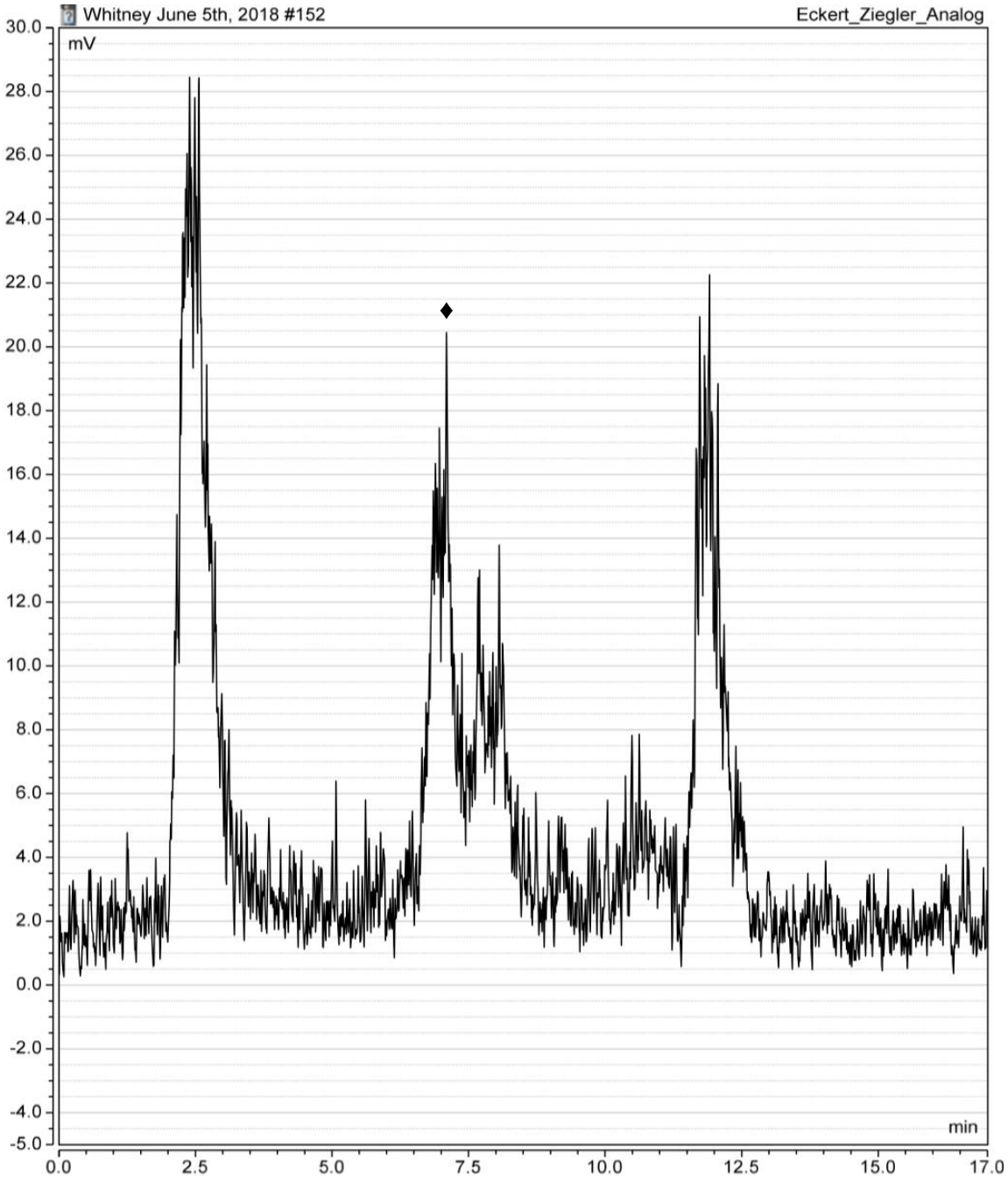

Figure A42. HPLC chromatogram of [^{19}F/^{18}F]-isotopic exchange reaction mixture for commercial BODIPY standard when subject to 100 eq $Mg(NO_3)_2$, 75.0 eq TEAB fixing agent at 37 °C for 5 minutes. Experimental conditions applied are outlined in entry 7 of **Table 3.2**. Chromatogram was obtained using a Thermo Fisher Vanquish UHPLC system equipped with a radioactivity detector set to 2000K sensitivity. Peak associated with the radiolabeled commercial BODIPY dye is denoted with the symbol (♦).

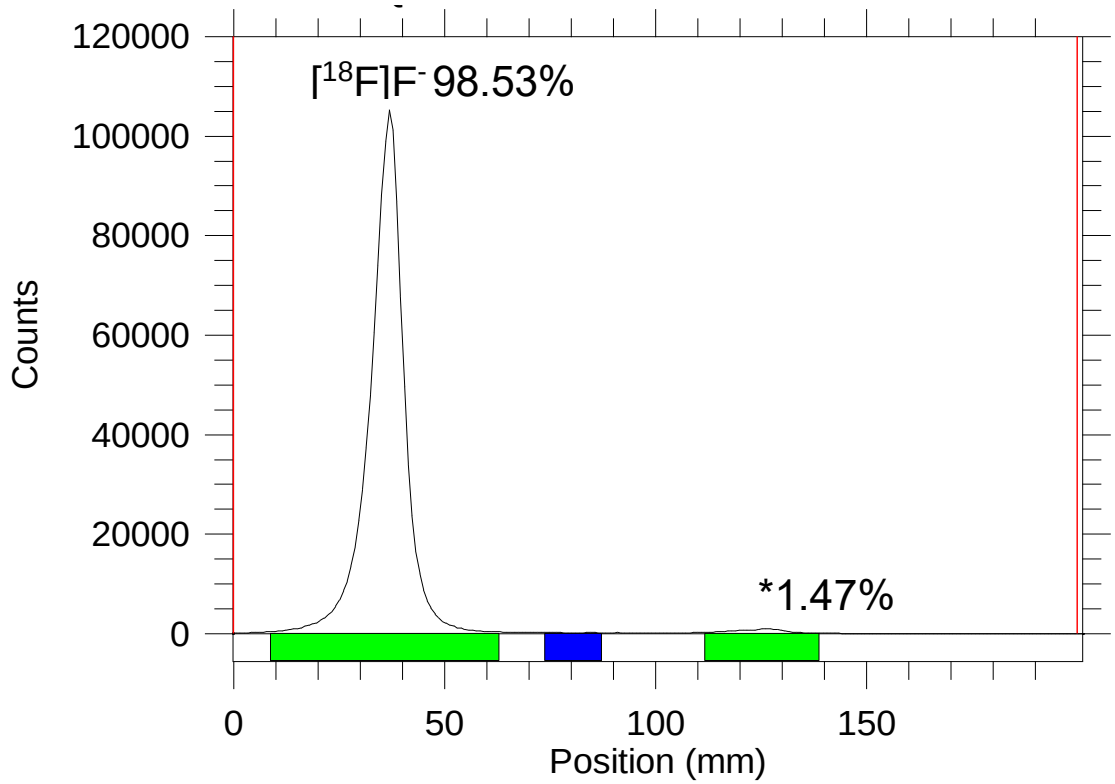

Figure A43. TLC chromatogram of [^{19}F/^{18}F]-isotopic exchange reaction mixture for commercial BODIPY standard when subject to 100 eq $Mg(NO_3)_2$ prepared in DMSO, 37 °C, 55.8 eq TEAB fixing agent for 5 minutes. Chromatogram obtained using Bioscan AR-2000 radio-TLC plate reader. This data is associated with entry 8 of **Table 3.2**. The radioactivity peak associated with free [^{18}F]F$^-$ is labeled as such while the product peak is indicated by the symbol (*).

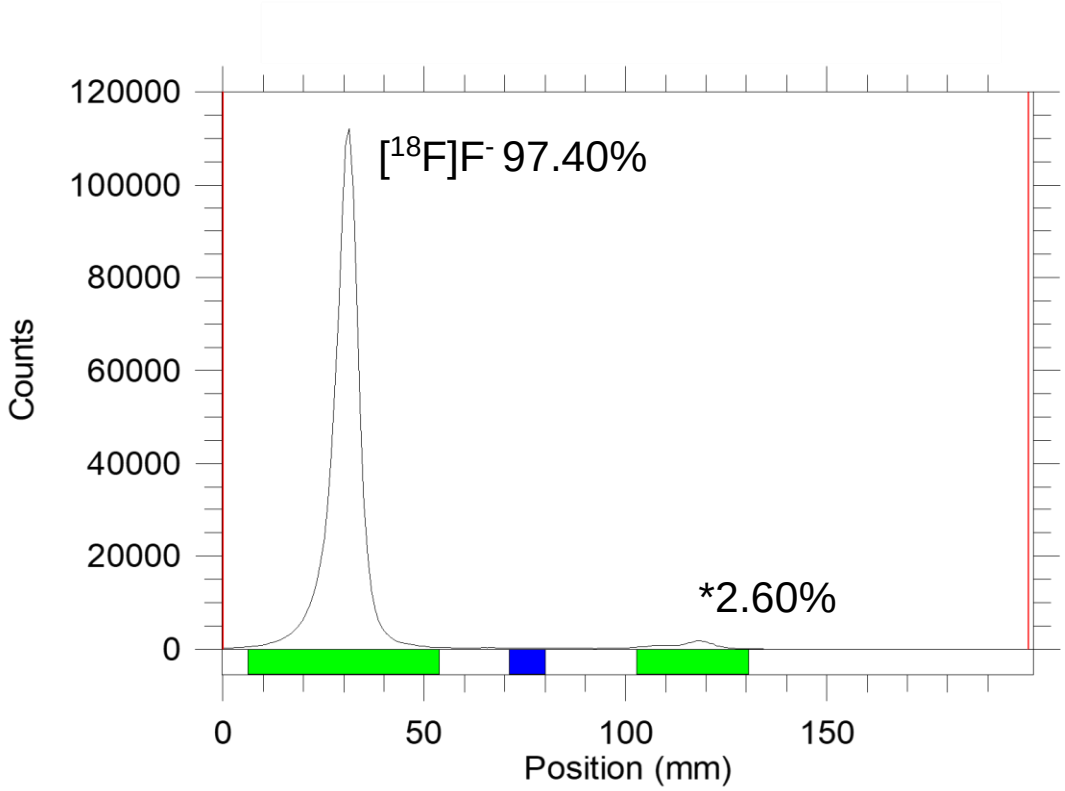

Figure A44. TLC chromatogram of [^{19}F/^{18}F]-isotopic exchange reaction mixture for commercial BODIPY standard when subject to 100 eq $Mg(NO_3)_2$ prepared in DMSO, 37 °C, 55.8 eq TEAB fixing agent for 15 minutes. Chromatogram obtained using Bioscan AR-2000 radio-TLC plate reader. This data is associated with entry 8 of **Table 3.2**. The radioactivity peak associated with free [^{18}F]F$^-$ is labeled as such while the product peak is indicated by the symbol (*).

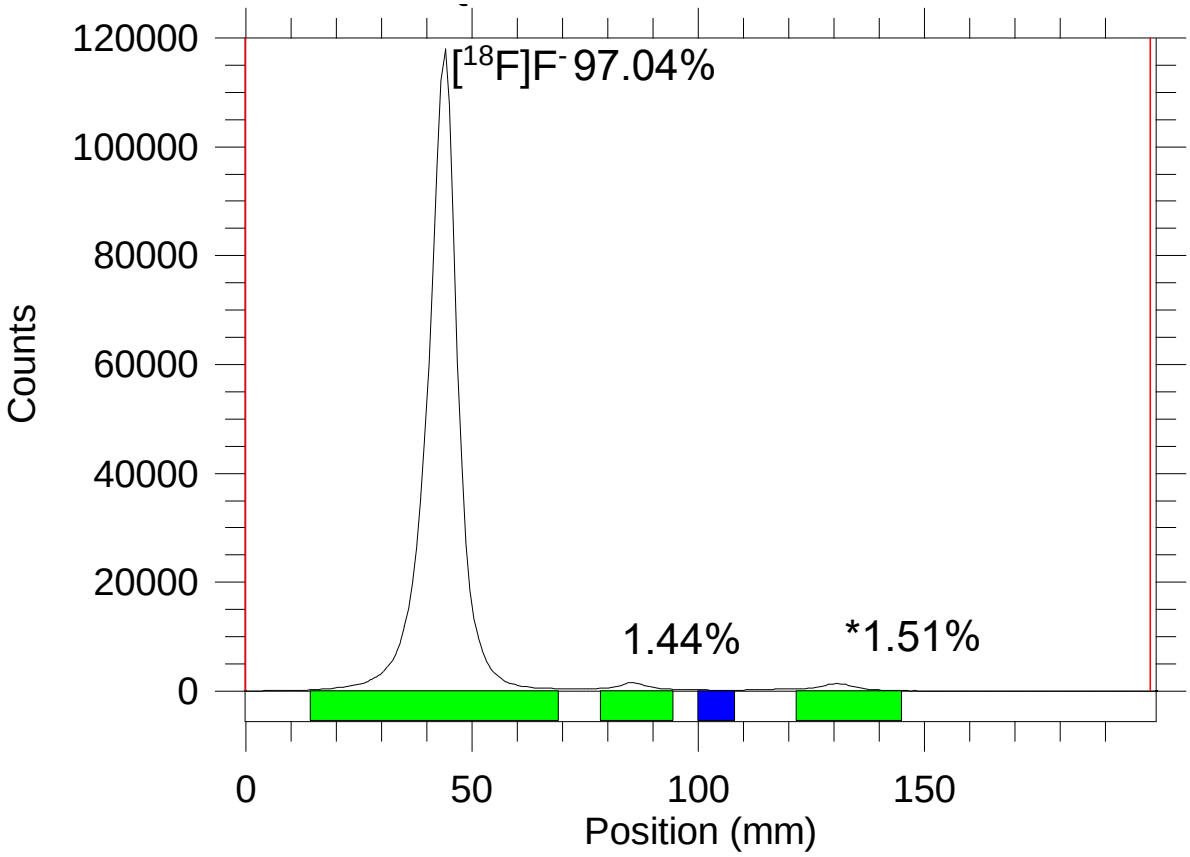

Figure A45. TLC chromatogram of [^{19}F/^{18}F]-isotopic exchange reaction mixture for commercial BODIPY standard when subject to 100 eq $Mg(NO_3)_2$ prepared in DMSO, 37 °C, 55.8 eq TEAB fixing agent for 30 minutes. Chromatogram obtained using Bioscan AR-2000 radio-TLC plate reader. This data is associated with entry 8 of **Table 3.2**. The radioactivity peak associated with free [^{18}F]F$^-$ is labeled as such while the product peak is indicated by the symbol (*).

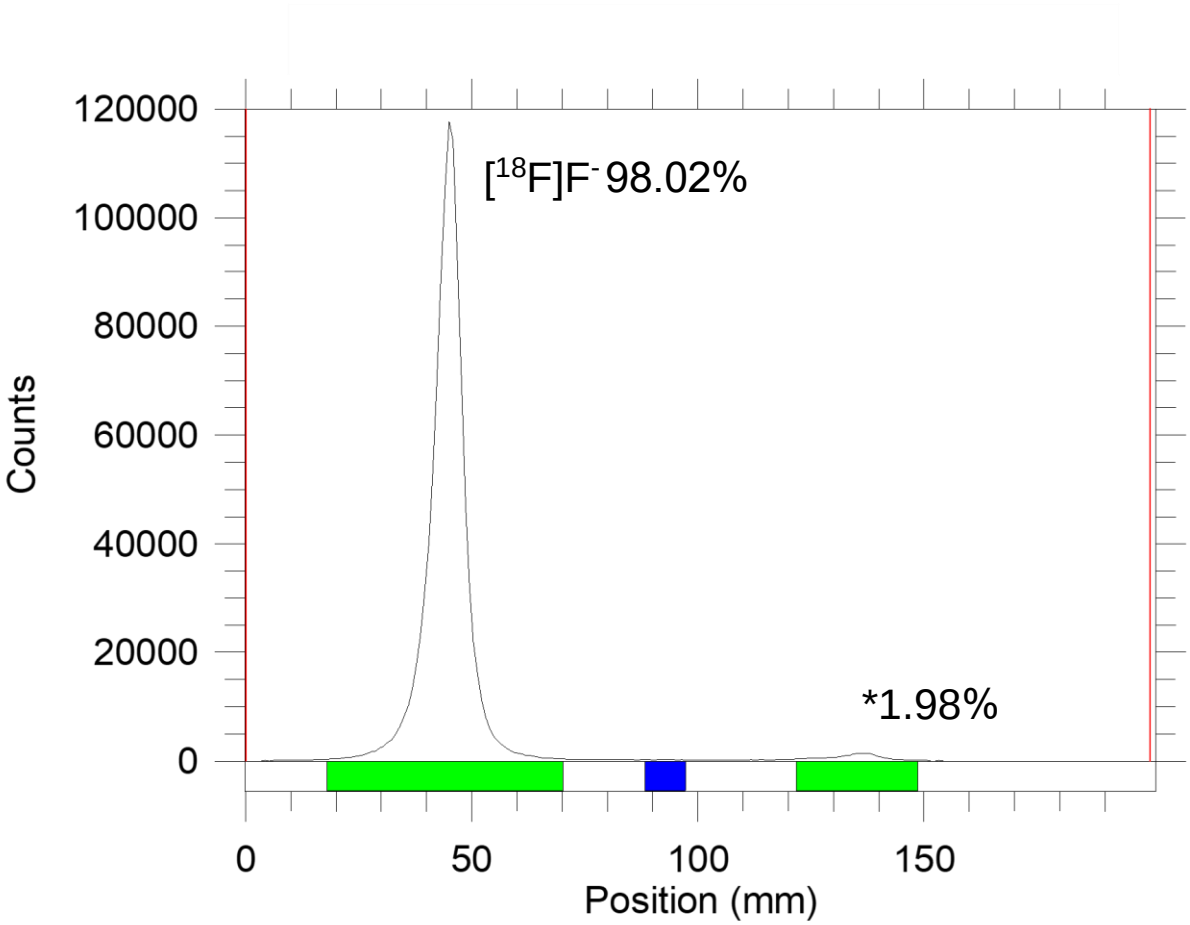

Figure A46. TLC chromatogram of [^{19}F/^{18}F]-isotopic exchange reaction mixture for commercial BODIPY standard when subject to 100 eq $Mg(NO_3)_2$ prepared in DMSO, 37 °C, 55.8 eq TEAB fixing agent for 45 minutes. Chromatogram obtained using Bioscan AR-2000 radio-TLC plate reader. This data is associated with entry 8 of **Table 3.2**. The radioactivity peak associated with free [^{18}F]F$^-$ is labeled as such while the product peak is indicated by the symbol (*).

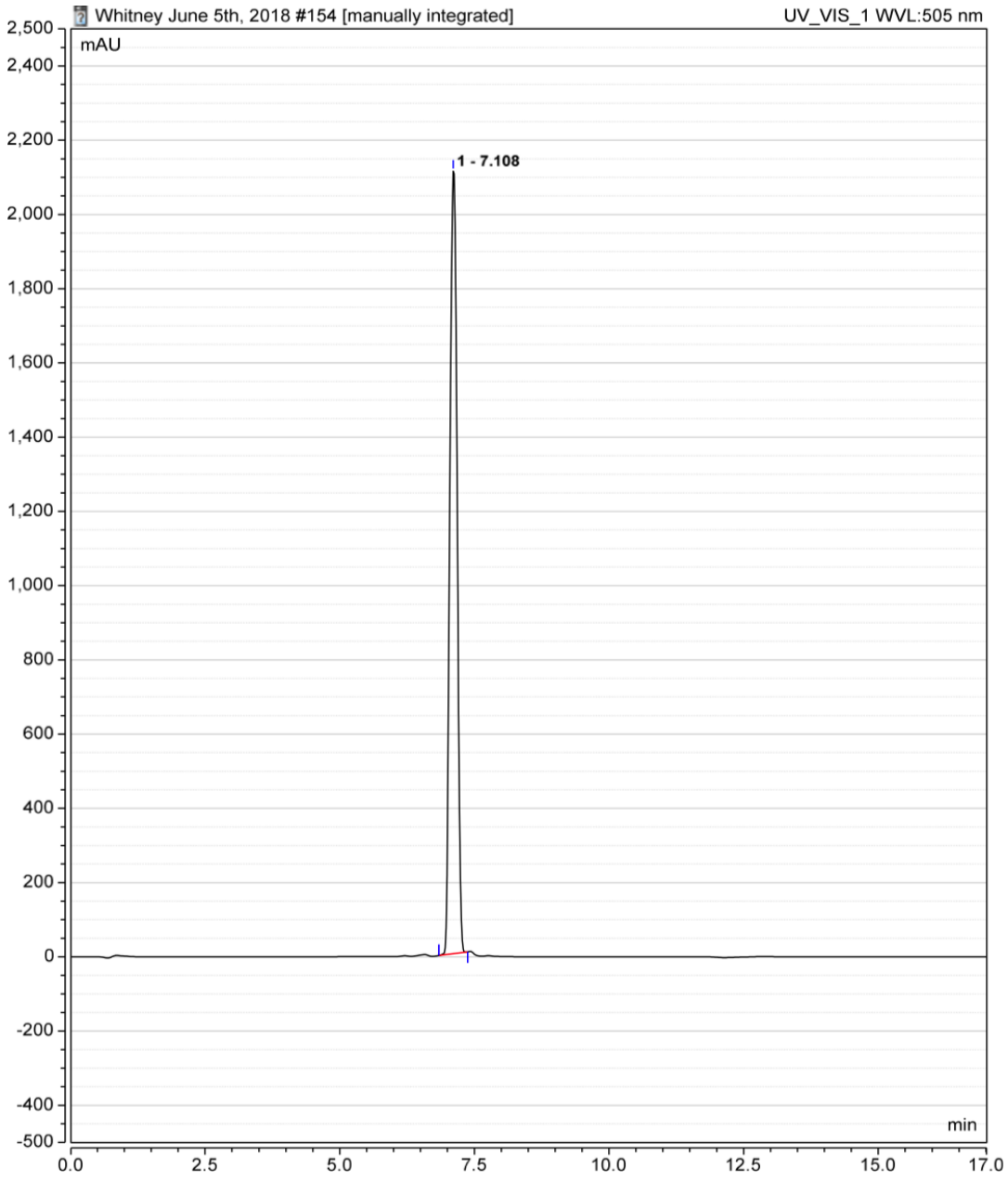

Figure A47. HPLC chromatogram of [^{19}F/^{18}F]-isotopic exchange reaction mixture for commercial BODIPY standard when subject to 100 eq $Mg(NO_3)_2$ (DMSO solution), 55.8 eq TEAB fixing agent at 37 °C for 5 minutes. Experimental conditions applied are outlined in entry 8 of **Table 3.2**. Chromatogram was obtained using a Thermo Fisher Vanquish UHPLC system equipped with a UV-Vis detector set to measure at 505 nm. Peak 1 (7.108 min) is associated with the commercial BODIPY dye.

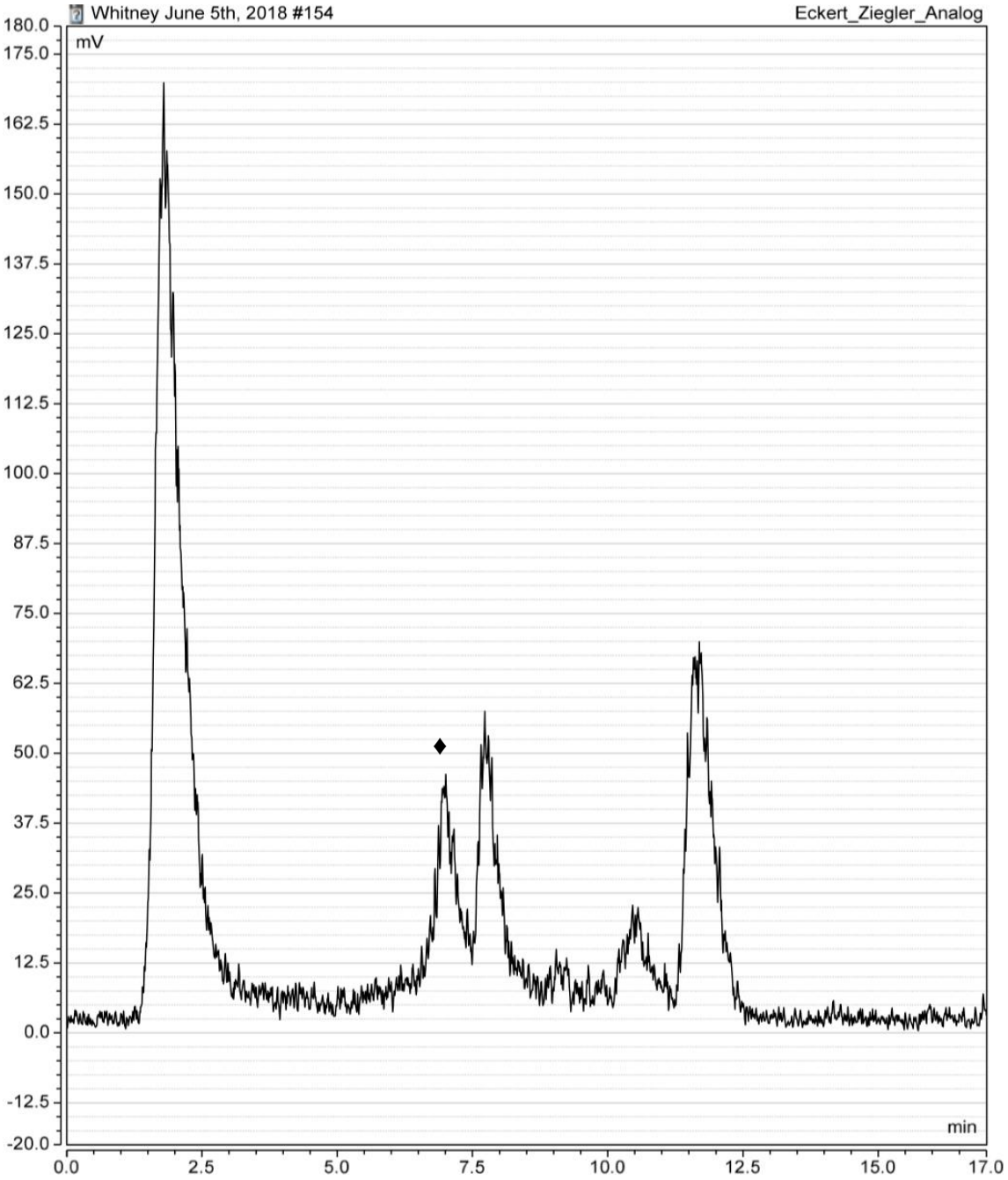

Figure A48. HPLC chromatogram of [^{19}F/^{18}F]-isotopic exchange reaction mixture for commercial BODIPY standard when subject to 100 eq $Mg(NO_3)_2$ (DMSO solution), 55.8 eq TEAB fixing agent at 37 °C for 5 minutes. Experimental conditions applied are outlined in entry 8 of **Table 3.2**. Chromatogram was obtained using a Thermo Fisher Vanquish UHPLC system equipped with a radioactivity detector set to 2000K sensitivity. Peak associated with the radiolabeled commercial BODIPY dye is denoted with the symbol (♦).

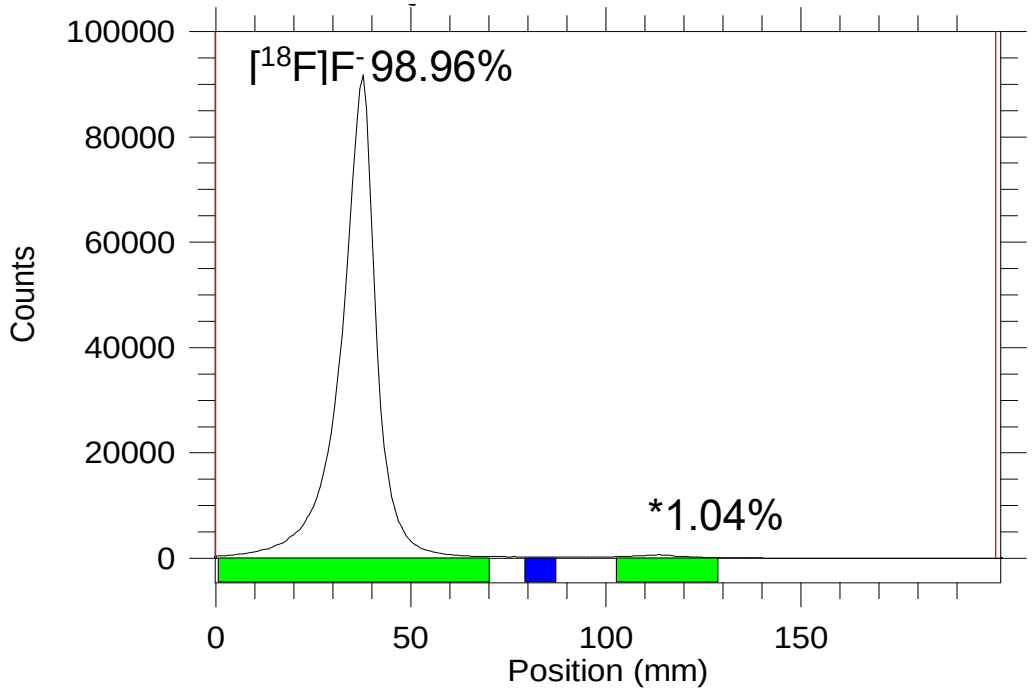

Figure A49. TLC chromatogram of [^{19}F/^{18}F]-isotopic exchange reaction mixture for commercial BODIPY standard when subject to 10 eq $Mg(NO_3)_2$ with excess H_2O, 37 °C, 55.8 eq TEAB fixing agent for 5 minutes. Chromatogram obtained using Bioscan AR-2000 radio-TLC plate reader. This data is associated with entry 9 of **Table 3.2**. The radioactivity peak associated with free [^{18}F]F$^-$ is labeled as such while the product peak is indicated by the symbol (*).

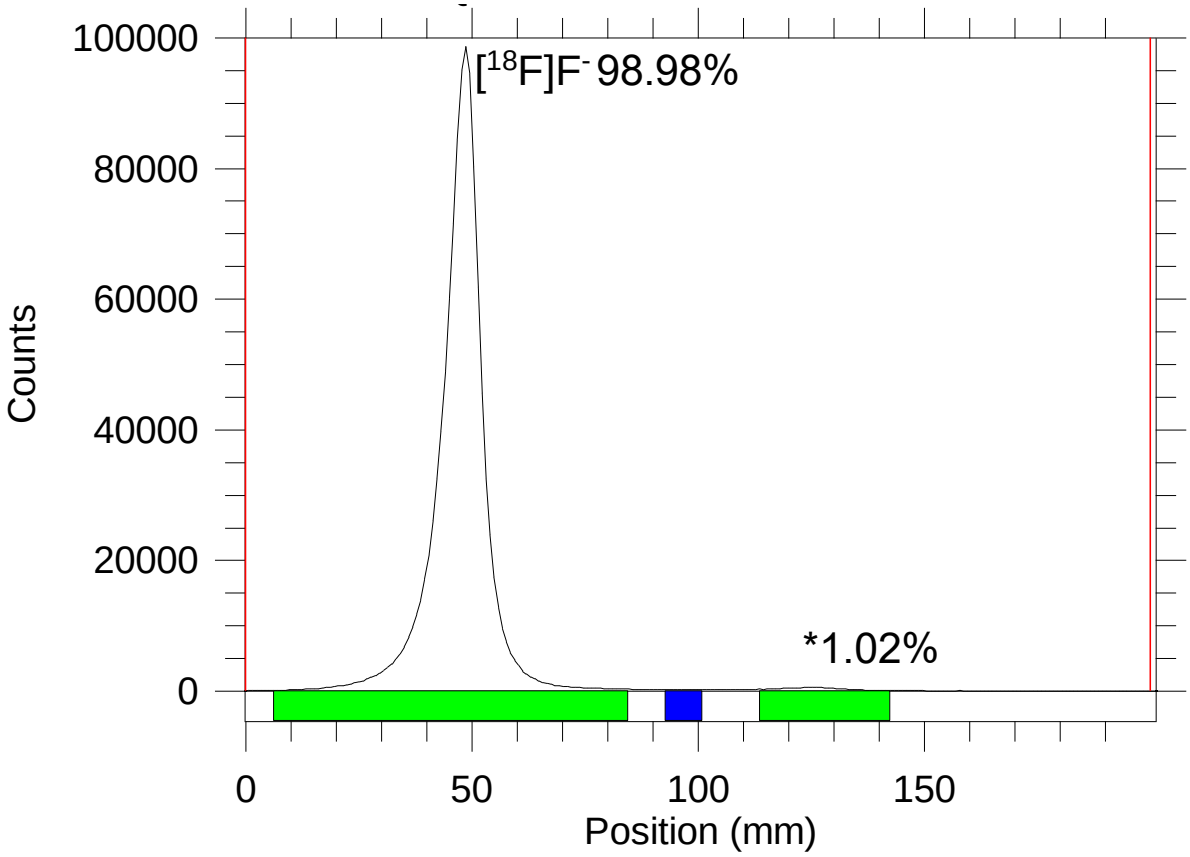

Figure A50. TLC chromatogram of [^{19}F/^{18}F]-isotopic exchange reaction mixture for commercial BODIPY standard when subject to 10 eq $Mg(NO_3)_2$ with excess H_2O, 37 °C, 55.8 eq TEAB fixing agent for 15 minutes. Chromatogram obtained using Bioscan AR-2000 radio-TLC plate reader. This data is associated with entry 9 of **Table 3.2**. The radioactivity peak associated with free [^{18}F]F$^-$ is labeled as such while the product peak is indicated by the symbol (*).

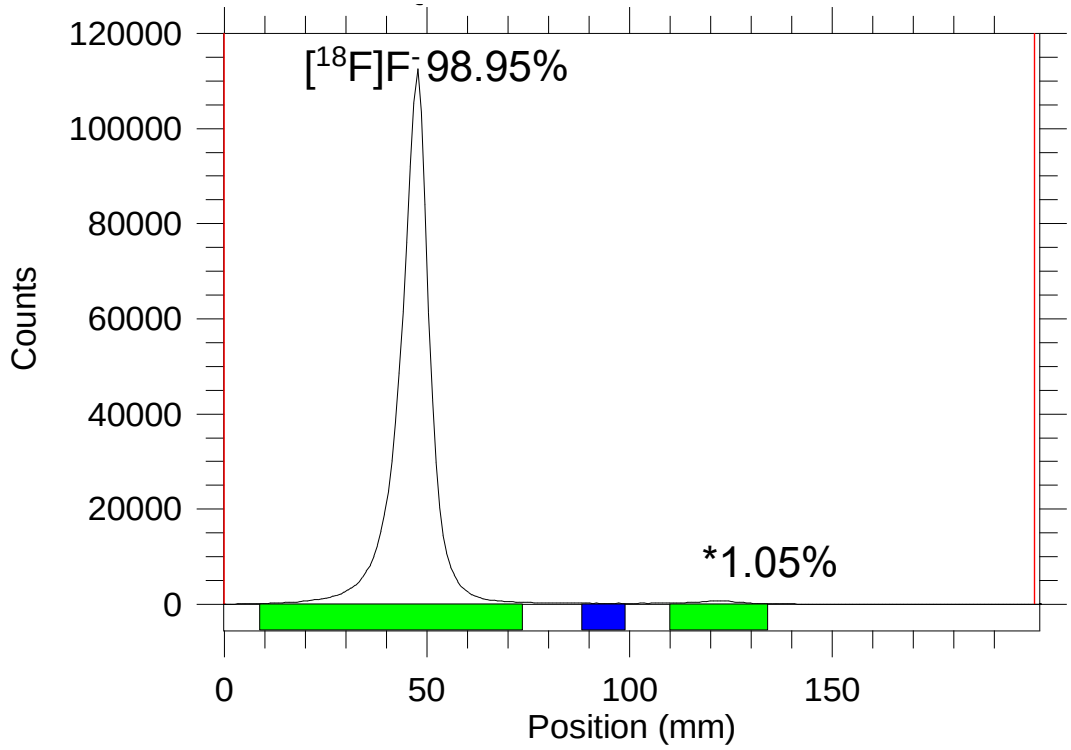

Figure A51. TLC chromatogram of [^{19}F/^{18}F]-isotopic exchange reaction mixture for commercial BODIPY standard when subject to 10 eq $Mg(NO_3)_2$ with excess H_2O, 37 °C, 55.8 eq TEAB fixing agent for 30 minutes. Chromatogram obtained using Bioscan AR-2000 radio-TLC plate reader. This data is associated with entry 9 of **Table 3.2**. The radioactivity peak associated with free [^{18}F]F$^-$ is labeled as such while the product peak is indicated by the symbol (*).

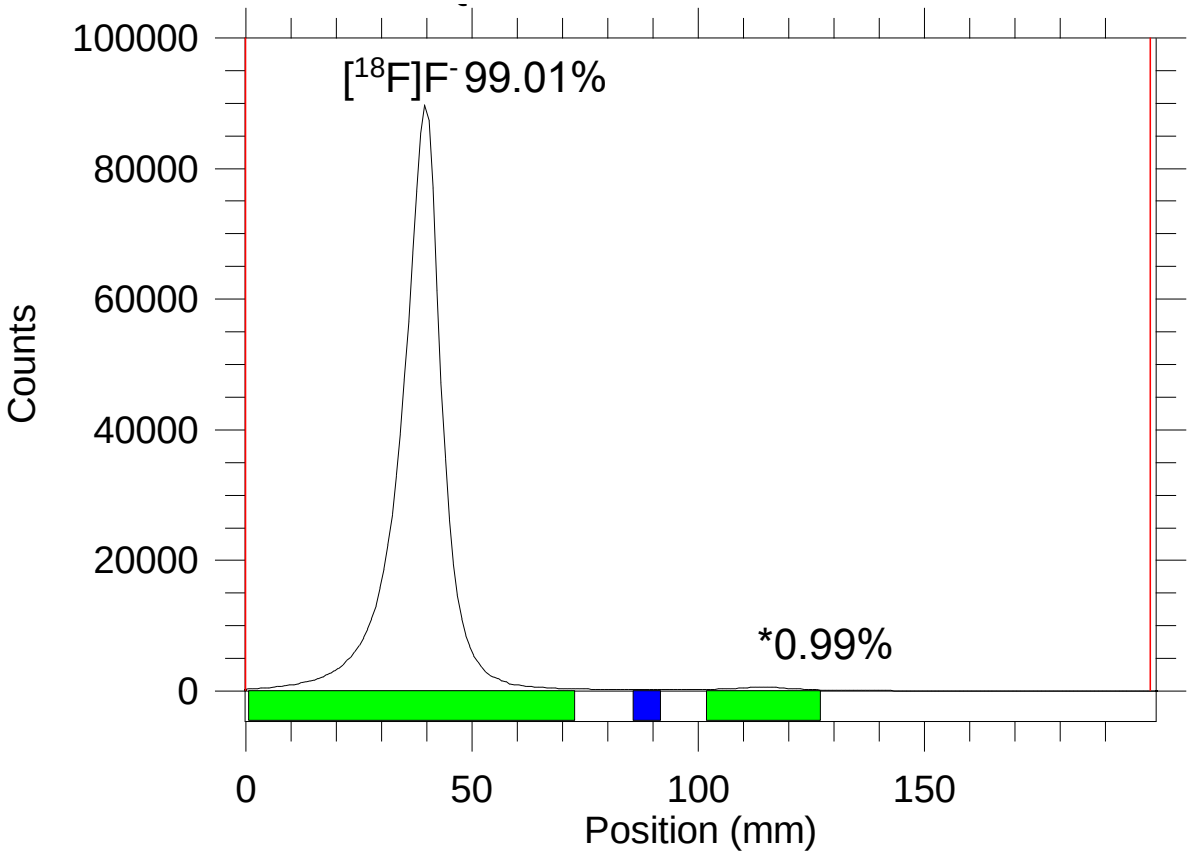

Figure A52. TLC chromatogram of [^{19}F/^{18}F]-isotopic exchange reaction mixture for commercial BODIPY standard when subject to 10 eq $Mg(NO_3)_2$ with excess H_2O, 37 °C, 55.8 eq TEAB fixing agent for 45 minutes. Chromatogram obtained using Bioscan AR-2000 radio-TLC plate reader. This data is associated with entry 9 of **Table 3.2**. The radioactivity peak associated with free [^{18}F]F$^-$ is labeled as such while the product peak is indicated by the symbol (*).

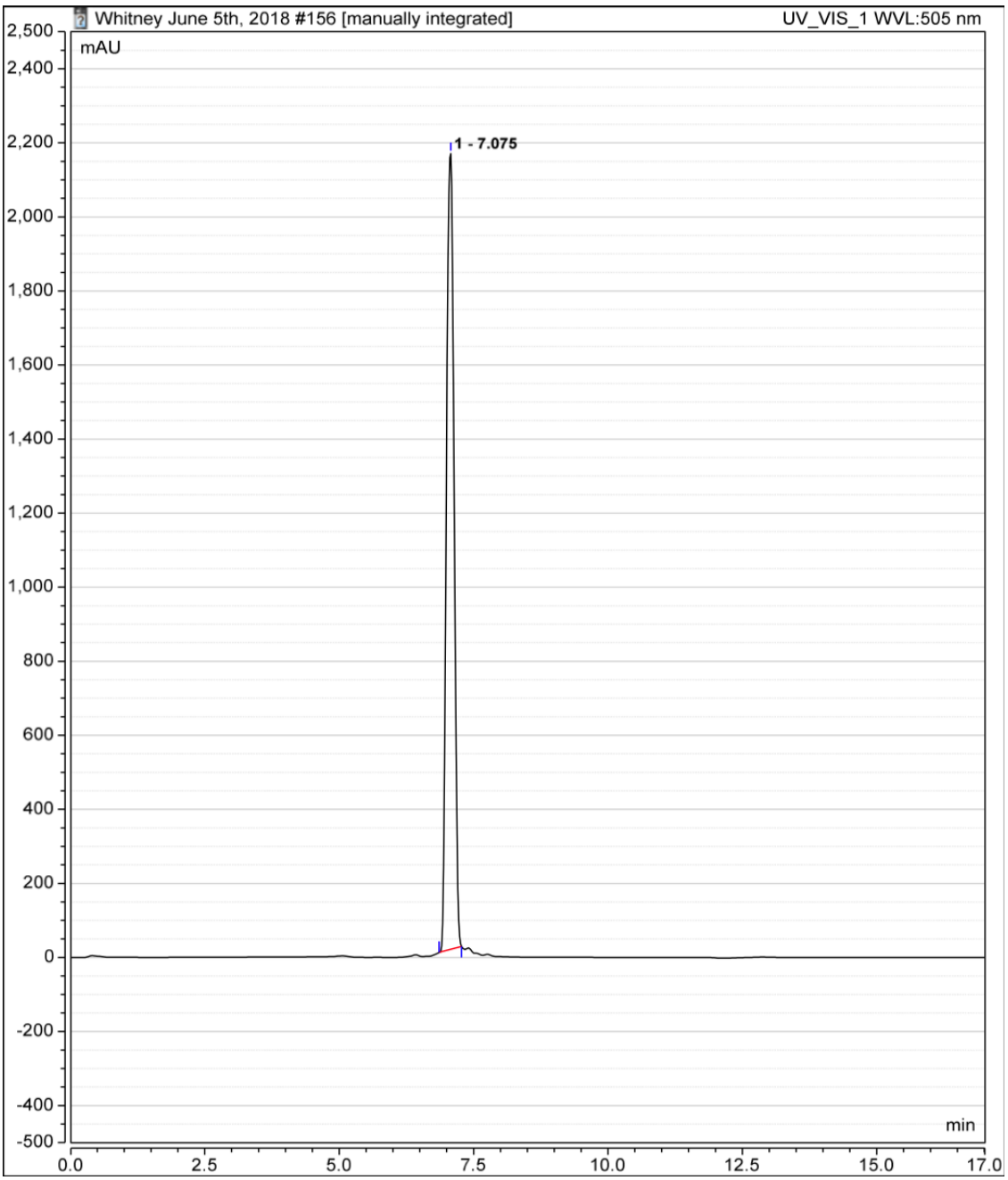

Figure A53. HPLC chromatogram of [^{19}F/^{18}F]-isotopic exchange reaction mixture for commercial BODIPY standard when subject to 10 eq $Mg(NO_3)_2$ (excess H_2O present), 55.8 eq TEAB fixing agent at 37 °C for 5 minutes. Experimental conditions applied are outlined in entry 9 of **Table 3.2**. Chromatogram was obtained using a Thermo Fisher Vanquish UHPLC system equipped with a UV-Vis detector set to measure at 505 nm. Peak 1 (7.108 min) is associated with the commercial BODIPY dye.

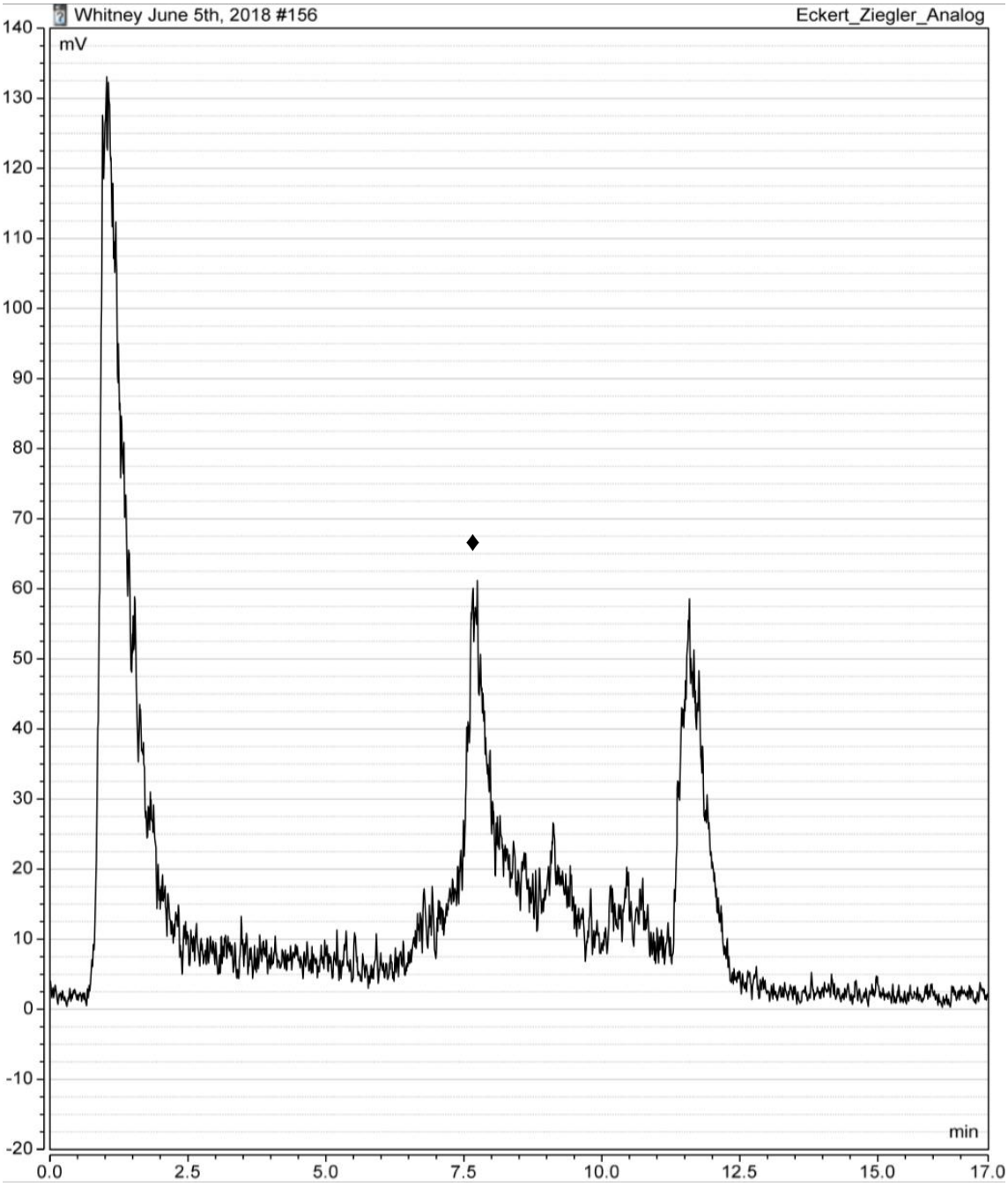

Figure A54. HPLC chromatogram of [^{19}F/^{18}F]-isotopic exchange reaction mixture for commercial BODIPY standard when subject to 10 eq $Mg(NO_3)_2$ ((excess H_2O present),), 55.8 eq TEAB fixing agent at 37 °C for 5 minutes. Experimental conditions applied are outlined in entry 9 of **Table 3.2**. Chromatogram was obtained using a Thermo Fisher Vanquish UHPLC system equipped with a radioactivity detector set to 2000K sensitivity. Peak associated with the radiolabeled commercial BODIPY dye is denoted with the symbol (♦).

Table A1. Line commands for Trasis miniAIO ^{18}F-solution preparation. Line advance comments correspond to setting commands on the Trasis mini AIO software such as command duration (measured in seconds (s) and minutes (m), heater (H1), vacuum (V), activity pump (P), and syringe actuators (where either SA1 and SA2 were used as the activity pump inlet and solution draw up/elute systems respectively). Pressure and vacuum are reported in pound per square inch (psi). Pressure flow setting is reported upon use of pressurized nitrogen gas within the Trasis mini AIO radiosynthesis module as either being high flow (HF) or low flow (LF). Cassette rotory positioning is reported as the visual flow path through the cassette during the associated line command. SA1 and SA2 volumes are reported in mililitre (mL) values for each line number along with the rates at which these syringe positions were set to draw up or elute their set contents (mL/min). Finally, reactor heat is presented in degrees Celsius (°C). Vacuum activation at the bottom left of the cassette (Va) is written as a binary response of 0 = false and 1 = true.

Line Number	Description	Label	Line Advance Comment	Pressure (psi)	Pressure Flow Setting	Vacuum (psi)	Cassette Rotory Positioning (Positions 1-6)	Va
0	Zeroing the Activity Sensors	Starting	SA1				- - - - - -	0
2	Ready to receive activity		Ready to Receive	500		-100	- - - - - -	0
3	Activity Received	Activity Received		500		-100	- - - - - -	0
4	Start Synthesis		Start Synthesis	500		-100	- - - - - -	0
5	Activity In Position		Insert Activity into Syringe	500	HF	-800	⌟ ⌞ ⌟ - - -	0
6	Recovering [^{18}O]-H_2O		SA1	500	HF	-800	⌟ ⌞ ⌟ - - -	0
7	Recovering [^{18}O]-H_2O		20 s	500	HF	-800	⌟ ⌞ ⌟ - - -	0
8	Recovering [^{18}O]-H_2O		20 s	500	HF	-800	⌟ ⌞ ⌟ - - -	0

Line Number	Description	Label	Line Advance Comment	Pressure (psi)	Pressure Flow Setting	Vacuum (psi)	Cassette Rotory Positioning (Positions 1-6)	Va
9	Recovering [^{18}O]-H_2O		60 s	500	HF	-800	⌟⌞ ⌟- - -	0
10	Pressure to Fixing Agent Vial		4 s	500	LF	0	- - - ⌟- -	0
11	Fixing Agent Elute		12s	0		0	- - - ⌞- -	1
12	Fixing Agent Elute		H1, P, SA1, SA2, V	500	HF	0	- - - - - -	1
13	Fixing Agent Elute		H1, P, SA2, V	0		0	⌞- - - - -	1
14	Fixing Agent Elute		H1, P, SA1, V	500	LF	-300	⌟⌞ ⌟- - -	1
15	Fixing Agent Elute		2 m	500	LF	-300	⌟⌞ ⌟- - -	1
16	Heat With Vacuum		4 m	100	LF	-40	- - ⌟- - -	1
17	Heat With Vacuum		4 m	200	LF	-200	- - ⌟- - -	1
18	Heat With Vacuum		2 m	400	LF	-500	- - ⌟- - -	1
19	Heat With Vacuum		20 s	500	HF	-1000	- - ⌟- - -	1
20	Pressurize Acetonitrile Vial		5 s	500	LF	0	- - - - - ⌟	0
21	Draw up 1 mL Acetonitrile		3 s	500		-300	- - - - - ⌞	0
22	Extra Air		H1, P, SA2, V	500	LF	0	- - - - - -	0
23	Add Acetonitrile		H1, P, SA2, V	0		0	⌞- - - - -	0
24	Add Acetonitrile		45 s	500	LF	-300	⌟⌞ ⌟- - -	1
25	Extra Air Flush		5 s	500	LF	-300	⌟⌞ ⌟- - -	1
26	Heat With Vacuum		2 m	100	LF	-40	- - ⌟- - -	1
27	Heat With Vacuum		2 m	300	LF	-200	- - ⌟- - -	1

Line Number	Description	Label	Line Advance Comment	Pressure (psi)	Pressure Flow Setting	Vacuum (psi)	Cassette Rotory Positioning (Positions 1-6)	Va
28	Heat With Vacuum		2 m	500	LF	-500	- - ⌟ - - -	1
29	Heat With Vacuum		20 s	500		-1000	- - ⌟ - - -	1
30	Pressurize Acetonitrile Vial		5 s	500	LF	0	- - - - - ⌟	0
31	Draw up 1 mL Acetonitrile		H1, P, SA2, V	0		0	- - - - - ⌞	0
32	Draw up 1 mL Acetonitrile		3 s	0		0	- - - - - ⌞	0
33	Extra Air		H1, P, SA2, V	500	LF	0	- - - - - -	0
34	Add Acetonitrile		H1, P, SA2, V	0		-300	- - ⌞ - - -	1
35	Extra Air Flush		5 s	500	LF	-300	- - - - - -	1
36	Heat With Vacuum		60 s	100	LF	-40	- - ⌟ - - -	1
37	Heat With Vacuum		60 s	300	LF	-200	- - ⌟ - - -	1
38	Heat With Vacuum		2 m	500	LF	-500	- - ⌟ - - -	1
39	Heat With Vacuum		20 s	500	HF	-1000	- - ⌟ - - -	1
40	Pressurize Acetonitrile Vial		5 s	500	LF	0	- - - - - ⌟	0
41	Draw up 1 mL Acetonitrile		H1, P, SA2, V	0		0	- - - - - ⌞	0
42	Draw up 1 mL Acetonitrile		3 s	0		0	- - - - - ⌞	0
43	Extra Air		H1, P, SA2, V	500	LF	0	- - - - - -	0
44	Add Acetonitrile		H1, P, SA2, V	0		-300	- - ⌞ - - -	1
45	Extra Air Flush		5 s	300	LF	-300	- - ⌟ - - -	1
46	Heat With Vacuum		60 s	100	LF	-40	- - ⌟ - - -	1

Line Number	Description	Label	Line Advance Comment	Pressure (psi)	Pressure Flow Setting	Vacuum (psi)	Cassette Rotory Positioning (Positions 1-6)	Va
47	Heat With Vacuum		60 s	300	LF	-200	- - ⌟ - - -	1
48	Heat With Vacuum		2 m	500	LF	-500	- - ⌟ - - -	1
49	Heat With Vacuum		20 s	500	HF	-1000	- - ⌟ - - -	1
50	Cool Down		12 m	500	HF	-1000	- - ⌟ - - -	1
51	Pressurize Reconstitution Acetonitrile Vial		10 s	500	LF	0	- - - - ⌟ -	0
52	Rinse line with Acetonitrile to Clean		3 s	0		0	- - - - ⌞ -	1
53	Rinse line with Acetonitrile to Clean		H1, P, SA2, V	300	LF	0	- - - - - -	1
54	Rinse line with Acetonitrile to Clean		H1, P, SA2, V	0		-300	- - ⌞ - - -	1
55	Pressurize Reconstitution Acetonitrile Vial		5 s	500	LF	0	- - ⌟ - - -	0
56	Draw up 3 mL Reconstitution Acetonitrile		10 s	0		0	- - ⌞ - - -	0
57	Extra Air		H1, P, SA2, V	500	LF	0	- - - - - -	0
58	Eject Reconstitution Acetonitrile		H1, P, SA2, V	0		-300	- - ⌞ - - -	1
59	Pressurize Reactor Vessel to Move Contents		5 s	500	LF	0	- - ⌟ - - -	0
60	Draw up Product		H1, P, SA2, V	300		0	- - ⌞ - - -	0

Line Number	Description	Label	Line Advance Comment	Pressure (psi)	Pressure Flow Setting	Vacuum (psi)	Cassette Rotory Positioning (Positions 1-6)	Va
61	Draw Up Extra Air		H1, P, SA2, V	0	LF	0	- - - - - -	0
62	Deliver Product to Product Vial		H1, P, SA2, V	0		0	- - ⌞ - - -	1
63	Full Stop		P, V	0	HF	0	- - - - - -	1

Line Number	Cassette Rotory Positioning (Positions 7-12)	SA1	SA2	Reactor Heat (ºC)
0	- - - - - /	6 mL		
2	- - - - - /			
3	- - - - - /			
4	- - - - - /			
5	⌞ ⌟ - - - /	6 mL	0 mL	
6	⌞ ⌟ - - - /	6 mL, 10 mL/min		
7	⌞ ⌟ - - - /			95
8	⌞ ⌟ - - - /			95
9	⌞ ⌟ - - - /			95
10	- - - - - /	6 mL		95
11	- - - - - /	6 mL	4 mL, 40 mL/min	95
12	- - - - - /	6 mL	13 mL, 40 mL/min	95
13	- - - - - /		0 mL, 20 mL/min	95
14	- ⌞ ⌟ - - /	6 mL		95
15	- ⌞ ⌟ - - /			95

Line Number	Cassette Rotory Positioning (Positions 7-12)	SA1	SA2	Reactor Heat (ºC)
16	- ⌞ ⌟ - - /			95
17	- ⌞ ⌟ - - /			95
18	- ⌞ ⌟ - - /			95
19	- ⌞ ⌟ - - /			95
20	- - - - - /	6 mL		95
21	- - - - - /		1 mL, 40 mL/min	95
22	- - - - - /		13 mL, 20 mL/min	95
23	- - - - - /		0 mL, 20 mL/min	95
24	- ⌞ ⌟ - - /			95
25	- ⌞ ⌟ - - /			95
26	- ⌞ ⌟ - - /			95
27	- ⌞ ⌟ - - /			95
28	- ⌞ ⌟ - - /			95
29	- ⌞ ⌟ - - /			95
30	- - - - - /	6 mL		95
31	- - - - - /		0 mL, 20 mL/min	95

Line Number	Cassette Rotory Positioning (Positions 7-12)	SA1	SA2	Reactor Heat (ºC)
32	- - - - - /		1 mL, 20 mL/min	95
33	- - - - - /		6 mL, 40 mL/min	95
34	- ⌞ ⌟ - - /		0 mL, 20 mL/min	95
35	- ⌞ ⌟ - - /			95
36	- ⌞ ⌟ - - /			95
37	- ⌞ ⌟ - - /			95
38	- ⌞ ⌟ - - /			95
39	- ⌞ ⌟ - - /			95
40	- - - - - /	6 mL		95
41	- - - - - /		0 mL, 20 mL/min	110
42	- - - - - /		1 mL, 40 mL/min	110
43	- - - - - /		6 mL, 40 mL/min	110

Line Number	Cassette Rotory Positioning (Positions 7-12)	SA1	SA2	Reactor Heat (ºC)
44	- ⌞ ⌟ - - /		0 mL, 20 mL/min	110
45	- ⌞ ⌟ - - /			110
46	- ⌞ ⌟ - - /			110
47	- ⌞ ⌟ - - /			110
48	- ⌞ ⌟ - - /			110
49	- ⌞ ⌟ - - /			110
50	- ⌞ ⌟ - - /			50
51	- - - - - /			50
52	- - - - - /		1 mL, 40 mL/min	50
53	- - - - - /		5 mL, 40 mL/min	50
54	⌞ ⌟ - - - /		0 mL, 20 mL/min	50
55	- - - - - /	6 mL		50
56	- - - - - /		3 mL, 40 mL/min	50
57	- - - - - /		12 mL, 40 mL/min	50

Line Number	Cassette Rotory Positioning (Positions 7-12)	SA1	SA2	Reactor Heat (ºC)
58	- ⌞ ⌟ - - /		0 mL, 20 mL/min	50
59	- ⌞ ⌟ - - /	6 mL		50
60	- ⌞ ⌟ - - /		12 mL, 30 mL/min	50
61	- - - - - /		18 mL, 40 mL/min	50
62	- ⌞ - - - /		0 mL, 30 mL/min	50
63	- - - - - /			Off

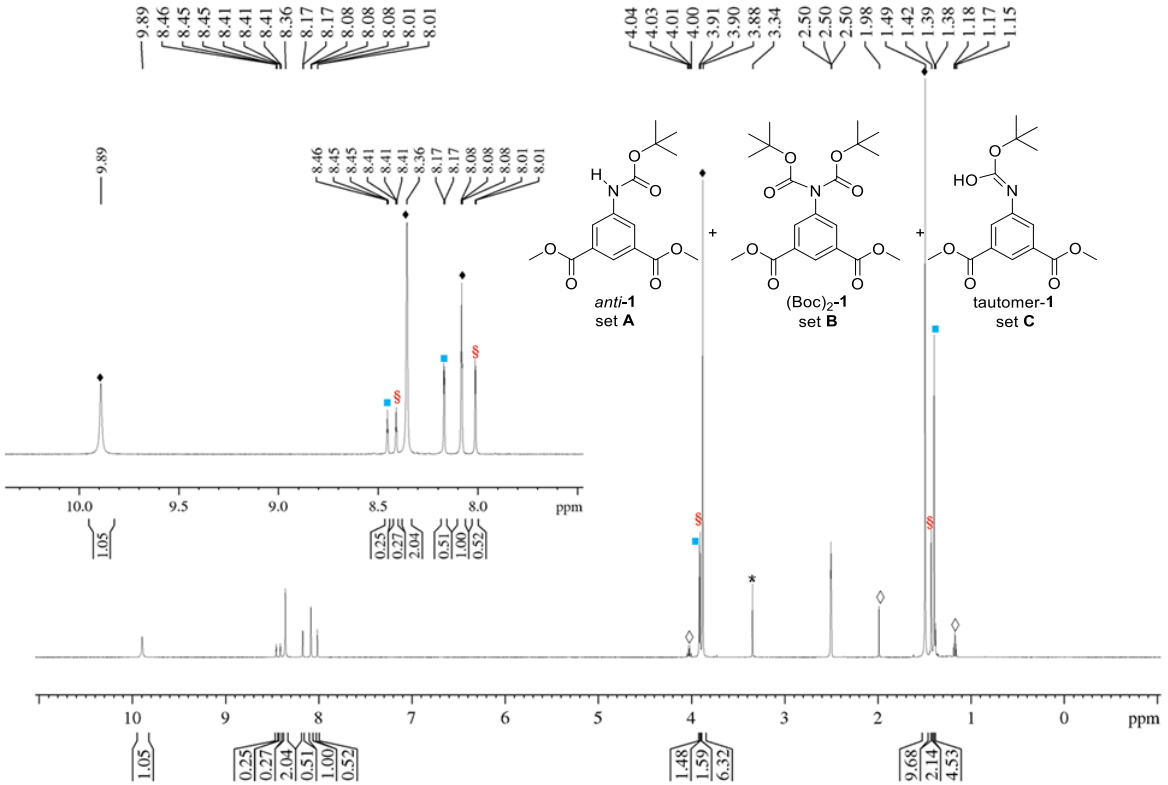

Figure A55. ^{1}H NMR spectrum of compound **1** crude mixture before precipitation in DMSO-d_6. Peaks associated with the *anti*-rotamers of compound **1** (*anti*-**1**, set **A**, ♦), a doubly Boc-protected derivative of compound **1** [$(Boc)_2$-**1**, set **B**, §), and an imidic acid tautomers of compound **1** (tautomer-**1**, set **C**, ■) are designated by the symbols ♦, § and ■ respectively. Peaks associated with water are labeled with the symbol *. Peaks associated with residual EtOAc are denoted by the symbol ◊. (For simplicity, only one stereoisomer of each component is shown in the inset). Figure reported in (Khozeimeh Sarbisheh *et al.*, 2020).[160]

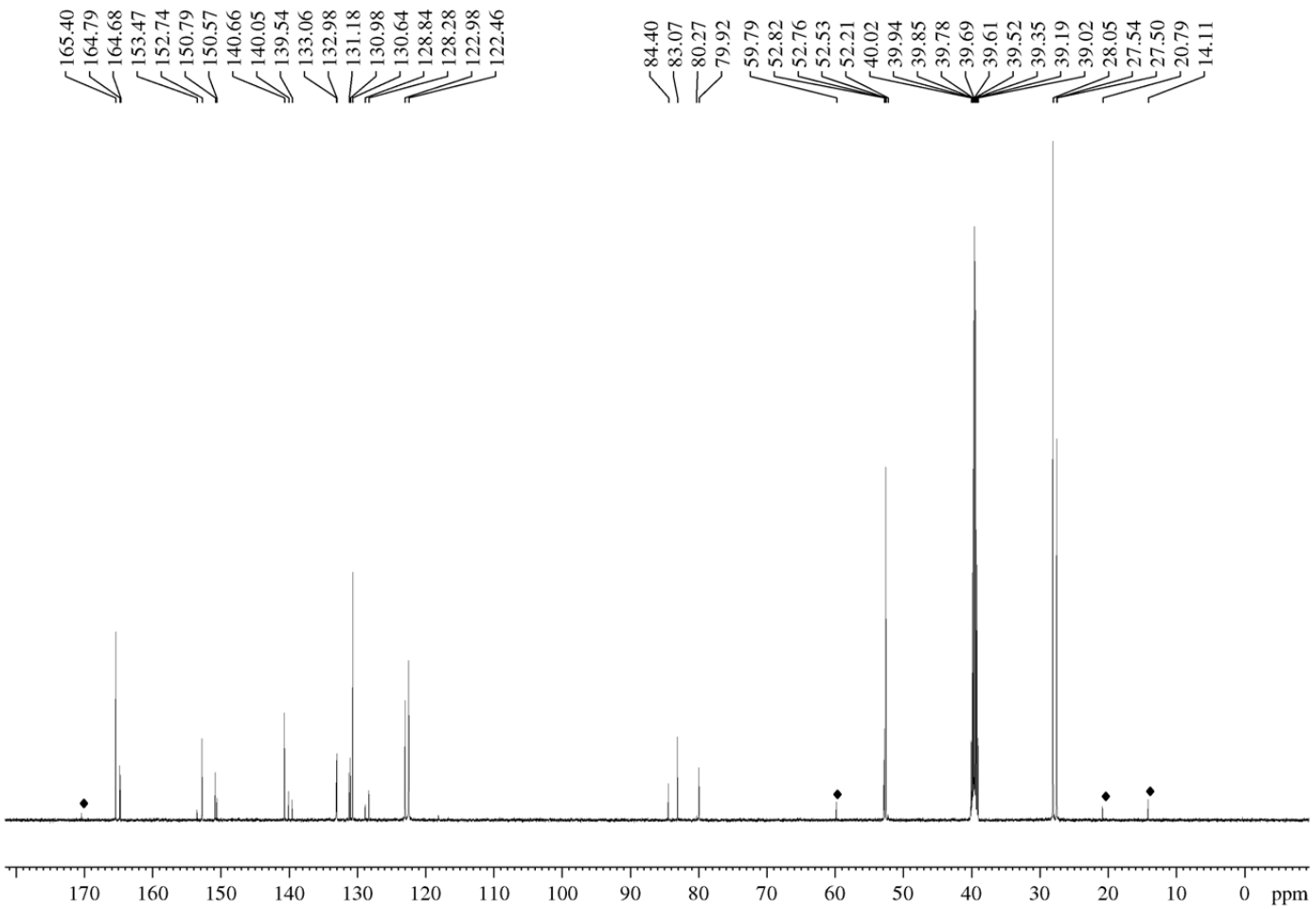

Figure A56. $^{13}C\{^{1}H\}$-UDEFT NMR spectrum of compound **1** crude mixture before precipitation or column chromatography in DMSO-d_6. The crude mixture containes compound **1**'s *anti*-rotamers (*anti*-**1**, set **A**), a doubly Boc-protected derivative of compound **1** [$(Boc)_2$-**1**, set **B**], and imidic acid tautomers of compound **1** (tautomer-**1**, set **C**). Peaks associated with EtOAc are denoted with the symbol (♦).

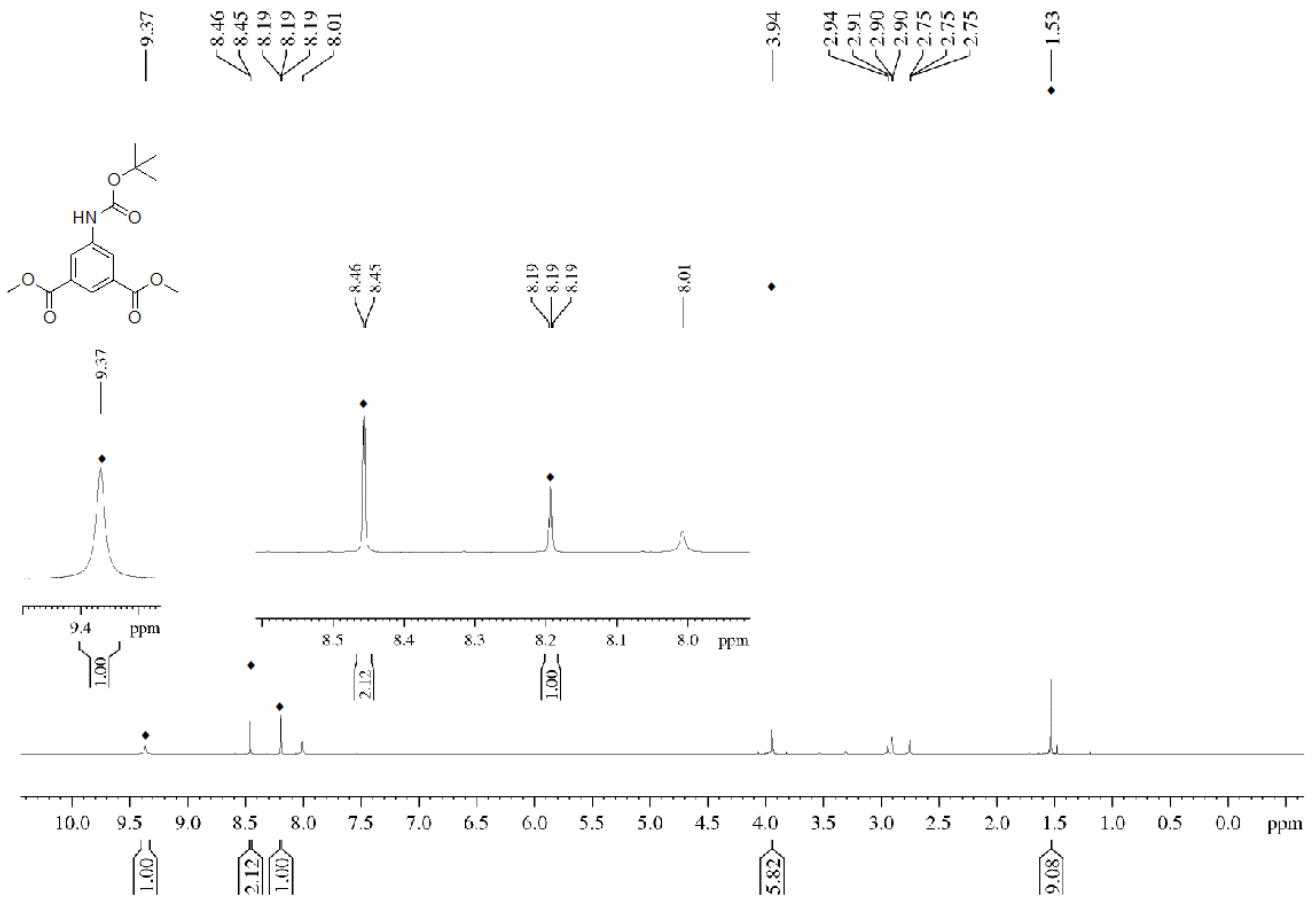

Figure A57. ^{1}H NMR spectrum of the *anti*-rotamers of compound **1** (*anti*-**1**, set **A**, ♦) in DMSO-d_6. For simplicity, only one rotamer is shown in the inset). Figure reported in (Khozeimeh Sarbisheh *et al.*, 2020).[160]

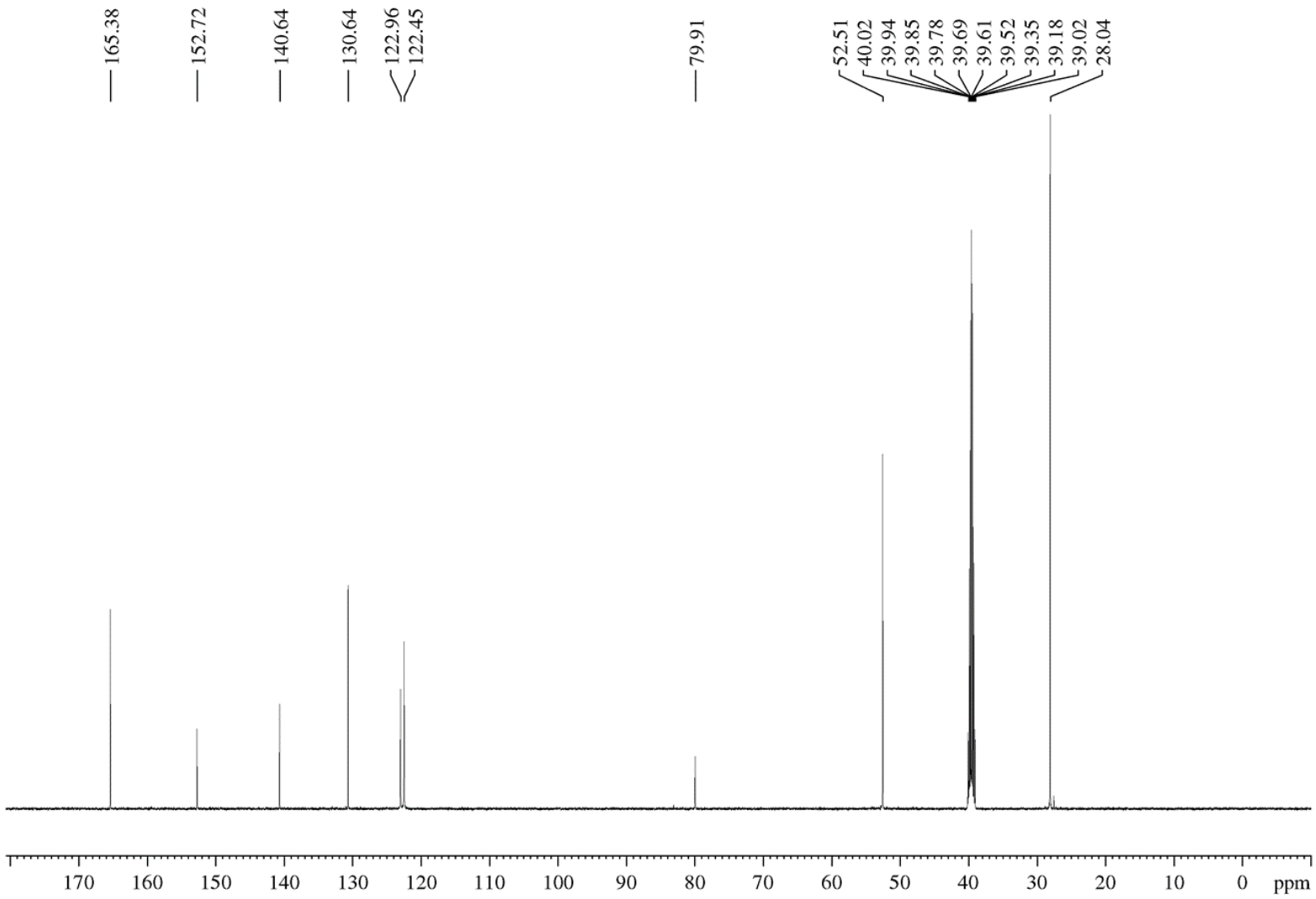

Figure A58. $^{13}C\{^{1}H\}$-UDEFT NMR spectrum of *anti*-rotamers (set **A**) of compound **1** in DMSO-d_6. Peak associated with DCM residue is denoted with the symbol (*). Figure reported in (Khozeimeh Sarbisheh *et al*., 2020).[160]

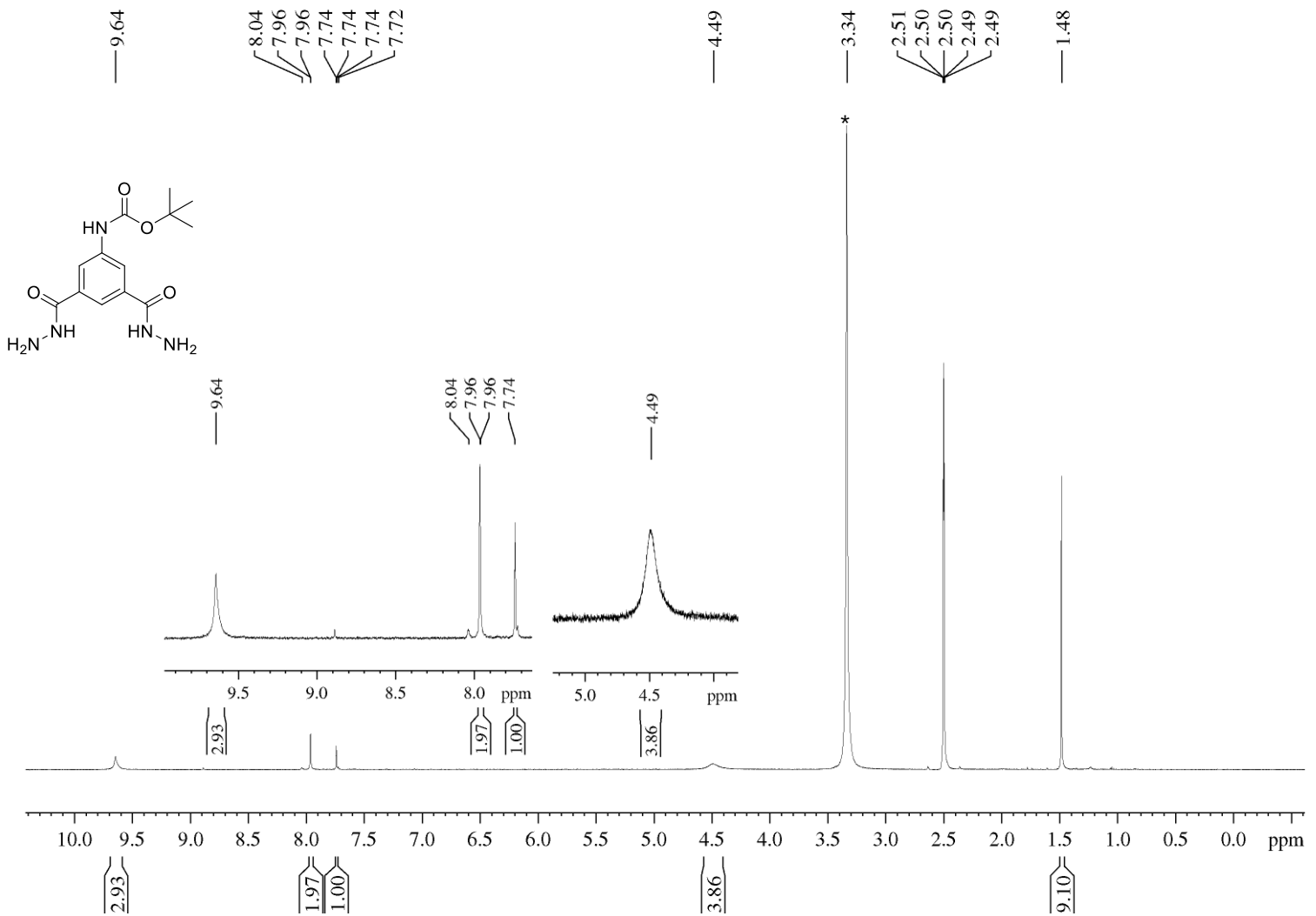

Figure A59. ^{1}H NMR spectrum of compound **2** in DMSO-d_6. Peak associated with water residue is denoted with the symbol (*).Figure reported in (Khozeimeh Sarbisheh *et al.*, 2020).[160]

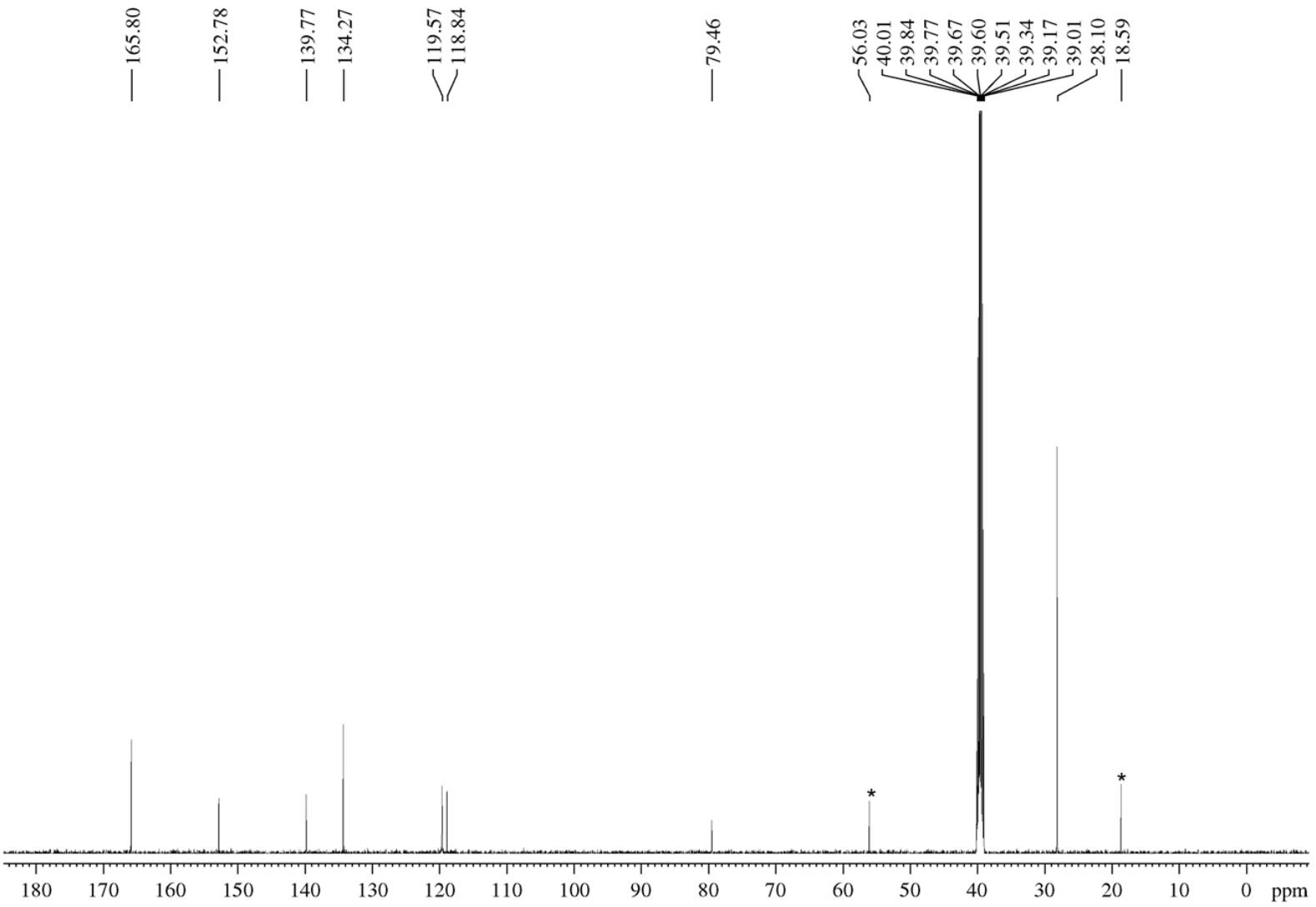

Figure A60. $^{13}C\{^{1}H\}$-UDEFT NMR spectrum of compound **2** in DMSO-d_6. Peaks associated with EtOH residues are denoted with the symbol (*). Figure reported in (Khozeimeh Sarbisheh *et al*., 2020).[160]

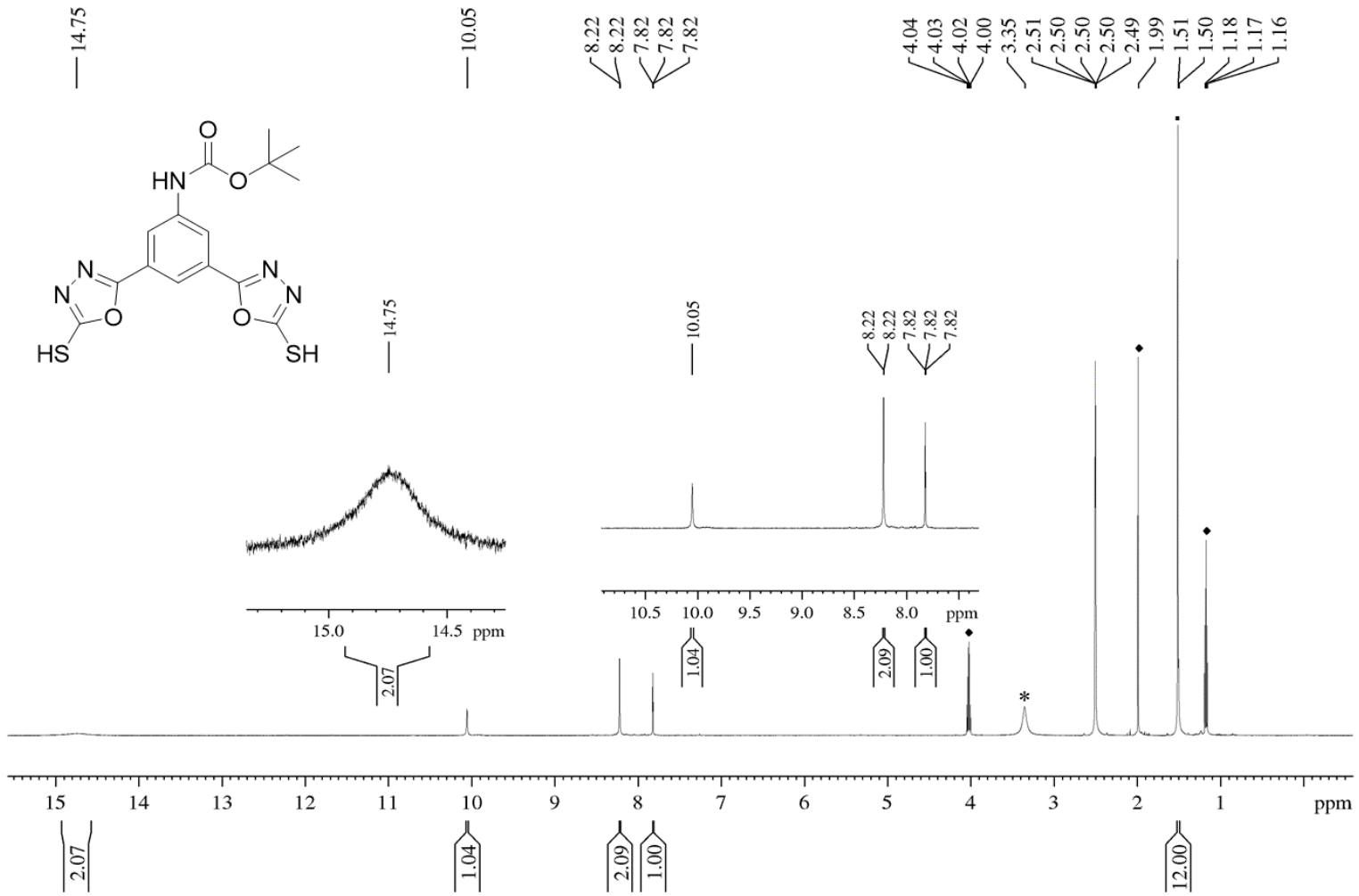

Figure A61. ^{1}H NMR spectrum of compound **3** in DMSO-d_6. Peak associated with water residue is denoted with the symbol (*). Peaks associated with EtOAc residues are denoted with the symbol (♦). The presence of residual Di-*tert*-butyl decarbonate impurity denoted with the symbol (⋆). Figure reported in (Khozeimeh Sarbisheh *et al*., 2020).[160]

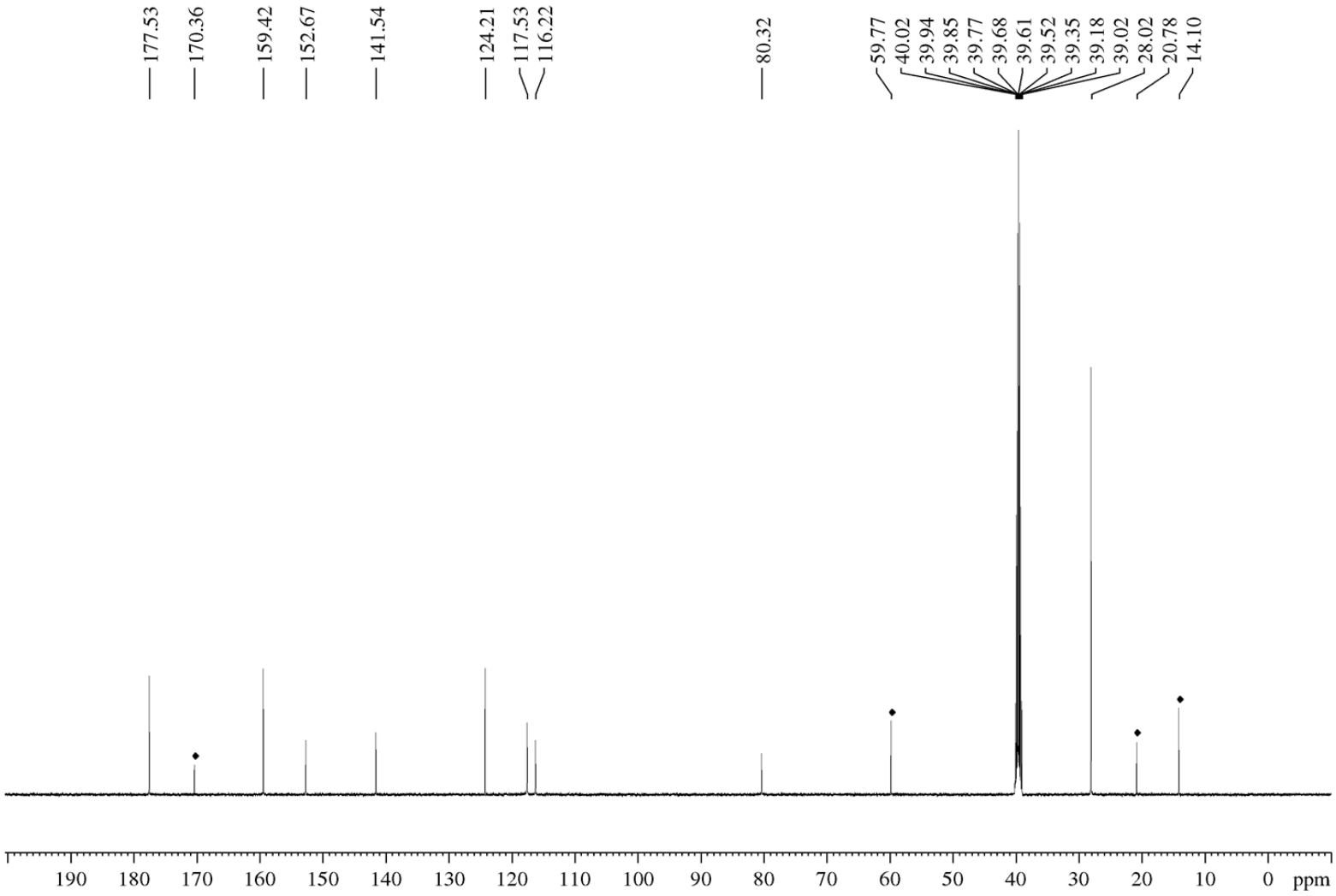

Figure A62. $^{13}C\{^{1}H\}$-UDEFT NMR spectrum of compound **3** in DMSO-d_6. Peaks associated with EtOAc residues are denoted with the symbol (♦). Figure reported in (Khozeimeh Sarbisheh *et al*., 2020).[160]

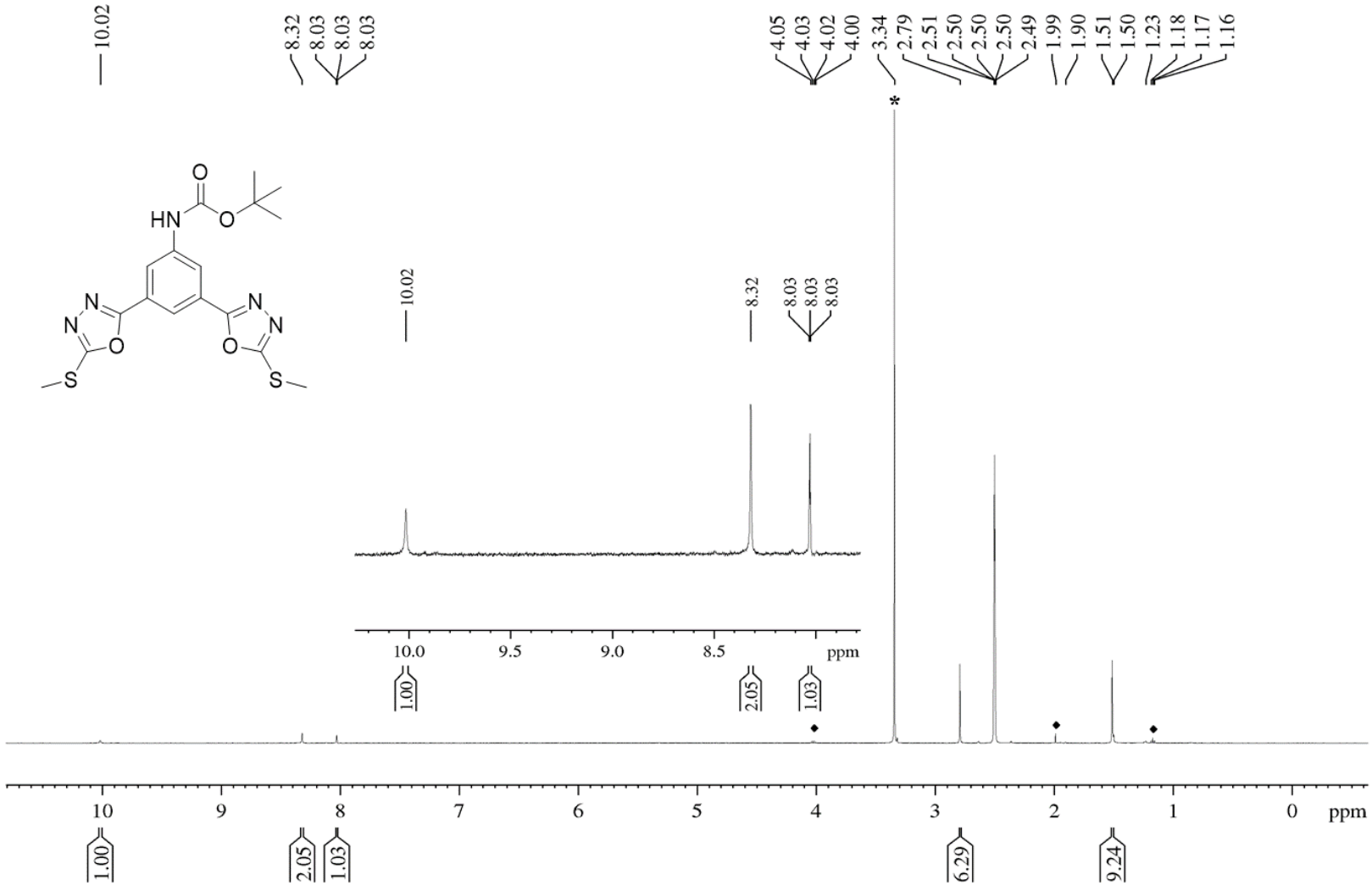

Figure A63. ^{1}H NMR spectrum of compound **4** in DMSO-d_6. Peak associated with water residue is denoted with the symbol (*). Peaks associated with EtOAc residues are denoted with the symbol (♦). Figure reported in (Khozeimeh Sarbisheh *et al*., 2020).[160]

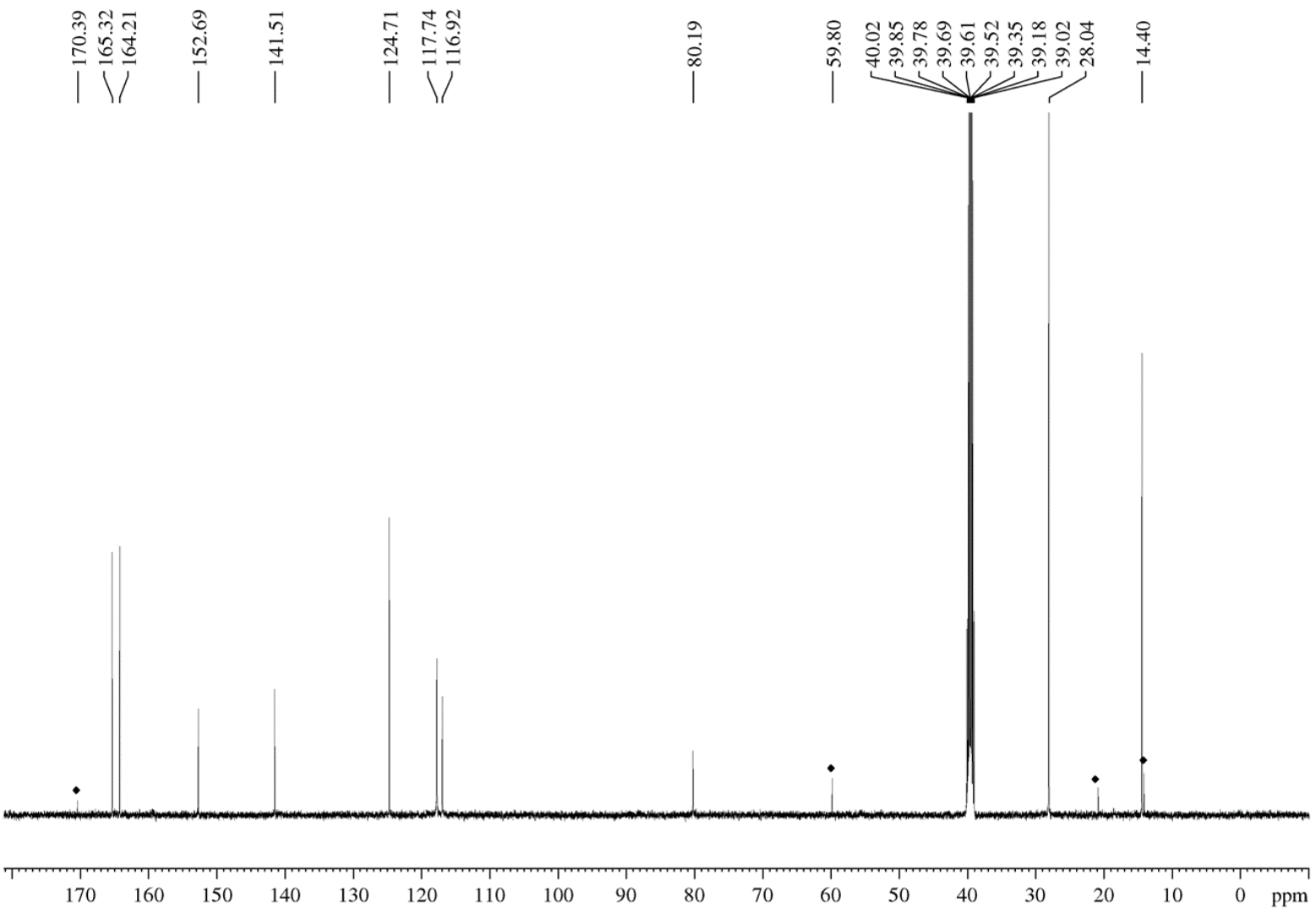

Figure A64. $^{13}C\{^{1}H\}$-UDEFT NMR spectrum of compound **4** in DMSO-d_6. Peaks associated with EtOAc residues are denoted with the symbol (♦). Figure reported in (Khozeimeh Sarbisheh *et al*., 2020).[160]

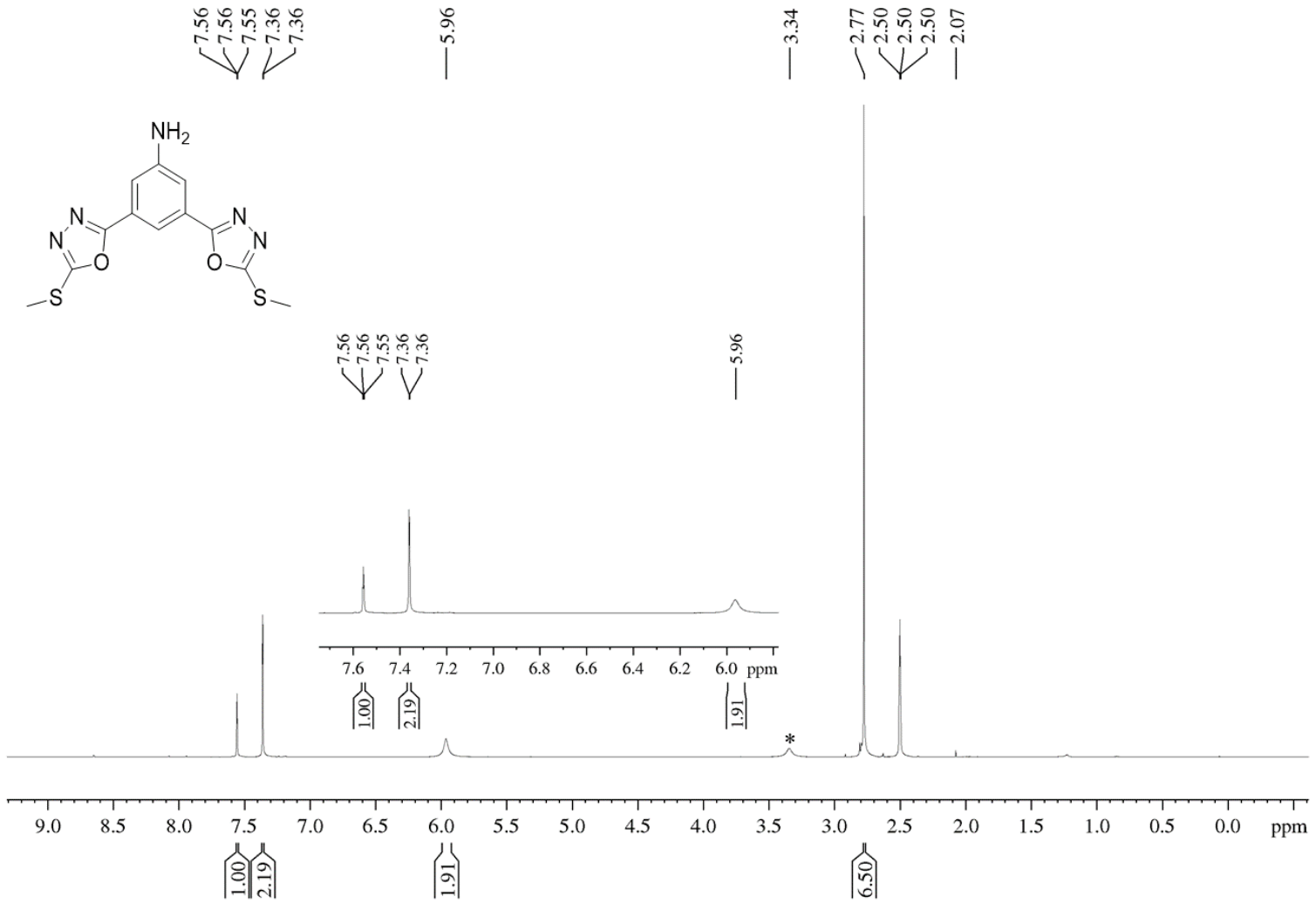

Figure A65. ^{1}H NMR spectrum of compound **7** in DMSO-d_6. Peak associated with water residue is denoted with the symbol (*). Figure reported in (Khozeimeh Sarbisheh *et al*., 2020).[160]

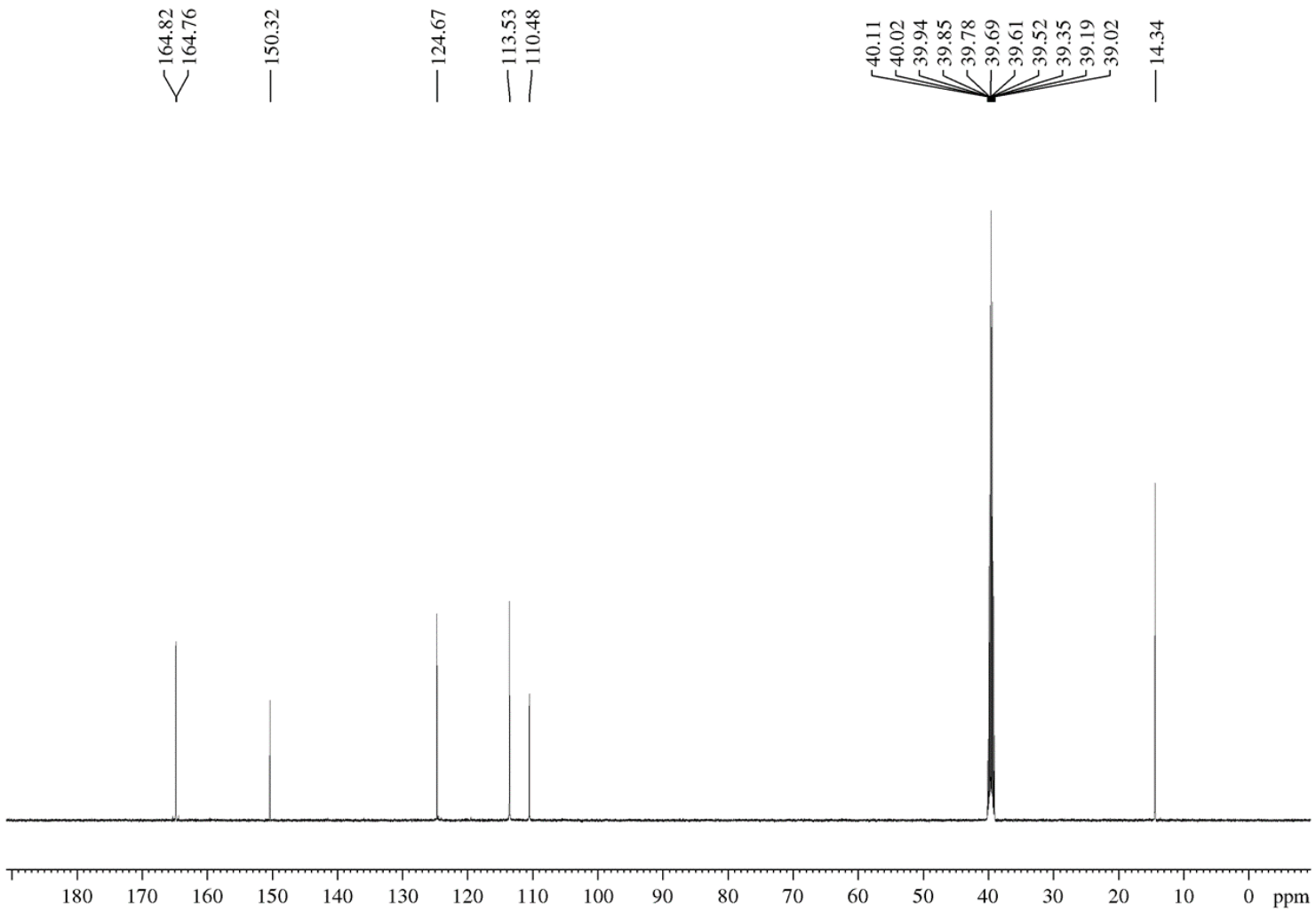

Figure A66. $^{13}C\{^{1}H\}$-UDEFT NMR spectrum of compound **7** in DMSO-d_6. Figure reported in (Khozeimeh Sarbisheh *et al.*, 2020).[160]

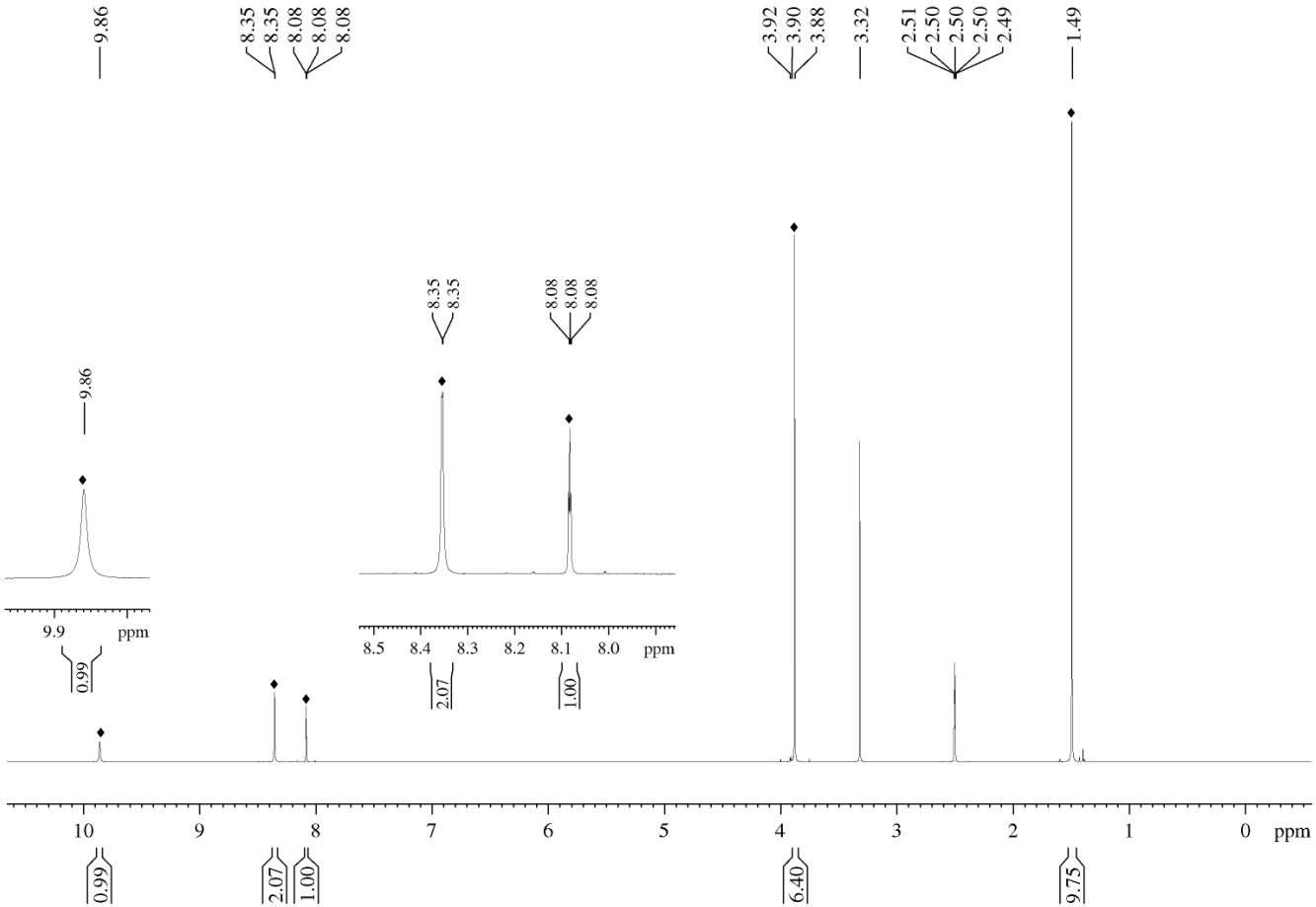

Figure A67. [1]H NMR spectrum of the *anti*-rotamers of compound **1** in DMSO-d_6 solvent at 25 °C. Peaks associated with set **A** (*anti*-**1**) are designated by the symbol ♦. Figure reported in (Khozeimeh Sarbisheh *et al*., 2020).[160]

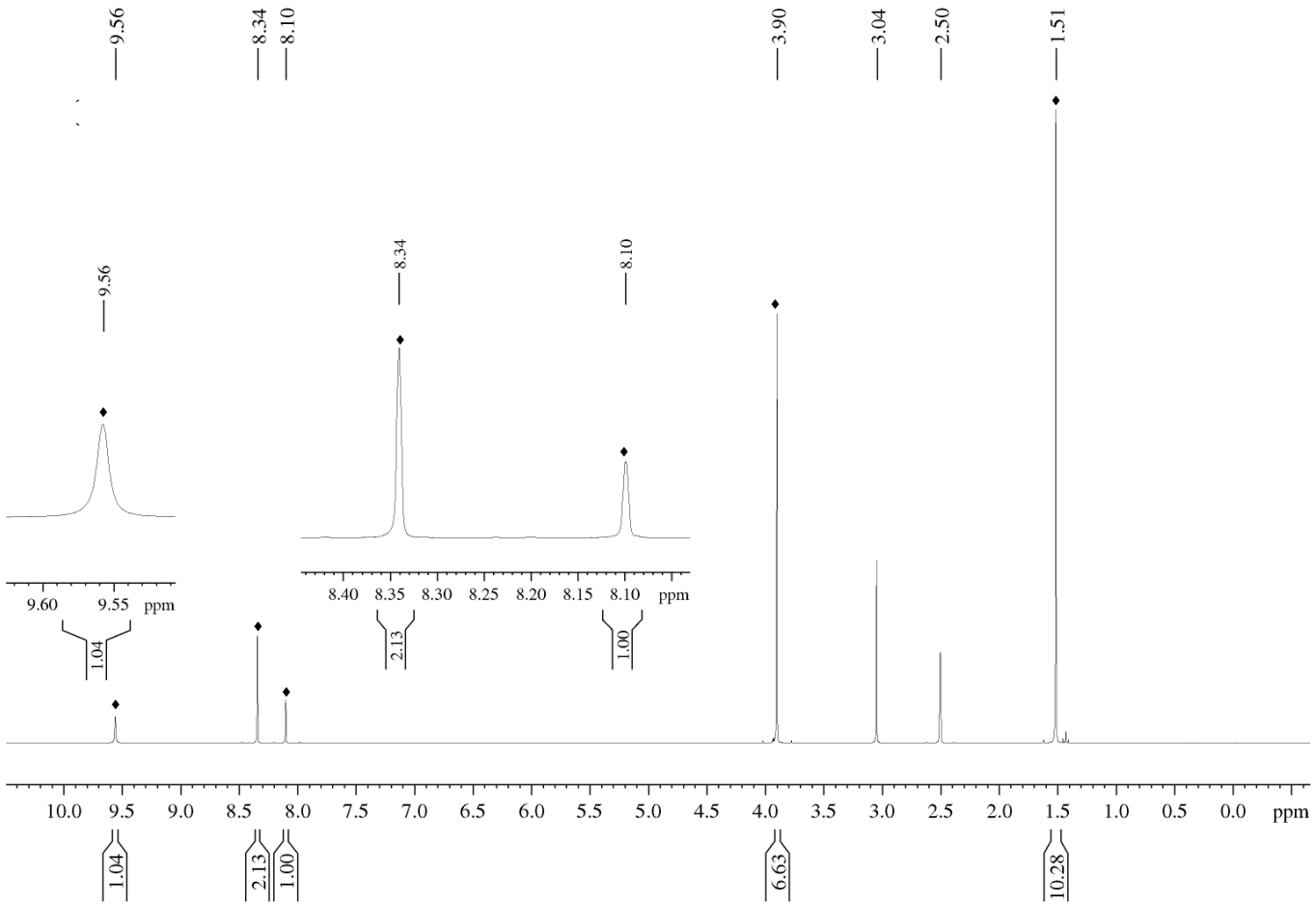

Figure A68. ^{1}H NMR spectrum of the *anti*-rotamers of compound **1** in DMSO-d_6 solvent at 75 °C. Peaks associated with set **A** (*anti*- **1**) are designated by the symbol ♦. Figure reported in (Khozeimeh Sarbisheh *et al*., 2020).[160]

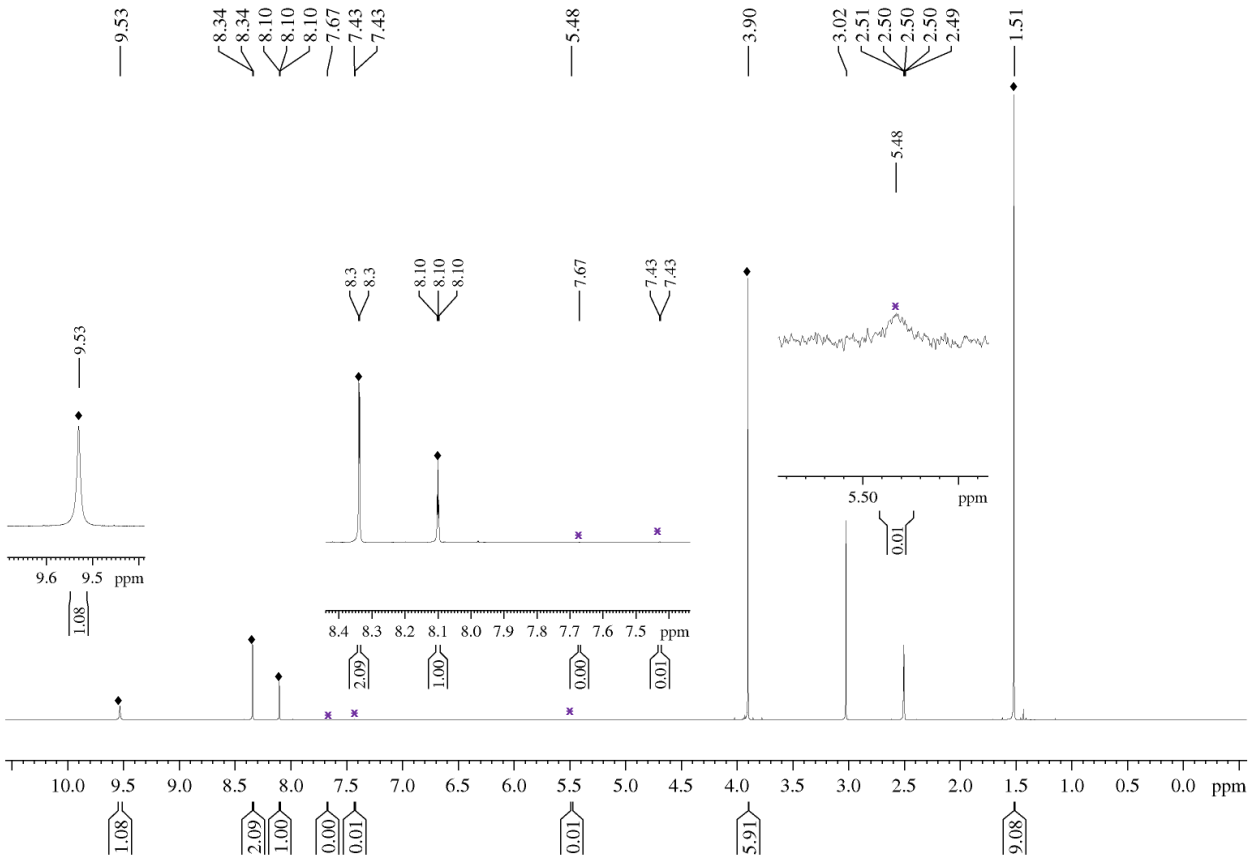

Figure A69. ^{1}H NMR spectrum of the *anti*-rotamers of compound **1** in DMSO-d_6 solvent at 80 °C. Peaks associated with set **A** (*anti*-**1**) and the deprotected derivative of compound **1** are designated by the symbols ♦ and x respectively. Figure reported in (Khozeimeh Sarbisheh *et al.*, 2020).[160]

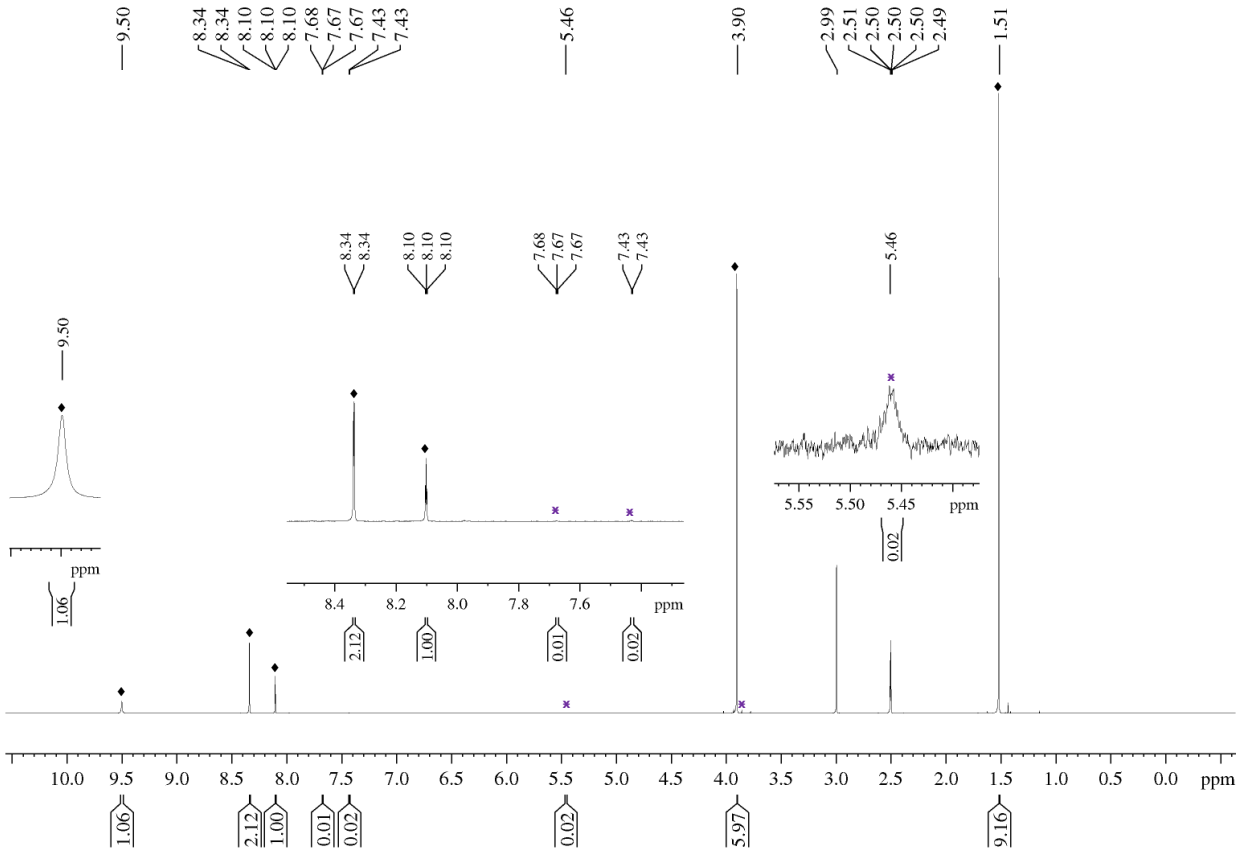

Figure A70. ^{1}H NMR spectrum of the *anti*-rotamers of compound **1** in DMSO-d_6 solvent at 85 °C. Peaks associated with set **A** (*anti*- **1**) and the deprotected derivative of compound **1** are designated by the symbols ♦ and x respectively. Figure reported in (Khozeimeh Sarbisheh et al., 2020).[160]

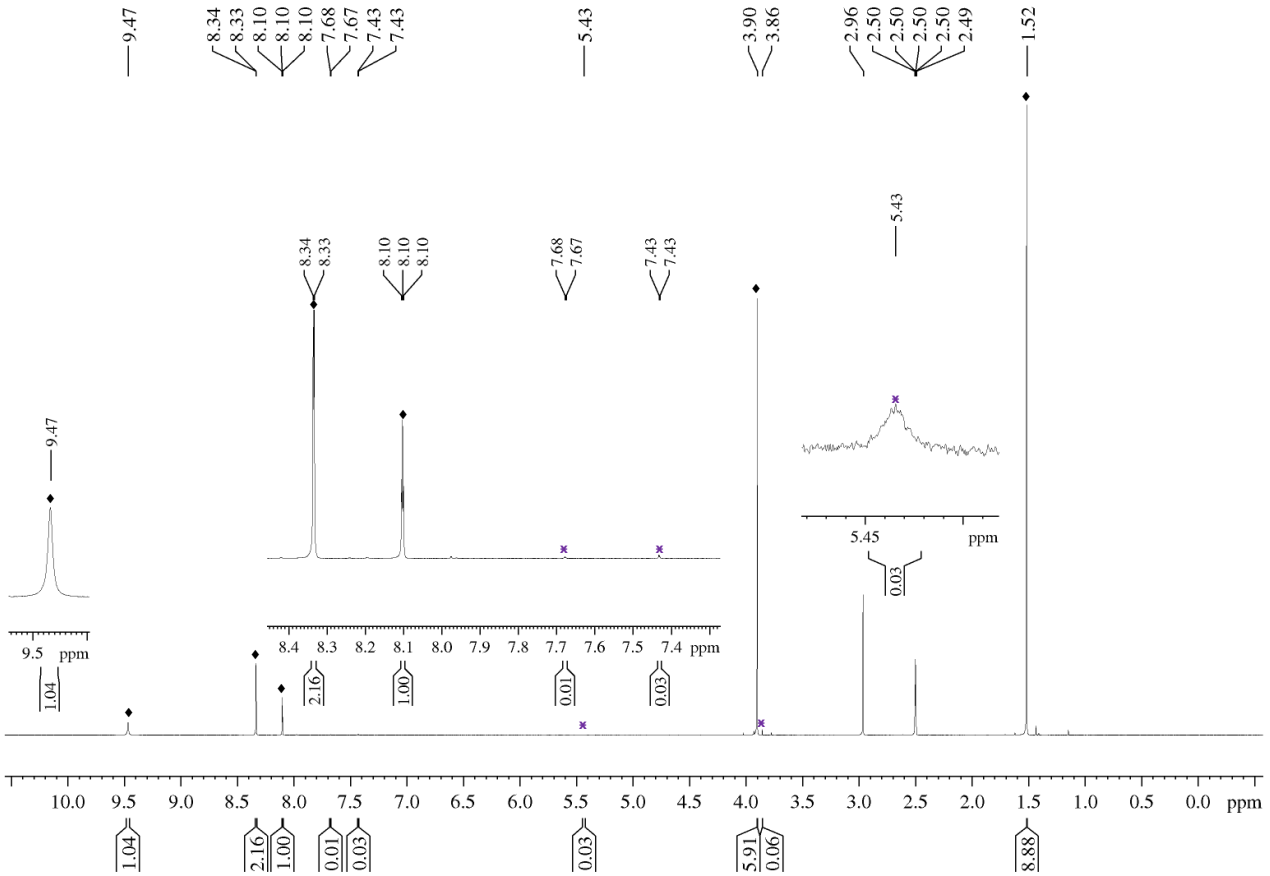

Figure A71. [1]H NMR spectrum of the *anti*-rotamers of compound **1** in DMSO-d_6 solvent at 90 °C. Peaks associated with set **A** (*anti*-**1**) and the deprotected derivative of compound **1** are designated by the symbols ♦ and x respectively. Figure reported in (Khozeimeh Sarbisheh et al., 2020).[160]

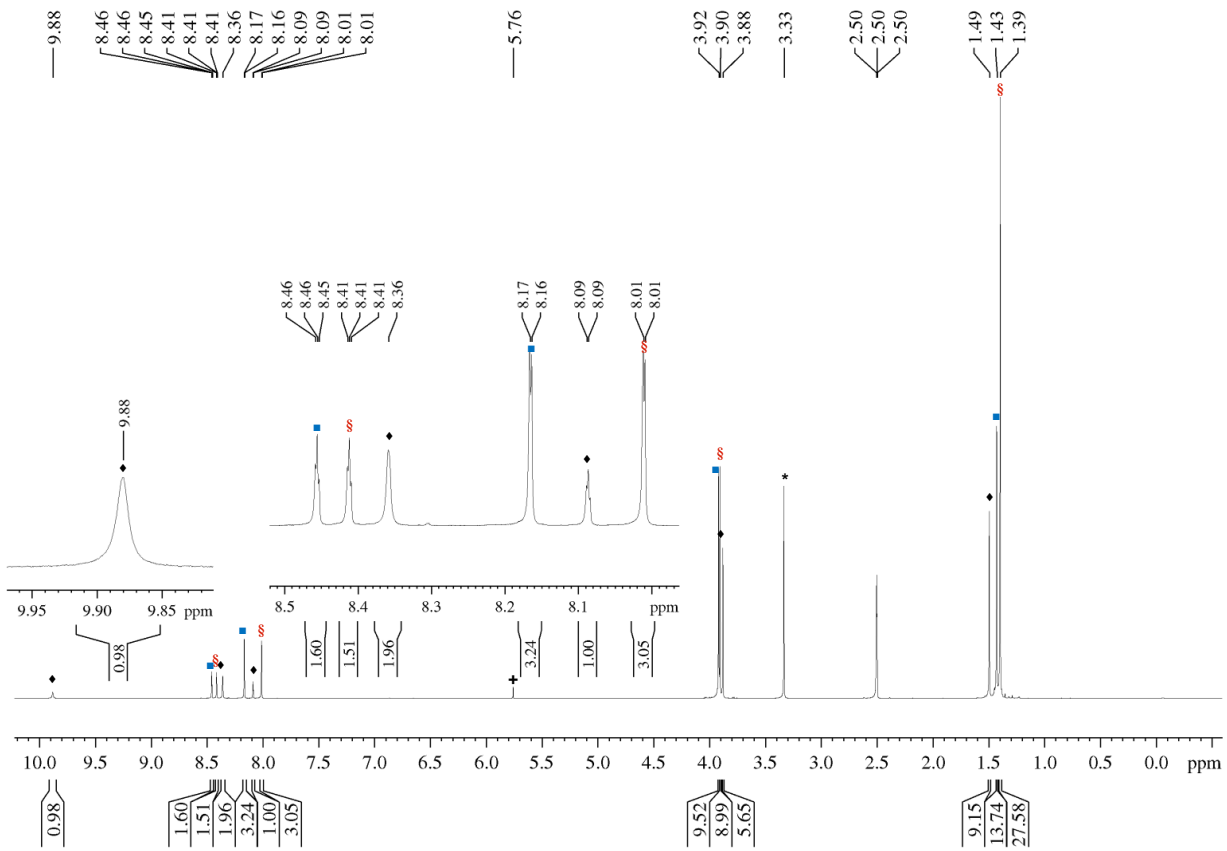

Figure A72. ^{1}H NMR spectrum of compound **1** product mixture in DMSO-d_6 solvent at 25 °C. Peaks associated with set **A** (*anti*-rotamers of compound **1**, *anti*-**1**), set **B** [doubly Boc-protected derivative of compound **1**, $(Boc)_2$-**1**], and set **C** (imidic acid tautomers of compound **1**, tautomer-**1**) are designated by the symbols ♦, § and ■ respectively. Peak associated with water residue is labeled with the symbol *. Peak associated with residual DCM Solvent is denoted by the symbol +. Figure reported in (Khozeimeh Sarbisheh *et al.*, 2020).[160]

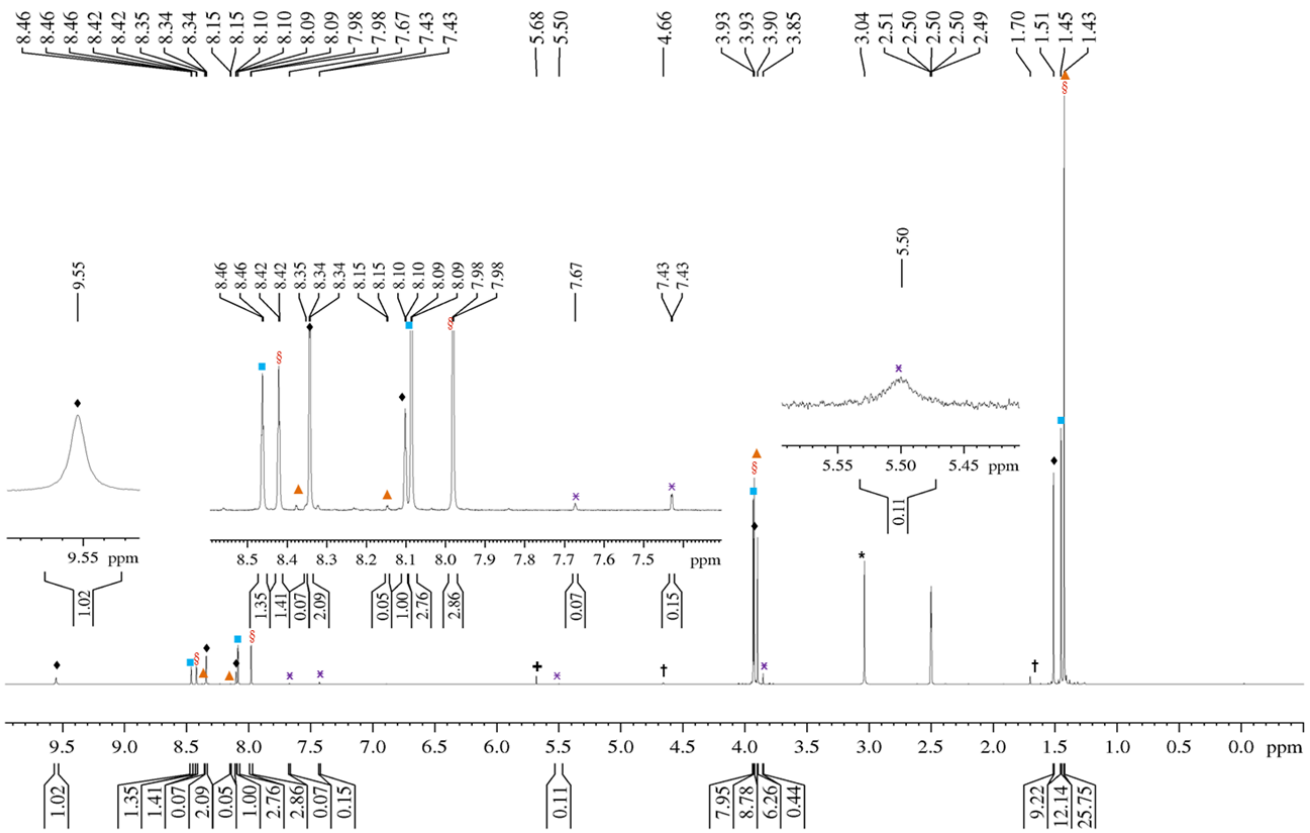

Figure A73. ^{1}H NMR spectrum of compound **1** product mixture in DMSO-d_6 solvent at 75 °C. Peaks associated with set **A** (*anti*-rotamers of compound **1**, *anti*-**1**), set **B** [doubly Boc-protected derivative of compound **1**, $(Boc)_2$-**1**], set **C** (imidic acid tautomers of compound **1,** tautomer-**1**), set **D** (*syn*-rotamers of compound **1**, *syn*-**1**), and the deprotected derivative of compound **1** are designated by the symbols ♦, §, ■, ▲, and x respectively. Peak associated with water residue is labeled with the symbol *. Peak associated with residual DCM solvent is denoted by the symbol +. Peaks associated with isobutylene are denoted by the symbol †. Figure reported in (Khozeimeh Sarbisheh *et al.*, 2020).[160]

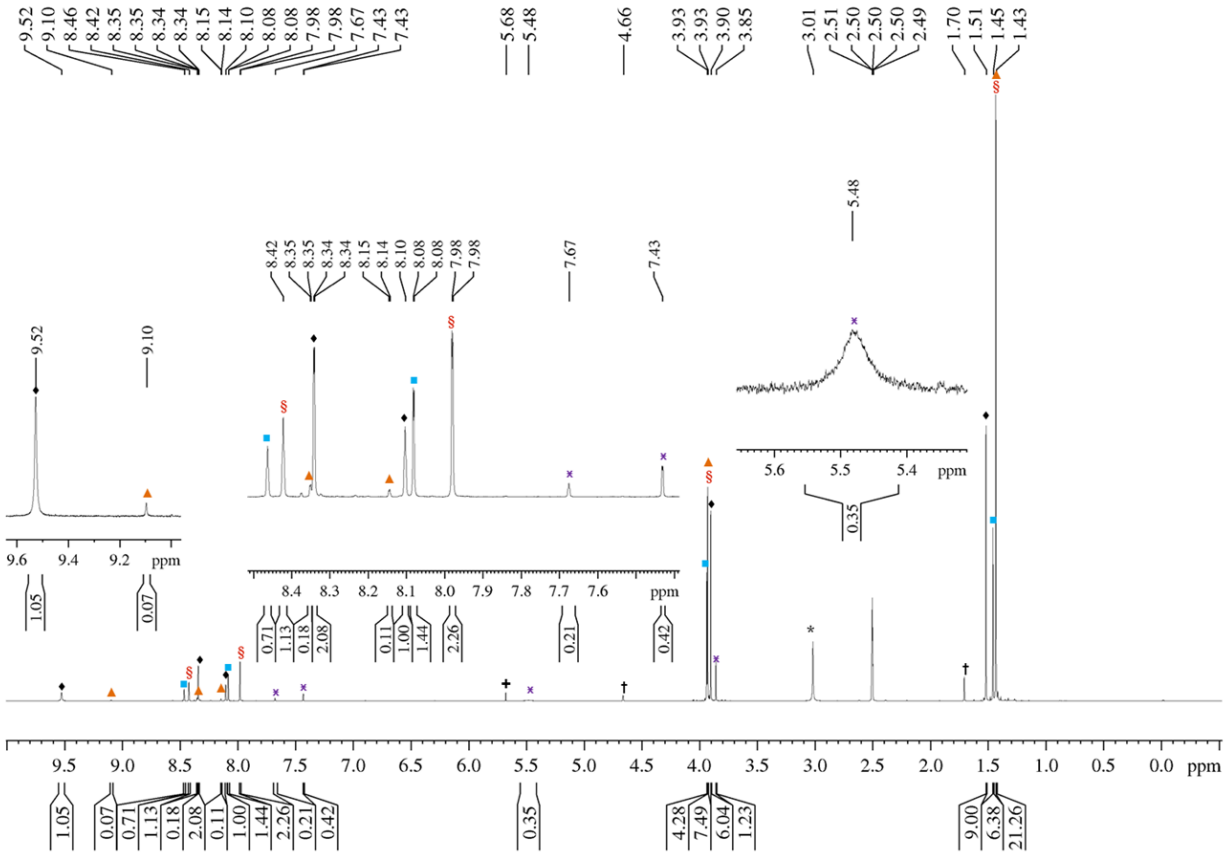

Figure A74. ^{1}H NMR spectrum of compound **1** product mixture in DMSO-d_6 solvent at 80 °C. Peaks associated with set **A** (*anti*-rotamers of compound **1**, *anti*-**1**), set **B** [doubly Boc-protected derivative of compound **1**, $(Boc)_2$-**1**], set **C** (imidic acid tautomers of compound **1,** tautomer-**1**), set **D** (*syn*-rotamers of compound **1**, *syn*-**1**), and the deprotected derivative of compound **1** are designated by the symbols ♦, §, ■, ▲, and x respectively. Peak associated with water residue is labeled with the symbol *. Peak associated with residual DCM solvent is denoted by the symbol +. Peaks associated with isobutylene are denoted by the symbol †. Figure reported in (Khozeimeh Sarbisheh *et al.*, 2020).[160]

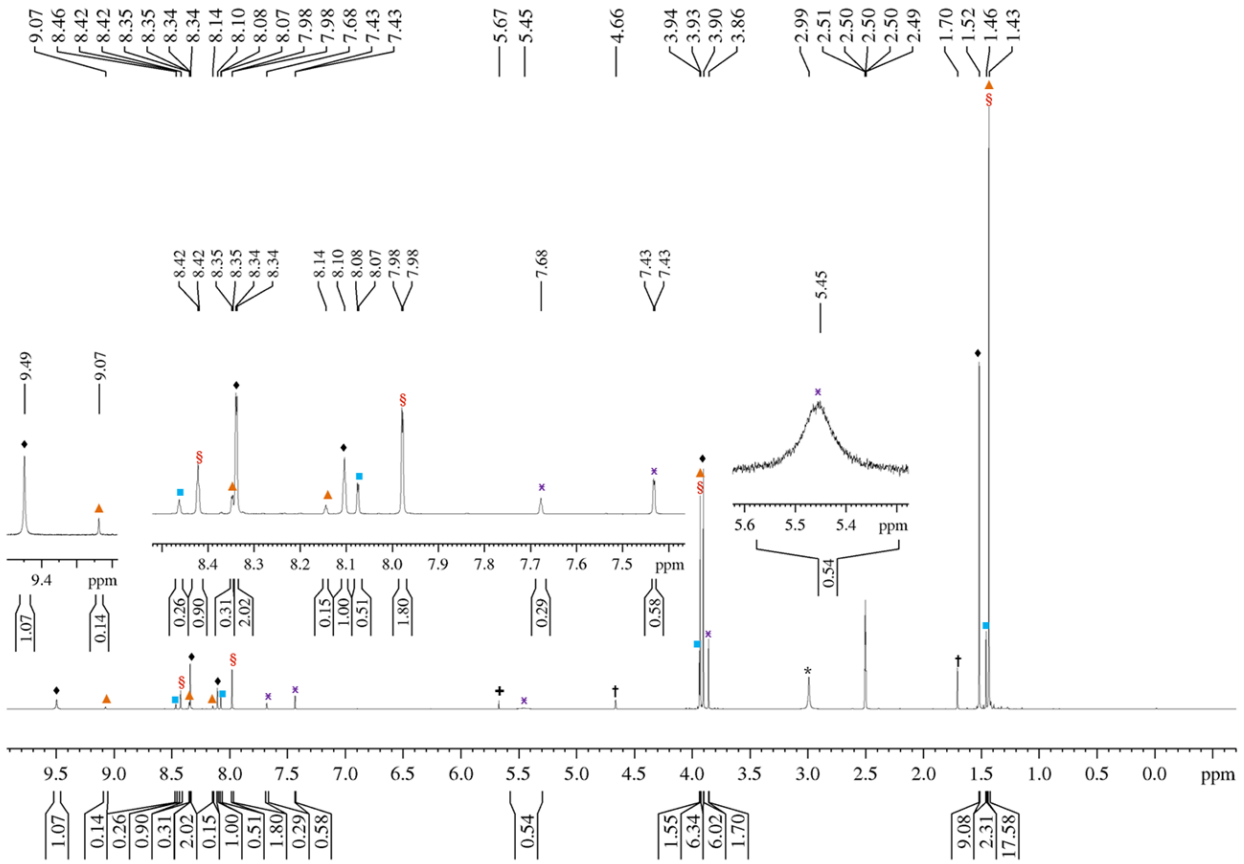

Figure A75. ^{1}H NMR spectrum of compound **1** product mixture in DMSO-d_6 solvent at 85 °C. Peaks associated with set **A** (*anti*-rotamers of compound **1**, *anti*-**1**), set **B** [doubly Boc-protected derivative of compound **1**, $(Boc)_2$-**1**], set **C** (imidic acid tautomers of compound **1,** tautomer-**1**), set **D** (*syn*-rotamers of compound **1**, *syn*-**1**), and the deprotected derivative of compound **1** are designated by the symbols ♦, §, ■, ▲, and x respectively. Peak associated with water residue is labeled with the symbol *. Peak associated with residual DCM solvent is denoted by the symbol +. Peaks associated with isobutylene are denoted by the symbol †. Figure reported in (Khozeimeh Sarbisheh *et al*., 2020).[160]

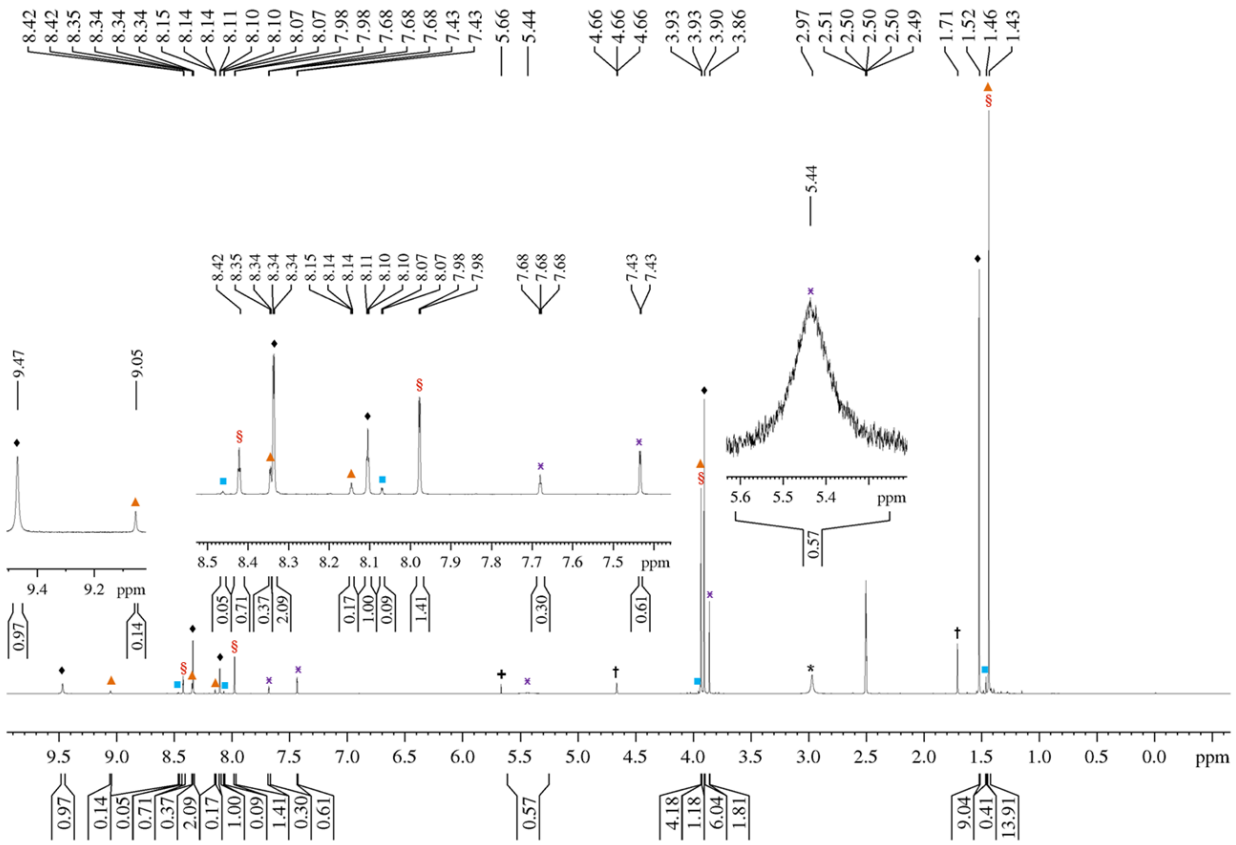

Figure A76. ^{1}H NMR spectrum of compound **1** product mixture in DMSO-d_6 solvent at 90 °C. Peaks associated with set **A** (*anti*-rotamers of compound **1**, *anti*-**1**), set **B** [doubly Boc-protected derivative of compound **1**, $(Boc)_2$-**1**], set **C** (imidic acid tautomers of compound **1,** tautomer-**1**), set **D** (*syn*-rotamers of compound **1**, *syn*-**1**), and the deprotected derivative of compound **1** are designated by the symbols ♦, §, ■, ▲, and x respectively. Peak associated with water residue is labeled with the symbol *. Peak associated with residual DCM solvent is denoted by the symbol +. Peaks associated with isobutylene are denoted by the symbol †. Figure reported in (Khozeimeh Sarbisheh *et al.*, 2020).[160]

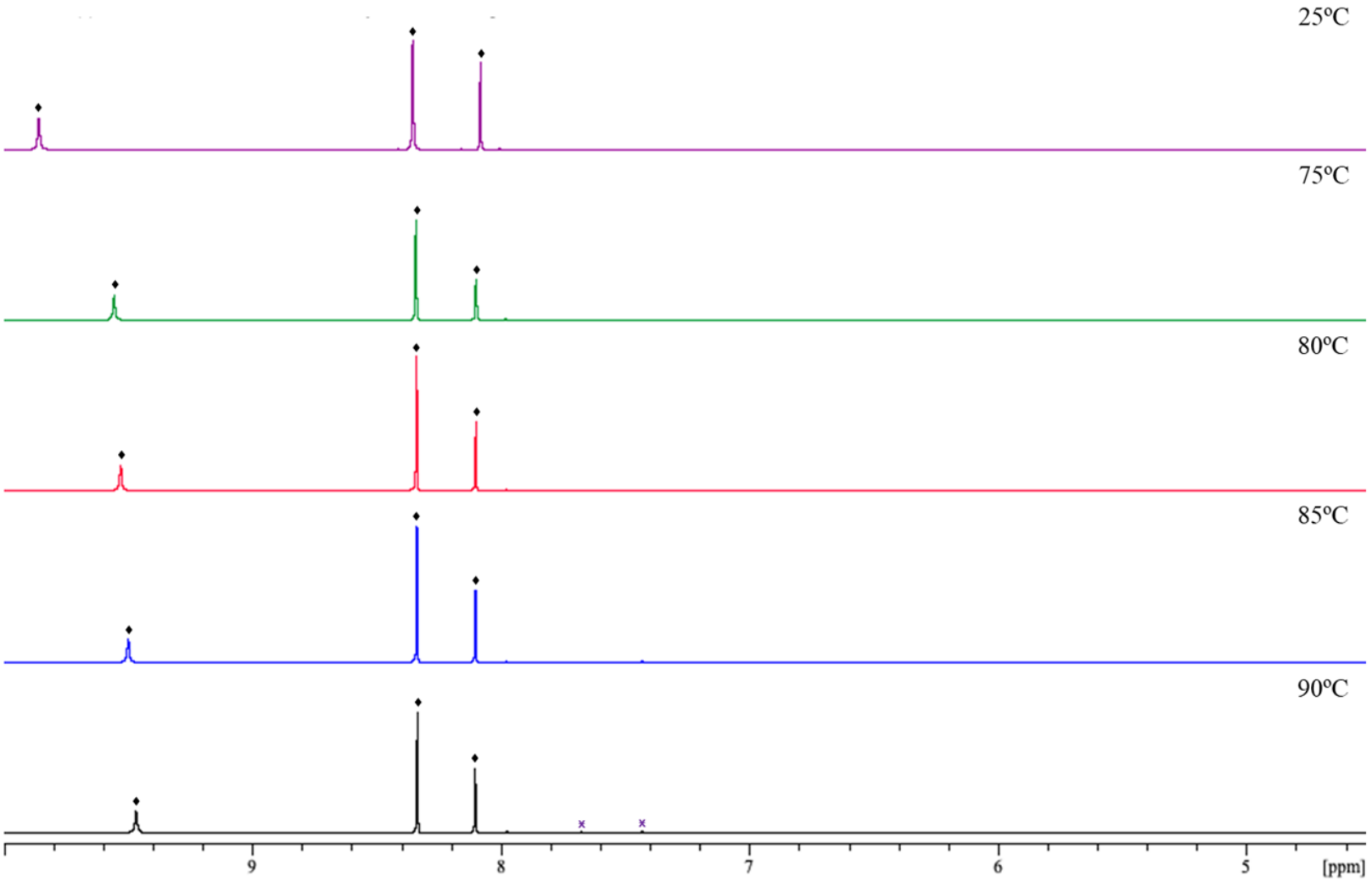

Figure A77. ^{1}H NMR spectrum of the *anti*-rotamers of compound **1** in DMSO-d_6 solvent at 25 °C to 90 °C. Peaks associated with set **A** (*anti*-**1**) and the deprotected derivative of compound **1** are designated by the symbols ♦ and x respectively.

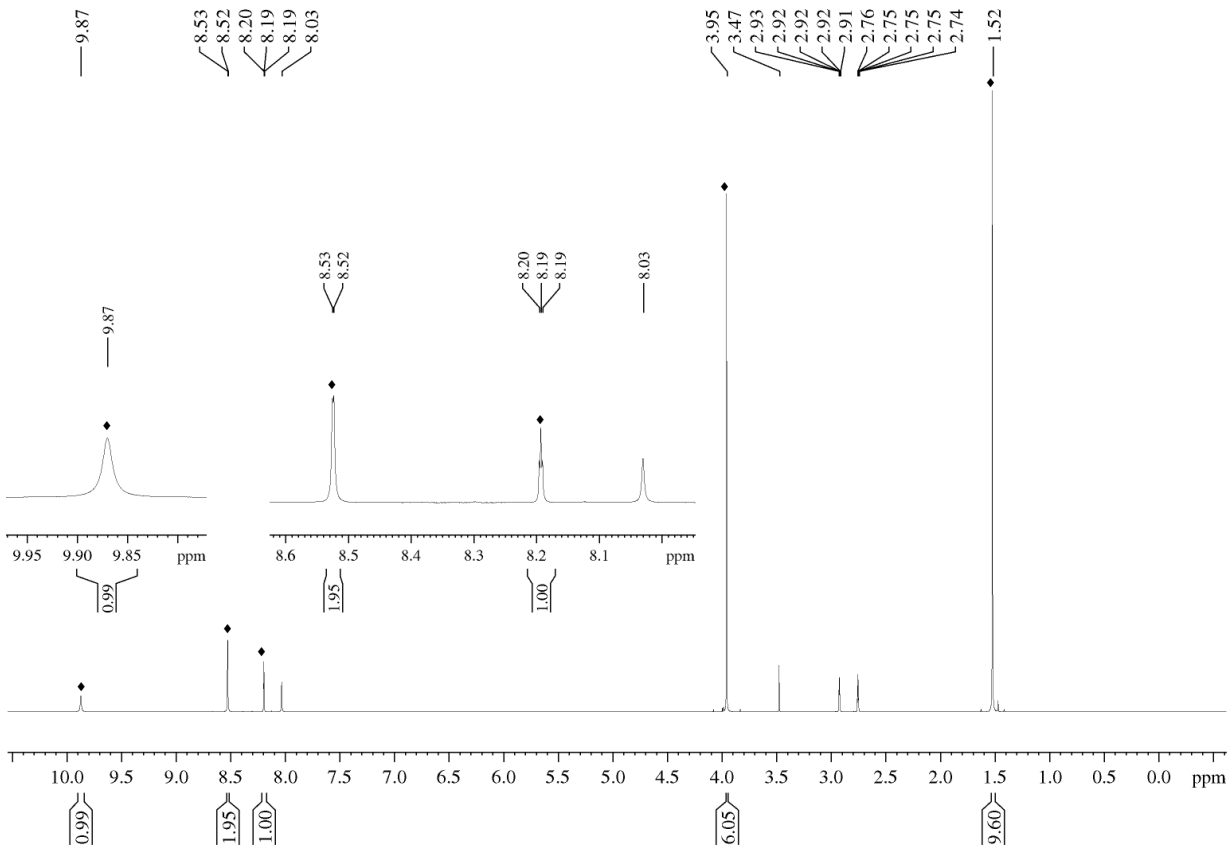

Figure A78. ^{1}H NMR spectrum of the *anti*-rotamers of compound **1** in DMF-d_7 solvent at 25 °C. Peaks associated with set **A** (*anti*-**1**) are designated by the symbol ♦.

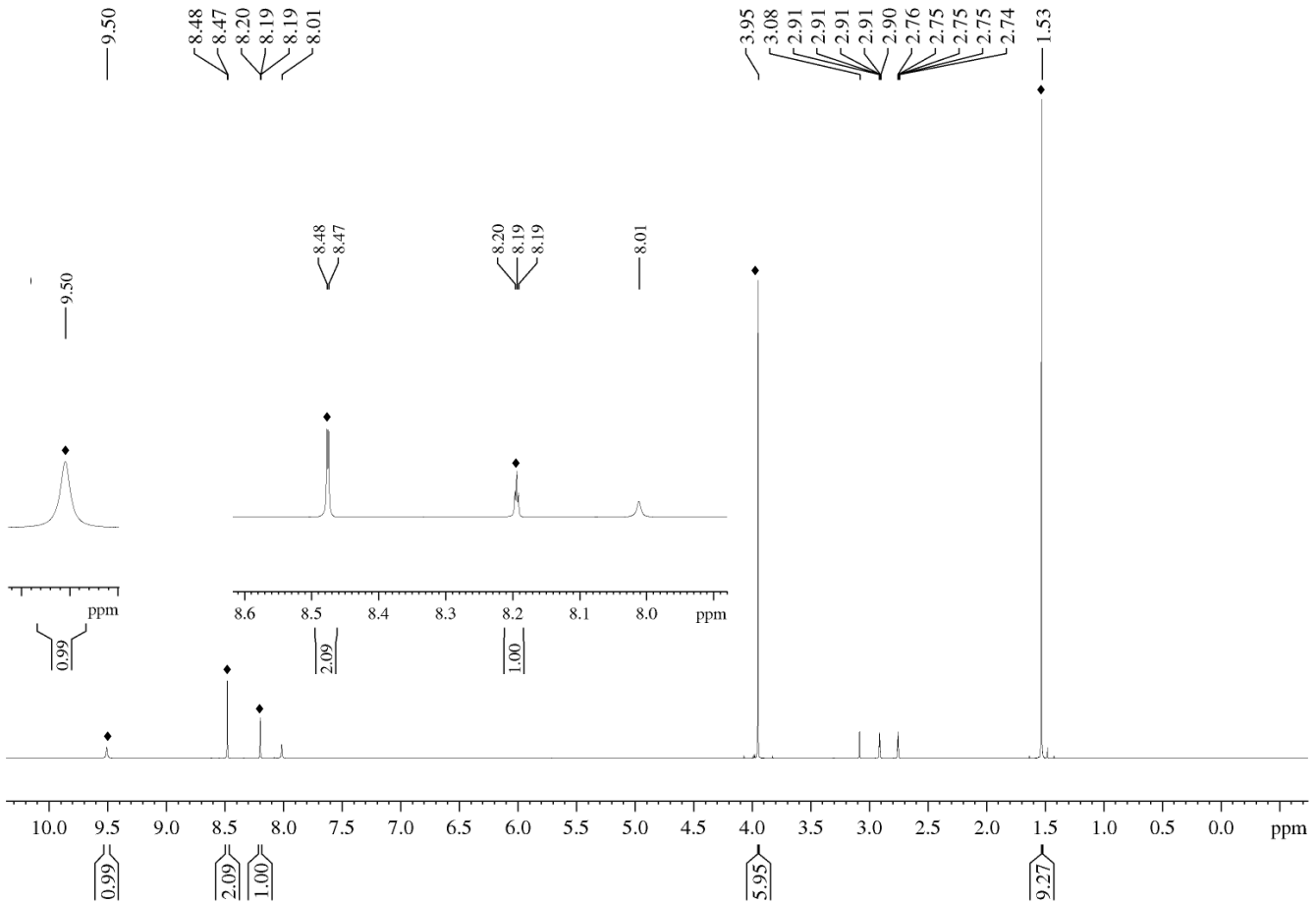

Figure A79. ^{1}H NMR spectrum of the *anti*-rotamers of compound **1** in DMF-d_7 solvent at 75 °C. Peaks associated with set **A** (*anti*-**1**) are designated by the symbol ♦.

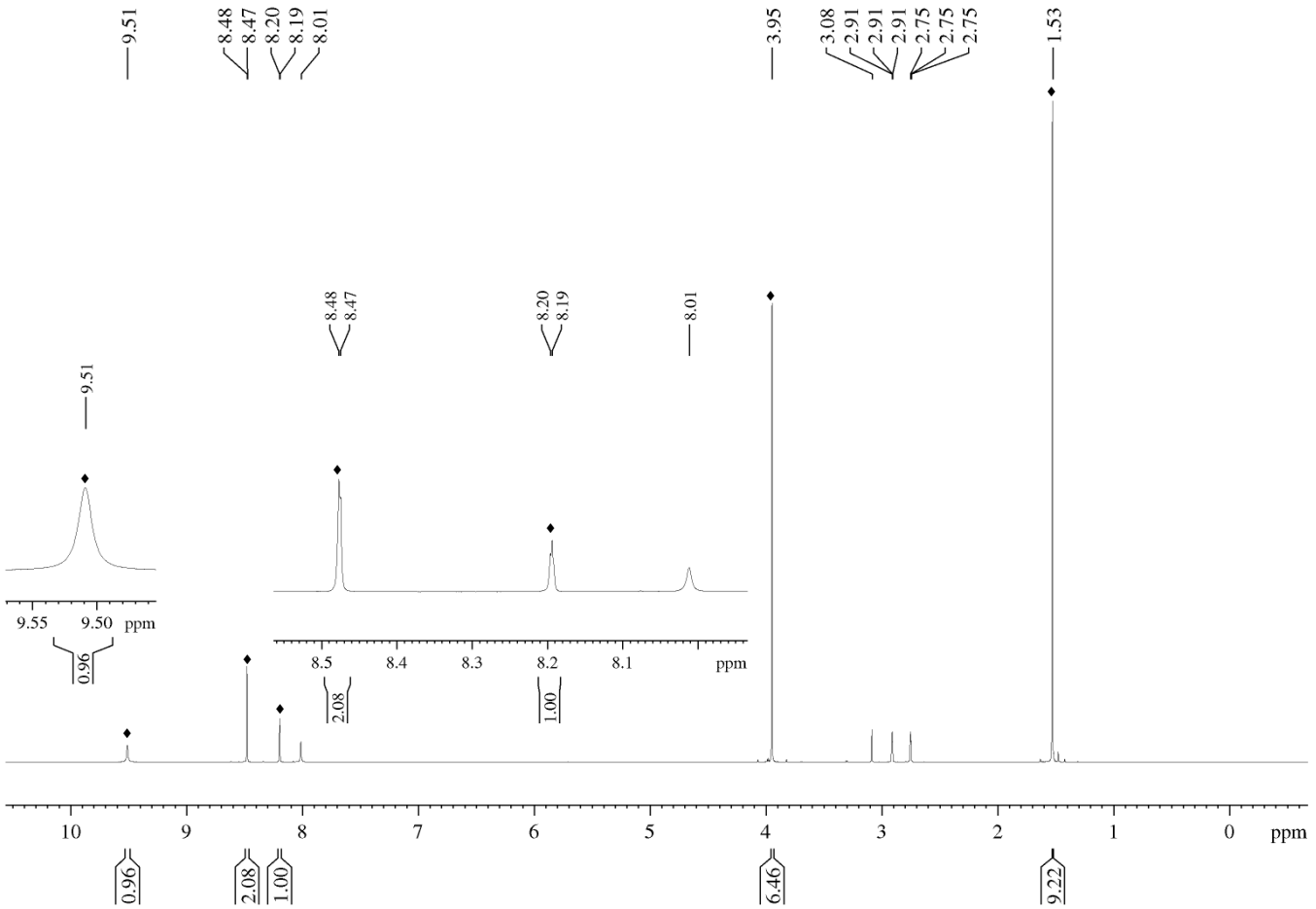

Figure A80. ^{1}H NMR spectrum of the *anti*-rotamers of compound **1** in DMF-d_7 solvent at 80 °C. Peaks associated with set **A** (*anti*-**1**) are designated by the symbol ♦.

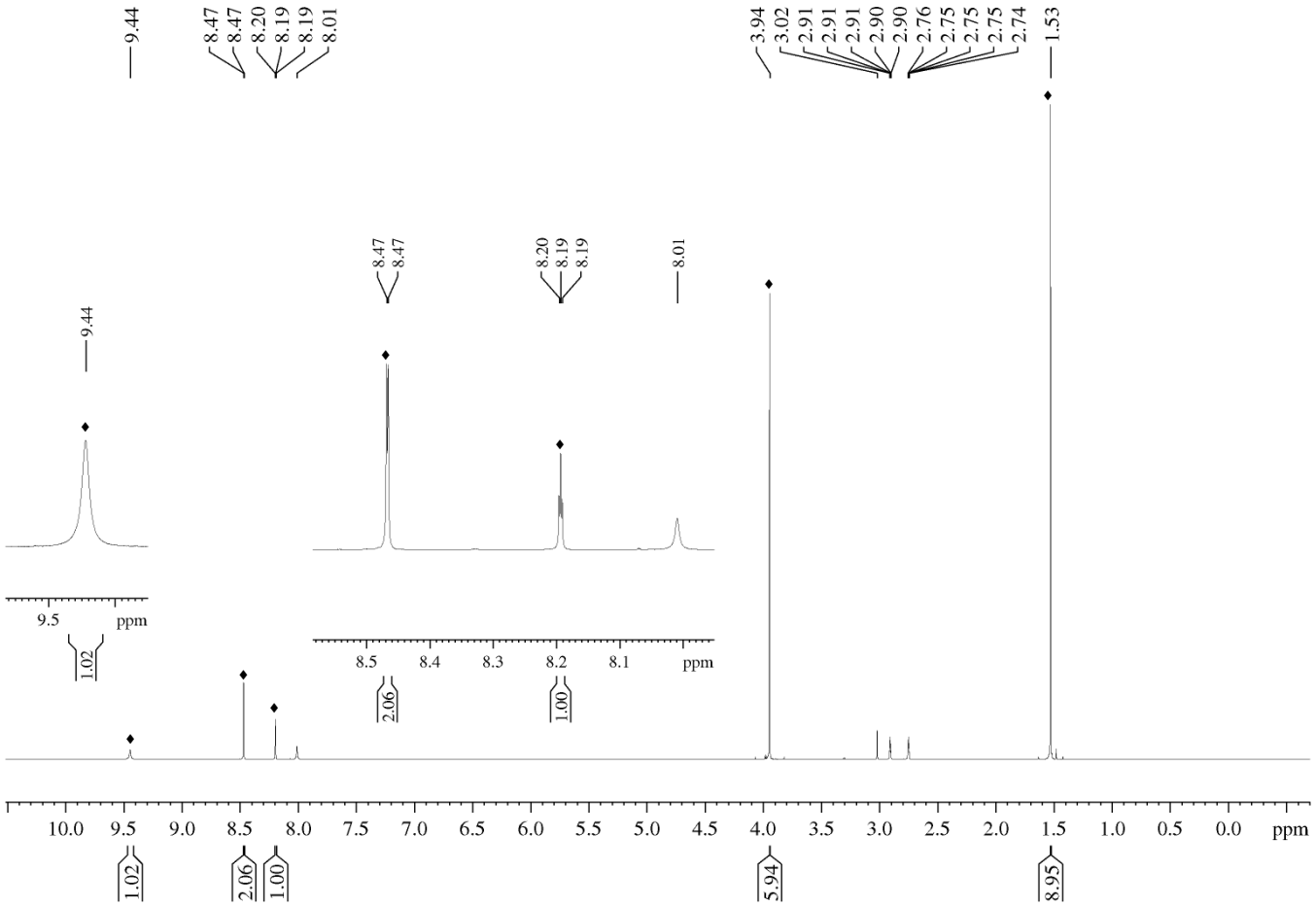

Figure A81. ^{1}H NMR spectrum of the *anti*-rotamers of compound **1** in DMF-d_7 solvent at 85 °C. Peaks associated with set **A** (*anti*-**1**) are designated by the symbol ♦.

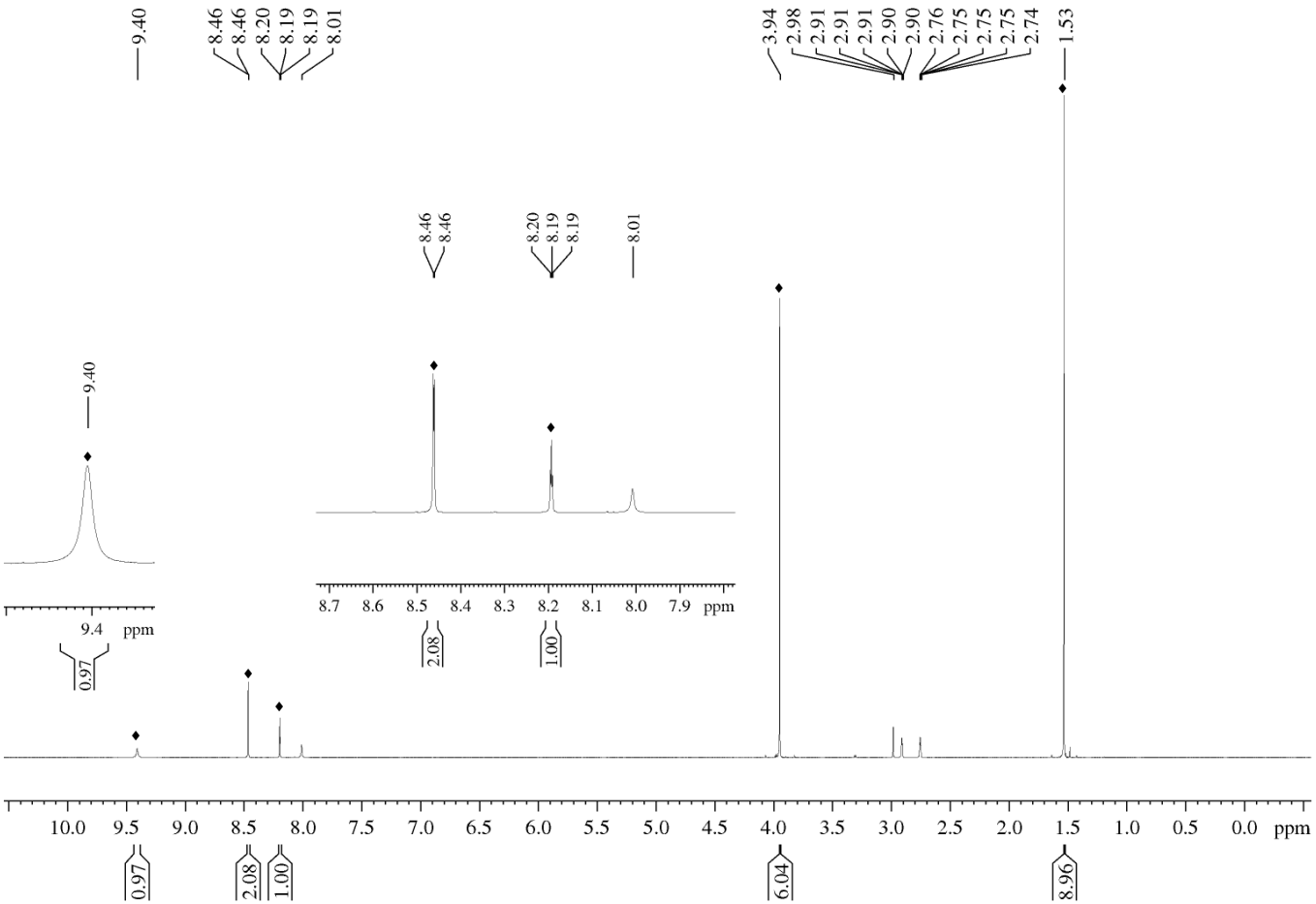

Figure A82. ^{1}H NMR spectrum of the *anti*-rotamers of compound **1** in DMF-d_7 solvent at 90 °C. Peaks associated with set **A** (*anti*-**1**) are designated by the symbol ♦.

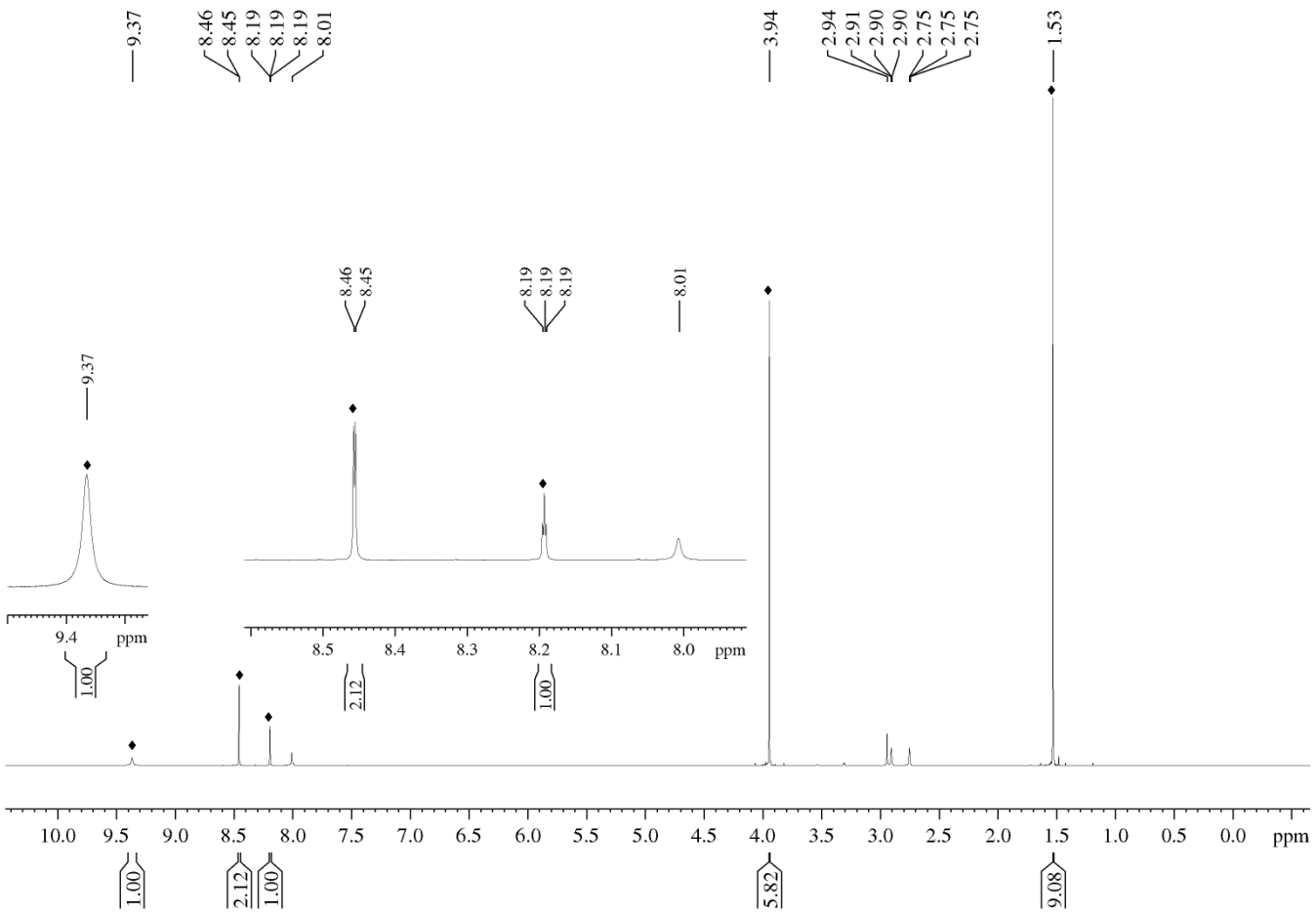

Figure A83. ^{1}H NMR spectrum of the *anti*-rotamers of compound **1** in DMF-d_7 solvent at -40 °C. Peaks associated with set **A** (*anti*-**1**) are designated by the symbol ♦.

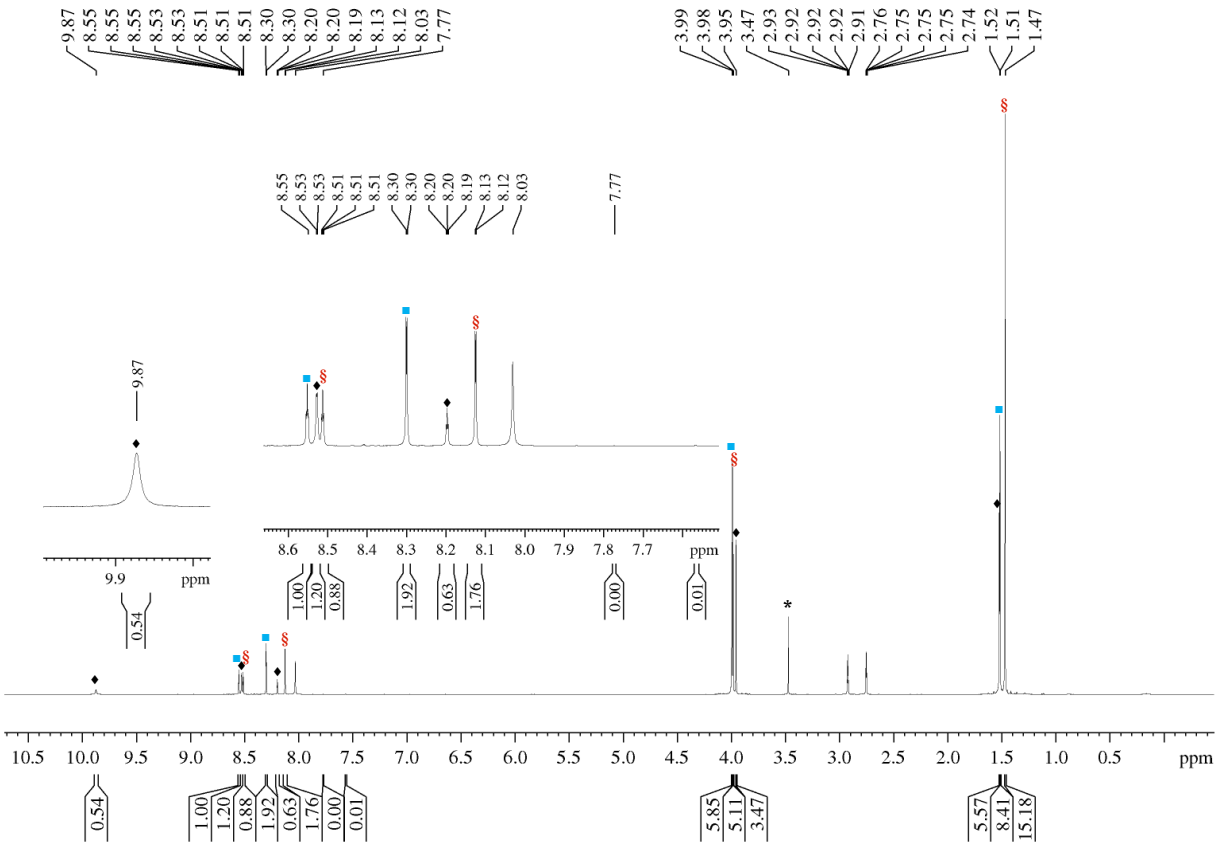

Figure A84. ^{1}H NMR spectrum of compound **1** product mixture in DMF-d_7 solvent at 25 °C. Peaks associated with set **A** (*anti*-rotamers of compound **1**, *anti*-**1**), set **B** [doubly Boc-protected derivative of compound **1**, $(Boc)_2$-**1**], and set **C** (imidic acid tautomers of compound **1**, tautomer-**1**) are designated by the symbols ♦, § and ■ respectively. Peak associated with water residue is labeled with the symbol *.

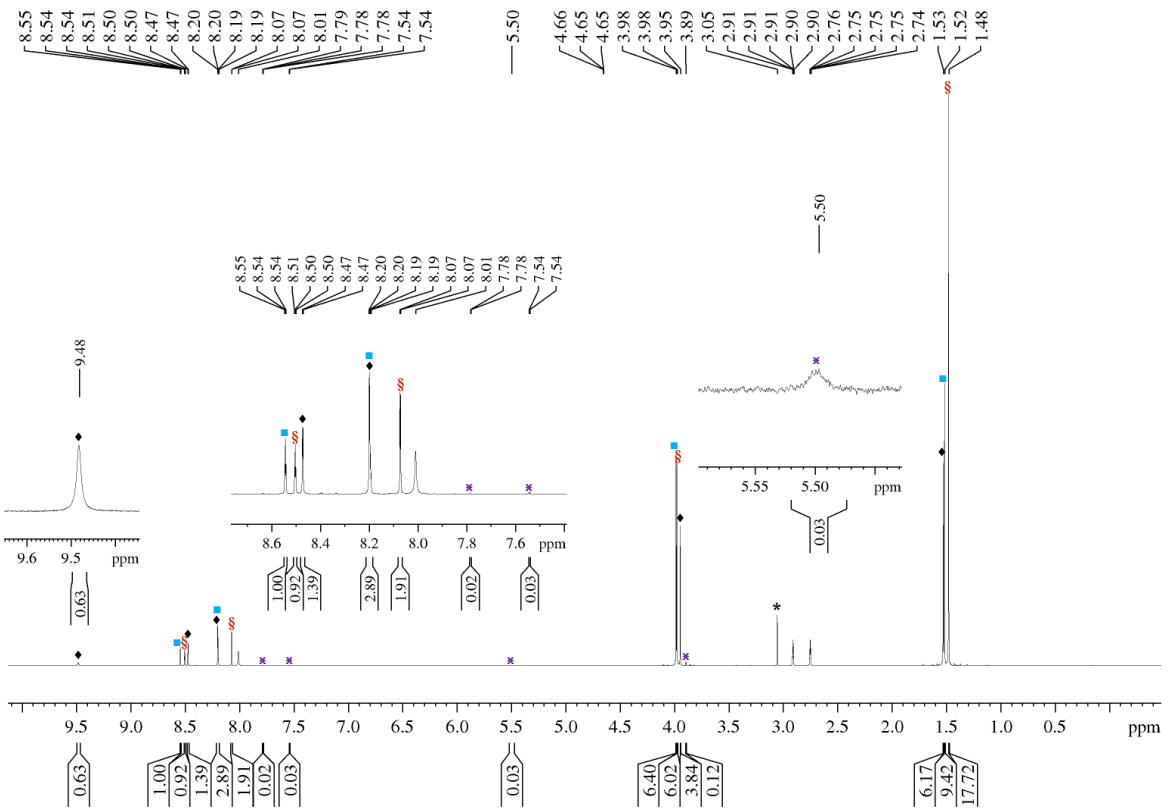

Figure A85. ^{1}H NMR spectrum of compound **1** product mixture in DMF-d_7 solvent at 75 °C. Peaks associated set **A** (*anti*-rotamers of compound **1**, *anti*-**1**), set **B** [doubly Boc-protected derivative of compound **1**, $(Boc)_2$-**1**], and set **C** (imidic acid tautomers of compound **1**, tautomer-**1**), and the deprotected derivative of compound **1** are designated by the symbols ♦, §, ■, and x respectively. Peak associated with water residue is labeled with the symbol *.

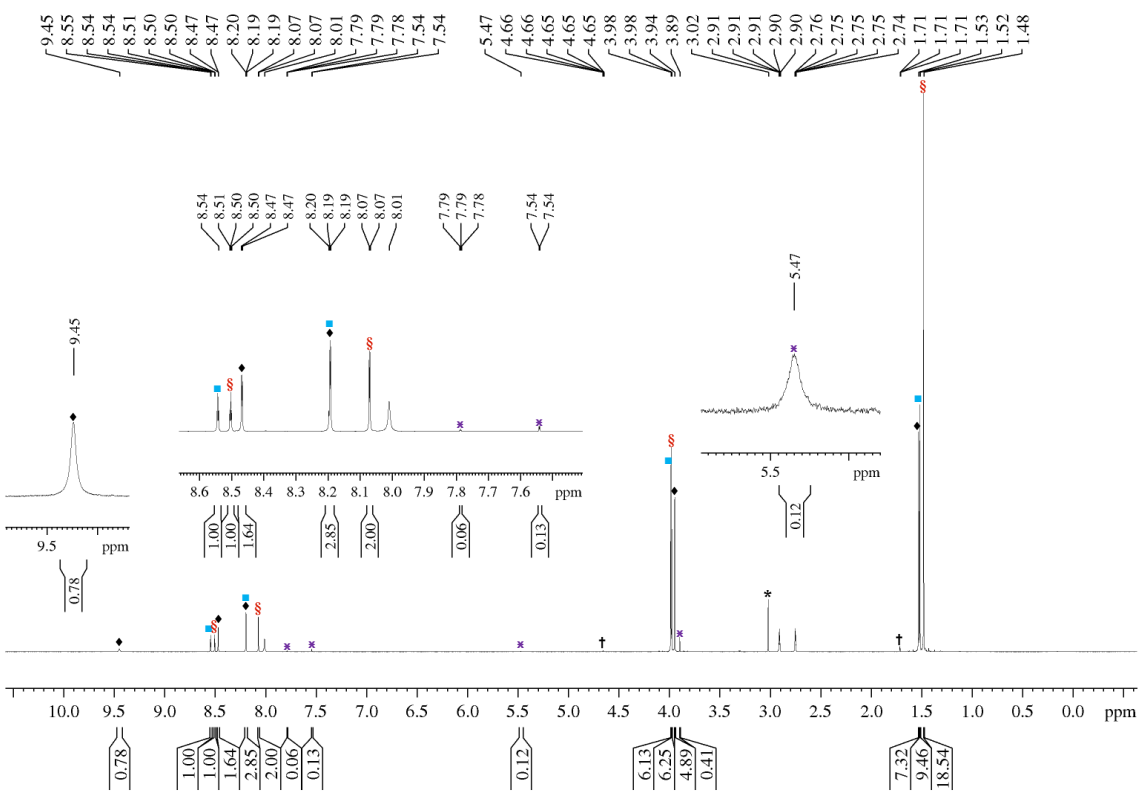

Figure A86. ^{1}H NMR spectrum of compound **1** product mixture in DMF-d_7 solvent at 80 °C. Peaks associated with set **A** (*anti*-rotamers of compound **1**, *anti*-**1**), set **B** [doubly Boc-protected derivative of compound **1**, $(Boc)_2$-**1**], and set **C** (imidic acid tautomers of compound **1**, tautomer-**1**), and the deprotected derivative of compound **1** are designated by the symbols ♦, §, ■, and x respectively. Peak associated with water residue is labeled with the symbol *. Peaks associated with isobutylene are denoted by the symbol †.

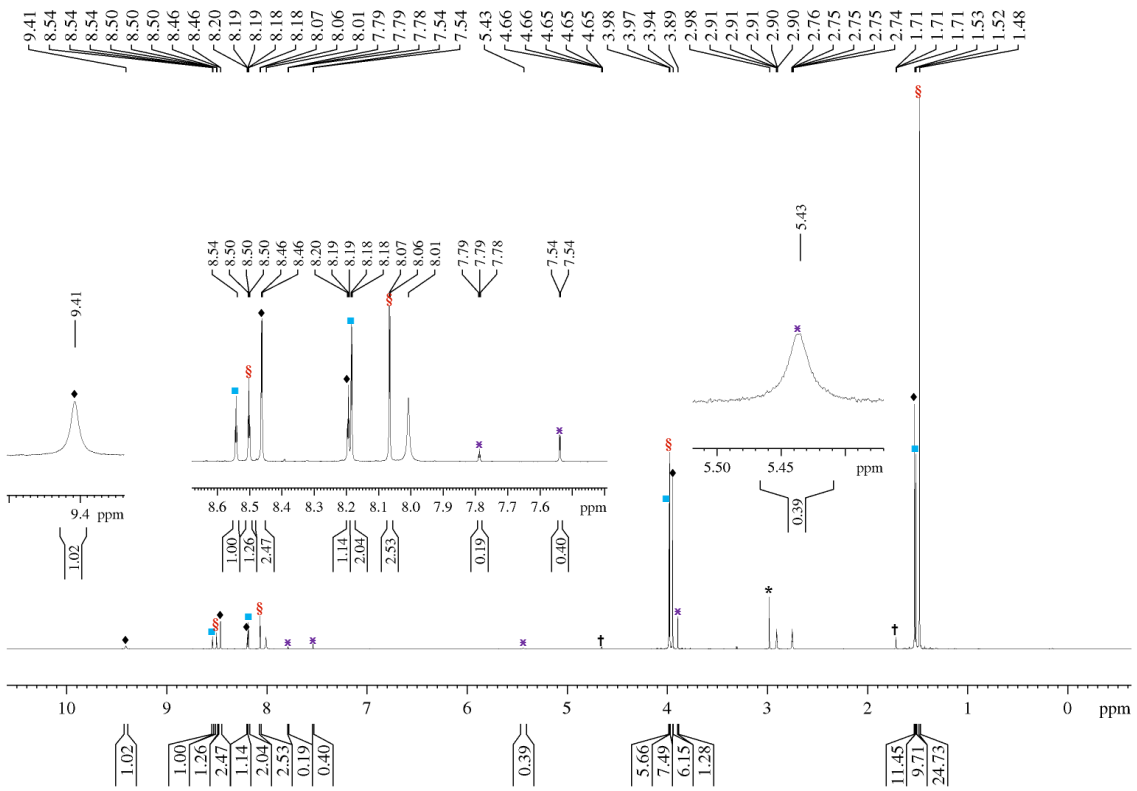

Figure A87. [1]H NMR spectrum of compound **1** product mixture in DMF-d_7 solvent at 85 °C. Peaks associated with set **A** (*anti*-rotamers of compound **1**, *anti*-**1**), set **B** [doubly Boc-protected derivative of compound **1**, $(Boc)_2$-**1**], and set **C** (imidic acid tautomers of compound **1**, tautomer-**1**), and the deprotected derivative of compound **1** are designated by the symbols ♦, §, ■, and x respectively. Peak associated with water residue is labeled with the symbol *. Peaks associated with isobutylene are denoted by the symbol †.

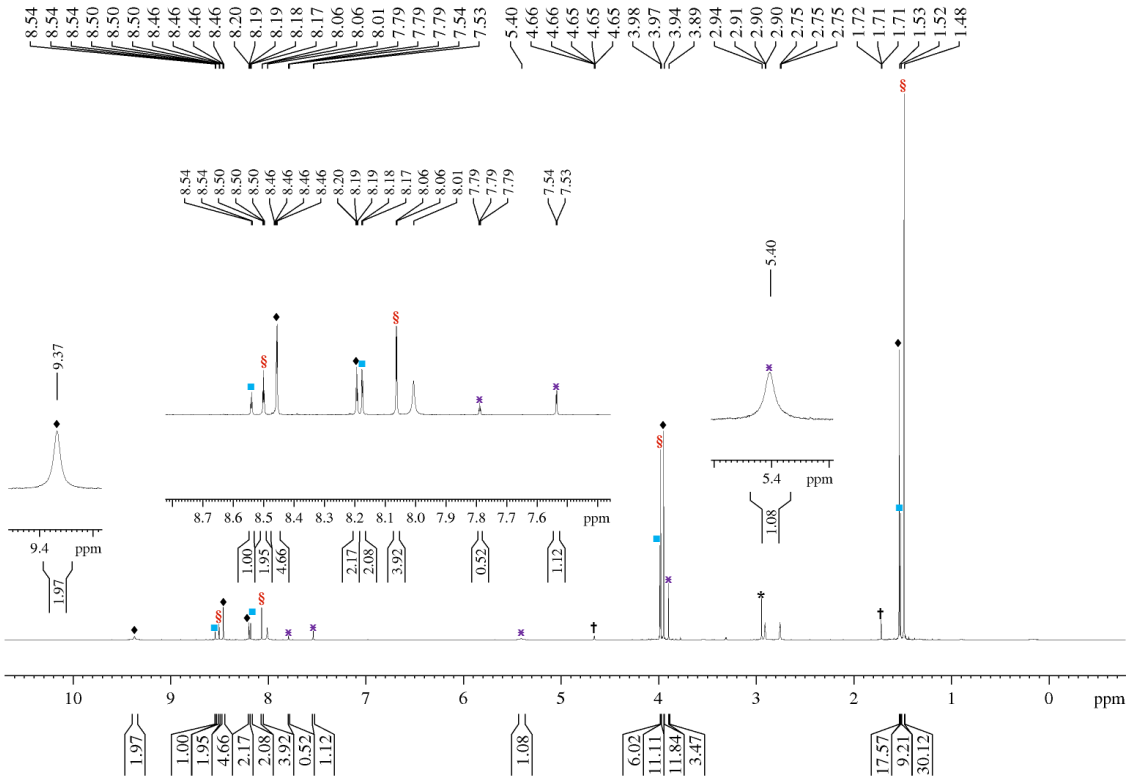

Figure A88. ^{1}H NMR spectrum of compound **1** product mixture in DMF-d_7 solvent at 90 °C. Peaks associated with set **A** (*anti*-rotamers of compound **1**, *anti*-**1**), set **B** [doubly Boc-protected derivative of compound **1**, $(Boc)_2$-**1**], and set **C** (imidic acid tautomers of compound **1**, tautomer-**1**), and the deprotected derivative of compound **1** are designated by the symbols ♦, §, ■, and x respectively. Peak associated with water residue is labeled with the symbol *. Peaks associated with isobutylene are denoted by the symbol †.

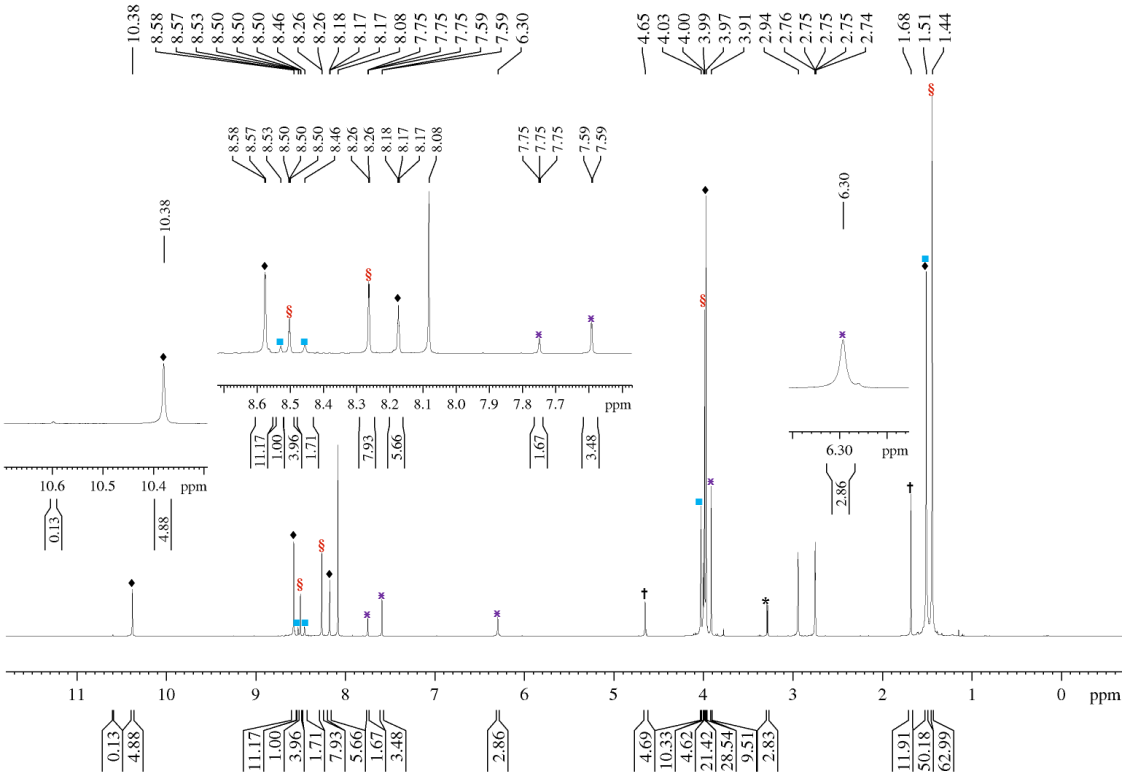

Figure A89. ^{1}H NMR spectrum of compound **1** product mixture in DMF-d_7 solvent at -40 °C. Peaks associated set **A** (*anti*-rotamers of compound **1**, *anti*-**1**), set **B** [doubly Boc-protected derivative of compound **1**, $(Boc)_2$-**1**], and set **C** (imidic acid tautomers of compound **1**, tautomer-**1**), and the deprotected derivative of compound **1** are designated by the symbols ♦, §, ■, and x respectively. Peak associated with water residue is labeled with the symbol *. Peaks associated with isobutylene are denoted by the symbol †.

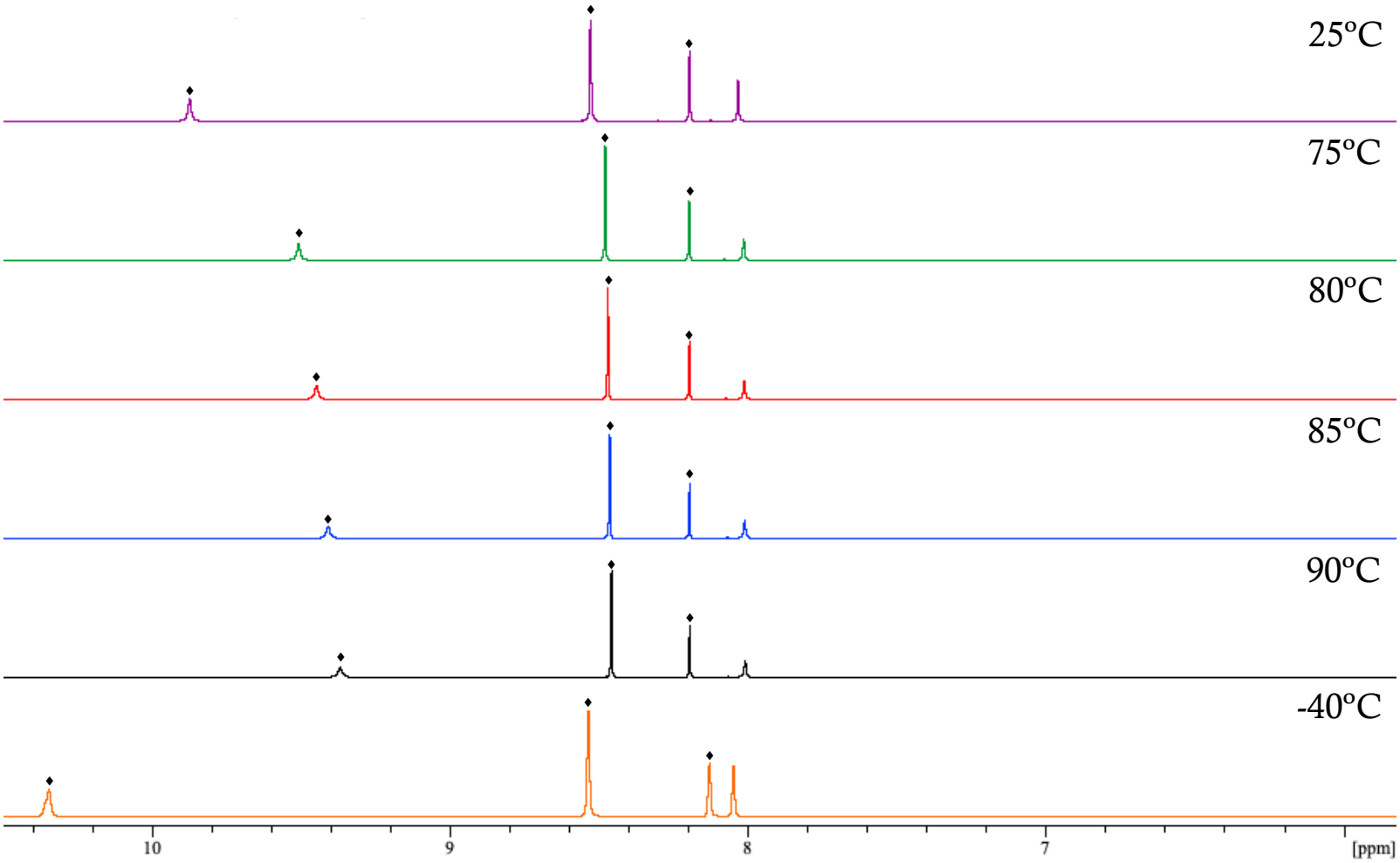

Figure A90. ^{1}H NMR spectrum of the *anti*-rotamers of compound **1** in DMF-d_7 solvent at 25 °C to 90 °C. Peaks associated with the *anti*-rotamers of compound **1** are designated by the symbols ♦.

References

[1] Drobny, J. G. In *Ionizing Radiation and Polymers*. William Andrew: Norwich, N.Y, **2013**.

[2] Issard, H. Radiation protection by shielding in packages for radioactive materials In *Safe and Secure Transport and Storage of Radioactive Materials*. Sorenson, K. B., Ed.; Woodhead: Cambridge, UK, **2015**, 123-140.

[3] Van Grieken, R.; de Bruin, M. Nomenclature For Radioanalytical Chemistry (IUPAC Recommendations 1994). *Pure Appl. Chem*. **1994**, *66(12)*, 2513-2526.

[4] de Bruin, M. Glossary of terms used in nuclear analytical chemistry. *Pure Appl. Chem*. **1982**, *54(8)*, 1533-1554.

[5] ACS Chemistry for Life. College to Career; Chemistry Careers; Nuclear Chemistry. https://www.acs.org/content/acs/en/careers/college-to-career/chemistry-careers/nuclear-chemistry.html (accessed May 18th, 2020).

[6] Reddy, V. P. *General Aspects of Organofluorine Compounds*. In *Organofluorine Compounds in Biology and Medicine*. Elsevier, **2015**.

[7] Wermuth, C. G.; Ciapetti, P.; Giethlen, B.; Bazzini, P. *Strategy and Drug Research*. In *Comprehensive Medicinal Chemistry II*, 2nd ed.; Taylor, J. B.; Triggle, D. J.; Elsevier, 2007.

[8] Jacobson, O.; Kiesewetter, D. O.; Chen, X. Fluorine-18 Radiochemistry, Labeling Strategies and Synthetic Routes. *Bioconjugate Chem.* **2015**, *26*, 1–18.

[9] Pretze, M.; Grosse-Gehling, P.; Mamat, C. Cross-Coupling Reactions as Valuable Tool for the Preparation of PET Radiotracers. *Molecules*. **2011**, *16(2)*, 1129– 1165.

[10] Meanwell, N. A. Fluorine and Fluorinated Motis in the Design and Application of Bioisosteres for Drug Design. *J. Med. Chem*. **2018**, *61*, 5822-5880.

[11] Gupta, V. P. Characterization of Chemical Reactions. In *Principles and Applications of Quantum Chemistry*.; Academic Press: London, **2016**, 385-433.

[12] Patani, G. A.; LaVoie, E. J. Bioisosterism: A Rational Approach in Drug Design. *Chem. Rev.* **1996**, *96*, 3147-3176.

[13] Kawada, K.; Iwamoto, M.; Sakai, Y. Mechanisms underlying ^{18}F-fluoroeoxyglucose accumulation in colorectal cancer. *World. J. Radiol*. **2016**, *8(11)*, 880-886.

[14] Yu, S. Review of F-FDG Synthesis and Quality Control. *Biomed. Imaging. Interv. J*. **2006**, *2(4)*, 1-11.

[15] Treibs, A.; Kreuzer, F. H. Elektrophile Substitution an Pyrrolen mit Acylchloriden. *Justus Liebigs Ann. Chem*. **1969**, *721*, 116-120.

[16] Gupta, M.; Parvathi, K.; Mula, S.; Maity, D. K.; Ray, A. K. Enhanced fluorescence of aqueous BODIPY by interactions with cavitand cucurbit[7]uril. *Photochem. Photobiol. Sci*. **2017**, *16*, 499-506.

[17] Awuah, S. G.; You, Y. Boron dipyrromethene (BODIPY)-based photosensitizers for photodynamic therapy. *RSC. Adv*. **2012**, *2*, 11169-11183.

[18] Yilmas, M. D.; Bozdemir, O. A.; Akkaya, E. U. Light Harvesting and Efficient Energy Transfer in a Boron-dipyrrin (BODIPY) Functionalized Perylenediimide Derivative. *Org. Lett.* **2006**, *8(13)*, 2871-2873.

[19] Kowada, T.; Maeda, H.; Kikuchi, K. BODIPY-based probes for the fluorescence imaging of biomolecules in living cells. *Chem. Soc. Rev*. **2015**, *44*, 4953-4972.

[20] Kamkaew, A.; Lim, S. H.; Lee, H. B.; Kiew, L. V.; Chung, L. Y.; Burgess, K. BODIPY dyes in photodynamic therapy. *Chem. Soc. Rev.* **2013,** *42*, 77-88.

[21] Dolmans, D.; Fukumura, D.; Jain, R. K. Photodynamic therapy for cancer. *Nat. Rev. Cancer* **2003**, *3*, 380-387.

[22] Zhang, J. Design and Development of BODIPY-Based Fluorescent Probes for Sensing and Imaging of Cyanide, Zn(II) Ions, Lysosomal pH and Cancer Cells. Master's Thesis, Michigan Technological University, Houghton, MI, **2015**.

[23] Llano, R. S.; Zaballa, E. A.; Bañuelos, J.; Durán, C. F. A. G.; Vázquez, J. L. B.; Cabrera, E. P.; Arbeloa, I. L. Tailoring the Photophysical Signatures of BODIPY Dyes: Toward Fluorescence Standards Across the Visible Spectral Region. In *Photochemistry and Photophysics – Fundamentals to Applications*; Saha, S.; Mondal, S., Ed.; BoD-Books on Demand, **2018**.

[24] Zha, J-. Y.; Lin, Y-. H.; Xu, J-. C.; Zhang, Y-. L.; Zeng, L-. T. Synthesis and Spectroscopic Properties of Some Novel BODIPY Dyes. *Spectroscopy and Spectral Analysis*. **2014**, *34(11)*, 3034-3039.

[25] Loudet, A.; Burgess, K. BODIPY Dyes and Their Derivatives: Syntheses and Spectroscopic Properties. *Chem. Rev*. **2007**, *107*, 4891-4932.

[26] Boens, N.; Leen, V.; Dehaen, W. Fluorescent indicators based on BODIPY. *Chem. Soc. Rev*. **2012**, *41*, 1130-1172.

[27] Thermo Fisher Scientific. BODIPY Dyes Series-Section 1.4. https://www.thermofisher.com/ca/en/home/references/molecular-probes-the-handbook/fluorophores-and-their-amine-reactive-derivatives/bodipy-dye-series.html. (accessed March 16th, 2018).

[28] Jaffer, F. A.; Libby, P.; Weisslerder, R. Optical and multimodality molecular imaging: insights into atherosclerosis. *Arterioscler. Thromb. Vasc. Biol*. **2009**, *29*, 1017-1024.

[29] Wang, X.; Connolly, T. M.; Biomarkers of Vulnerable Atheromatous Plaques: Translational Medicine Perspectives. In *Advances in Clinical Chemistry;* Makowski, G. S., Ed.; Academic Press: London, 2010; Vol. 50; 1-22.

[30] Pouratian, N.; Toga, A. W. Optical Imaging Based on Intrinsic Signals. In *Brain Mapping: The Methods*, 2nd ed.; Toga, A. W.; Mazziotta, J. C. Ed.; Academic Press: London, 2002;. 97-140.

[31] Dang, X.; Bardhan, N. M.; Qi, J.; Gu, L.; Eze, N. A.; Lin, C-W.; Kataria, S.; Hammond, P. T.; Belcher, A. M. Deep-tissue optical imaging of near cellular-sized features. *Scientific Reports*. **2019**, *9*, 1-12.

[32] Ehman, R. L.; Hendee, W. R.; Welch, M. J.; Dunnick, N. R.; Bresolin, L. B.; Arenson, R. L. Blueprint for imaging in biomedical research. *Radiology*, **2007**, *244*, 12-27.

[33] Hayes, J. S. Synthesis, Characterization, and Evaluation of Novel BODIPY Dyes With Theranostic Applications. Ph. D. Dissertation, Louisiana State University and Agricultural and Mechanical College, Baton Rouge, LA, 2010.

[34] Chen, K.; Chen, X. Positron Emission Tomography Imaging of Cancer Biology: Current Status and Future Prospects. Semin Oncol. 2011, 38(1), 70-86.

[35] Conti, M.; Eriksson, L. Physics of pure and non-pure positron emitters for PET: a review and a discussion. *EJNMMI Phys*. **2016**, *3*, 1-17.

[36] Ametamey, S. M.; Honer, M.; Schubiger, P. A. Molecular Imaging with PET. *Chem. Rev*. **2008**, *108*, 1501-1516.

[37] Thompson, S.; Kilbourn, M. R.; Scott, P. J. H. Radiochemistry, PET Imaging, and the Internet of Chemical Things. *ACS. Cent. Sci*. **2016**, *2(8)*, 497-505.

[38] Berger, A. Positron emission tomography. *BMJ*. **2003**, *326(7404)*, 1449.

[39] Vaquero, J. J.; Kinahan, P. Positron Emission Tomography: Current Challenges and Opportunities for Technological Advances in Clinical and Preclinical Imaging Systems. *Annu Rev Biomed Eng*. **2015**, *17*, 385-414.

[40] Fox, P. T.; Mintun, M. A.; Raichle, M. E.; Miezin, F. M.; Allman, J. M.; Van Essen, D. C. Mapping human visual cortex with positron emission tomography. *Nature*, **1986**, *323*, 806-809.

[41] Singh, D.; Gott, M. D.; Pietzsch, H-. J.; Stephan, H. Nuclear and Optical Dual-Labelled Imaging Agents Design and Challenges. *Nuklearmedizin*. **2016**, *55(2)*, 41-50.

[42] Encyclopedia Britannica. Brønsted-Lowry theory chemistry. https://www.britannica.com/science/Bronsted-Lowry-theory (accessed Nov. 13th, 2019).

[43] Chemistry LibreTexts. Brønsted Concepts of Acids and Bases. https://chem.libretexts.org/Bookshelves/Physical_and_Theoretical_Chemistry_Textbook_Maps/Supplemental_Modules_(Physical_and_Theoretical_Chemistry)/Acids_and_Bases/Acid/Bronsted_Concept_of_Acids_and_Bases (accessed Nov. 13th, 2019).

[44] Khan Academy. Brønsted-Lowry acid base theory. https://www.khanacademy.org/science/chemistry/acids-and-bases-topic/acids-and-bases/a/bronsted-lowry-acid-base-theory (accessed Nov. 13th, 2019).

[45] Clugston, M.; Flemming, R. *Advanced Chemistry: A new mainstream text for the new specifications*; OUP Oxford: Oxford, United Kingdom, 2000; pp 208.

[46] Hendricks, J. A.; Keliher, E. J.; Wan, D.; Hilderbrand, S. A.; Weissleder, R.; Mazitschek, R. Synthesis of [^{18}F]BODIPY as Bifunctional Reporter for Hybrid Optical/PET imaging. *Angew. Chem. Int. Ed.* **2012**, *51*, 4603-4606; *Angew. Chem.* **2012**, *124*, 4681-4684.

[47] BCcampus. Chapter 15. Equilibria of Other Reaction Classes. 15.2 Lewis Acids and Bases. https://opentextbc.ca/chemistry/chapter/15-2-lewis-acids-and-bases/ (accessed Nov. 14th, 2019).

[48] Patrick, G. *G4 Lewis acids and bases*. In *Instant Notes in Organic Chemistry*, 2nd ed. Taylor & Francis: New York, USA, 2004; pp 91.

[49] Jensen, W. B. The Lewis Acid-Base Definitions: A Status Report. *Chem Rev*. **1978**, *78 (1)*, 1-22.

[50] Bodner Research Lab. The Lewis Definitions of Acids and Bases. https://chemed.chem.purdue.edu/genchem/topicreview/bp/ch11/lewis.php (accessed Nov. 17th, 2019).

[51] Priyam Study Centre. Hard soft acids-bases HSAB principles. https://www.priyamstudycentre.com/2019/09/hard-soft-acid-base-list.html (accessed May 17th, 2020).

[52] Pearson, R. G. Hard and Soft Acids and Bases. *J. Am. Chem. Soc.* **1963**, *85(16)*, 3533- 3539.

[53] Liu, S.; Lin, T-.P.; Li, D.; Leamer, L.; Shan, H.; Li, Z.; Gabbaï, F. P.; Conti, P. S. Lewis Acid-Assisted Isotopic 18F-19F Exchange in BODIPY Dyes: Facile Generation of Positron Emission Tomography/Fluorescence Dual Modality Agents for Tumor Imaging. *Theranostics*, **2013**, *3(3)*, 181-189.

[54] Gutmann VHT. The solvent benzoyl chloride. I. The formation of anhydrous chlorides and their behavior in benzoyl chloride. *Monatsh Chem.* **1957**, *88*, 216-27.

[55] Warram, J. M.; de Boer, E.; Sorace, A. G.; Chung, T. K.; Kim, H.; Pleijhuis, R. G.; van Dam, G. M.; Rosenthal, E. L. Antibody-based imaging strategies for cancer. *Cancer and Metastasis Reviews.* **2014**, *33*, 809-822.

[56] Chari, R. V. J.; Miller, M. L.; Widdison, W. C. Antibody-drug conjugates: an emerging concept in cancer therapy. *Angew. Chem. Int. Ed. Engl.* **2014**, *53*, 3796-3827.

[57] Perez, H. L.; Cardarelli, P. M.; Deshpande, S.; Gangwar, S. Antibody-drug conjugates: current status and future directions. *Drug. Discov. Today*. **2014**, *19*, 869-881.

[58] Diamantis, N.; Banerji, U. Antibody-drug conjugates-an emerging class of cancer treatment. *Br. J. Cancer*. **2016**, *114*, 362-367.

[59] Diamantis, N.; Banerji, U. Antibody-drug conjugates-an emerging class of cancer treatment. *British Journal of Cancer*. **2016**, *114*, 362-367.

[60] Tsuchikama, K.; An, Z. Antibody-drug conjugates: recent advances in conjugation and linker chemistries. *Protein & Cell*. **2018**, *9*, 33-46.

[61] Nolting, B. Linker Technologies for Antibody-Drug Conjugates. In *Antibody-Drug Conjugates*; Ducry, L., Ed.; Humana Press: Totowa, NJ, **2013.**

[62] Tsuchikama, K.; An, Z. Antibody-drug conjugates: recent advances in conjugation and linker chemistries. *Protein Cell*. **2018**, *9*(1), 33-46.

[63] Tang, H.; Liu, Y.; Yu, Z.; Sun, M.; Lin, L.; Liu, W.; H, Q.; Wei, M.; Jin, Y. The Analysis of Key Factors Related to ADCs Structural Design. *Front. Pharmacol*. **2019**, *10*, 1-11.

[64] Lu, J.; Jiang, F.; Lu, A.; Zhang, G. Linkers having a crucial role in antibody-drug conjugates. *Int. J. Mol. Sci.* **2016**, *17(4)*, 1-22.

[65] Vidarsson, G.; Dekkers, G.; Rispens, T. IgG Subclasses and Allotypes: From Structure to Effector Functions. *Front. Immunol*. **2014**, *5*, 1-17.

[66] Chalker, J. M.; Bernardes, G. J. L.; Lin, Y. A.; Davis, B. G. Chemical Modification of Proteins at Cysteine: Opportunities in Chemistry and Biology. *Chem.-Asian. J*. **2009**, *4*, 630.

[67] Boutureira, O.; Bernardes, G. J. L. Advances in Chemical Protein Modification. *Chem. Rev*. **2015**, *115*, 5, 2174-2195.

[68] Wakankar, A. A.; Feeney, M. B.; Rivera, J.; Chen, Y.; Kim, M.; Sharma, V. K.; Wang, J, Y. Trastuzumab-DM1: Changes due to Modification and Conjugation Processes. *Bioconjugate Chem.* **2010**, *21*, 1588-1595.

[69] Wang, L.; Amphlett, G.; Blattler, W. A.; Lambert, J. M.; Zhang, W. Structural characterization of the maytansinoid-monoclonal antibody immunoconjugate, huN901-DM1, by mass spectrometry. *Protein Sci*. **2005**, *14*, 2436-2446.

[70] McCombs, J. R.; Owen, S. C. Antibody Drug Conjugates: Design and Selection of Linker, Payload and Conjugation Chemistry. *AAPS. L*. **2015**, *17(2)*, 339-351.

[71] Sun, M, M. C.; Beam, K. S.; Cerveny, C. G.; Hamblett, K. J.; Blackmore, R. S.; Torgov, M. Y.; Handley, F. G. M.; Ihle, N. C.; Senter, P. D.; Alley, S. C. Reduction-Alkylation Strategies for the Modification of Specific Monoclonal Antibody Disulfides. *Bioconjugate Chem*. **2005**, *16*, 1282-1290.

[72] Gaciarz, A. Production of Antibody Fragments and Other Disulfide Bonded Proteins in the Cytoplasm of *Escherichia coli*. Ph.D. Dissertation, University of Oulu, Finland, **2017**.

[73] Absolute antibody. Antibody Structure. https://absoluteantibody.com/antibody-resources/antibody-overview/antibody-structure/ (accessed April 7th, 2020).

[74] Liu, H.; May, K. Disulfide bond structures of IgG molecule Structural variations, chemical modifications and possible impacts to stability and biological function. *mAbs*, **2012**, *4*, 17-23.

[75] Albone, E. F.; Spidel, J. L.; Cheng, X.; Park, Y. C.; Jacob, S.; Milinichik, A. Z.; Vaessen, B.; Butler, J.; Bradford Kline, J.; Grasso, L. Generation of therapeutic immunoconjugates via Residue-Specific Conjugation Technologies (RESPECT) utilizing a native cysteine in the light chain framework of *Oryctolagus cuniculus*. *Cancer Biol Ther*. **2017**, *18(5)*, 347-357.

[76] Lodish, H.; Berk, A.; Zipursky, S. L.; Matsudaira, P.; Baltimore, D.; Darnell, J. Protein Structure and Function. In *Molecular Cell biology*, 4th ed; W. H. Freeman: New York, 2000.

[77] Brocchini, S.; Godwin, A.; Balan, S.; Choi, J-W.; Zloh, M.; Shaunak, S. Disulfide bridge based PEGylation of proteins. *Advanced Drug Delivery Reviews*. **2008**, *60(1)*, 3-12.

[78] Khoo, K. K.; Norton, R. S. Role of Disulfide Bonds in Peptide and Protein Conformation. In *Amino Acids, Peptides and Proteins in Organic Chemistry Volume 5, Analysis and Function of Amino Acids and Peptides*, 1st ed; Hughes, A. B., Ed.; Wiley: Germany, **2012.**

[79] Shaunak, S.; Godwin, A.; Choi, J-W.; Balan, S.; Pedone, E.; Vijayarangam, D.; Heidelberger, S.; Teo, I.; Zloh, M.; Brocchini, S. Site-specific PEGylation of native disulfide bonds in therapeutic proteins. *Nature chemical Biology*. **2006**, *2*, 312-313.

[80] Wedemeyer, W. J.; Welker, E.; Narayan, M.; Scheraga, H. A. Disulfide Bonds and Protein Folding. *Biochemistry*, **2000**, *39(15)*, 4207-4216.

[81] Guo, Z. Y.; Jia, X. Y.; Feng, Y. M. Replacement of the interchain disulfide bridge-forming amino acids A7 and B7 by glutamate impairs the structure and activity of insulin. *Biological Chemistry*. **2004**, *385(12)*, 1171-1175.

[82] Smith, M. E. B.; Schumacher, F. F.; Ryan, C. P.; Tedaldi, L. M.; Papaioannou, D.; Waksman, G.; Caddick, S.; Baker, J. R. Protein Modification, Bioconjugation, and Disulfide Bridging Using Bromomaleimides. *J. Am. Chem. Soc*. **2010**, *132(6)*, 1960-1965.

[83] Shen, B. Q.; Xu, K.; Liu, L.; Raab, H.; Bhakta, S.; Kendrick, M.; Parsons-Reponte, K. L.; Tien, J.; Yu, S-F.; Mai, E.; Li, D.; Tibbitts, J.; Baudys, J.; Saad, O. M.; Scales, S. J.; McDonald, P. J.; Hass, P. E.; Eigenbrot, C.; Nguyen, T.; Solis, W. A.; Fuji, R. N.; Flagella, K. M.; Patel, D.; Spencer, S. D.; Khawli, L. A.; Ebens, A.; Wong, W. L.; Vandlen, R.; Kaur, S.; Sliwkowski, M. X.; Scheller, R. H.; Polakis, P.; Junutula, J. R. Conjugation site modulates the *in vivo* stability and therapeutic activity of antibody-drug conjugates. *Nat. Biotech*. **2012**, *30(2)*, 184-191.

[84] Nunes, J. P. M.; Morais, M.; Vassileva, V.; Robinson, E.; Rajkumar, V. S.; Smith, M. E.; Pedley, R. B.; Caddick, S.; Baker, J. R.; Chudasama. Functional native disulfide bridging enables delivery of a potent, stable and targeted antibody-drug conjugate (ADC). *Chem. Commun*., **2015**, *51*, 10624-1627.

[85] Jain, N.; Smith, S. W.; Ghone, S.; Tomczuk, B. Current ADC linker chemistry. *Pharm. Res.* **2015**, *32*, 3526-3540.

[86] Luo, Q.; Tap, Y.; Sheng, W.; Lu, J.; Wang, H. Dinitroimidazoles as bifunctional bioconjugation reagents for protein functionalization and peptide macrocyclization. *Nature Communications*. **2019**, *10*, 1-9.

[87] Senter, P. D.; Sievers, E. L. The discovery and development of brentuximab vedotin for use in relapsed Hodgkin lymphoma and systemic anaplastic large cell lymphoma. *Nat. Biotechnol*. **2012**, *30*, 631-637.

[88] Dan, N.; Setua, S.; Kashyap, V. K.; Khan, S.; Jaggi, M.; Yallapu, M. M.; Chauhan, S. C. Antibody-Drug Conjugates for Cancer Therapy: Chemistry to Clinical Implications. *Pharmaceuticals*. **2018**, *11*, 32, 1-22.

[89] Baldwin, A. D., Kiick, K. L.; Tunable Degradation of Maleimide-Thiol Adducts in Reducing Environments. *Bioconjugate Chem*. **2011**, *22*, 10, 1946-1953.

[90] Alley, S. C.; Benjamin, D. R.; Jeffrey, S. C.; Okeley, N. M.; Meyer, D. L.; Sanderson, R. J.; Senter, P. D.; *Bioconjugate. Chem*. **2008**, *19*, 759-765.

[91] Baldwin, A. D.; Kiick, K. L.; *Bioconjugate. Chem*. **2011**, *22*, 1946-1953.

[92] Shen, B. Q.; Xu, K.; Liu, L.; Raab, H.; Bhakta, S.; Kendrick, M.; Parsons-Reponte, K. L.; Tien, J.; Yu, S. F.; Mai, E.; Li, D.; Tibbitts, J.; Baudys, J.; Saad, O. M.; Scales, S. J.; McDonald, P. J.; Hass, P. E.; Eigenbrot, C.; Nguyen, T.; Soils, W. A.; Fuji, R. N.; Flagella, K. M.; Patel, D.; Spencer, S. D.; Khawli, L. A.; Ebens, A.; Wong, W. L.; Vandlen, R.; Kaur, S.; Sliwkowski, M. X.; Sheller, R. H.; Polakis, P.; Junutula, J. R. *Nat. Biotechnol*. **2012**, *30*, 184-189.

[93] Lin, D.; Saleh, S.; Liebler, D. C.; *Chem. Res. Toxicol*. **2008**, *21*, 2361-2369.

[94] Cal, P. M. S. D.; Bernardes, G. J. L.; Gois, P. M. P. Cysteine-Selective Reactions for Antibody Conjugation. *Angew. Chem. Int. Ed*. **2014**, *53*, 10585-10587.

[95] Adumeau, P.; Davydova, M.; Zeglis, B. M. Thiol-Reactive Bifunctional Chelators for the Creation of Site-Selectively Modified Radioimmunoconjugates with Improved Stability. *Bioconjugate Chem.* **2018**, *29*, 1364-1372.

[96] Zhang, D.; Devarie-Baez, N. O.; Li, Q.; Lancaster Jr., J. R.; Xian, M. Methylsulfonyl Benzothiazole (MSBT): A Selective Protein Thiol Blocking Reagent. *Org. Lett*. **2012**, *14*, 13, 3396-3399.

[97] Toda, N.; Asano, S.; Barbas, C. F. Rapid, stable, Chemoselective labeling of thiols with Julia−Kocieński-like reagents: A serum-stable alternative to maleimide-based protein conjugation. *Angew. Chem., Int. Ed*. **2013**, *52(48)*, 12592-12596.

[98] Chiotellis, A.; Sladojevich, F.; Mu, L.; Müller Herde, A.; Valverde, I. E.; Tolmachev, V.; Schibli, R.; Ametamey, S. M.; Mindt, T. L. Novel chemoselective ^{18}F-radiolabeling of thiol-containing biomolecules under mild aqueous conditions. *Chem. Commun*. **2016**, *52*, 6083-6086.

[99] Kim, J-.Y.; Sahu, S.; Yau, Y-.H.; Wang, X.; Shochat, S. G.; Nielsen, P. H.; Dueholm, M. S.; Otzen, D. E.; Lee, J.; Salido Delos Santos, M. M.; Yam, J. K. H.; Kang, N-. Y.; Park, S-. J.; Kwon, H.; Seviour, T.; Yang, L.; Givskov, M.; Chang, Y-. T. Detection of Pathogenic Biofilms with Bacterial Amyloid Targeting Fluorescent Probe, CDy11-FL. *J. Am. Chem. Soc.* **2016**, *138*, 402-407.

[100] Wu, W.; Jin, Y.; Bai, F.; Jin, S. Pseudomonas aeruginosa. In *Molecular Medicinal Microbiology*, 2nd ed.; Tang, Y-.W.; Sussman, M.; Liu, D.; Poxton, I.; Schwartzman. J., Ed.; Academic Press: London, 2015; Vol. 2; 753-767.

[101] Prince, A. S. Pseudomonas aeruginosa. In *Principles and Practice of Pediatric Infectious Diseases*, 4th ed. Long, S. S.; Pickering, L. K.; Prober, C. G., Ed.; Churchill Livingstone: London, 2012; Vol 3; 842-846.e2.

[102] Rolsma, S.; Frank, D. W.; Barbieri, J. T. Pseudomonas aeruginosa Toxins. In *The Comprehensive Sourcebook of Bacterial Protein Toxins*, 4th ed. Ladant, D.; Popoff, M. R.; Alouf, J. E., Ed.; Academic Press: London, 2015; 133-160.

[103] Colmer-Hamood, J. A.; Dzvova, N.; Kruczek, C.; Hamood, A. N. *In Vitro* Analysis of Pseudomonas aeruginosa Virulence Using Conditions That Mimic the Environment at Specific Infection Sites. In *Progress in Molecular Biology and Translational Science.* San Franscisco, M.; San Franscisco, B., Ed. Academic Press: London, 2016; Vol. 142; p 151-191.

[104] Moghaddam, M. M.; Khodi, S.; Mirhosseini, A. Quarum Sensing in Bacteria and a Glance on *Pseudomonas aeruginosa. Clin Microbial*. **2014**, *3(4*), 156.

[105] Maurice, N. M.; Bedi, B.; Sadikot, R. T. *Pseudomonas aeruginosa* Biofilms: Host Response and Clinical Implications in Lung Infections. Am J Respir Cell Mol Biol. [Online early access] DOI: 10.1165/rcmb.2017-0321TR. Published online: January 26th, 2018. https://www.atsjournals.org/doi/abs/10.1165/rcmb.2017-0321TR?url_ver=Z39.88-2003&rfr_id=ori%3Arid%3Acrossref.org&rfr_dat=cr_pub%3Dpubmed (accessed March 5th, 2018).

[106] Rasamiravaka, T.; Labtani, Q.; Duez, P.; El Jaziri, M. The formation of Biofilms by *Pseudomonas aeruginosa*: A Review of the Natural and Synthetic Compounds Interfering with Control Mechanisms. *BioMed Res. Int*. **2015**, *2015*, p 1-17.

[107] Nickel, J. C.; Ruseska, I.; Wright, J. B.; Costerton, J. W. *Antimicrob. Agents Chemother.* **1985**, *27*, 619-624.

[108] Rabin, N.; Zheng, Y.; Opoku-Temeng, C.; Du, Y.; Bonsu, E.; Sintim, H. O. Agents that inhibit bacterial biofilm formation. *Future Med. Chem*. **2015**, *7(5)*, 647-671.

[109] Golemi-Kotra, D. Pseudomonas Infections. In *xPharm: The Comprehensive Pharmacology Reference*. Enna, S. J.; Bylund, D. B., Ed.; Amsterdam: Boston, 2008; p 1-8.

[110] Wilson, R.; Dowling, R. B. Pseudomonas aeruginosa and Other Related Species. *Thorax*, **1998**, *53*, 213-219.

[111] Basaran, N. C.; Ascioglu, S. Epidemiology and management of healthcare-associated bloodstream infections in non-neutropenic immunosuppressed patients: a review of the literature. *Ther. Adv. Infectious. Dis*. **2017**, *4(6)*, 171-191.

[112] Ortega, M.; Almela, M.; Soriano, A.*; et al*. Bloodstream infections among human immunodeficiency virus-infected adult patients: epidemiology and risk factors for mortality. *Eur J Clin Microbiol Infect Dis.* **2008**, *27(10)*, 969–976.

[113] Wu, M.; Li, X. *Klebsiella pneumoniae* and *Pseudomonas aeruginosa*. In *Molecular Medicinal Microbiology*, 2nd ed. Tang, Y-. W.; Sussman, M.; Liu, D.; Poxton, I.; Schwartzman, J., Ed.; Academic Press: London, 2015; Vol. 3; 1547-1564.

[114] Branski, L.K.; Al-Mousawi, A.; Rivero, H.; Jeschke, M. G.; Sanford, A. P.; Herndon, D. N. Emerging infections in burns. *Surg Infect*. **2009**, *10*, 389–397.

[115] Oluyombo, O.; Diggle, S. P.; Penfold, C. N. Competition in Biofilms Between Cystic Fibrosis Isolates of Pseudomonas aeruginosa is Driven by R-Pyocins. BioRxiv. [Online early access]. DOI: https://doi.org/10.1101/264580. Published online: February 13th, 2018. https://www.biorxiv.org/content/early/2018/02/13/264580 (accessed March 11th, 2018).

[116] Flemming, H.-C.; Wingender, J. The biofilm matrix. *Nat. Rev. Microbiol*. **2010**, *8*, 623-633.

[117] Vasdev, K.; Dewasthale, S.; Mani, I. Microbial biofilm: current challenges in health care industry. *J Appl Biotechnol Bioeng*. **2018**, *5 (3)*, 156-160.

[118] Costerton, J. W.; Lewandowski, Z.; Caldwell, D. E.; Korber, D. R.; Lappin-Scott, H. M. Microbial Biofilms. *Annu. Rev. Microbiol*. **1995**, *49*, 711-745.

[119] Palmer, J.; Flint, S.; Brooks, J. Bacterial cell attachment, the beginning of a biofilm. *J. Ind. Microbiol. Biotechnol.* **2007**, *65(7*), 3710-3713.

[120] Limoli, D. H.; Jones, C. J.; Wozniak, D. J. Bacterial Extracellular Polysaccharides in Biofilm Formation and Function. *Microbiol Spectr.* **2015**, *3(3)*, 1-30.

[121] Rabin, N.; Zheng, Y.; Opoku-Temeng, C.; Du, Y.; Bonsu, E.; Sintim, H. O. Biofilm formation mechanisms and targets for developing antibiofilm agents. *Future Med. Chem.* **2015**, *7(4)*, 493-512.

[122] Flemming, H-. C.; Wingender, J.; Szewzyk, U.; Steinberg, P.; Rice, S. A.; Kjelleberg, S. Biofilms: an emergent from of bacterial life. *Nat. Rev. Microbiol*. **2016**, *14*, 563-575.

[123] Larsen, P.; Nielson, J. L.; Dueholm, M. S.; Wetzel, R.; Otzen, D.; Nielson, P. H.; Amyloid adhesins are abundant in natural biofilms. *Environ Microbiol*. **2007**, *9*, 3077-3090.

[124] Zeng, G.; Vad, B. S.; Dueholm, M. S.; Christiansen, G.; Nilsson, M.; Tolker-Nielsen, T.; Nielsen, P. H.; Meyer, R. L.; Otzen, D. E. Functional bacterial amyloid increases Pseudomonas biofilm hydrophobicity and stiffness. *Front Microbiol*. *2015*, *6 (1099*), 1-14.

[125] Dueholm, M. S.; Petersen, S. V.; Sonderkaer, M.; Larsen, P.; Christiansen, G.; Hein, K. L.; Enghild, J. J.; Nielsen, J. L.; Nielsen, K. L.; Nielsen, P. H.; Otzen, D. E. Functionally amyloids in *Pseudomonas*. *Mol Microbiol.* **2010**, *77(4)*, 1009-1020.

[126]Romero, D.; Aguilar, C.; Losick, R.; Kolter, R. Amyloid fibers provide structural integrity to *Bacillus subtilis* biofilms. *Proc Natl Acad Sci USA*. **2010**, *107*, 2230-2234.

[127] Carlucci, G.; Carney, B.; Brand, C.; Kossatz, S.; Irwin, C. P.; Carlin, S. D.; Keliher, E. J.; Weber, W.; Reiner, T. Dual-Modality Optical/PET Imaging of PARP1 in Glioblastoma. *Mol Imaging Biol*. **2015**, *17*, 848-855.

[128] Paulus, A.; Maenen, M.; Drude, N.; Nascimento, E. B. M.; van Marken Lichtenbelt, W. D.; Mottaghy, F. M.; Bauwens, M. Synthesis, radiosynthesis and *in vitro* evaluation of ^{18}F-Bodipy-C_{16}/triglyceride as a dual modal imaging agent for brown adipose tissue. *PLOS ONE*. **2017**, *12(8)*, 1-13.

[129] Ferreira, A. B.; Cardoso, A. L.; da Silva, M. J. Tin-Catalyzed Esterification and Transesterification Reactions: A Review. *ISRN Renewable Energy*. **2012**, 1-13.

[130] B. deB. Darwent, *National Standard Reference Data Series,* National Bureau of Standards, no. 31, Washington, **1970**.

[131] Luo, Y-R. Bond Dissociation Energies. In *CRC Handbook of Chemistry and Physics*, 89th ed.; Lide, D. R. Ed.; CRC Press/ Taylor and Francis: Boca Raton, FL, **2009**.

[132] Shannon, R. D. Acta Crystallogr. In *Handbook of Chemistry and Physics*, 74th ed. Lide, D. R. Ed.; CRC Press, Boca Raton, FL, **1974**.

[133] Yang, L.; Dong, T.; Revankar, H. M.; Zhang, C-P. Recent progress on fluorination in aqueous media. *Green Chem*. **2017**, *19*, 3951-3992.

[134] Li, Z.; Chansaenpak, K.; Liu, S.; Wade, C. R.; Conti, P. S.; Gabbaï, F. P. Harvesting ^{18}F-fluoride ions in water *via* direct ^{18}F-^{19}F isotopic exchange: radiofluorination of zwitterionic aryltrifluoroborates and *in vivo* stability studies. *MedChemComm*. **2012**, *3*, 1305-1308.

[135] Zhao, H.; Leamer, L. A.; Gabbaï, F. P. Anion capture and sensing with cationic boranes: on the synergy of Coulombic effects on onium ion-centred Lewis acidity. *Dalton Trans*. **2013**, *42*, 8164-8178.

[136] Collet, C.; Vucko, T.; Ariztia, J.; Karcher, G.; Pellegrini-Moïse, N.; Lamandé-Langle, S. Fully automated radiosynthesis of [^{18}F]fluoro-*C*-glyco-c(RGDfC): exploiting all the abilities of the AllInOne synthesizer. *React. Chem. Eng*. **2019**, *4*, 2088-2098.

[137] Brooks, A. F.; Topczewski, J. J.; Ichiishi, N.; Sanford, M. S.; Scott, P. J. Lat-stage [^{18}F]fluorination: new solutions to old problems. *Chem. Sci*. **2014**, *5*, 4545-4553.

[138] Allott, L.; Da Pieve, C.; Turton, D. R.; Smith, G. A general [^{18}F]AlF radiochemistry procedure on two automated synthesis platforms. *React. Chem. Eng*. **2017**, *2*, 68-74.

[139] Boc Sciences. Best of Chemicals. Tetrabutylammonium hydrogen carbonate-CAS 17351-62-1. https://www.bocsci.com/product/tetrabutylammonium-hydrogen-carbonate-cas-17351-62-1-70141.html (accessed August 31st, 2020).

[140] Millipore Sigma. Tetraethylammonium bicarbonate. https://www.sigmaaldrich.com/catalog/product/aldrich/11268?lang=en&region=CA (accessed August 31st, 2020).

[141] Chansaenpak, K. Organoboranes as ^{18}F-Fluoride Anion Captors. Ph.D Dissertation, Texas A&M University, College Station, TX, **2015**.

[142] Khozeimeh Sarbisheh, E.; Dewaele-Le Roi, G.; Shannon, W. E.; Tan, S.; Xu, Y.; Zeglis, B. M.; Price, E. W. DiPODS: A Reagent for Site-Specific Bioconjugation via the Irreversible Rebridging of Disulfide Linkages. *Bioconjugate Chemistry*. **2020**, *31 (12)*, 2789-2806.

[143] Roos, G.; Roos, C. Isomers and Stereochemistry. In *Organic Chemistry Concepts*; Elsevier, **2015**, 1-236.

[144] Lister, D. G.; MacDonald, J. N.; Owen, N. L. *Internal Rotation and Inversion*, Academic Pres: London, UK, 1978, 87-92.

[145] Frank, J. H.; Powder-George, Y. L.; Ramsewak, R. S.; Reynolds, W. F. Variable-Temperature ^{1}H-NMR Studies on Two *C*-Glycosylflavones. *Molecules*. **2012**, *17*, 7914-7926.

[146] Katrizky, A. R.; Ramsden, C. A.; Joule, J. A.; Zhdankin, V. V. Structure of Five-Membered Rings with One Heteroatom. In *Handbook of Heterocyclic Chemistry*, 3rd Ed.; Elsevier, **2010**, 1-1010.

[147] Potapov, V. M. *Stereochemistry*; Mir Publishers: Moscow, Russia, **1978**, 27-28.

[148] Mastering Organic Chemistry. Staggered vs Eclipsed Conformations of Ethane. https://www.masterorganicchemistry.com/2020/02/28/staggered-vs-eclipsed-conformations-of-ethane/ (accessed August 10th, 2020).

[149] Cleveland, C. J.; Morris, C. Dictionary of Energy, 2nd Ed.; Elsevier, **2015**, 1-700.

[150] Scott, K. Electrochemical Principles and Characterization of Bioelectrochemical Systems. In *Microbial Electrochemical and Fuel Cells Fundamentals and Applications*.; Elsevier, **2016**, 29-66.

[151] Nagashima, H.; Martineau-Corcos, C.; Tricot, G.; Trébosc, J.; Pourpoint, F.; Amoureux, J-P.; Lafon, O. Recent Developments in NMR Studies of Aluminophosphoates. In *Annual Reports on NMR Spectroscopy*, Webb, G. A. Ed.; Academic Press, **2018**, 113-171.

[152] Roy, J. Organic Analysis Using Spectroscopic Techniques. In *A Self-Study Guide to The Principles of Organic Chemistry Key Concepts, Reaction Mechanisms, and Practice Questions for the Beginner*.; Universal Publishers, **2013**, 1-260.

[153] Cambridge Isotope Laboratories, Inc., *[NMR Solvent Data Chart]*, Cambridge Isotope Laboratories, Inc., Tewksbury, MA, **2020**.

[154] Fulmer, G. R.; Miller, A. J. M.; Sherden, N. H.; Gottlieb, H. E.; Nudelman, A.; Stoltz, B. M.; Bercaw, J. E.; Goldberg, K. I. *Organometallics* **2010**, *29*, 2176-2179.

[155] Ohta, Y.; Kamijyo, Y.; Fujii, S.; Yokoyama, A.; Yokozawa, T. Synthesis and Properties of a Variety of Well-Defined Hyperbranched N-Alkyl and N-H Polyamides by Chain-Growth Condensation Polymerization of AB2Monomers. *Macromolecules.* **2011**, *44* (13): 5112-5122.

[156] Humbert, N.; Larionov, E.; Mantilli, L.; Nareddy, P.; Besnard, C.; Guénée, L.; Mazet, C. Highly Modular C1-Symmetric Chiral (P, N) Ligands with a Stereolibile P Center: Experimental and Theoretical Studies. *Chem. Eur. J.* **2014**, *20*, 745-751.

[157] Claridge, T. D. W. Practical Aspects of High-Resolution NMR. In *High-Resolution NMR Techniques in Organic Chemistry*.; Elsevier, **2016**, 1-552.

[158] Moraczewski, A. L.; Banaszynski, L. A.; From, A. M.; White, C. E.; and Smith, B. D. Using Hydrogen Bonding to Control Carbamate C-N Rotamer Equilibria. *J. Org. Chem.* **1998**, *63*, 7258-7262.

[159] Marcovici-Mizrahi, D.; Gottlieb, H. E.; Marks, V.; and Nudelman, A. On the Stabilization of the Syn-Rotamer of Amino Acid Carbamate Derivatives by Hydrogen Bonding. *J. Org. Chem.* **1996**, *61*, 8402-8406.

[160] Khozeimeh Sarbisheh, E.; Dewaele-Le Roi, G.; Shannon, W. E.; Tan, S.; Xu, Y.; Zeglis, B. M.; Price, E. W. Supporting Information DiPODS: A Reagent for Site-Specific Bioconjugation via the Irreversible Rea-bridging of Disulfide Linkages. *Bioconjugate Chemistry*. **2020**, *31 (12)*, 2789-2806.